

Diss. ETH No. 24559

# **Multi-Objective Optimization of Power Electronics and Generators of Airborne Wind Turbines**

A thesis submitted to attain the degree of

**DOCTOR OF SCIENCES of ETH ZURICH**  
(Dr. sc. ETH Zurich)

presented by

**CHRISTOPH GAMMETER**

**MSc ETH**

born on 30.01.1985

citizen of Zürich, Switzerland

accepted on the recommendation of

Prof. Dr. Johann W. Kolar, examiner

Prof. Dr. Hans-Peter Nee, co-examiner

2017

ETH Zurich  
Power Electronic Systems Laboratory  
Physikstrasse 3 | ETL I16  
8092 Zurich | Switzerland

<http://www.pes.ee.ethz.ch>

© 2017 by Christoph Gammeter

*Für meine Frau*



# Acknowledgments

**F**IRST and foremost, I would like to thank Prof. Johann W. Kolar for giving me the opportunity to be part of the excellent working environment he has set up at the Power Electronic Systems (PES) Laboratory of ETH Zurich. I thank Prof. Dr. Hans-Peter Nee for his interest in my thesis. I sincerely appreciate that he found time to travel to Zurich to be the co-examiner at my PhD defense.

A great thanks goes to Gabriel Ortiz, who took me under his wing and taught me a great deal before, during, and after my master thesis at PES. I want to thank Florian Krismer for supervising me for the first part of my PhD. I'm grateful for the wealth of knowledge he always found time to share. I also thank Arda Tüysüz for teaching me an abundance of things about electrical machines, his support with the FEM simulations and for always keeping up the good mood.

A great thanks also goes to Jonas Huber, who accompanied me on my journey at PES from the very beginning until the very end and always kept my spirit up. I've had the pleasure to share an office with Michael Leibl, Lukas Schrittwieser, David Boillat, and Jon Azurza Anderson. Thank you Michael for all you've taught me about inductor, transformer, and filter design (and all the chocolate). Thank you Lukas for sharing all your expertise in micro-controller, FPGA and SoC programming, and your insight on industrial relevance. Thank you all for the fruitful discussions and the good times besides work. Thank you Roman Bosshard for organizing/helping me organize the PES ski-weekend year after year and ensuring that the good customs and social activities were being kept alive at the institute.

Each interaction with every single current and past PES member has contributed to making my stay at PES unforgettable. The excellent spirit of work at PES is a result of the great collaboration and mutual support among its team members: Daniel Rothmund, Dominik Bortis, Dominik Neumayr, Mattia Guacci, Mario Mauerer, Matthias Kasper, Maurus Kaufmann, Michael Flankl, Pedro Bezerra, Hirofumi Uemura, Ralph Burkart, Thomas Guillod, Toke Andersen, Patricio Cortes, Julian Böhler, Jannik Schäfer, Michalis Antivachis, Papamanolis Panteleimon, Spasoje Miric, Tobias Wellerdieck, Marcel Schuck, Patricio Peralta, Thomas Holenstein, Pascal Püntener, Oliver Knecht, and Yanick Lobsiger. I would like to thank all of them for all the good times and interesting technical discussions we had. I enjoyed the time we spent together at PES or at the various events that we organized outside of

work. I also want to thank Ivan Subotic for his help during the last part of my PhD.

I had the chance to be the thesis supervisor/co-supervisor for plenty of students. I would like to thank all of them for the good work they did. Among them, I would like to acknowledge the support of Yannick Drapela, Clemens Stadlinger, Raphael Bernhard and Franziska Bosshard, whose works contributed directly to this thesis. And a special thanks goes to Yannick for sharing the knowledge he gained from his time at the AMZ and consequently teaching me about the design and construction of electric machines.

I would like to thank Peter Albrecht, Peter Seitz, Monica Kohn-Müller, Prisca Maurantonio, Roswitha Coccia, Damaris Egger, Yvonne Schnyder-Liebherr and Beat Seiler for maintaining the clockwork organization of PES. A big thank you goes to Claudia Stucki and Markus Berger for providing us with high quality IT services.

Thanks to Martin Vogt, Daniel Wegmann and Stefan Brassel from the D-ITET Workshop for their excellent high precision work and always lending a helping hand.

I huge thanks to my brother Stephan for all his support, and especially for taking up the hobby of CNC-machining. Without the access to his Tormach PCNC the timely construction of the electric machines would not have been possible.

Finally, I would like to thank my family for everything that I am and everything that I have. And a special thanks to my wife for all her love and support, even while I'm writing this PhD thesis on our honeymoon.

Croatia, July 2017  
Christoph Gammeter

# Abstract

**I**NCREASING consumption of electric energy, environmental issues, and limited availability of fossil fuels have led to a multitude of developments related to the generation of electricity from renewable energy sources. One innovative system in this context is the Airborne Wind Turbine (AWT), which generates electricity from high altitude winds. High altitude winds are known to be more stable and faster than winds close to ground-level and, thus, enable a more reliable and effective generation of electric energy. AWTs represent a radically new and fascinating concept for future harnessing of wind power. This concept consists of realizing only the blades of a conventional wind turbine (CWT) in the form of a power kite flying at high speed perpendicular to the wind. Furthermore, the AWT is essentially a flying wing with a significantly lower construction effort of the power generation system making it economically favorable to CWTs. The AWT considered in this thesis is a flying wing with air powered on-board power generators and is tied to the ground with an approximately 1 km long tether. Because of the high flight speed of the power kite, several times the actual wind speed, only a very small swept area of the on-board turbines is required according to Betz's Law, which yields turbines of low weight for the generation of a given electric power. The tether, a fiber and cable combination, provides both the required mechanical strength and the electrical link to the ground station, which is connected to the medium voltage (MV) grid. For takeoff and landing of the power kite, the turbines act as propellers and the generators as motors, i.e. electric power is supplied so that the system can be maneuvered like a helicopter. The greatest challenge with respect to the realization of the electrical system of the AWT is to achieve light-weight generators, power converters, and a light-weight cable. In the present work the configuration of power electronics converters for the implementation of a 100 kW AWT is considered. The major aspect here is the trade-off between power-to-weight ratio (kW/kg) and efficiency.

The multi-objective optimization of the electrical machine required for the AWT system is detailed first. Presented investigations include the analysis of the power-to-weight ratio versus efficiency limits,  $\gamma$ - $\eta$  Pareto Fronts, of radial and axial flux machine topologies employing analytical models. Analytical models, describing the electromagnetic and thermal behavior are summarized. A simple optimization is performed, since the use of analytical models, instead of finite element methods,

allows the evaluation of the whole design space in a computationally efficient manner. The results reveal that the best performance in this case is achieved with a RFM Halbach inrunner reaching a power-to-weight ratio of,  $\gamma \approx 6.3 \text{ kW/kg}$ , at an efficiency of  $\eta \approx 95 \%$ . Experimental results validate the proposed design procedure.

Modeling of power electronics for multi-objective optimization is detailed with a focus on analytical semiconductor loss calculations and the optimization of forced convection cooling systems, composed of fan and parallel plate fin heat sinks. The presented investigations detail the optimization of the heat sink's fins with respect to minimum weight and the selection of a suitable fan for minimum overall system weight. A new analytical cooling system model is introduced. The calculated results are compared to the results determined with a pre-existing analytical model and Finite Element Method (FEM) simulations. The comparison to experimental results demonstrate the accuracy improvements achieved with the proposed methods. It is shown that compared to commercially available products a weight reduction of  $\approx 50 \%$  is achieved.

A voltage source inverter (VSI) is designed employing the previously detailed models. A VSI prototype is built, which achieves a power-to-weight ratio of  $18.9 \text{ kW/kg}$  and shows that the weight contribution of the VSI to the total weight of the AWT is small.

The fundamentals of the tether design are explained to outline the importance of a MV power transmission between the airborne wing of the AWT and the ground station interface to the mains. This motivates the design, the implementation, and the experimental verification of a minimum weight input series output parallel (ISOP) structured Dual Active Bridge (DAB) converter for the AWT system. The main power components of the DAB converter, in particular the bridge circuits, the actively cooled high frequency (HF) transformer and inductor, and the cooling system, which largely contribute to the total system weight, are designed and realized based on multi-objective considerations, i.e. with respect to weight and efficiency. Furthermore, the design includes all necessary considerations to realize a fully functional prototype, i.e. it also considers the auxiliary supply, the control for stable operation of the system, which also comprises an input filter, over the specified operating range, and the startup and shutdown procedure. These considerations show the complex interactions of the various system parts and reveal that a comprehensive conceptualization is necessary to arrive

at a reliable minimum weight design. Experimental results validate the proposed design procedure. The prototype features a power-to-weight ratio of 4.28 kW/kg (1.94 kW/lb) and achieves a maximum full-load efficiency of 97.5 %.

In conclusion, the essential results of the work are summarized. To enable the reader to make simplified calculations and a comparison of a CWT with an AWT, the aerodynamic fundamentals of both systems are summarized in highly simplified form in an Appendix, and numerical values are given for the 100 kW system discussed in this work.



# Kurzfassung

**S**TEIGENDER Verbrauch von elektrischer Energie, Umweltfragen und begrenzte Verfügbarkeit fossiler Brennstoffe haben zu einer Vielzahl von Entwicklungen im Zusammenhang mit der Stromerzeugung aus erneuerbaren Energiequellen geführt. Ein innovatives System in diesem Zusammenhang ist eine fliegende Windturbine, die Strom aus Höhenwinden erzeugt. Höhenwinde sind dafür bekannt stabiler und schneller zu sein als der Wind in der Nähe des Bodenniveaus und ermöglichen so eine zuverlässigere und effektivere Erzeugung von elektrischer Energie. Fliegende Windturbinen stellen ein radikal neues und faszinierendes Konzept für die zukünftige Nutzung von Windenergie dar. Dieses Konzept besteht darin, nur die Rotorblätter einer konventionellen Windturbine in Form eines Drachen zu realisieren, welcher mit hoher Geschwindigkeit senkrecht zum Wind fliegt. Damit ist die fliegende Windturbine im Wesentlichen ein fliegendes Rotorblatt mit einem deutlich geringeren Bauaufwand des Stromerzeugungssystems, was es wirtschaftlich lukrativer macht als konventionelle Windturbinen. Die fliegende Windturbine, die in dieser Arbeit betrachtet wird, ist ein fliegendes Rotorblatt mit propellerbetriebenen Bordnetzgeneratoren und ist mit einem ungefähr 1 km langen Kabel an den Boden gebunden. Wegen der hohen Fluggeschwindigkeit, ein Vielfaches der tatsächlichen Windgeschwindigkeit, ist nach dem Betz-Gesetz nur eine sehr kleine von den Turbinenpropeller überstrichene Fläche erforderlich, was den Einsatz von Generatoren mit geringem Gewicht für die Erzeugung einer gegebenen elektrischen Leistung ermöglicht. Das Kabel, eine Faser- und Leiterkombination bietet sowohl die erforderliche mechanische Festigkeit als auch die elektrische Verbindung zur Bodenstation, die mit dem Mittelspannungsnetz verbunden ist. Für den Start und die Landung des Drachen wirken die Turbinen als Propeller und die Generatoren als Motoren, d.h. der fliegende Teil wird mit elektrischer Energie versorgt, sodass das System wie ein Hubschrauber manövriert werden kann. Die grösste Herausforderung in Bezug auf die Realisierung der elektrischen Anlage der fliegenden Windturbine ist die Herstellung von Leichtbaugeneratoren, Stromrichtern und eines leichten Kabels. In der vorliegenden Arbeit wird die Konfiguration von Leistungselektronik-Wandlern für die Implementierung einer 100 kW fliegenden Windturbine behandelt. Der Hauptaspekt ist hierbei der Kompromiss zwischen dem Leistungsgewicht (kW/kg) und dem Wirkungsgrad.

Die Mehrziel-Optimierung der für das fliegende Windturbinensystem

benötigten elektrischen Maschine wird zuerst beschrieben. Die Untersuchungen beinhalten die Analyse des Leistung-zu-Gewicht Verhältnisses gegenüber Effizienzgrenzwerten,  $\gamma$ - $\eta$  Pareto Fronten, von Radial- und Axialflussmaschinentopologien mit analytischen Modellen. Analytische Modelle, die das elektromagnetische und thermische Verhalten beschreiben, sind zusammengefasst. Eine einfache Optimierung wird durchgeführt, da der Einsatz von analytischen Modellen anstelle von Finite-Elemente-Methoden die Auswertung des gesamten Designraums rechnerisch effizient ermöglicht. Die Ergebnisse zeigen, dass die beste Leistung in diesem Fall mit einer Radialflussmaschine mit Halbach Rotor erreicht wird, und ein Leistung-zu-Gewicht-Verhältnis von  $\gamma \approx 6.3 \text{ kW/kg}$  resultiert, bei einer Effizienz von  $\eta \approx 95 \%$ . Experimentelle Ergebnisse bestätigen das vorgeschlagene Designverfahren.

Die Modellierung der Leistungselektronik für die Mehrziel-Optimierung wird beschrieben mit Fokus auf analytischen Halbleiterverlustberechnungen und der Optimierung Zwangskonvektionskühlsystemen, bestehend aus Lüfter und Kühlkörpern mit durch parallele Platten gebildeten Finnen. Die vorgestellten Untersuchungen beschreiben die Optimierung der Kühlkörperfinnen in Bezug auf Mindestgewicht und die Auswahl eines geeigneten Lüfters für minimales Gesamtsystemgewicht. Ein neues analytisches Kühlsystemmodell wird eingeführt, die berechneten Ergebnisse werden mit den Ergebnissen verglichen, die mit einem bereits vorhandenen analytischen Modell und Finite-Element-Methoden (FEM) Simulationen ermittelt wurden. Der Vergleich mit experimentellen Ergebnissen zeigt die mit den vorgeschlagenen Methoden erzielten Genauigkeitsverbesserungen. Es wird gezeigt, dass im Vergleich zu handelsüblichen Produkten eine Gewichtsreduktion von  $\approx 50 \%$  erreichbar ist.

Ein Wechselrichter mit eingepprägter Eingangsspannung wird mit den vorher detaillierten Modellen konzipiert. Es wird ein Prototyp erstellt, der ein Leistungsgewicht von  $18.9 \text{ kW/kg}$  erreicht und zeigt, dass der Gewichtsbeitrag des Wechselrichters zum Gesamtgewicht der fliegenden Windturbine klein ist. Die Grundlagen des Kabeldesigns werden erläutert, um die Bedeutung einer Mittelspannungs-Leistungsübertragung zwischen dem Drachen der fliegenden Windturbine und der Bodenstationsschnittstelle zum Netz zu skizzieren. Dies motiviert das Design, die Implementierung und die experimentelle Verifikation eines Dual Active Bridge (DAB) Wandlers mit minimalem Gewicht für das fliegende Windturbinensystem. Die Hauptleistungskomponenten des DAB-

Wandlers, insbesondere die Brückenschaltungen, der aktiv gekühlte Hochfrequenz-Transformator und die Induktivität sowie das Kühlsystem, die weitgehend zum Gesamtsystemgewicht beitragen, werden auf der Basis von Mehrziel-Überlegungen in Bezug auf Gewicht und Effizienz konstruiert und realisiert. Darüber hinaus umfasst das Design alle notwendigen Überlegungen zur Realisierung eines voll funktionsfähigen Prototyps, d.h. er berücksichtigt auch die Hilfsspannungsversorgungen, die Steuerung für einen stabilen Betrieb des Systems, welche auch ein EingangsfILTER benötigt, sowie die Einschalt- und Ausschalt-Verfahren. Diese Überlegungen zeigen die komplexen Wechselwirkungen der verschiedenen Systemteile und machen deutlich, dass eine umfassende Konzeptualisierung notwendig ist, um zu einer zuverlässigen Mindestgewichtskonstruktion zu gelangen. Experimentelle Ergebnisse bestätigen das vorgeschlagene Designverfahren. Der Prototyp verfügt über ein Leistungsgewicht von 4.28 kW/kg (1.94 kW/lb) und erreicht eine maximale Vollast-Effizienz von 97.5 %.

Abschließend werden die wesentlichen Ergebnisse der Arbeit zusammengefasst. Um dem Leser vereinfachte Berechnungen und einen Vergleich einer konventionellen Windturbine mit einer fliegenden Windturbine zu ermöglichen, werden die aerodynamischen Grundlagen beider Systeme in einer vereinfachten Form in einem Anhang zusammengefasst und numerische Werte für das 100 kW-System dieser Arbeit diskutiert.



# Contents

<b>Abstract</b>	<b>vii</b>
<b>Kurzfassung</b>	<b>xi</b>
<b>1 Introduction</b>	<b>1</b>
1.1 The Airborne Wind Turbine Concepts . . . . .	1
1.2 Power Kite Electrical System . . . . .	6
1.3 Goals and Contributions of the Thesis . . . . .	9
1.4 Outline of the Thesis . . . . .	9
<b>2 Multi-Objective Optimization of El. Motors/Generators</b>	<b>11</b>
2.1 Specifications and Design Strategy . . . . .	12
2.2 Radial Flux Machine Topologies . . . . .	15
2.2.1 RFM Electro-Magnetic Models . . . . .	15
2.2.2 RFM Thermal Models . . . . .	28
2.2.3 RFM Weight Models . . . . .	30
2.2.4 RFM Optimization and Comparison . . . . .	32
2.2.5 RFM FEM Verification . . . . .	36
2.3 RFM Prototype . . . . .	38
2.3.1 Winding Configuration . . . . .	40
2.3.2 Construction and Assembly . . . . .	44
2.3.3 Measurement Results . . . . .	51
2.4 Axial Flux Machine Topologies . . . . .	65
2.4.1 AFM Electro-Magnetic Models . . . . .	73
2.4.2 AFM Thermal Models . . . . .	79
2.4.3 AFM Weight Models . . . . .	81
2.4.4 AFM Optimization and Comparison . . . . .	82
2.5 AFM Prototype . . . . .	85
2.5.1 Construction and Assembly . . . . .	87
2.5.2 Measurement Results . . . . .	96
2.6 Summary of Chapter . . . . .	104
<b>3 Modeling of Power Electronics for Multi-Objective Optimization</b>	<b>105</b>
3.1 Semiconductors . . . . .	105
3.1.1 Losses in 2-Level Bridge Legs . . . . .	110
3.1.2 Losses in 3-level T-Type Bridge Legs . . . . .	114
3.1.3 Losses in 3-level NPC Bridge Legs . . . . .	123

3.1.4	Losses in 3-level ANPC Bridge Legs . . . . .	132
3.2	Passive Components . . . . .	142
3.2.1	Capacitors . . . . .	143
3.2.2	Inductive Components . . . . .	143
3.3	Cooling System Modeling . . . . .	146
3.3.1	Heat Spreading . . . . .	147
3.3.2	Forced Convection . . . . .	151
3.3.3	Cooling System Optimization . . . . .	167
3.4	Summary of Chapter . . . . .	175
<b>4</b>	<b>Electric Machine Drive Design Considerations</b>	<b>177</b>
4.1	VSI Topology Comparison . . . . .	178
4.2	Inverter and Machine Interactions . . . . .	186
4.2.1	Optimal Number of Turns . . . . .	186
4.2.2	Optimal Switching Frequency . . . . .	187
4.3	Hardware Prototype . . . . .	188
4.4	Summary of Chapter . . . . .	192
<b>5</b>	<b>Tether (Transmission Cable)</b>	<b>193</b>
<b>6</b>	<b>Multi-Obj. Optimization of the All-SiC 2kV/700V DAB</b>	<b>199</b>
6.1	Minimum Weight DAB Power Converter . . . . .	203
6.1.1	Optimal Converter Operation, optimal $n$ and $L$ . . . . .	203
6.1.2	Power Semiconductors . . . . .	205
6.1.3	Optimization of the DAB Transformer and Inductor	209
6.1.4	Minimum Weight Cooling System . . . . .	215
6.1.5	Design of the Filter Networks . . . . .	221
6.2	Control: Concept and Implementation . . . . .	227
6.2.1	ISOP Structured DAB Control Concept . . . . .	227
6.2.2	ISOP Structured DAB Controller Implementation	228
6.2.3	ISOP Structured DAB Controller Design . . . . .	230
6.3	Auxiliary Power Supplies and Startup . . . . .	234
6.3.1	Auxiliary Power Supplies . . . . .	234
6.3.2	Startup . . . . .	242
6.4	Hardware Prototype . . . . .	245
6.4.1	Efficiency and Temperature Measurements . . . . .	247
6.4.2	Cost Decomposition . . . . .	250
6.5	Summary of Chapter . . . . .	252
<b>7</b>	<b>Conclusion</b>	<b>253</b>

<b>Appendices</b>	<b>255</b>
<b>A Basics of Aerodynamics of Conventional Wind Turbines and Power Kites</b>	<b>257</b>
A.1 Conventional Wind Turbines . . . . .	257
A.2 Geometrical Dimensions of the Rotor Blades of CWTs .	260
A.3 Crosswind Power Kite Modeling . . . . .	264
A.4 Power Kite Area and Turbines . . . . .	267
A.5 Numerical Results . . . . .	269
<b>List of Publications</b>	<b>271</b>
<b>Bibliography</b>	<b>273</b>
<b>Curriculum Vitae</b>	<b>285</b>



# 1

## Introduction

**T**HE FOLLOWING description is taken from [1], which considers the conceptualization and multi-objective optimization of the electrical system of an Airborne Wind Turbine (AWT) and served as the foundation of this thesis.

### 1.1 The Airborne Wind Turbine Concepts

Wind power and solar thermal energy are currently the economically most viable forms of renewable energy. For the conversion of the kinetic energy of wind into electrical energy, ground-based windmills with horizontal axis are generally employed. The generator, driven by the rotor blades via a gearbox, and the connected power electronics converter for coupling to the grid are housed in a nacelle at the top of a tower. The tower height is dimensioned according to the length of the rotor blades and/or the power of the windmill since according to Betz [2], the maximum power that can be extracted from the wind is given by

$$P_{T,i} = \frac{8}{27} \rho A_T v_W^3 \quad (1.1)$$

(cf. Appendix A), where  $A_T$  is the area swept by the rotor blades,  $\rho$  the density of air, and  $v_W$  the wind speed. Windmills of high power hence require high towers and overall a very large fraction of mechanically supporting parts at high cost. For example, even a very small windmill with 100 kW output already involves an overall weight of the tower of 18 t, whereby the weight of the nacelle is an additional 4.4 t and that of the rotor blades 2.3 t (3-blade rotor,  $\omega_T = 47$  rpm, dimensioned

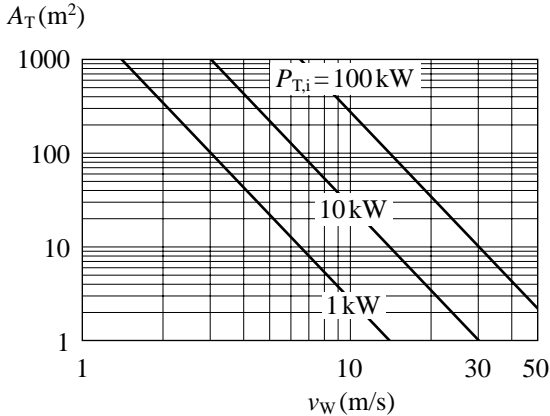


**Fig. 1.1:** Dependency of the maximum output power  $P_{T,i}$  of a wind turbine on the area  $A_T$  swept by the rotor blades and the wind speed  $v_W$  (cf. (1.1) and (A.8), parameter  $c_P = c_{P,i} = 0.59$ ).

for  $v_W = 13$  m/s). This fundamental limitation of conventional wind turbines and the lower ground friction and hence increasing wind speed  $v_W$  and constancy with increasing altitude  $h$  given by

$$v_W(h) = v_W^* \left( \frac{h}{h^*} \right)^{\alpha_H} \quad (1.2)$$

( $h^*$  and  $v_W^*$  are a reference height and speed, and  $\alpha_H = 0.1 \dots 0.6$  is the Hellmann's exponential, depending on the ground surface and vertical temperature gradients) have led to the suggestion of radically new concepts for wind energy exploitation, based on initial considerations by Loyd [3]. The basic idea here consists of implementing only the blades of the windmill in the form of a power kite flying at high speed perpendicular to the wind, thus avoiding the entire mechanical support structure of conventional windmills. The ideas go as far as exploitation of the wind energy in the jetstream at an altitude of 10'000 m with wind speeds of up to 50 m/s (compared to typically 10 m/s near the ground) and/or a 125-fold higher power density ( $\text{W}/\text{m}^2$ ) according to (1.1) compared for example to  $v_W = 10$  m/s. However, also an increase in  $v_W$  by only 25% already results in a doubling of the power density (cf. Fig. 1.1). Now the technical challenge of this fascinating



**Fig. 1.2:** Demonstrator of an Airborne Wind Turbine (AWT) system of Joby Energy [11].

concept consists in transmitting the wind power to the ground. For this purpose two possible methods are discussed: on the one hand, the power absorbed by the power kite could be converted via a tether into torque on a tether drum situated on the ground, which drives a generator. To suppress twisting in the tether, the power kite is flown in a figure-of-eight trajectory and the tether is unrolled by the pull of the kite; in a recovery phase the kite is subsequently turned out of the wind, lowering the force acting upon it, and the tether rolled up again. The cycle is then periodically repeated. The versions of this concept, generally known as a pumping power kite, range from direct conversion (SwissKitePower, [4]) to carousel-like structures with several kites (KiteGen, Univ. of Torino, [5,6]) and Laddermill structures [7], whereby a significant challenge is caused not only by the construction, but also by the optimal flight control of the kite to assure maximum power gain [8–10].

Alternatively, the power kite may be equipped with a turbine and an electric generator, together with a power electronics converter, and the power is transmitted electrically to the ground (cf. Fig. 1.2 and Fig. 1.3). Since the power kite flies at very high speed perpendicular to the wind, i.e. at several times the actual wind speed, only a very small turbine area is required according to (1.1) or a turbine of low weight for the generation of a given electric power, compared with ground-based systems (cf. Fig. 1.1 and Fig. 1.4). Moreover, because of the high turbine speed, no gear transmission is necessary and the size of the generator is also reduced.

For takeoff and landing of the power kite, the turbines act as propellers and the generators as motors, i.e. electric power is supplied so

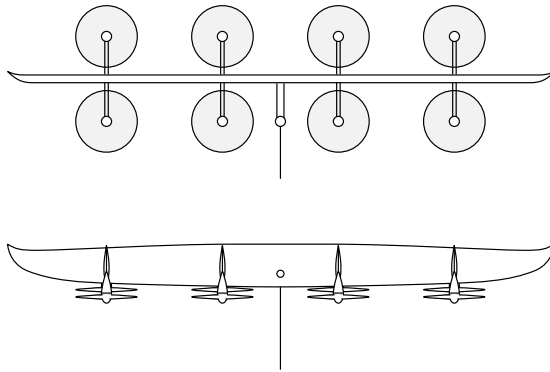


**Fig. 1.3:** Conceptual drawing of aerofoil and turbines of a 100 kW AWT system of Joby Energy [11]; length / width: 11 m / 1 m.

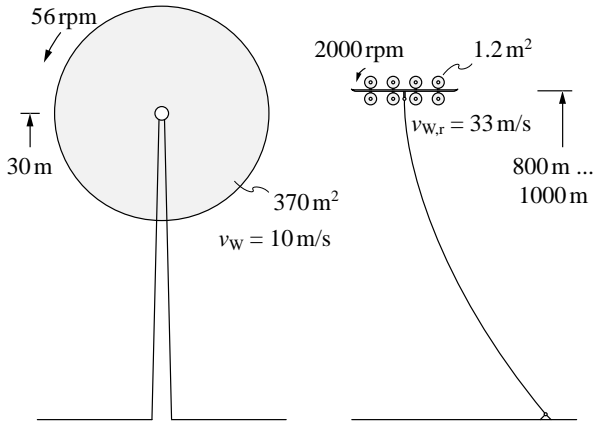


**Fig. 1.4:** Comparison of the physical size of a conventional ground-based 100 kW wind turbine and an AWT of equal power output. For the calculation of the given numerical values please see Appendix A.5.

that the system can be maneuvered like a helicopter. In general, flight trajectory control is here also one of the challenges, whereby it must be said that compared to a pumping power kite, where only mechanical

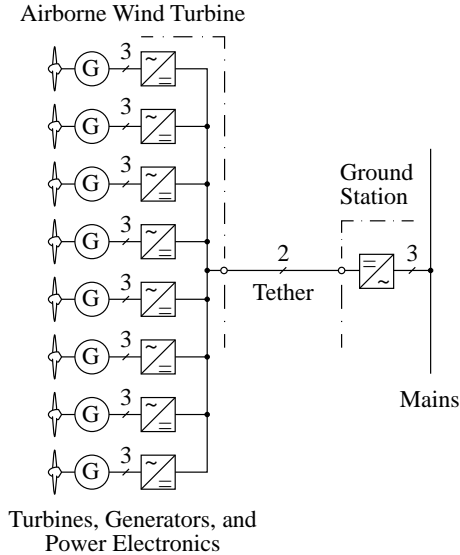


**Fig. 1.5:** AWT basic electric system structure.

control is possible, a more direct control influence is available via the generators/motors. This concept, generally known as Airborne Wind Turbine (AWT), is being pursued by several innovative companies such as Sky WindPower [12], and Windlift [13] / Makani Power [14], partly supported by the US Department of Energy (DoE) and Google.

Investigations and demonstrations of AWT to date have been mainly limited to the aerodynamic part, i.e. to the aerofoils, as well as the generators, the connected rectifier/inverter and the cable for energy transmission (tether) to the ground. This motivates an overall analysis of the electrical and power electronics systems required for the implementation of an AWT (cf. Fig. 1.5) in the present work. Here the main question, apart from the structure of the power electronics system, is the voltage level of the power transmission to the ground and in general the trade-off between power-to-weight ratio (W/kg) and efficiency of the individual converter stages, since the weight of the electrical system, including the transmission cable, must be supported by the power kite. On the basis of this analysis, favorable parameters can be de-

terminated and the technical feasibility assured. A further motivation is the multi-disciplinary character of the subject, which is of increasing importance for power electronics research at universities. Furthermore, there exist close couplings of this subject to current questions in the area of More Electric Aircraft [15] and Smart Grids [16] or in general to the multi-objective optimization of converter systems [17, 18].

The analysis is conducted with the example of a demonstrator system of Joby Energy with 8 turbines on an aerofoil made of composite material with an overall power of the turbines (shaft) of 100 kW. The system is designed to fly at 800...1000 m. To reduce the complexity, the system is initially not considered as a whole, but divided up into main functional elements, which are analyzed separately; the results are then consolidated.

The work is supplemented by an Appendix which summarizes the aerodynamic fundamentals of CWTs and power kites in highly simplified form to enable the reader to make basic calculations and a comparison of the two concepts; finally, numerical values are given for the 100 kW system discussed in this work.

## 1.2 Power Kite Electrical System

Because the AWT is planned to fly at 800...1000 m, power transmission to the ground must be at MV in order to assure low electrical losses at low weight, i.e. low conductor cross-sections of the transmission cable. Here only direct current can be considered; a three-phase medium frequency transmission would lead to high reactive currents owing to the close proximity of adjacent conductors, and/or the high capacitance of the cable; single-phase alternating current is also eliminated owing to a power flow pulsating at twice the frequency, and the weight of the additional capacitive storage thus required.

Apart from the fundamental choice of the voltage level (which will be discussed in more detail in Chapter 5), it is important to note that for determining the structure of the electrical system, or the configuration of the power electronics converters, apart from generator operation, motor operation must also be managed for the takeoff and landing of the AWT. All the converter stages must hence be designed for bidirectional operation.

In order to obtain a high transmission voltage, direct series connection of the intrinsically potential-free generator outputs after rectifica-

tion would be near at hand. Because of the mostly different wind conditions and hence different power and voltage generation of the individual generators and the potentially required motor operation of individual machines for control maneuvers, however, only a parallel connection of the subsystems is possible. The only possibility remaining is thus splitting the system into subgroups. Finally, the question remains whether the entire airborne power electronics (including the generators) should be designed for the transmission voltage level, or whether power generation and rectification should be done at low voltage. In the latter case, bidirectional dc–dc converters must be provided for coupling to the transmission cable, e.g. implemented as dual active bridge converters with MV output.

Possible concepts are shown in Fig. 1.6, whereby (a) and (b) are meant for LV generators and (c) for MV generators. For Fig. 1.6(a), as an alternative, the power of all generators could be collected via a LV dc bus and only a single coupling converter to the MV cable used. Splitting up as shown into 4 coupling converters, on the other hand, offers higher reliability and improved weight distribution over the aerofoil. For the system shown in Fig. 1.6(b), the rectifier stages and the coupling converters are integrated into individual single-stage three-phase ac–dc converters with high frequency isolation. However, the potentially lower weight of this system must be set against a considerably higher complexity as compared to Fig. 1.6(a). In addition, there is no possibility of e.g. integrating a battery storage for handling emergencies such as landing during mains failure or rupture of the tether. For these reasons, this system is not pursued further for an initial analysis.

If the generators are implemented with MV output, an isolation in the coupling of the rectifier output to the MV cable can be avoided. However, because of the required insulation distances and the required implementation of the rectifier as a multi-level converter (with a larger number of power semiconductors, gate driver stages, etc.), a higher weight for both the generator and the converter must be expected.

At the ground station, the power must be fed into the LV or MV grid at fixed voltage amplitude and frequency. In contrast to the airborne part of the system, weight and volume are here of secondary importance, so that a conventional industrial converter system can be employed. Hence for the sake of brevity, the power electronics implementation of the ground station will not be discussed further. It should only be pointed out that for coupling to the LV grid (400 V or 680 V

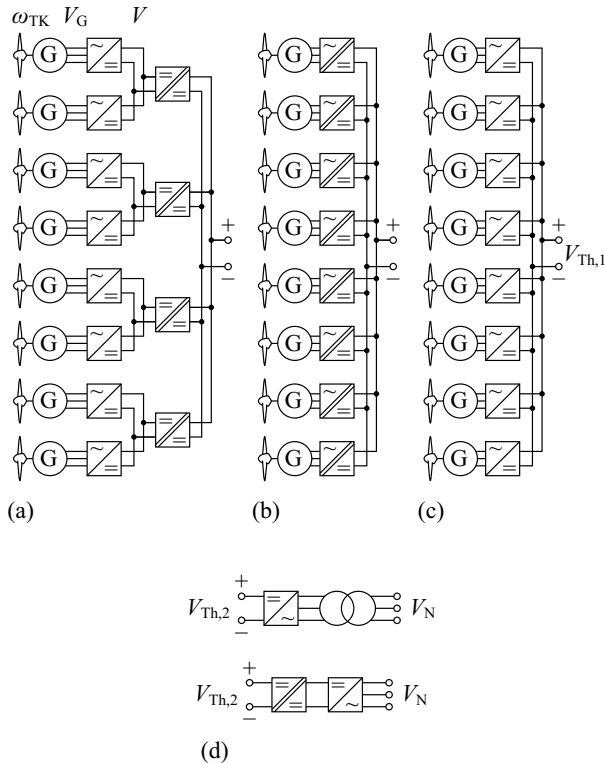


**Fig. 1.6:** Selection of possible concepts of AWT power electronics; (a), (b) LV generators, (c) MV generators; (d) possible structures of the ground station power electronics and connection to the three-phase mains.

line-to-line rms voltage), instead of a three-phase MV inverter with a transformer at the output, the dc-dc converter used on the aerofoil could be used with primary and secondary sides interchanged and a downstream LV inverter [cf. Fig. 1.6(d)]. This concept would have the advantage of higher control dynamics and would result in presumably lower realization costs, however at a (slightly) lower efficiency.

## 1.3 Goals and Contributions of the Thesis

In this work a comprehensive design method for the electrical system components of an AWT is presented. In order to characterize the trade-off between the power-to-weight ratio and the efficiency, also known as  $\gamma$ - $\eta$  Pareto Front, detailed modeling of each system component is described and optimization algorithms are presented. This thesis should serve as a guideline to engineers developing weight and efficiency optimized electrical system components, which is not limited to AWT applications only, but also useful for the development of new electrical systems in the general aerospace industry, e.g. of hybrid electric propulsion concepts. Moreover, the cross-couplings between the system components are outlined, to show how the design of the individual components affect the design of the neighboring elements.

## 1.4 Outline of the Thesis

The first part of Chapter 2 details analytical models for most types of radial flux machine (RFM) topologies. The analytic models describe the electro-magnetic and thermal aspects of the machine/generator design and also consider structural elements in a simplified manner. An optimization of all types of RFM topologies is performed, whereafter the results are presented and discussed. A most promising candidate is selected and analyzed in further depth, to finally arrive at a prototype design. A RFM prototype is constructed and tested to verify the analytical models and the design procedures. The second part of Chapter 2 details analytical models for core-less types of axial flux machine (AFM) topologies. The analytic models describe the electro-magnetic and thermal aspects of the machine/generator design and again consider structural elements in a simplified manner. An optimization of the different types of core-less AFM topologies is performed, whereafter the results are presented and discussed. A most promising candidate is selected and analyzed in further depth, to finally arrive at a prototype design. An AFM prototype is constructed and tested to verify the analytical models and the design procedures.

In Chapter 3 the modeling of power electronic circuits required for multi-objective optimization purposes is summarized. Detailed semiconductor loss models are described at the beginning of Chapter 3 to enable an estimation of the conduction and switching losses for the

most fundamental power electronic circuit configurations. Secondly, a detailed cooling system model is developed and validated. A novel optimization procedure for cooling system designs is presented which reveals how large of a reduction in converter weight is possible if a custom optimized cooling system is considered instead of a standard off-the-shelf solution. For completeness, simple models for the selection of passive components are provided.

Chapter 4 shows that new semiconductor technologies, e.g. SiC-MOSFETs, enable a simple realization of the motor/generator power electronics featuring high efficiency and low weight. Furthermore, interdependencies between the electric machine and the drive design are discussed, which yields an optimal number of turns for the stator windings of the motor/generator and optimal switching frequencies for the operation of the power electronic converter. As a benchmark a hardware prototype is presented, which is designed based on the models previously presented in Chapter 3.

Chapter 5 covers the fundamentals of the tether design, to outline the importance of a MV power transmission between the airborne wing of the AWT and the ground station interface to the mains.

This motivates Chapter 6, where the multi-objective optimization of an all-SiC 8 kV/700 V dual active bridge (DAB) is detailed. A hardware prototype is designed and built, based on a comprehensive analysis of an input series output parallel (ISOP) structured DAB, which includes transformer design, control concepts, controller design, auxiliary components, and startup procedures. At the end of Chapter 6, measurements verify the performance of the DAB prototype in terms of power-to-weight ratio and efficiency.

Finally, Chapter 7 concludes and summarizes the achieved developments of the electrical system for AWT and/or aerospace applications.

# 2

## Multi-Objective Optimization of Electric Motors/Generators

**T**O CHARACTERIZE the trade-off between the power-to-weight ratio and the efficiency of the AWT generators, different machine topologies are modeled analytically.

Section 2.1 first describes the specifications of the AWT motors/generators and the design approach. Subsequently, Section 2.2 summarizes most types of radial flux machine (RFM) topologies which were considered for optimization. The analytic electro-magnetic models for the RFM topologies are compiled in Section 2.2.1. Section 2.2.2 follows up and details the thermal models used to identify thermally infeasible designs. Section 2.2.3 describes the models used to estimate the required structural mass and completes the analytical models for the RFM topologies. With a complete analytic description of the considered RFM topologies an optimization procedure and results thereof are presented in Section 2.2.4. Finally a RFM prototype optimized for high power-to-weight ratio and efficiency is designed, built, and tested in Section 2.3 to verify the design approach.

Analogously, Section 2.4 summarizes all types of axial flux machine (AFM) topologies which were considered for optimization. The analytic electro-magnetic models for the AFM topologies are compiled in Section 2.4.1. Section 2.4.2 follows up and details the thermal models used to identify thermally infeasible designs. Section 2.4.3 completes the analytical description for the AFM topologies and describes the models used to estimate the required structural mass. With a complete analytic description of the considered AFM topologies an optimization procedure and results thereof are presented in Section 2.4.4. Finally,

an AFM prototype optimized for high power-to-weight ratio and efficiency is designed, built, and tested in Section 2.5 to verify the design approach.

## 2.1 Specifications and Design Strategy

Fig. 2.1 depicts the electrical system proposed for the AWT; four bi-directional dc–dc converters are linking eight generators with voltage source rectifiers to a tether and a bi-directional dc–ac converter connects the tether to the three-phase grid on the ground. The converter topology for the dc–dc converter will be detailed in Chapter 6. The AWT uses the electrical machines in generator operation during cross wind flight and in motor operation for launching and landing sequences. The optimization of the electrical machines with respect to minimum weight is the scope of this chapter and of particular interest, as they contribute about half of the total electrical system weight installed on the AWT.

Ragot [19,20] optimized a brushless direct current (BLDC) machine with internal rotor for a solar airplane application. Ragot’s system description has 110 parameters linked by 70 equations and is optimized using a commercial software, which provides a solution minimizing an objective function while satisfying a set of constraints. This approach, however, relies on an objective function, which can only be properly defined with knowledge of the sensitivity of competing objectives, e.g.  $d\eta/d\gamma$ , which may not be known a priori. Van der Geest [21] recognizes the importance of proper machine topology selection at the beginning of a project, i.e. for each set of specifications, and gives a procedure to compare different machines based on numerical two–dimensional (2D) finite element analysis (FEA) guided by particle swarm optimization (PSO). The loss of insight originating from the objective function required for PSO is circumvented by multi-target optimization enabling the results to be presented as Pareto optimal fronts. Van der Geest then applies his method in [22] to select a machine for an aerospace starter/generator, by comparing seven surface mounted permanent magnet (SPM) machines and two switched reluctance machines (SRM). Van der Geest’s approach however relies on FEA which is computationally expensive and therefore limited to 2D analysis. Although sensitivity analysis of competing objectives may be achieved, there is limited insight gained on the influence of specific design parameters and

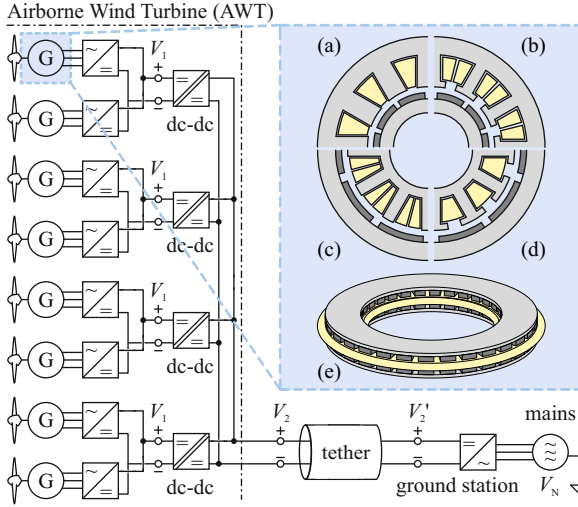


**Fig. 2.1:** Electrical system of the Airborne Wind Turbine (AWT); four bi-directional dc-dc converters are linking eight generators with voltage source rectifiers, port voltage  $V_1$ , to a tether ( $\approx 1$  km), port voltage  $V_2$ . The ground station, i.e. bi-directional dc-ac converter, connects the tether to the three-phase grid. (a)–(d) Geometrical models of the considered radial flux machines (RFM), (e) geometrical model of the considered double-rotor axial flux machines (AFM).

constraints.

In this work, in order to characterize the trade-off between the power-to-weight ratio and the efficiency, also known as  $\gamma$ - $\eta$  Pareto Front, of the AWT generators, different machine topologies are modeled analytically. Using analytical models, the whole design space can be evaluated in a computationally efficient manner, without the need for a complicated optimization routine. Furthermore, analyzing the whole design space yields data which can be used for sensitivity analysis, i.e. to evaluate the effect of any design parameter on the performance.

Table 2.1 lists the expected operating points of the AWT generators, where the operating points #1–3 occur equally distributed over the power generation time and normal hover, i.e. motor operation which occurs during the launch and landing sequences. In case of a fault condition in one of the system components inhibiting the use of a machine

#	Name	$\frac{P}{\text{kW}}$	$\frac{T}{\text{Nm}}$	$\frac{n}{\text{r/min}}$	$\frac{u_{\text{conv}}}{\text{m/s}}$
1	Generation point 1	8.3	35.3	2251	55
2	Generation point 2	12.9	38.5	3200	55
3	Generation point 3	12.5	26.5	4507	55
4	Hover normal	6.5	19.7	3121	16
5	Hover (rotor out)	11.1	28.4	3728	21
6	No load (rotor out)	0	0.0	7010	55

**Tab. 2.1:** Operating points of the AWT generators/motors.

pair, the AWT should still safely land for maintenance, resulting in operating points #5–6. Because the majority of the operation time is spent generating power, only the operating points #1–3 will be considered for efficiency calculations, while #4–6 are considered as thermal and electro-magnetic constraints, where  $u_{\text{conv}}$  is the convective air speed behind the propeller.

The aim of the analysis is to investigate the limits of the  $\gamma$ - $\eta$  characteristics of potential machine topologies in order to identify the optimal machine for the given set of specifications.

The system down time due to maintenance is to be minimized for economic reasons, therefore, only direct drive solutions are considered in this work, omitting mechanical gears, which are maintenance intensive. Furthermore, only permanent magnet (PM) machine topologies are considered, as they reach higher efficiencies, while maintaining a high power density in comparison to their separately excited counterparts or induction machines.

This work considers PM radial flux machines (RFM) featuring internal or external rotors, cf. Fig. 2.2. The rotors employ either radially magnetized SPM or radially and tangentially magnetized SPM creating a segmented Halbach configuration. Although the winding factor is smaller compared to traditional distributed windings, only single and double layer concentrated windings are considered, since the conduction losses and the weight are reduced due to the shorter end-windings [22, 23]. As the last distinction within the RFM topologies, stators with and without tooth-tips are considered, as they lead to different winding filling factors, radii and pronouncing of slotting effects.

As double-rotor axial flux machines (AFM) have been proposed for applications with challenging requirements on power density and efficiency, such as flywheel systems, electric vehicles and wind power gen-

eration [24], this work also considers a coreless stator AFM, as shown in [24–26], cf. Fig. 2.36. AFMs with distributed and concentrated windings are analyzed.

The design space of each machine topology is characterized by a set of geometric parameters as shown in Fig. 2.2 and Fig. 2.36, as well as materials employed for the windings, the magnetic core and permanent magnets. Moreover, each machine is analyzed assuming sinusoidal (BLAC) and block-shaped (BLDC) currents, enabling the evaluation of different driving methods.

Once the design space is defined as in Section 2.2.4 and Section 2.4.4,  $\gamma$  and  $\eta$  are calculated for each combination of the parameters. The evaluation of the electro-magnetic and structural mass models yields the total mass,  $m_{\text{tot}}$ , conduction losses,  $P_{\text{cond}}(\theta_W)$ , and iron losses,  $P_{\text{Fe}}(f)$ , of each machine at a winding temperature of  $\theta_W = \theta_{\text{amb}} = 25^\circ\text{C}$ . The winding temperature is then determined iteratively. The iteration evaluates the thermal model and consequently updates the temperature dependent losses, i.e. the inputs to the thermal model. The round trip efficiency is defined as

$$\eta = \frac{1}{3} \sum_{\# = 1}^3 \frac{T_{\#} \frac{2\pi n_{\#}}{60}}{T_{\#} \frac{2\pi n_{\#}}{60} + P_{\text{cond},\#} + P_{\text{Fe},\#}}, \quad (2.1)$$

where  $P_{\text{cond},\#}$ , and  $P_{\text{Fe},\#}$  are the losses at the operating points steady state temperatures. The power-to-weight ratio is defined by the maximum output power in Tab. 2.1:

$$\gamma = T_{\#2} \frac{2\pi n_{\#2}}{60} \frac{1}{m_{\text{tot}}}. \quad (2.2)$$

## 2.2 Radial Flux Machine Topologies

The geometric models of the considered radial flux machines are shown in Fig. 2.2. The independent parameters are the pole pair  $p$  slot number  $Q_s$  combinations,  $p/Q_s$ , the stator radius  $R_s$ , the magnet height  $h$ , the air-gap width  $g$ , the slot depth  $d_s$ , the pole and slot coverage factors  $\alpha_p$  and  $\alpha_q$ , the stack length  $L$  of the machine, and the materials employed.

### 2.2.1 RFM Electro-Magnetic Models

For a given set of independent parameters the back Electro-Motive-Force (EMF) waveform can be calculated. First the open circuit radial

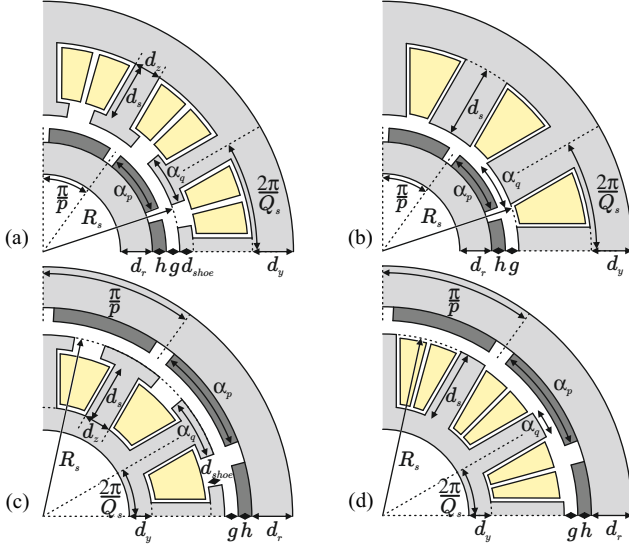


**Fig. 2.2:** Geometrical models of the considered radial flux machines, (a) with internal rotor and double layer concentrated windings and stator with tooth-tips, (b) with internal rotor and single layer concentrated windings and stator without tooth-tips, (c) with external rotor and single layer concentrated windings and stator with tooth-tips, (d) with external rotor and double layer concentrated windings and stator without tooth-tips.

air-gap field at the stator  $B_r(R_s, \alpha, \theta)$ , generated by the permanent magnets, is calculated for one electrical rotation of the rotor, i.e.  $\theta = \omega t \in [-\frac{\pi}{p}, \frac{\pi}{p}]$ , according to [27, 28].

The magnetic flux density in the air-gap (as well as the magnets) in polar coordinates is calculated assuming a slotless stator. The field vectors to be calculated are the following:

$$\begin{aligned} \vec{B}_I &= \mu_0 \vec{H}_I && \text{in the air-gap} \\ \vec{B}_{II} &= \mu_0 \mu_r \vec{H}_{II} + \mu_0 \mu_r \vec{M} && \text{in the magnet} \end{aligned} \quad (2.3)$$

It is assumed that the magnets are operated in their linear range, the magnetization  $M$  is calculated as  $M = \frac{B_{rem}}{\mu_0}$ , where  $B_{rem}$  is the remanent flux density of the PM. By solving the resulting differential equation of the scalar magnetic potential ( $\vec{H} = -\nabla\varphi$ ) a general solu-

tion in polar coordinates is obtained. The constants are determined by following boundary conditions<sup>1</sup>:

- ▶ the field lines enter the stator radially;
- ▶ the field lines enter the rotor radially;
- ▶ the magnetic field density is continuous,

which yields the boundary condition equations

$$\begin{aligned}
 H_{\theta I}(r, \theta)|_{r=R_s} &= 0, \\
 H_{\theta II}(r, \theta)|_{r=R_r} &= 0, \\
 B_{rI}(r, \theta)|_{r=R_m} &= B_{rII}(r, \theta)|_{r=R_m}, \\
 B_{\theta I}(r, \theta)|_{r=R_m} &= B_{\theta II}(r, \theta)|_{r=R_m},
 \end{aligned} \tag{2.4}$$

where  $R_r$  is the radius of the rotor iron,  $R_m$  is the radius of the PM surface in the air-gap and  $R_s$  is the stator radius. The calculations lead to the radial magnetic flux density distribution in the air-gap of a slotless RFM,  $B_{r,PM}(r, \varphi)$ , which is expressed as follows:

$$B_{r,PM}(r, \varphi) = \sum_{n=1,3,5,\dots}^{\infty} K_B(n) f_{B_r}(r) \cos(np\varphi). \tag{2.5}$$

The functions  $K_B(n)$  and  $f_{B_r}(r)$  are found in [27]. In order to describe the slotting of the machine a relative permeance model, as described in detail in [30], is used. This function can be regarded as a mask or filter that is applied to the field. The function is derived assuming that:

- ▶ the slots are of rectangular shape;
- ▶ the slot depth is infinite;
- ▶ the permanent magnets can be replaced by material without magnetization but same permeability;
- ▶ effects of adjacent slots can be neglected.

As in SPM machines the effective or equivalent air-gap  $g' = g + \frac{h_m}{\mu_r}$  is large<sup>2</sup>, the considered function must be two-dimensional, i.e. be dependent on the radius. The calculations lead to the permeance function

<sup>1</sup>The derivation of the open circuit field for the Halbach magnetization is similar, cf. [29].

<sup>2</sup>Most permanent magnet material have a recoil permeability of  $\mu_r \approx 1$ .

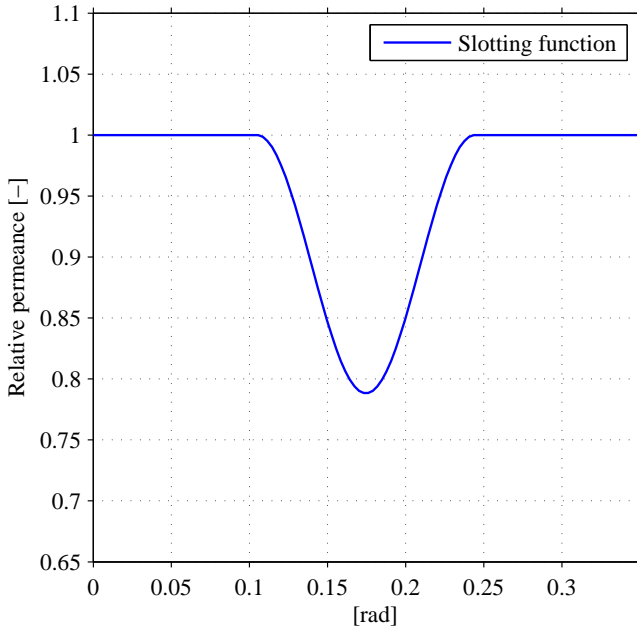


**Fig. 2.3:** Relative permeance (slotting function) for an inrunner machine at radius  $R_m = 27 \text{ mm}$  in a 18 slots machine. The slot coverage is  $\alpha_q = 0.75$  and the machine has an equivalent air-gap of 4.083 mm, of which 0.75 mm form the physical air-gap.

$\lambda(r, \varphi)$ . Thus the magnetic flux density distribution in the air-gap of a slotted machine can be calculated as

$$B_{r,\text{PM}}^{\text{slotted}}(r, \varphi) = B_{r,\text{PM}}(r, \varphi)\lambda(r, \varphi). \quad (2.6)$$

For segmented Halbach magnetization the air-gap field  $B_{r,\text{PM}}(r, \varphi)$  is calculated according to [29].

The flux linkage in phase A is calculated by integration of the radial field seen by the phase coils,

$$\Psi_{\text{ph,A}}(\theta) = N_{\text{turns}} L R_s \sum_{k \in \text{ph,A}} \int_{-\alpha_k}^{\alpha_k} B_{r,\text{PM}}(R_s, \varphi + \theta) \cdot \lambda(R_s, \varphi) \, d\varphi. \quad (2.7)$$

Here the rotational angle,  $\theta$ , is introduced to represent the angular position of the rotor with respect to the stator.  $L$  is the axial length of the stator and  $N_{\text{turns}}$  the number of turns per coil of the winding. The integration limits

$$\alpha_k = \frac{\pi}{Q_s} \left( 1 + \frac{4(k-1)}{N_c} \right), \quad (2.8)$$

start and stop in the middle of the slot openings next to the stator teeth belonging to the corresponding coils of the phase winding, where  $N_c$  is 1 for single layer windings and 2 for double layer windings. This way, not only the fundamental component but the complete back EMF waveform

$$u_{\text{ind,A}} = -\frac{d}{dt} \Psi_{\text{ph,A}} \quad (2.9)$$

is captured and the performance of the machine under BLAC or BLDC drive currents can be estimated.

From a power balance between electrical and mechanical power the current needed to generate the demanded torque,  $T$ , can be calculated under the assumptions that current and voltage are in phase and neither switching ripples nor time delays occur.

For sinusoidal drive currents only the fundamental component,  $u_{\text{ind,A,(1)}}$ , of the back-EMF generates a net torque and the power balance is given by

$$P = T \cdot \omega = 3 \cdot I_{\text{ph,A}} \cdot U_{\text{ind,A}} = \frac{3}{2} \hat{I}_{\text{ph,A}} \cdot \hat{U}_{\text{ind,A,(1)}}. \quad (2.10)$$

Solving for the required current leads to

$$I_{\text{ph,A}} = \frac{\hat{I}_{\text{ph,A}}}{\sqrt{2}} = \frac{\sqrt{2}}{3} \frac{T \cdot \omega}{\hat{U}_{\text{ind,A,(1)}}}. \quad (2.11)$$

For block-shaped current not only the fundamental component of the back-EMF but also its harmonics can generate an average torque.

The power balance becomes

$$P = T \cdot \omega = \frac{3}{2\pi} \int_{-\pi}^{\pi} i_{\text{ph},A}^{\text{block}}(\omega t) u_{\text{ind},A}(\omega t) d\omega t, \quad (2.12)$$

with

$$i_{\text{ph},A}^{\text{block}}(\omega t) = \begin{cases} -\hat{I}_{\text{block}} & \text{for } -\pi \leq \omega t \leq -\frac{2\pi}{3} \\ 0 & \text{for } -\frac{2\pi}{3} < \omega t < -\frac{\pi}{3} \\ \hat{I}_{\text{block}} & \text{for } -\frac{\pi}{3} \leq \omega t \leq \frac{\pi}{3} \\ 0 & \text{for } \frac{\pi}{3} < \omega t < \frac{2\pi}{3} \\ -\hat{I}_{\text{block}} & \text{for } \frac{2\pi}{3} \leq \omega t \leq \pi \end{cases} \quad (2.13)$$

under the assumption that  $u_{\text{ind},A}(\omega t)$  is an even quarter-wave symmetric function. The power balance then reduces to

$$P = T \cdot \omega = \frac{3}{2\pi} 4\hat{I}_{\text{block}} \int_0^{\frac{\pi}{3}} u_{\text{ind},A}(\omega t) d\omega t. \quad (2.14)$$

Solving for the RMS value current yields

$$I_{\text{block}} = \sqrt{\frac{2}{3}} \hat{I}_{\text{block}} = \frac{\pi}{3\sqrt{6}} \frac{T \cdot \omega}{\int_0^{\frac{\pi}{3}} u_{\text{ind},A}(\omega t) d\omega t}. \quad (2.15)$$

Once the current for the desired maximum torque is known, the armature reaction field can be calculated. The armature reaction field is needed to later predict the thickness of the stator and iron yokes, as well as to calculate the machine inductance. The calculation is the same for sine or block current. The calculation of the armature reaction is made under following assumptions:

- ▶ the stator is assumed to be slotless;
- ▶ the stator slotting can be accounted for by the permeance function  $\lambda(r, \varphi)$ ;
- ▶ the current contained in the slot can be represented by a current sheet at the top of the slot with uniform current density along the arc of the slot opening;

- the permanent magnets can be replaced by material without magnetization but same permeability;

Under these assumptions, the magnetic flux density in the air-gap produced by one single coil ( $\varphi = 0$  corresponding to the axis of the coil) is calculated according to [31] as

$$B_{r,\text{coil}}(r, \varphi, \omega t) = \frac{2\mu_0 N_{\text{turns}} i(\omega t)}{\pi g'} \sum_{\nu=1}^{\infty} \frac{K_{\nu} \cos(\nu\varphi)}{\nu}, \quad (2.16)$$

with  $K_{\nu} = K_{so,\nu} K_{p,\nu} F_{\nu}$ . The factor  $K_{\nu}$  is composed of the slot opening factor  $K_{so,\nu}$ , the winding pitch factor  $K_{p,\nu}$  and the 2D radial function  $F_{\nu}$ . The winding pitch factor is

$$K_{p,\nu} = \sin\left(\frac{\nu\alpha_y}{2}\right), \quad (2.17)$$

where  $\alpha_y$  is the winding pitch; the slot opening factor is

$$K_{so,\nu} = \frac{\sin\left(\frac{\nu b}{2R_s}\right)}{\frac{\nu b}{2R_s}}. \quad (2.18)$$

The 2D radial function

$$F_{\nu}(r) = g' \frac{\nu}{r} \left(\frac{r}{R_s}\right)^{\nu} \frac{1 + \left(\frac{R_r}{r}\right)^{2\nu}}{1 - \left(\frac{R_r}{R_s}\right)^{2\nu}} \quad (2.19)$$

accounts for the influence of the large effective air-gap. Finally, the total magnetic flux density in the air-gap is found utilizing linear superposition

$$B_{r,\text{arm}}(r, \varphi, \omega t) = \sum_{k=1}^{N_{\text{coils}}} \left( \frac{2\mu_0 N_{\text{turns}} i(\omega t)}{\pi g'} \sum_{\nu=1}^{\infty} \frac{K_{\nu} \cos(\nu\alpha_k)}{\nu} \right), \quad (2.20)$$

with the number of coils  $N_{\text{coils}} = \frac{N_c Q_s}{2}$ , and the position of the coils  $\alpha_k = \varphi - (k-1) \frac{4\pi}{N_c Q_s}$ . Finally the permeance function needs to be applied to the armature reaction

$$B_{r,\text{arm}}^{\text{slotted}}(r, \varphi, \omega t) = B_{r,\text{arm}}(r, \varphi, \omega t) \lambda(r, \varphi). \quad (2.21)$$

At this point the magnetic flux density in the air-gap is known as a function of time and space, therefore the iron geometry of the machine can be dimensioned. The dimensions of the rotor and stator to be determined are (cf. Fig. 2.2):

- ▶ the rotor yoke thickness  $d_r$ ;
- ▶ the stator tooth thickness  $d_z$ ;<sup>3</sup>
- ▶ the tooth-tip height  $d_{\text{shoe}}$  (if existent);
- ▶ the stator yoke thickness  $d_y$ .

The iron path is dimensioned such, that no saturation occurs when the maximum torque is demanded. The main contribution to the rotor yoke flux is due to the PM excitation of the rotor. Although the contribution due to the armature reaction is of lesser importance it cannot be neglected. To avoid saturation of the rotor iron the yoke thickness is

$$d_r = \frac{\Psi_{\text{PM}} + \Psi_{\text{arm}}}{LB_{\text{sat}}}, \quad (2.22)$$

where  $B_{\text{sat}}$  is the saturation flux density of the employed iron. The maximum flux of the PMs to be guided through the rotor yoke is

$$\Psi_{\text{PM}} = LR_m \int_0^{\frac{\pi}{2p}} B_{r,\text{PM}}^{\text{slotted}}(R_m, \varphi) d\varphi, \quad (2.23)$$

i.e. the PM flux of half a pole at the magnet surface, since the flux of the PM splits into two parts below the center of the magnet in the rotor yoke. The contribution of the armature reaction flux can be evaluated for one fixed point in time,  $t^*$ , when the current in phase A is at its maximum

$$\Psi_{\text{arm}} = L(R_s - g') \int_0^{\frac{\pi}{2p}} B_{r,\text{arm}}^{\text{slotted}}(R_s - g', \varphi, \omega t^*) d\varphi. \quad (2.24)$$

The thickness of the stator tooth,  $d_z$ , without leakage is defined by the maximum flux entering the stator tooth at radius  $R_s$ . If the stator teeth feature tooth-tips the thickness can be reduced to

$$d_z = \frac{\Psi_{k,A,\text{max}}}{LB_{\text{sat}}}, \quad (2.25)$$

---

<sup>3</sup>In machines with straight teeth (no tooth-tip), the tooth width is defined by  $\alpha_q$

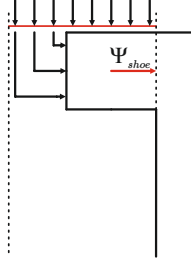


**Fig. 2.4:** Flux responsible for the tooth-tip height.

where  $\Psi_{k,A,\max} = \max(\Psi_{k,\text{tot}}(t))$  is the maximum flux in time, as superposition of PM flux and armature flux, in stator tooth  $k$ , with

$$\Psi_{k,\text{tot}}(t) = LR_s \int_{\frac{(k-1)\pi}{Q_s}}^{\frac{k\pi}{Q_s}} B_{r,\text{PM}}^{\text{slotted}}(R_s, \varphi, \omega t) + B_{r,\text{arm}}^{\text{slotted}}(R_s, \varphi, \omega t) d\varphi. \quad (2.26)$$

The stator tooth thickness  $d_z$  is corrected to account for leakage flux. If the flux density in any stator tooth  $k$  exceeds the saturation flux density of the soft magnetic material,  $B_{\text{sat}}$ , the machine is discarded for either designs (with and without tooth-tips), i.e. if

$$\frac{\Psi_{k,A,\max}}{B_{\text{sat}}} > \alpha_q \frac{2\pi R_s L}{Q_s}. \quad (2.27)$$

If the stator tooth features tooth-tips, its height needs to be determined. Fig. 2.4 schematically shows the air-gap flux, which flows through the tooth-tip, thus the flux is calculated as

$$\Psi_{\text{shoe}}(t) = LR_s \int_{\frac{d_z}{2R_s}}^{\frac{\pi}{Q_s}} B_{r,\text{PM}}^{\text{slotted}}(R_s, \varphi, \omega t) + B_{r,\text{arm}}^{\text{slotted}}(R_s, \varphi, t) d\varphi. \quad (2.28)$$

The tooth-tip height therefore needs to be

$$d_{\text{shoe}} = \frac{\max(\Psi_{\text{shoe}}(t))}{LB_{\text{sat}}}. \quad (2.29)$$

The stator yoke is calculated in function of the stator tooth thickness. At first it was assumed that the flux splits into two equivalent

parts. However it was seen in FEA that this is not always the case for concentrated windings. As no analytical relation could be found, following approximation is used:

$$d_y = \frac{2}{3}d_z. \quad (2.30)$$

While this is only an assumption it is relatively accurate for meaningful machine designs.

To enable later analysis of inverter and machine interactions the machine inductance is estimated. Of main interest is the direct axis inductance

$$L_d = \frac{3M}{2} + L_s, \quad (2.31)$$

where  $M$  is the mutual inductance and  $L_s$  is the stray inductance.

Because of the large equivalent air-gap of surface mounted PM machines, the stray inductance is generally in the same order of magnitude as the mutual inductance. Therefore, the model needs to account for leakage flux, which has been neglected so far. Furthermore, a change in the thickness of  $d_z$  is required for machines with tooth-tips, as the leakage flux is more pronounced.

The tooth-tip leakage is calculated for machines with tooth-tips. The inductance is calculated by assigning a reluctance to the tangential air-gap between the neighboring stator teeth at the stator bore  $R_s$ , where the tooth-tips are. The reluctance is defined with the method proposed in [32] which enables to account for fringing. The parameters needed for the model have been tuned using FEA analysis. The result is the reluctance  $R_{tip,1}$  (per slot).

The slot leakage is the flux crossing the slot. According to [33] the slot leakage reluctance (per slot) can be approximated as

$$R_{slot,1} = \frac{3w_{top}}{\mu_0 d_s} L, \quad (2.32)$$

where  $w_{top}$  is the slot width at radius  $r = R_s \pm d_{shoe}$ , with  $+$  for inrunner and  $-$  for outrunner designs.

The leakage inductance  $L_s$  is calculated using the reluctances  $R_{tip,1}$  and  $R_{slot,1}$ . The leakage inductance for a machine with tooth-tips is

$$L_s = N_{turns}^2 \frac{1}{R_{tot}} = N_{turns}^2 \frac{N_c Q_s}{3} \frac{R_{slot,1} + R_{tip,1}}{R_{slot,1} \cdot R_{tip,1}}, \quad (2.33)$$

and for machine designs without tooth-tips, the leakage inductance is

$$L_s = N_{turns}^2 \frac{N_c Q_s}{3} \frac{1}{R_{slot,l}}. \quad (2.34)$$

The d-axis inductance can be determined by the flux of phase A created by a current in phase A (and B). Therefore the time  $t = t^*$  to calculate the flux by the armature reaction is chosen where in phase A the current is  $i$ , in phase B  $-i$  and 0 in phase C. This flux is

$$\Psi_{ind,A}(t^*) = N_{turns} L R_s \sum_{k \in \text{ph,A}} \int_{-\alpha_k}^{\alpha_k} B_{r,arm}^{\text{slotted}}(R_s, \varphi, \omega t^*) d\varphi, \quad (2.35)$$

with  $\alpha_k$  given in (2.8). Hence the inductance is

$$L_{d,air-gap} = \frac{\Psi_{ind,A}(t^*)}{i_{ph,A}(t^*)}. \quad (2.36)$$

The reluctance  $R_{tip,l}$  can be used to correct the tooth width  $d_z$  to account for the leakage flux not entering the air-gap. In single layer windings the phases are magnetically isolated from each other. This means that no leakage flux from phase A is seen in phase B or C. Hence, the leakage flux seen in a tooth of a single layer winding design is

$$\Psi_{leak,max} = 2 N_{turns} \frac{\hat{I}_{ph,A}}{R_{tip,l}}. \quad (2.37)$$

In double layer winding designs, however, a slot can have coils of different phases or of the same phase. Furthermore, the direction in which those coils are wound is not known a priori. This means that in the case of double layer winding the additional flux  $\Psi_{leak,max}$  has to be calculated for each tooth, while accounting for the current in the neighboring coils. It is assumed that a current  $\hat{I}_{ph,A}$  flows in phase A, while  $-\frac{1}{2}\hat{I}_{ph,A}$  flows in phases B and C. In this way the additional flux  $\Psi_{leak,max}$  flowing in the most critical tooth of phase A is found. In either case the tooth thickness has to be increase by

$$\Delta d_z = \frac{\Psi_{leak,max}}{B_{sat}}. \quad (2.38)$$

At this point, the geometry of the machine is finally defined, which enables the estimation of the phase resistances assuming that:

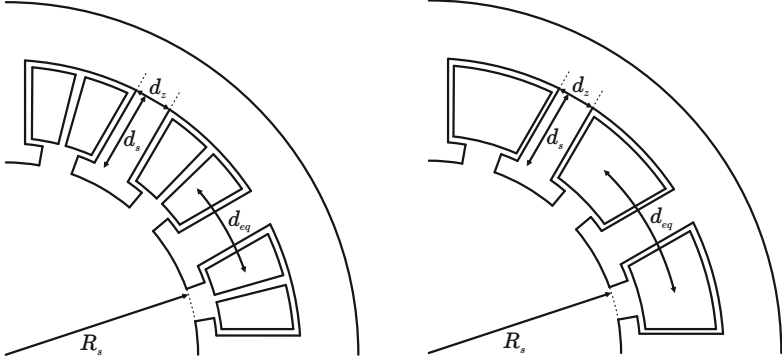


**Fig. 2.5:** Modeling of the end-winding length.

- ▶ the coil can be described by two parts, i.e. the end-winding and the active winding part only;
- ▶ the end-winding can be described by a semi-circle in top view;
- ▶ the circumferential connection of the coils can be neglected.

The third assumption implies  $N \gg 1$ , as then the length of the circumferential connection is small in comparison to the total coil length. Figures 2.2 and 2.5 show the geometry of the end-winding/coil.

For an inrunner machine design the coil end-winding length is approximated as

$$l_{\text{end}} = d_{\text{eq}} \frac{\pi}{2} = \left( d_z + 2\pi \frac{R_s + d_{\text{shoe}} + \frac{d_s}{2}}{N_c Q_s} - \frac{d_z}{N_c} \right) \frac{\pi}{2}, \quad (2.39)$$

with  $d_{\text{shoe}} = 0$  in case of tooth-tip-less designs. For an outrunner machine design the coil end-winding length is approximated as

$$l_{\text{end}} = d_{\text{eq}} \frac{\pi}{2} = \left( d_z + 2\pi \frac{R_s - d_{\text{shoe}} - \frac{d_s}{2}}{N_c Q_s} - \frac{d_z}{N_c} \right) \frac{\pi}{2}. \quad (2.40)$$

Finally the total coil length is

$$l_{\text{coil}} = N_{\text{turns}}(2(L + d_{\text{eq}} - d_z) + 2l_{\text{end}}). \quad (2.41)$$

The term  $d_{\text{eq}} - d_z$  accounts for the fact that the winding has a physical width. Finally, the coil resistance can then be calculated using the coil length and cross section

$$R_{\text{coil}} = \frac{1}{\sigma(\theta)} \frac{l_{\text{coil}}}{k_{\text{cu}} A_w}, \quad (2.42)$$

where  $\sigma(\theta)$  is the conductivity of the winding material at temperature  $\theta$  and  $A_w$  the slot area. Because the windings need to be wound manually onto machines with tooth-tips, a winding filling factor of  $k_{\text{cu}} = 60\%$  for machines with tooth-tips is assumed. For machines with straight teeth the windings can be wound on coil formers and pressed to increase the filling factor, therefore a higher filling factor of  $k_{\text{cu}} = 80\%$  is assumed. The phase resistance finally is the sum of the resistance of all the coils connected in series<sup>4</sup>,

$$R_{\text{phase}}(\theta) = \frac{N_{\text{coils}}}{3} R_{\text{coil}}(\theta). \quad (2.43)$$

If the temperature of the winding is known the conduction losses are given as

$$P_{\text{v,w}}(\theta) = \begin{cases} R_{\text{phase}}(\theta) I_{\text{ph,A}}^2 & \text{for BLAC} \\ R_{\text{phase}}(\theta) I_{\text{block}}^2 & \text{for BLDC} \end{cases}, \quad (2.44)$$

and the core losses are approximated according to [34], neglecting the effect of rotating and non-sinusoidal fields

$$P_{\text{v,Fe}} = V_s \left( k_h f \hat{B}^2 + k_c (f \hat{B})^2 + k_e (f \hat{B})^{1.5} \right), \quad (2.45)$$

where  $V_s$  is the stator core volume,  $f$  the fundamental electric frequency and  $\hat{B}$  is the maximum flux density in the stator core.

---

<sup>4</sup>The option to connect coils in parallel is not considered in this thesis, because higher motor output voltages are favorable for the AWT electrical system.

## 2.2.2 RFM Thermal Models

As described in Section 2.2.1 the machines are designed such that they operate on the limits imposed by the electro-magnetic components. A second modeling step describes the machine's thermal behaviour, which in return influences important temperature dependent material properties, such as electric conductivity, and therefore influences the torque and losses of the machine. Boglietti [35] outlined the qualities and limitations of different modeling approaches, i.e. FEM simulations, computational fluid dynamics (CFD) and lumped parameter thermal networks (LPTN). As low computational effort is required simplified LPTN are used [36] to calculate the approximate temperatures of the windings and the permanent magnets.

The simplified LPTN for the RFM is shown in Fig. 2.6. The thermal resistance from the winding to the stator teeth (and yoke) is approximated as

$$R_{\text{wir}} = \frac{1}{Q_s L} \left( \frac{t_{\text{iso}}}{k_{\text{iso}} l_{\text{slot}}} \right), \quad (2.46)$$

with insulation thickness  $t_{\text{iso}} = 0.2 \text{ mm}$ , insulation conductivity  $k_{\text{iso}} = 0.2 \text{ W/mK}$  and slot perimeter  $l_{\text{slot}}$ .

The remaining conductive thermal resistances are approximated as hollow cylinders [36],

$$R_{\text{th,cond}} = \frac{1}{2\pi k L} \ln \left( \frac{R_{\text{out}}}{R_{\text{in}}} \right), \quad (2.47)$$

where  $R_{\text{out}}$  is the outer,  $R_{\text{in}}$  the inner radius of the hollow cylinder and  $k$  the materials thermal conductivity, cf. Tab. 2.2. This defines the radial thermal resistance of the rotor yoke  $R_{\text{ri}}$ , the permanent magnets  $R_{\text{pm}}$  and first ( $R_{\text{sy1}}$ ) and second ( $R_{\text{sy2}}$ ) half of the stator yoke. For the thermal resistance of the stator teeth to rotor yoke  $R_{\text{st}}$ , the thermal resistance is diminished by the percentage of stator teeth volume to stator teeth and slot volume

$$\approx \frac{d_z d_s}{\frac{\pi}{Q_s} [\pm(R_s \pm d_{\text{shoe}} \pm d_s)^2 \mp (R_s \pm d_{\text{shoe}})^2]}. \quad (2.48)$$

The convective thermal resistances are expressed as

$$R_{\text{th,conv}} = \frac{1}{A_c h_c} \quad (2.49)$$

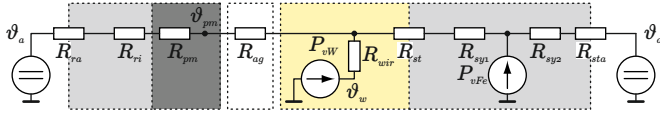


**Fig. 2.6:** Simplified radial lumped parameter thermal network (LPTN) of the RFM. The thermal resistances are:  $R_{ra}$  convective resistance from rotor yoke to air,  $R_{ri}$  conductive resistance through rotor yoke,  $R_{pm}$  conductive resistance through PM,  $R_{ag}$  convective resistance in the air-gap,  $R_{wir}$  conductive resistance from winding to stator,  $R_{st}$  equivalent conductive resistance through the stator teeth, first ( $R_{sy1}$ ) and second ( $R_{sy2}$ ) half of conductive resistance through the stator yoke and convective resistance from stator to ambient air  $R_{sta}$ .  $P_{vW}$  are the conduction losses and  $P_{vFe}$  are the core losses.

with the convective surface area  $A_c$  and the average heat transfer coefficient  $h_c$ .

For the air-gap thermal resistance the model given in [37] is employed. The convective surface area is  $A_{c,ag} = 2\pi R_m L$ , where  $R_m$  is the radius of the PM surface, and the air-gap average heat transfer coefficient is given as

$$h_{c,ag} = \frac{k_{air}}{2g} \cdot 0.03 \left( \frac{2g\omega R_m}{\nu_{air}} \right)^{0.8}, \quad (2.50)$$

with the rotor's angular velocity  $\omega$ , the thermal conductivity  $k_{air}$  and viscosity of air  $\nu_{air}$ .

At last, a heat transfer coefficient of  $h_{c,sta} = 750 \text{ W/m}^2\text{K}$  for the stator surface and  $h_{c,ra} = 250 \text{ W/m}^2\text{K}$  for the rotor surface is assumed, based on the models presented in Section 3.3.2. No axial heat transfer is considered.

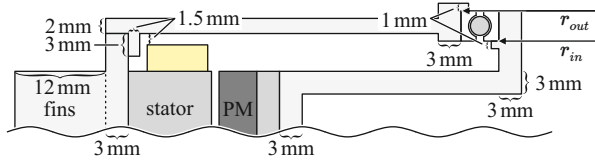


**Fig. 2.7:** Sectional drawing of an internal rotor machine including the electromagnetically inactive materials. The magnets and the rotor core are mounted on a 3 mm thick hollow shaft. The stator housing features cooling fins, which have a thickness of 1 mm, a height of 12 mm, and a spacing of 3.5 mm. The bearing shields are approximated as 2 mm thick discs.

### 2.2.3 RFM Weight Models

As the weight of the electro-magnetic material is minimized, the contributions of the electromagnetic inactive material, such as bearings and housings, to the total machine weight,  $m_{\text{tot}}$ , becomes more pronounced. In order to choose the right machine, the weight of those components is estimated. The structural mass models use a list of 27 ball bearings, which can operate at the maximum rotational speed of 7010 r/min. The list provides discrete values for the bearings mass, and the bearings inner and outer radii. For each machine the bearing, which results in minimal structural mass, is selected.

Fig. 2.7 shows the model to estimate the structural mass of an internal rotor RFM. The bearings, magnets, and rotor core are mounted on a 3 mm thick hollow aluminum shaft. The bearing outside radius is limited to  $r_{\text{out}} \leq R_s - 3 \text{ mm}$ , and the inside radius is limited to  $r_{\text{in}} \leq R_s - g - h - d_r$ . In order to avoid collisions between the end-windings and the respective parts, the end-winding height is estimated from the stator geometry and a clearance of 1.5 mm is added. The bearing shields are approximated as 2 mm thick discs, which connect to the 3 mm thick housing with cooling fins. In order to guarantee the cooling properties assumed in Section 2.2.2, the RFMs feature aluminum cooling fins, which have a thickness of 1 mm, a height of 12 mm, and a spacing of 3.5 mm.

Fig. 2.8 shows the model to estimate the structural mass of an external rotor RFM. The stator is mounted on a 3 mm thick housing with the same cooling fin structure as an internal rotor RFM, which then connect to a bearing sleeve and the bearings. The bearing outside ra-

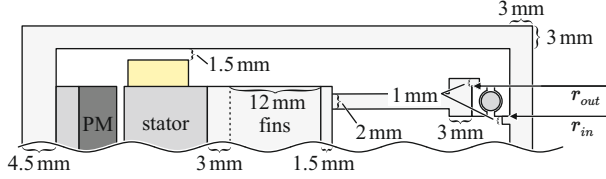


**Fig. 2.8:** Sectional drawing of an external rotor RFM including electromagnetically inactive materials. The stator is mounted on a 3 mm thick housing with cooling fins, which have a thickness of 1 mm, a height of 12 mm, and a spacing of 3.5 mm. A bearing sleeve connects the housing and bearings. The shaft extends, on one side, around the stator to hold the magnets and the rotor core.

dius is limited to  $r_{out} \leq R_s - d_{shoe} - d_s - d_y - 18$  mm. The shaft extends around the stator on one side and holds the magnets and rotor core. The added clearance between the end-windings and the shaft is also 1.5 mm.

## 2.2.4 RFM Optimization and Comparison

As described in Section 2.2 the design space is characterized by the range of free geometric parameters and the considered materials. Tab. 2.2 lists the properties of the considered materials. The considered materials are: aluminum and copper windings; neodymium iron boron (NdFeB) magnets, samarium cobalt (SmCo) magnets, and samarium iron nitride bonded (SmFeN) magnets. Although the density of cobalt iron (CoFe) is about 4% higher than the density of silicon iron (SiFe), only cobalt iron (0.1 mm Vacoflux 48) is considered. In terms of weight reduction a better performance is always achieved with CoFe, because of the higher saturation flux density (2.3 T versus 1.8 T); e.g. for the same flux the thickness of a stator tooth can be reduced by at least 25% with CoFe. The core loss coefficients  $k_h$ ,  $k_c$ , and  $k_e$  in (2.45) were fitted to experimental lab data of 0.1 mm Vacoflux 48, provided by Vacuumschmelze.

The RFMs considered in this work feature the pole pair slot number combinations:  $\frac{p}{Q_s} = \left\{ \frac{20}{42}, \frac{20}{48}, \frac{21}{36}, \frac{22}{42}, \frac{23}{48}, \frac{24}{54}, \frac{25}{48}, \frac{25}{60}, \frac{26}{54}, \frac{28}{54}, \frac{28}{48}, \frac{29}{60}, \frac{30}{72} \right\}$ . The stack length  $L$  ranges from 15 mm to 75 mm with a step size of 2.5 mm. The slot depth  $d_s$  ranges from 5 mm to 25 mm with a step size of 5 mm. The stator radius  $R_s$  ranges from 35 mm to 95 mm, for internal rotor machines, and from 45 mm to 105 mm, for external rotor machines, where the step size is 7.5 mm for internal rotor and external

Material	Electric Resistivity $\Omega\text{m}$	Thermal Conductivity $\text{W/mK}$	Relative Permeability	Rem. Flux Density T	Mass Density $\text{kg/m}^3$
Cu	$1.72\text{E}^{-8}$	350	1	-	8940
Al	$2.78\text{E}^{-8}$	210	1	-	2700
SiFe	$5.00\text{E}^{-7}$	30	$\infty$	-	7800
CoFe	$8.50\text{E}^{-7}$	30	$\infty$	-	8120
NdFeB	$1.60\text{E}^{-6}$	8	1.05	1.25	7800
SmCo	$6.75\text{E}^{-7}$	10	1.03	1.05	8300
SmFeN	$1.00\text{E}^4$	1	1.10	0.7	4800

**Tab. 2.2:** Material properties.

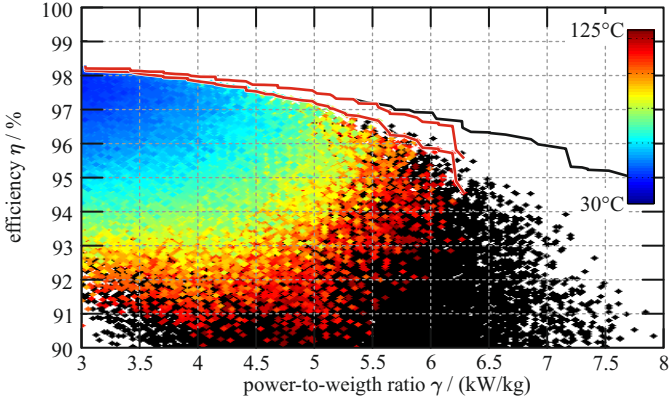


**Fig. 2.9:** Winding temperatures of the internal rotor Halbach RFM without tooth-tips, in the power-to-weight ratio versus efficiency plane, i.e.  $\gamma$ - $\eta$  plane. Machines with winding temperatures  $\theta_W > 125^\circ\text{C}$  or PM temperatures  $\theta_{PM} > 90^\circ\text{C}$ , are colored black. The Pareto optimal designs, i.e. the Pareto Front, for a winding temperature of only  $\theta_W = 30^\circ\text{C}$ , is superimposed.

rotor machines. The magnet height  $h$  ranges from 2 mm to 8 mm with a step size of 2 mm. For Halbach magnetized rotors the pole coverage factor is  $\alpha_p = 100\%$ , otherwise  $\alpha_p$  ranges from 60% to 100% with a step size of 10%. The slot coverage factor  $\alpha_q$  ranges from 60% to 85% with a step size of 6.25% for designs with tooth-tips, and from 40% to 65% with a step size of 5%, for designs without tooth-tips. The air-gap width  $g$  is set to 1 mm.

Fig. 2.9 shows the winding temperatures of the swept internal rotor Halbach RFMs in the  $\gamma$ - $\eta$  plane. Thermally infeasible designs, i.e. winding temperatures  $\theta_W > 125^\circ\text{C}$  or PM temperatures  $\theta_{PM} > 90^\circ\text{C}$ , are colored black. The Pareto Fronts neglecting the temperature dependent increase of the losses are superimposed to visualize the loss of efficiency caused by the increased winding temperature.

The direct search grid can be checked a posteriori, to ensure that the grid ranges cover the relevant design space. Fig. 2.10 shows the Pareto Fronts of solution subsets, for the internal rotor Halbach RFM without tooth-tips. Each solution subset contains only a single slot depth value,  $d_s$ . It can be concluded that the full range of relevant slot depths is covered by the grid, because neither of the subsets at the edges of the

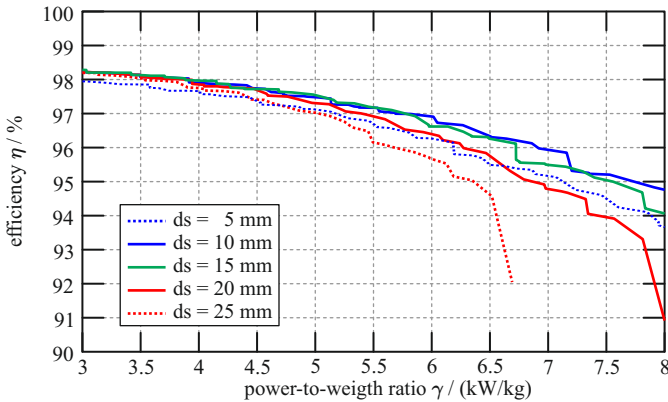


**Fig. 2.10:** Pareto Fronts of internal rotor Halbach RFMs without tooth-tips for each slot depth value,  $d_s$ , covered by the grid defined in Section 2.2.4.

grid, i.e.  $d_s = 5$  mm and  $d_s = 25$  mm, yield the best performance.

The comparison of Pareto Fronts is a useful tool to analyse the sensitivity of any of the grid parameters on the overall performance. It can also be used to compare discrete design choices, which can be summarized as:

- ▶ All machine topologies perform best with NdFeB magnets. However, because the eddy current losses in the magnets are neglected, magnet segmentation may be required.
- ▶ Double layer windings perform better than single layer windings for all RFM topologies. This can be attributed to the shorter length of the end-windings.
- ▶ For all RFM topologies the use of aluminum windings instead of copper windings yields no change in performance.
- ▶ RFM designs with tooth-tips do not increase the performance. This indicates that, with a high number of pole pairs, the increase in flux linkage with tooth-tips is overcompensated by (i) the worse winding fill factor, (ii) additional weight of the tooth-tips, and (iii) the resulting greater stator or rotor yoke radius.
- ▶ If the inverter losses are neglected, all topologies are more efficient when driven with BLAC, rather than BLDC.

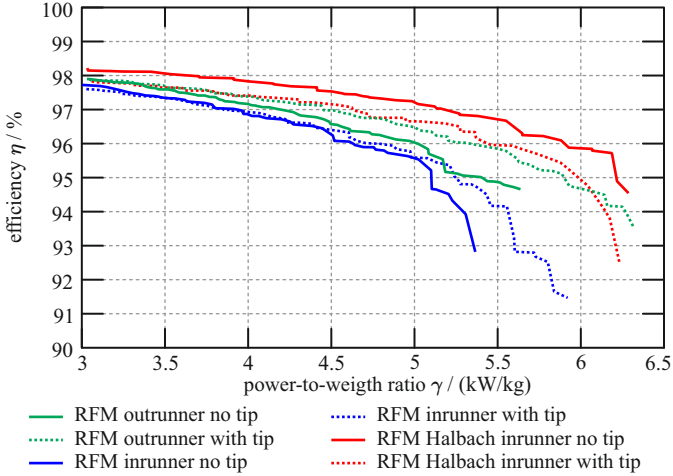


**Fig. 2.11:** Power-to-weight ratio versus efficiency  $\gamma$ - $\eta$  Pareto Fronts of all considered machine topologies, for the parameter ranges described in Section 2.2.4. Each design fulfills the specifications listed in 2.1 and is thermally feasible.

Fig. 2.11 shows the  $\gamma$ - $\eta$  Pareto Fronts for all considered machine topologies. The Pareto Fronts include the temperature dependent losses. From Fig. 2.11 the following machine topology comparisons may be deduced:

- ▶ Halbach magnetized rotors significantly increase the performance for RFM topologies, which can be attributed to the higher air-gap flux density achieved with the Halbach magnetization and lower rotor weight.
- ▶ The external rotor RFM designs perform better than the internal rotor designs.
- ▶ Any RFM design should feature an efficiency above  $\eta \approx 95\%$ , in spite of the high external heat transfer coefficient,  $h_{c,sta} = 750 \text{ W/m}^2\text{K}$ , assumed at the stator surface.

The highest achievable power-to-weight ratio for the specifications given in Tab. 6.1 is  $\gamma \approx 6.3 \text{ kW/kg}$ , considering only thermally feasible designs and including the structural mass ( $\approx 33\%$ ). The Pareto optimal

machine topology in this case is an internal rotor Halbach RFM with straight teeth.

### 2.2.5 RFM FEM Verification

Each analytical model was found to be in accordance with FEM simulations. An example machine is the internal rotor Halbach RFM near the Pareto Front with  $\gamma \approx 6.2 \text{ kW/kg}$  and  $\eta \approx 96 \%$ . The example machine parameters are  $p/Q_s = 25/60$ ,  $R_s = 60 \text{ mm}$ ,  $L = 26.25 \text{ mm}$ ,  $d_s = 10 \text{ mm}$ ,  $h = 6 \text{ mm}$ ,  $g = 1 \text{ mm}$ ,  $\alpha_q = 37.5 \%$ ,  $d_z = 2.36 \text{ mm}$ ,  $d_y = 1.6 \text{ mm}$ , and  $d_r = 0 \text{ mm}$ , i.e. air cored rotor. The machine weighs  $2.092 \text{ kg}$  of which only  $1.387 \text{ kg}$  are from electromagnetically active parts.

Fig. 2.12 shows a FEM simulation (ANSYS Maxwell) of the example machine, where the core's B-H curve is assumed to be linear with a relative permeability of  $\mu_r = 400000$ , to directly verify the linear analytical models where  $\mu_r = \infty$ . The maximum flux density at the load condition #2 is  $\approx 2.3 \text{ T}$ .

As the analytical model enforces a maximum flux density of  $2.3 \text{ T}$  the analytical results are in accordance with the (linear) FEM simulation. The results were also compared to FEM simulations with the CoFe's nonlinear B-H curve. Fig. 2.12 shows the back EMF waveform of the three models. The deviations from the analytical result are  $-0.43 \%$  with the linear material FEM simulation and  $-1.16 \%$  with the nonlinear material FEM simulation. The results are summarized in Tab. 2.3.

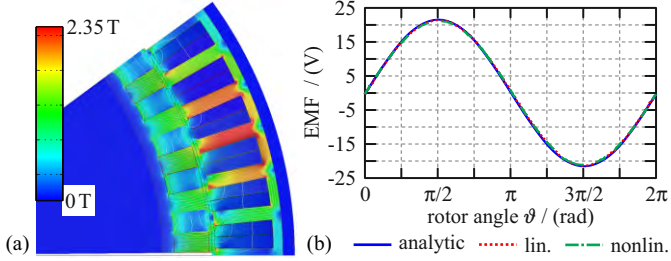


**Fig. 2.12:** (a) FEM simulation with constant permeability  $\mu_r = 400000$ ; at load condition #3 the maximum flux density is 2.3 T. (b) single winding back EMF waveform calculated with the analytical model, as well as linear material FEM and nonlinear material FEM simulations. The machine is an internal rotor Halbach RFM with parameters:  $p/Q_s = 25/60$ ;  $R_s = 60$  mm;  $L = 26.25$  mm;  $d_s = 10$  mm;  $h = 6$  mm;  $g = 1$  mm;  $\alpha_q = 37.5\%$ ;  $d_z = 2.36$  mm;  $d_y = 1.6$  mm;  $d_r = 0$  mm.

Calculation Method	Torque $T/\text{Nm}$	Winding Losses $P_{\text{cond}}/\text{W}$	Core Losses $P_{\text{Fe}}/\text{W}$	Eddy Current Losses /W
Analytic	38.5	434	63.3	N/A
Linear FEM (deviation)	37.8 1.7 %	N/A —	N/A —	43.3 —
Nonlin. FEM (deviation)	36.7 4.6 %	N/A —	57.2 9.6 %	43.3 —

**Tab. 2.3:** Results for the example machine at load condition #3.

## 2.3 RFM Prototype

A design near the Pareto Front is chosen to be implemented as a prototype to verify the design approach. The prototype is an inrunner machine with segmented Halbach magnetization of the rotor. The geometric parameters defining all the geometric degrees of freedom are listed in Tab. 2.4. The expected machine characteristics are listed in Tab. 2.5 and 2.6. The expected losses, temperatures and efficiencies for the generation points #1–3 are listed in Tab. 2.7. A picture of the prototype machine and its components is shown in Fig. 2.13.

Degree of Freedom	Variable	Value
Number of pole pairs	$p$	25
Number of slots	$Q_s$	60
Number of winding layers	$N_c$	2
Machine axial length	$L$	25 mm
Tooth-tip height	$d_{\text{shoe}}$	0 mm
Tooth coverage factor	$\alpha_q$	43 %
Slot depth	$d_s$	9 mm
Stator radius	$R_s$	67 mm
Air-gap distance	$g$	1 mm
Magnet height	$h$	6.5 mm
Radial magnet fraction	$R_{\text{mp}}$	50 %
Rotor iron thickness	$d_r$	0 mm
Number of turns per coil	$N_{\text{turns}}$	TBD

**Tab. 2.4:** Geometric parameters of the RFM prototype.

Derived Weight Component	Variable	Value
Stator iron mass	$m_{\text{Fe}}$	528 g
Copper winding mass	$m_{\text{Cu}}$	460 g
Permanent magnet mass	$m_{\text{PM}}$	500 g
Passive material mass	$m_{\text{passiv}}$	792 g

**Tab. 2.5:** Analytic estimation of required weight for the components of the RFM prototype.

Degree of Freedom	Variable	$N_{\text{turns}} = 1$	$N_{\text{turns}} = 12$
Phase resistance	$R_{\text{ph},A}$	2 m $\Omega$	292 m $\Omega$
Direct axis inductance	$L_d$	2 $\mu\text{H}$	299 $\mu\text{H}$
Torque constant	$k_T$	0.155 Nm/A <sub>rms</sub>	1.86 Nm/A <sub>rms</sub>
Voltage constant	$k_V$	0.4 V/Hz	4.9 V/Hz

**Tab. 2.6:** Analytically calculated performance parameters of the RFM prototype.

Generation Point Number	# 1	# 2	# 3	Unit
Torque	35.5	38.5	26.5	Nm
Speed	2300	3200	4500	rpm
Iron losses	46.1	74.2	112	W
Winding losses	387	475	201	W
Total losses	433	549	314	W
Efficiency	94.9	95.7	97	%
Winding temperature $\theta_w$	80	94	62	$^{\circ}\text{C}$
Stator teeth temperature	69	81	56	$^{\circ}\text{C}$
Surface temperature	65	75	53	$^{\circ}\text{C}$
Magnet temperature $\theta_{\text{pm}}$	63	74	53	$^{\circ}\text{C}$

**Tab. 2.7:** Analytically calculated losses, efficiencies and temperatures for the generation points #1–3 (cf. Tab. 2.1).



**Fig. 2.13:** Pictures of the RFM prototype assembled (left) and of the components before assembly, i.e. the bearing shields including the bearings, the rotor with a segmented Halbach array and the stator with 60 prewound coils.

### 2.3.1 Winding Configuration

The machines electro-magnetic performance is already characterized before the number of turns per coil,  $N_{\text{turns}}$ , is defined. Electro-magnetically the machine design is marginally influenced by the number of turns per coil, from an analytical point of view. However, without a thorough analysis of the winding configuration and potential (external) proximity losses, a significant deviation from the analytically calculated losses may occur. The RFM prototype features a pole-pair/slot number combination of  $\frac{p}{Q_s} = \frac{25}{60}$  which is a multiple (5x) of the basic configuration  $\frac{p}{Q_s} = \frac{5}{12}$ . The basic winding layout is given by [38] and shown in Fig. 2.14.

The number of turns per coil should be chosen to suite the power electronics converter driving the electric generator/motor. Considering the specifications given in Tab. 2.1 some limitations to  $N_{\text{turns}}$  are deduced, where operating point # 6 restricts the maximum number of turns per coil to

$$N_{\text{turns}} \leq \left\lfloor \frac{V_{\text{dc-link,max}}}{\sqrt{3} \hat{u}_{\text{ind},A,\text{max}}} \right\rfloor, \quad (2.51)$$

such that the dc-link voltage doesn't exceed  $V_{\text{dc-link,max}}$  when the maximum peak voltage per turn  $\hat{u}_{\text{ind},A,\text{max}}$  is induced. At this point it is assumed that 1200 V SiC-MOSFET semiconductors will be used. Furthermore, because operating point # 6 only occurs when the drive train for one of the propellers fails, a maximum dc-link voltage of  $V_{\text{dc-link,max}} = 1130 \text{ V}$  is chosen to be acceptable, since the motor/generator isn't actively driven in this operating point. With the maximum induced peak back-EMF voltage of  $\hat{u}_{\text{ind},A,\text{max}} = 54.2 \text{ V}$  at 7100 rpm this yields

$$N_{\text{turns}} \leq 12.$$

This yields the maximum phase-to-phase voltage  $\hat{u}_{\text{ph-ph,ind}}$  at the different operating points listed in Tab. 2.8.

To avoid a common pitfall, an analysis of the winding losses including eddy current effects in the windings is performed. Fig. 2.15 shows the investigated structures. As a reference the machine is simulated in ANSYS without eddy current effects, where the total fill factor of a slot is assumed to be 61% (with coil/slot 87% and copper/coil 70%). The losses of the end-windings are estimated with the rms-currents, copper cross sections and approximate end-winding length.

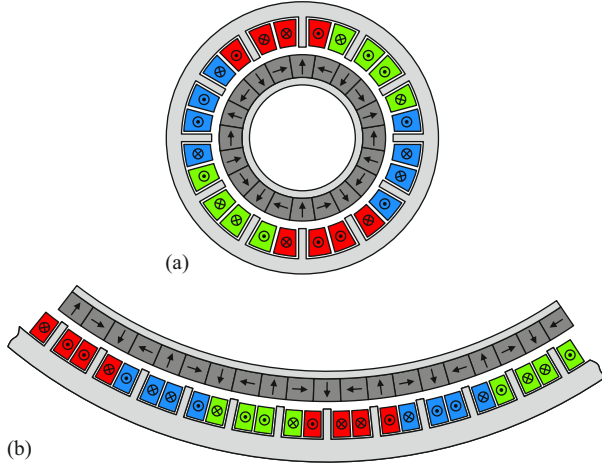


**Fig. 2.14:** (a) Winding configuration of a RFM with  $\frac{p}{Q_s} = \frac{5}{12}$  and double layer concentrated windings. (b) Winding configuration of a RFM with  $\frac{p}{Q_s} = \frac{25}{60}$  and double layer concentrated windings, the pattern repeats 5 times.

Operating Point	#1	#2	#3	#4	#5	#6
$\hat{u}_{\text{ph-ph,ind}}$	362 V	514 V	724 V	501 V	599 V	1127 V

**Tab. 2.8:** Maximum induced phase-to-phase voltage  $\hat{u}_{\text{ph-ph,ind}}$  at the different operating points given in Tab. 2.1 for  $N_{\text{turns}} = 12$ .

This "Base Machine" (cf. Fig. 2.15(a)) serves as a reference and approximately matches the analytical results, if thermal effects are neglected. Since 86 % of the losses in operating point # 2 are conduction losses, a winding configuration with a high fill factor is advantageous. The first considered winding configuration is a helical coil winding as shown in Fig. 2.15(b), with conductor dimensions of 1.8 mm x 0.6 mm. The helical coil winding provides a higher fill factor of almost 71 % potentially reducing the conduction losses by 15 %. However, very high external proximity losses occur, which ultimately increases the losses in the coils by 84 %. Hence the helical winding configuration is not feasible.

Most of the external proximity losses occur in the turn of the coil, which is closest to the air-gap. Therefore it may be advantageous to remove the copper in this region of high flux density by removing the

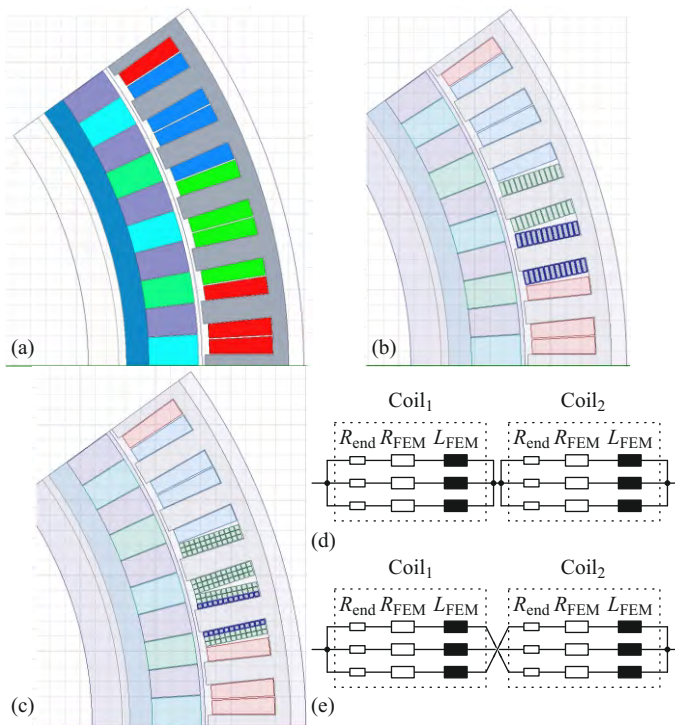


**Fig. 2.15:** Pictures of the ANSYS electro-magnetic model (a) omitting eddy current effects, (b) with helical coil windings, (c) with helical coil winding segmented into three parallel windings. Considered end-winding connection configuration of the segmented helical coil windings considering easy manufacturing (d) or equalization of the dc-resistance of the segments (e).

bottom turn of the coil. This already significantly reduces the external proximity losses, in return the copper fill factor is reduced to 65% and ultimately the losses in the coils are 32% higher than the reference.

As an attempt to reduce the influence of the external proximity losses the coil can be segmented into multiple coils, which are wound around each other, as schematically shown in Fig. 2.15(c). At this point the end-winding connection configuration has to be taken into account, as multiple current path exist and currents circulating within the different coils may significantly increase the losses in the coils. Two

Configuration	Base Machine	Helical Coil	Helical Coil
$N_{\text{turns}}$	12	12	11
End turn losses	104 W	86 W	112 W
Analytic losses	412 W	352 W	428 W
FEM losses	413 W	758 W	544 W
Losses normalized	100 %	184 %	132 %
Configuration	Segm. Coil	Segm. Coil	Segm. Coil
$N_{\text{turns}}$	12	12	11
Nr. of segments	3	3	3
Connection config.	Fig. 2.15(d)	Fig. 2.15(e)	Fig. 2.15(d)
End turn losses	82 W	84 W	89 W
Analytic losses	347 W	372 W	379 W
FEM losses	468 W	457 W	437 W
Losses normalized	113 %	111 %	106 %
Configuration	Segm. Coil	Segm. Coil	Segm. Coil
$N_{\text{turns}}$	11	12	12
Nr. of segments	3	16	16
Connection config.	Fig. 2.15(e)	Fig. 2.15(d)	Fig. 2.15(e)
End turn losses	91 W	73 W	80 W
Analytic losses	343 W	349 W	378 W
FEM losses	434 W	405 W	412 W
Losses normalized	105 %	98 %	100 %

**Tab. 2.9:** Results of the winding configuration analysis including the effects of eddy currents. The results show the end-turn losses, the total losses based on analytical calculations omitting the effects of eddy currents (but including the end-turn losses), and the total losses calculated by FEM analysis including eddy current effects (and the analytically calculated end-turn losses). Eddy current effects are omitted in the FEM analysis of the "Base Machine" as a reference.

different end-winding connection configurations are investigated. From a production point of view, the simplest configuration is a short circuit of the parallel windings at each end of the coil, as shown in Fig. 2.15(d), i.e. the solder joint short circuits all segments. Alternatively, the end-windings could be soldered individually, which would equalize the dc-resistance of the segments already for a coil pair. Ultimately the losses are still 11 – 13 % higher than the reference. Again the copper can be removed from the region of high flux density to further reduce the total

losses while sacrificing copper fill factor.

The above comparison shows that it is advantageous for this application to create multiple parallel coils through segmentation of the wire, i.e. there is a trade-off to be considered: an increase of the segments reduces the effects of circulating currents and eddy currents, but on the other hand the copper fill factor of the coil is reduced due to the additional layers of insulation between the segments. Fortunately Wellascent [39] provides a large variety of fine and ultra-fine rectangular enameled copper wires featuring very thin enamel-insulation layers and self-bonding layers. Finally a winding configuration with 16 segmentations of the coil constructed with ultra-fine rectangular enameled copper wire of dimensions 0.65 mm x 0.1 mm is chosen. An end-winding connection configuration according to Fig. 2.15(d) is chosen to enable a more simple manufacturing. The results of the comparison are summarized in Tab. 2.9.

### 2.3.2 Construction and Assembly

In this section the different manufacturing steps are described. Fig. 2.16 shows a three quarter section view of the fully assembled RFM prototype. The bearing shields and the rotor are manufactured in the D-ITET Workshop (machined of EN AW-7075-T6 aluminum). The stator iron is produced by Vacuumschmelze by stacking 0.1 mm thick sheets of Vacoflux 48 material to a solid block with their VACSTACK technology. Thereafter, the stator geometry is cut by wire-cut electrical discharge machining and finally annealed in order to restore the materials magnetic properties along the edges where the material has been cut. The rotor is held by two hybrid ball bearings, which are press-fitted onto the rotor, as well as one of the bearing shields and slide-fits into the second bearing shield. Furthermore, the bearings are damped with NBR 90 O-rings from Maagtechnic between the bearing shields and the bearings, and a wave spring pretensions the bearings in the axial direction. The cooling fins are glued directly onto the surface of the stator with an epoxy featuring high thermal conductivity. Also shown in the CAD drawing is the possibility to attach an encoder via a small coupling for speed sensing and control purposes.

Fig. 2.17 shows a picture of the final assembly with the 25 pole pair segmented Halbach array consisting of 100 magnets, also shown is a three quarter section view of the rotor assembly. The rotor provides

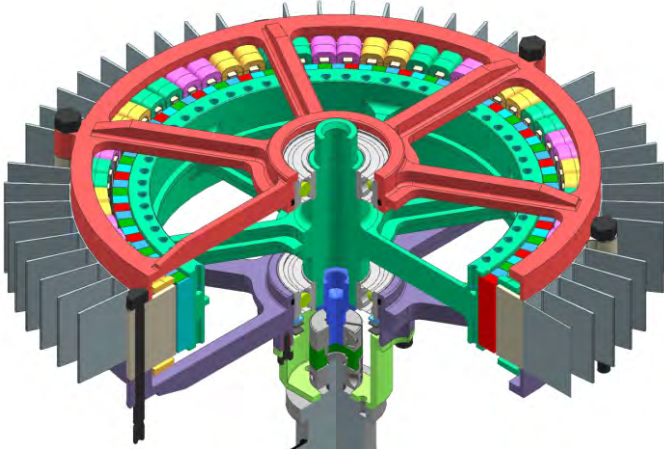


**Fig. 2.16:** Three quarter section view of the RFM prototype’s CAD design.

an array of M3 threads on each side for balancing purposes once the magnets have been mounted. All magnets feature the same shape, but 3 different magnetization directions are required, 25 which are magnetized outwards and 25 inwards in the radial direction, and 50 which are magnetized in the tangential direction. The magnets were produced and assembled onto the aluminum rotor by AIC Magnetics Ltd. (Shanghai). The magnets are sintered NdFeB of grade N48M with black epoxy coating. Loctite 326 was used to attach the magnets.

The copper coils are wound with ultra-fine rectangular enameled copper wire from Wellascent, which feature a very thin enamel-insulation layer and a self-bonding layer. The coils have 12 turns and consist of 16 parallel 0.65 mm x 0.1 mm wires. A custom made winding tool is used to first wind all 16 parallel layers simultaneously, then the coil is constrained and pressed to enforce the coils outside dimensions and finally the wire is electrically heated to 150 °C, which melts the self-bonding layer and creates a firm coil with a very high fill factor. The coils are dimensioned such that a 0.1 mm gap remains between the coils and the stator iron. As edge protection, a layer of Kapton tape is placed on the inside of the coils covering the end-windings. Furthermore, a layer of Kapton tape is placed between coils, which belong to different phases. The coils are slid onto the stator iron and connected. The

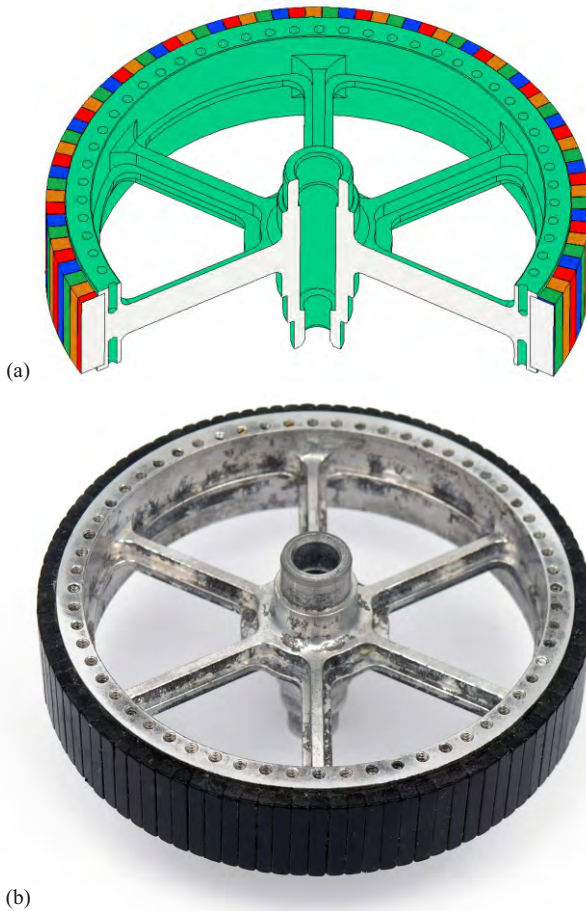


**Fig. 2.17:** (a) Three quarter section view of the RFM prototype's rotor, the coloring of the magnets indicates the different magnetization orientations. (b) Picture of the final rotor assembly with the 25 pole pair segmented Halbach array consisting of 100 magnets.

coil cross connections and their solder joints are also carefully isolated with shrinking tubes and Kapton tape. To monitor the stator and coil temperatures nine negative temperature coefficient (NTC) resistors are

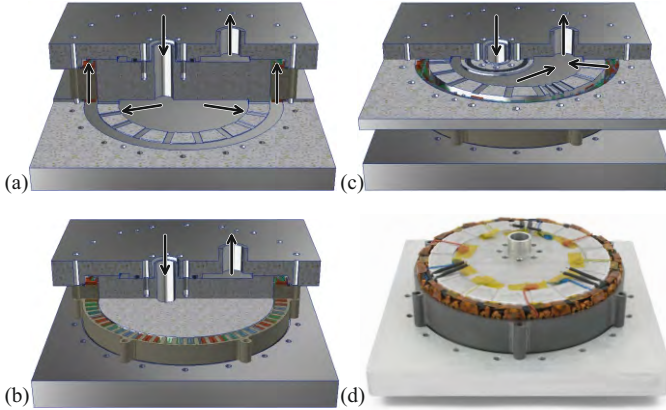


**Fig. 2.18:** (a)-(c) Section views of the stator potting mold assembly. The stator is placed between two aluminum plates with o-ring seals covering the 2 mm wide iron yoke. A mandrel with a through hole is placed inside the stator to keep the epoxy away from the rotor position and the air-gap. To account for tolerances a 1 mm thick PTFE-foil is placed between the stator and the mandrel. (a) The epoxy flows from the inlet through the mandrel and spreads radially at the bottom, passing through thin branches, which will become predetermined breaking points. (b) The epoxy has to flow upwards through the small gaps between the coils and the stator. (c) At the top the epoxy contracts radially to the center into a reservoir before it finally reaches the outlet. (d) Picture of the potting mold assembly with the top plate removed.

placed between the end-windings of the coils. Once the stator assembly is complete, it is placed into a potting mold, which allows the epoxy to be applied under vacuum and cured at ambient pressure. The employed epoxy is Wevopox 2513 and features a high thermal conductivity of  $1.4 \text{ W}/(\text{m K})$ .

Because the outside surface of the stator iron needs to remain epoxy free, for mechanical and thermal reasons, a sophisticated potting mold is required. Fig. 2.18 shows a picture and section views of the potting mold. The section views illustrate the flow of the epoxy. A reservoir of epoxy is connected via a valve and hose to the inlet, where a vacuum seal is easily achieved with some insulation-tape. A vacuum pump is attached via an overflow container (or a long hose acting as such). Once

a vacuum is established inside the potting mold the valve which holds back the epoxy from the reservoir is opened. The epoxy is then pushed through the mold with 1 atm until it reaches the overflow container at the outlet. At this point the vacuum can be released and the epoxy is continuously pushed into the mold with 1 atm from the inlet and outlet. Finally, the epoxy is cured in an oven according to the data sheet instructions. Fig. 2.19 shows the stator assembly before and after the potting process.

In order to avoid any damage of the machine parts during the final construction step, where the stator and rotor assemblies are put together, an assembly aid was constructed. The assembly aid depicted in Fig. 2.20 allows for an assembly or disassembly of the rotor and stator components in a safe manner. The assembly steps are as follows:

- ▶ press bearing into bottom bearing shield;
- ▶ press bearing shield with bearing onto the rotor assembly;
- ▶ press opposite bearing onto rotor assembly;
- ▶ mount stator and rotor assemblies on the assembly aid;
- ▶ press stator assembly bearing shield onto the bearing of the rotor assembly;
- ▶ fix bearing shields and stator assembly together and remove from assembly aid;
- ▶ finally, add the bearing wave spring and (if required) attach the encoder.

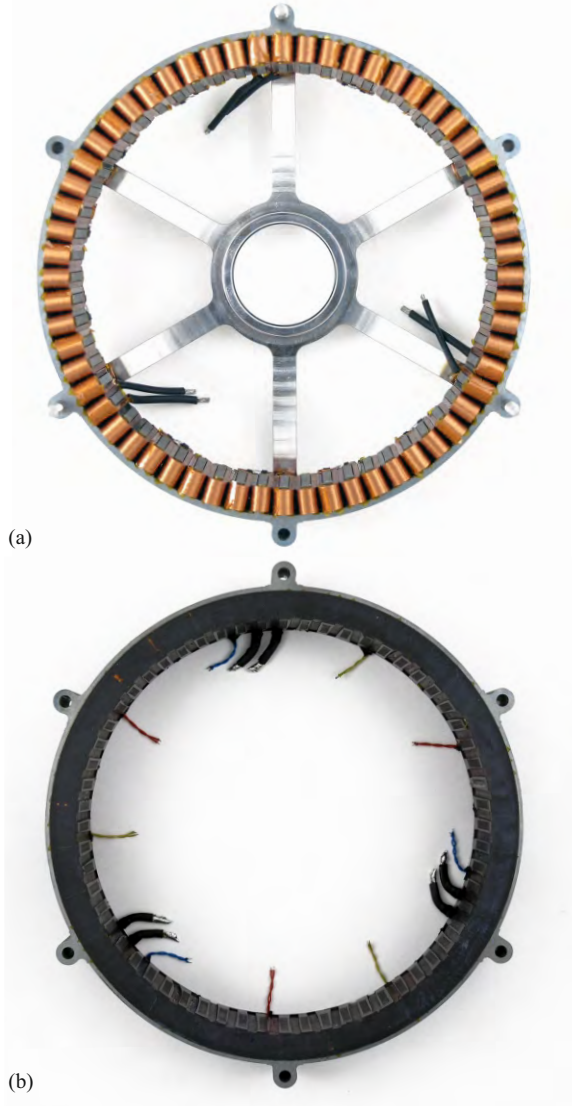


**Fig. 2.19:** Stator assembly before (a) and after (b) the potting process. The epoxy mechanically fixtures the coils in place and increases the robustness of the assembly, furthermore it provides a good thermal contact between the coils and the stator iron, while also providing electrical insulation.

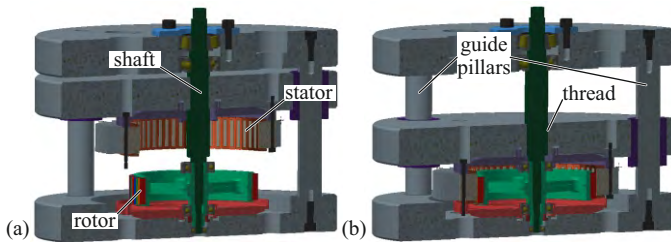


**Fig. 2.20:** Half section views of the RFM machine assembly aid. (a) Initial position: the rotor with bearing shield is held in place centered on a bottom plate by a threaded shaft. The stator assembly with bearing shield is screwed to a middle plate, which is centered and guided by three guide pillars and linear ball bearings, i.e. it can only move in axial direction remaining parallel and centered to the bottom plate. The middle plates axial position is held by the thread of the shaft. (b) Final position: screwing of the shaft lowers the stator assembly onto the rotor assembly without any danger of the magnetic attraction forces causing a collision of the rotor and stator assemblies. The stator assembly can be pressed onto the bearing already in position on the shaft of the rotor. Finally, the bearing shields and the stator assembly are screwed together and the connection to the middle plate can be unscrewed.

### 2.3.3 Measurement Results

There exist multiple ways to characterize the machine performance. Because of the equipment readily available in the lab an induction machine and an industrial drive are used to mechanically drive the RFM prototype. The machines are coupled through a Magtrol TF series torque flange sensor, which also features a speed sensor. The measurement setup is depicted in Fig. 2.21.

The impedance of the stator windings are measured with an Agilent 4294A precision impedance analyzer over a wide range of frequencies, before the rotor is inserted into the stator assembly. Due to mechanical resonances at 160 Hz, it has proven difficult to produce a clean measurement of the impedances once the rotor has been inserted. Furthermore, the mutual inductance has shown a dependence on the rotor position, which can be explained by the high flux density in the stator teeth excited by the permanent magnets, i.e. due to the change in permeability of the cobalt iron near the saturation flux density. Fig. 2.22 shows the impedances between the star point and the three phases (without the rotor). It can be seen that the impedances of the three phases are identical up to a frequency of  $\approx 1$  MHz. A further measurement is required to determine the mutual inductance. The impedance of phase *A* and

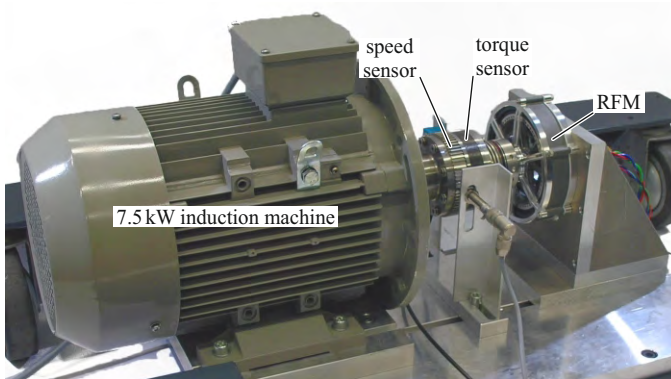


**Fig. 2.21:** Measurement setup of the RFM prototype. An induction machine is driven by an industrial drive and mechanically drives the RFM prototype. A Magtrol TF series torque flange sensor, which also features a speed sensor couples the two machines.

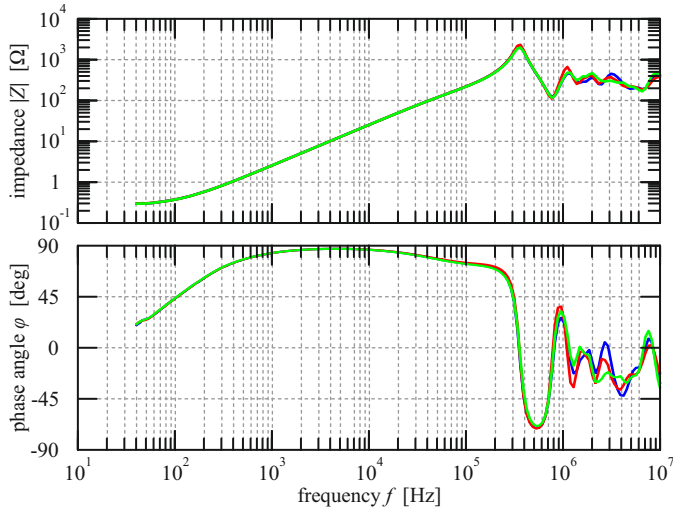


**Fig. 2.22:** Impedance measurement of the stator windings to the star point before the rotor is inserted into the stator assembly.

$B$  connected in series, such that  $i_A = i_B$ , is also measured. Fig. 2.23 shows the measured inductances and ac-resistances. With the two measurements

$$L_A = L_\sigma + M = 405 \mu\text{H} \text{ and } L_{AB} = L_\sigma + \frac{M}{2} = 363 \mu\text{H}, \quad (2.52)$$

the stray, mutual, and d-axis inductance are determined to be

$$L_d = L_\sigma + \frac{3}{2}M = 447 \mu\text{H} \text{ with } L_\sigma = 321 \mu\text{H} \text{ and } M = 84 \mu\text{H}. \quad (2.53)$$

The dc-resistance of the machine phases is obtained with a 4-wire resistance measurement on a Agilent 34410A 6 $\frac{1}{2}$  digit multimeter to be  $R_s = 293 \text{ m}\Omega$ , which matches extremely well with the predicted value of  $292 \text{ m}\Omega$ .

## Flux Linkage

The flux linkage is measured by driving the RFM prototype mechanically without any loads connected on the terminals. In this case the

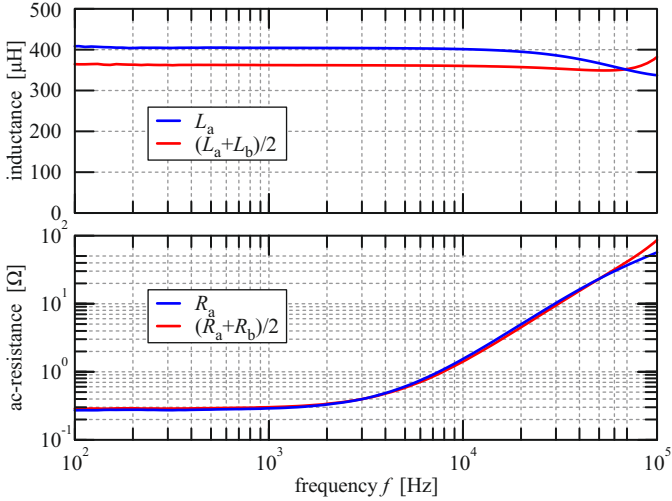


**Fig. 2.23:** Inductance (top) and ac-resistance (bottom) measurement of the stator winding of phase  $A$  and half of the series connection of stator windings  $A$  and  $B$ . Both measurements are required to determine the stray inductance,  $L_\sigma$ , and the mutual inductance,  $M$ , values. The d-axis inductance is  $L_d = L_\sigma + \frac{3}{2}M = 447 \mu\text{H}$  with  $L_\sigma = 321 \mu\text{H}$  and  $M = 84 \mu\text{H}$ .

measured phase voltages, shown in Fig. 2.24(a), are equal to back-EMF voltages and an integration over time yields the flux linkages depicted in Fig. 2.24(b). The amplitude of the flux linkages is  $\hat{\Psi}_{\text{ind},A} = 34.5 \text{ mWb}$  and matches the predicted value of  $35 \text{ mWb}$  very well.

### Torque Constant

Under the assumption that the phase currents are in phase with the back-EMF voltage the torque constant can be derived directly from the flux linkage as

$$k_T = \frac{T}{\hat{I}_q} = \frac{3}{2} \hat{\Psi}_{\text{ind},A} p = 1.31 \text{ Nm/A}, \quad (2.54)$$

i.e. it can theoretically be captured by the no-load measurement already presented in Fig. 2.24. However, the armature reaction flux can potentially limit the available torque, due to saturation of the stator

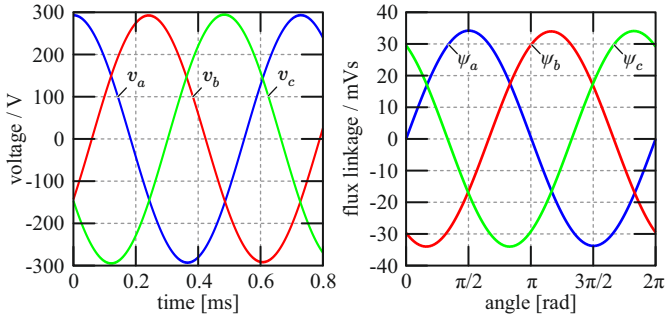


**Fig. 2.24:** Measurement of the phase voltages (left). An integration over time yields the flux linkages (right). The amplitude of the flux linkages is  $\Psi_{\text{ind},A} = 34.5 \text{ mWb}$  and matches the predicted value of  $35 \text{ mWb}$  very well.

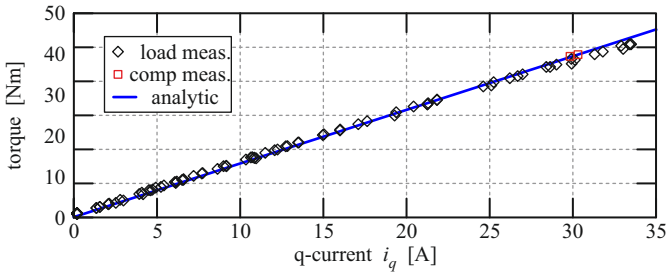


**Fig. 2.25:** Torque dependence on the q-current component measured at different speeds.

iron. Therefore, it still needs to be verified that the full torque can be produced by the RFM prototype. For that purpose the RFM prototype is mechanically driven by the induction machine and loaded electrically with variable three phase resistors. Because the thermal boundary conditions in the test setup are significantly different to the thermal boundary conditions of the AWT application, only transient measurements can be performed. Two synchronized Lecroy HDO4054 oscilloscopes are used to measure the three phase voltages, the three phase currents, and the outputs of the torque and speed sensors. The inductances of the load resistors and the inductance of the machine cause the phase currents to be out of phase with the back-EMF voltage. Hence, the q-component of the phase currents needs to be extracted from the mea-

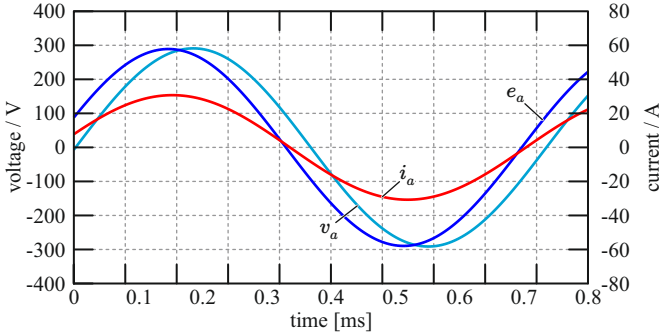


**Fig. 2.26:** Induced voltage  $e_a$ , output voltage  $v_a$  and current  $i_a$  of phase  $A$  for nominal current operation at a speed of  $\approx 3300$  rpm with a reactive power compensation at the load resistors.

surements, since only the q-component of the current produces a net torque. Fig. 2.25 shows the measurements in the torque/q-current plain. It can be seen, that the measurements match the analytic predictions very well. At high currents, above 25 A, the torque constant seems to deteriorate. Such a behavior could potentially be caused by saturation of the stator iron due to armature reaction flux. This is not the case, but slight field weakening in the stator due to high d-currents is observed. This is verified by two measurements, where capacitors are connected in parallel to the load resistor, in order to achieve reactive power compensation.

The phase voltage  $v_a$  and phase current  $i_a$  for nominal current operation at a speed of  $\approx 3300$  rpm with the reactive power compensation are shown in Fig. 2.26. As all machine parameters are known it is possible to obtain the back-EMF  $e_a$  based on measured voltages and currents. D-q components of the phase voltages, currents and back-EMFs are given in Fig. 2.27. It can be seen that the current d-component has a zero value, i.e. the reactive power compensation has been tuned correctly. Finally, in Fig. 2.28 the torque, speed and input and output powers are depicted for the same operating point as the one described above.

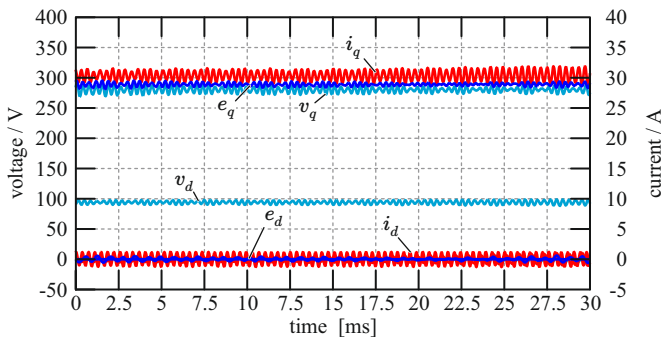


**Fig. 2.27:** D-q components of the phase voltages, currents and back-EMFs for nominal current operation at a speed of  $\approx 3300$  rpm with a reactive power compensation at the load resistors.

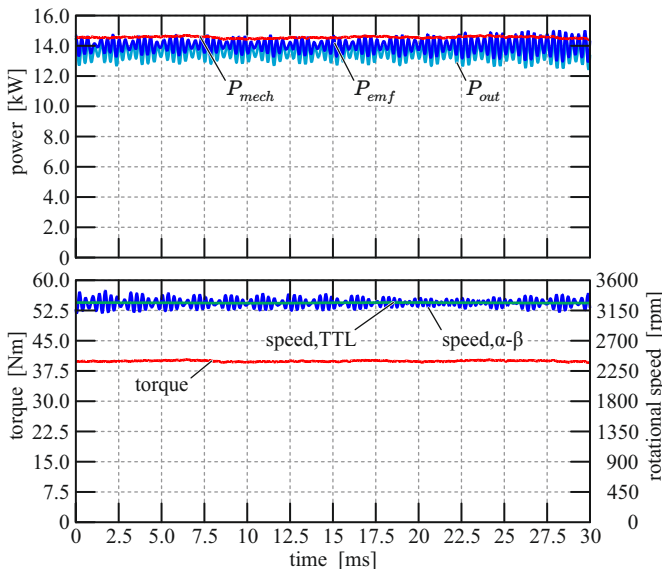


**Fig. 2.28:** Torque, speed and input and output powers for nominal current operation at a speed of  $\approx 3300$  rpm with a reactive power compensation at the load resistors.

### No-load Losses

So far only the torque dependent loss components have been identified, i.e. the torque constant and the phase resistance. The sum of the frequency dependent losses are also measured with the test setup. Fig. 2.29 shows torque and losses of the RFM prototype in dependence of the rotational frequency. The transient measurements are depicted in blue. However, bearing losses for example are higher at first until the bearing grease has reached its operating temperature, at which point the bearing losses can be significantly lower. Therefore, these measurements do not provide reliable data. In order to get consistent data, the machine is first accelerated to 55 Hz and left to run for 20 min, then the losses are measured consecutively stepping down with 5 Hz steps. The no-load torque shows a linear dependency on the rotational frequency with a small offset, hence the losses show a superposition of linear and quadratic loss components. The no-load torque can be approximated with

$$T_{\text{no-load}}(f_{\text{rot}}) = 116.5 \text{ mNm} + 8.664 \text{ mNm/Hz} \cdot f_{\text{rot}}, \quad (2.55)$$

where  $f_{\text{rot}}$  is the mechanical rotation frequency. Consequently the losses are approximated as

$$P_{\text{no-load}}(f_{\text{rot}}) = (116.5 \text{ mNm} + 8.664 \text{ mNm/Hz} \cdot f_{\text{rot}}) \cdot 2\pi f_{\text{rot}}. \quad (2.56)$$

In order to separate the mechanical losses from the electromagnetic losses a dummy machine, without rotor iron or permanent magnets, is also measured in the same way as the RFM prototype. These results are also depicted in Fig. 2.29 and approximated as

$$T_{\text{no-load}}^{\text{dummy}}(f_{\text{rot}}) = 59.27 \text{ mNm} + 2.013 \text{ mNm/Hz} \cdot f_{\text{rot}} \quad (2.57)$$

and

$$P_{\text{no-load}}^{\text{dummy}}(f_{\text{rot}}) = (59.27 \text{ mNm} + 2.013 \text{ mNm/Hz} \cdot f_{\text{rot}}) \cdot 2\pi f_{\text{rot}}. \quad (2.58)$$

Analytically only iron losses have been considered, for that reason the no-load losses deviate significantly from the predicted values. However, for optimization purposes it doesn't make sense to include these additional loss components, as they are almost independent of the analytical degrees of freedom and are more related to the physical implementation of the RFM prototype. E.g., Fig. 2.29 shows that a significant part of

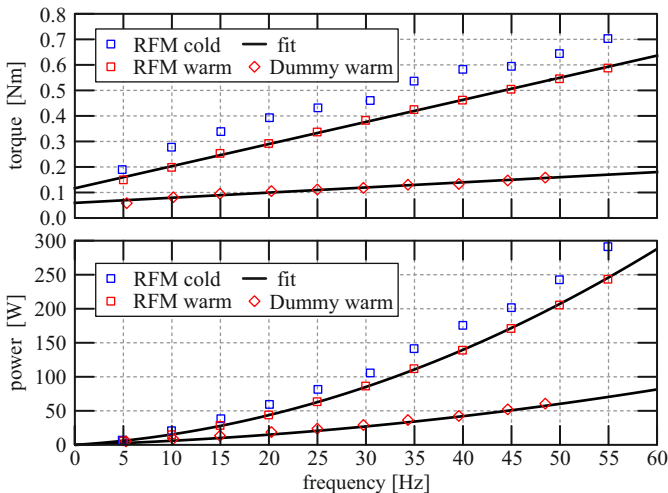


**Fig. 2.29:** Measured torque and losses in dependence of the rotational frequency of the RFM prototype without an electrical load attached. Also shown are measured torque and losses of a mechanical dummy machine without rotor iron or permanent magnets.

the no-load losses are of mechanical nature, i.e. 29% at 3200 rpm. Or eddy current losses in the coils due to external proximity effects are expected to be 25 W by FEA, but could be much larger, as described in Section 2.3.1. Further, eddy current losses in the rotor are estimated to be 44.5 W at 3200 rpm by FEA, which could be reduced by segmentation of the rotor magnets, but would result in a more challenging construction process. After these loss components are subtracted from the measured losses only 69 W remain (36% of the total no-load losses at 3200 rpm). These losses can be attributed to iron losses in the cobalt iron stator and match the analytically predicted value of 74 W well.

### Efficiency in the Torque-Speed Plane

The machine efficiency in the torque-speed plane can be extrapolated from the no-load loss measurement, the torque constant and the measured phase resistances. Fig. 2.30 shows the extrapolation for the three rotational speeds of the generation points #1–3, which are indicated

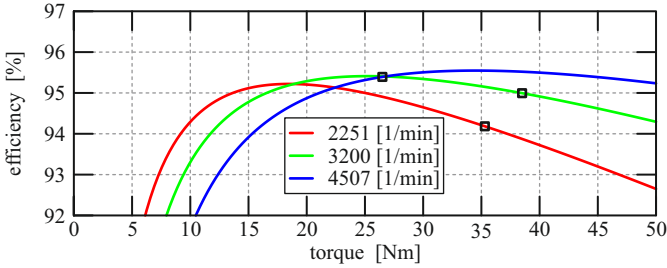


**Fig. 2.30:** Extrapolated efficiency in dependence of the torque characteristics of the RFM prototype for the rotational speeds of the three generation points (cf. Tab. 2.1). The three generation points are indicated by the squares.

with squares. The efficiency is calculated as

$$\eta = \frac{T 2\pi f_{\text{rot}} - P_{\text{loss}}(T, f_{\text{rot}})}{T 2\pi f_{\text{rot}}}, \quad (2.59)$$

with

$$P_{\text{loss}}(T, f_{\text{rot}}) = P_{\text{no-load}}(f_{\text{rot}}) + 3R_{\text{ph},A} \left( \frac{T}{k_T} \right)^2, \quad (2.60)$$

where  $R_{\text{ph},A} = 352 \text{ m}\Omega$  is the phase resistance at  $80^\circ\text{C}$ . Fig. 2.30 shows that, in spite of the higher no-load losses, the machine efficiency is  $\approx 95\%$  at the generation points #1–3.

### Thermal Model Verification

The electro-magnetic performance of the RFM prototype has been predicted well. However, it still needs to be shown that the temperatures of the RFM prototype under load will remain within the specified limits. Tab. 2.10 lists the thermal resistance values of the 1-dimensional LPTN (cf. Fig. 2.6) and Tab. 2.11 shows how much of the thermal power flow is estimated to flow from the stator through the air-gap.

It can be seen that the most significant contributions to the thermal resistances originate from  $R_{\text{ra}}$  and  $R_{\text{sta}}$ , which are derived from the boundary condition assumptions. Since the calculated operating temperatures are most significantly influenced by these two assumptions, it will be sufficient to validate these boundary conditions, in order to verify that the RFM prototype will not exceed the specified operating temperatures under load.

$R_{ra}$	$R_{ri}$	$R_{pm}$	$R_{ag}$	$R_{wir}$	$R_{st}$	$R_{sy1}$	$R_{sy2}$	$R_{sta}$	
427	0	82.5	87.6	29.1	10.8	2.8	2.8	109	[K/kW]
		597		29.1			125		[K/kW]

**Tab. 2.10:** Analytically calculated thermal resistances for the geometry of the RFM prototype (cf. Fig. 2.6).

Generation Point Number	# 1	# 2	# 3	Unit
Iron losses	46.1	74.2	112	W
Winding losses	387	475	201	W
Total losses	433	549	314	W
Power flow through air-gap	74	74	32	W
Power flow through air-gap	17	13.5	10	%

**Tab. 2.11:** Analytically calculated losses and expected power flow through the air-gap for the generation points #1-3 (cf. Tab. 2.1 and Fig. 2.6).

In order to verify the boundary condition assumptions, a test setup is designed. The setup, shown in Fig. 2.31, consist of a stator segment (one sixth) machined of aluminum and a wind tunnel. Nine coils are placed on the stator segment and connected in series (cf. Fig. 2.31(a)). Six negative temperature coefficient (NTC) resistors are placed between the end-windings of the coils at the positions shown in Fig. 2.31(a) & (b). A picture of the stator segment after potting with epoxy is depicted in Fig. 2.31(c). This thermal measurement dummy is placed on the end of a wind tunnel, which guides the air across the outside surface of the segment. A Xantrex XHR 20-50 dc power supply is used to control a dc-current in the winding to generate thermal losses. The coil current and voltage are measured with two Agilent 34410A 6<sup>1/2</sup> digit multimeters and a precision 10 mΩ shunt. The temperatures of the NTC-resistors are measured with a custom made "NTC-temperature acquisition board". Figs. 2.32 and 2.33 show the data captured in a thermal measurement of the stator segment before and after the cooling fins are mounted on the stator surface. The air-speed of 22 m/s in the wind tunnel is measured with a Fluke 922 Airflow Meter. Figs. 2.32 and 2.33 show the coil current  $i_{coil}$ , the coil voltage  $v_{coil}$ , the thermal losses  $p_{coil}$  and the temperature response of the NTC-resistor. Furthermore, the average coil temperature,  $\theta_{coil}$ , is calculated using the linear temperature coefficient of copper resistivity,  $\alpha_{Cu} = 0.003862$ , which

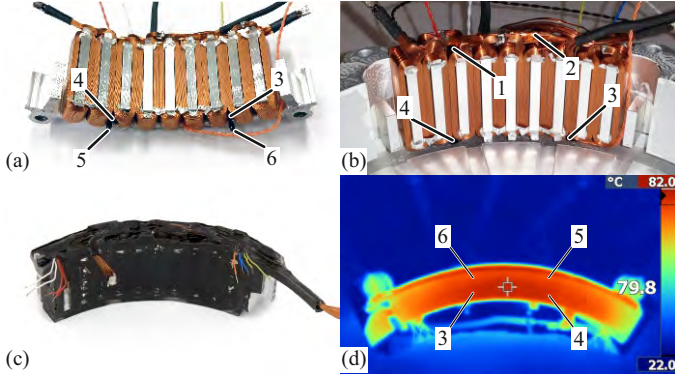


**Fig. 2.31:** Test setup for the verification of the thermal boundary conditions. (a) Nine coils are placed on a stator segment and connected in series, (a-b) six NTC-resistors are placed between the end-windings of the coils. (c) Picture of the thermal measurement dummy after the potting process. (d) Thermal image of the test setup taken with a Fluke Ti10 thermal imaging camera.

describes the temperature dependency of the coils resistance as

$$R_{\text{coil}}(\theta_{\text{coil}}) = R_{\text{coil},0} (1 + \alpha_{\text{Cu}}(\theta_{\text{coil}} - \theta_0)), \quad (2.61)$$

where  $R_{\text{coil},0}$  and  $\theta_0$  are initial coil resistance and temperature and  $R_{\text{coil}}(\theta_{\text{coil}})$  denominates the coil resistance at temperature  $\theta_{\text{coil}}$ . Solving (2.61) for  $\theta_{\text{coil}}$  yields

$$\theta_{\text{coil}}(t) = \theta_0 + \frac{1}{\alpha_{\text{Cu}}} \left( \frac{R_{\text{coil}}(\theta_{\text{coil}}(t))}{R_{\text{coil},0}} - 1 \right), \quad (2.62)$$

with

$$R_{\text{coil}}(\theta_{\text{coil}}(t)) = \frac{v_{\text{coil}}(t)}{i_{\text{coil}}(t)}, \quad (2.63)$$

hence the average coil temperature is captured by  $i_{\text{coil}}$  and  $v_{\text{coil}}$ . Then a parameter identification routine is used to fit the state space model,

$$\frac{d}{dt} \Delta\theta_{\text{coil}} = \frac{-1}{R_{\text{th,meas}} C_{\text{th,meas}}} \Delta\theta_{\text{coil}} + \frac{1}{C_{\text{th,meas}}} p_{\text{coil}}, \quad (2.64)$$

to the measurement data  $\Delta\theta_{\text{coil}}(t) = \theta_{\text{coil}} - \theta_{\text{amb}}$  and  $p_{\text{coil}}(t)$ , which yields  $R_{\text{th,meas}}$  and  $C_{\text{th,meas}}$ .

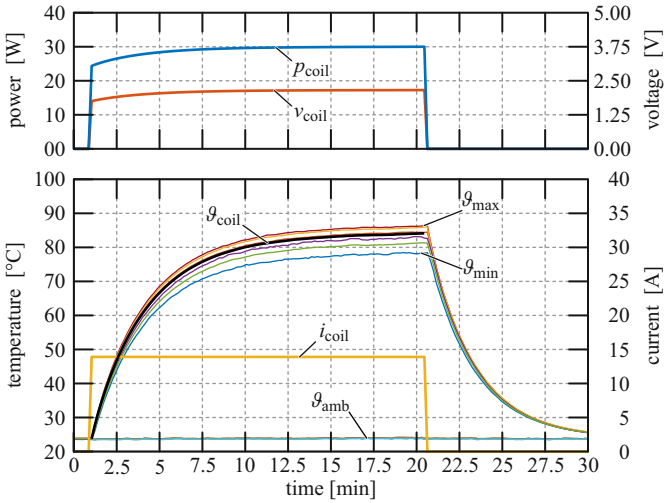


**Fig. 2.32:** Data captured in a thermal measurement of the stator segment without cooling fins mounted on the stator surface at an air-speed of 22 m/s.

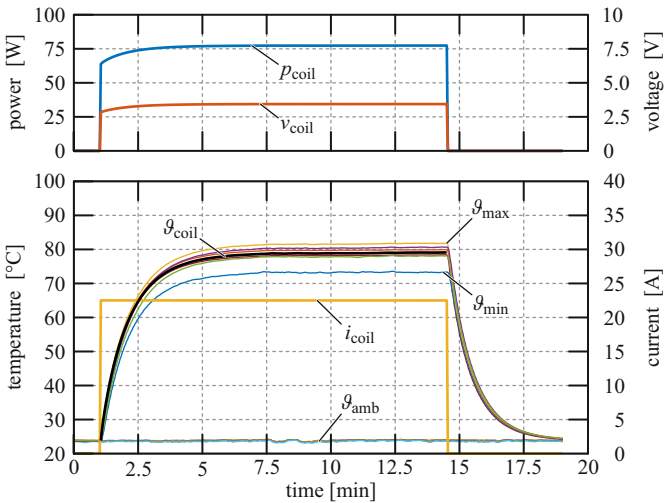


**Fig. 2.33:** Data captured in a thermal measurement of the stator segment with cooling fins mounted on the stator surface at an air-speed of 22 m/s.

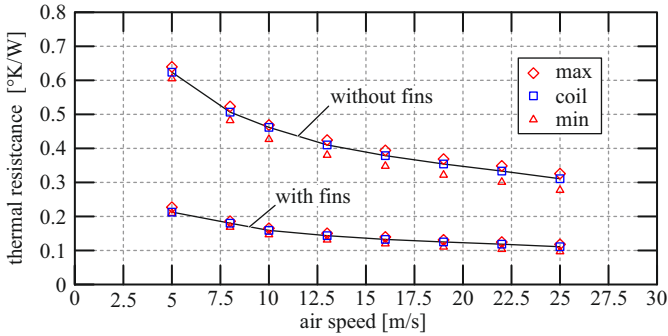


**Fig. 2.34:** Total thermal resistance of the windings to ambient measured for the RFM prototype at different air-speeds.

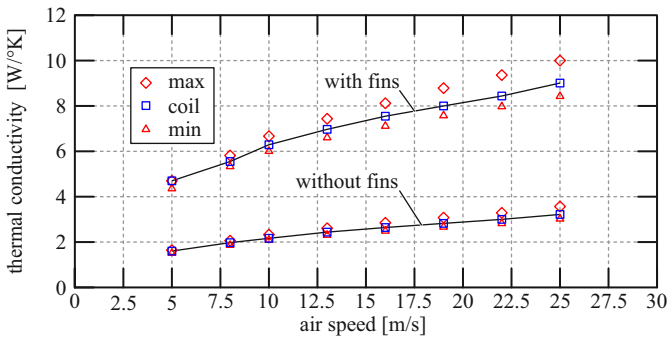


**Fig. 2.35:** Total thermal conductance of the windings to ambient measured for the RFM prototype at different air-speeds.

The results of the thermal measurements are summarized in Fig. 2.34 and 2.35. They show the total thermal resistance and thermal conductance of the windings to ambient for the RFM prototype in dependency on the air-speed in the wind-tunnel. The measurements clearly show, that the RFM prototype features a thermally feasible design, i.e. even if, as a more than worst case approximation, a total of 750 W of losses would occur in the windings, while no thermal power flows through the air-gap, the average coil temperature could be limited to 120 °C already at an air-speed of 22 m/s (assuming 30 °C ambient temperature).

Component	Analytical	CAD	Measured
Stator iron	528 g	597 g	585 g
Windings (+epoxy)	459 g	565 g	521 g
Magnets	500 g	488 g	664 g
Rotor shaft	249 g	185 g	
Total weight	2271 g	2230 g	2157 g

**Tab. 2.12:** Calculated and measured weights of the RFM prototype.

### Weights

Finally a comparison of the RFM prototype weights calculated and measured is given in Tab. 2.12, although there are some deviations the total predicted weights match well with a deviation of  $-5\%$ .

## 2.4 Axial Flux Machine Topologies

In this section the basic topologies of axial flux machines (AFM) with different stator and rotor configurations are presented. Furthermore, the degrees of freedom for the following optimization process are emphasized. All topologies in this section are realized with permanent magnet excitation. Axial flux permanent magnet motors (AFPM) generally reveal a high torque-to-weight ratio and good heat removal compared to conventional radial flux permanent-magnet (RFPM) motors [40]. Hence they are investigated in more detail in this thesis. The presented investigations have partially been published at IECON 2014 and provided the foundation for the work submitted for review at IET Electric Power Applications by academic guest Dr. Ivan Subotic as the first author (cf. List of Publications on pages 271–272).

To introduce the reader to the basic geometry of AFMs, a core-less double rotor single stator AFM is shown in Fig. 2.36. The machine consist of two axially magnetized rotor discs. The stator in between the rotor discs is an air cored distributed or concentrated winding. There exist several possible topologies when building an axial flux machine. Basically, these machines are of disk type, which means that both, the stator and the rotor are disks, separated by an air-gap. Both components have multiple options to be realized. Three basic configurations are:

- ▶ single rotor - single stator structure (single-sided);
- ▶ double rotor - single stator structure;
- ▶ multiple rotors - multiple stators structure (multi-stage).

A schematic representation of these topologies is given in Fig. 2.37. The single-sided topology only consists of one stator and one rotor disk. An iron core is necessary on the stator in order to provide a low reluctance path for the magnetic flux. Such a structure requires a significant effort in order to ensure a mechanically stable design, e.g. thicker rotor disks and a more complex bearing arrangement. Furthermore, lamination of the stator iron is difficult in such a structure. For these reasons, this topology is assumed to be not suitable.

Compared to a single-sided machine, the double rotor single stator structure can be realized with air-cored stator coils as it consists of one stator disk in between two rotor disks with permanent magnets, which

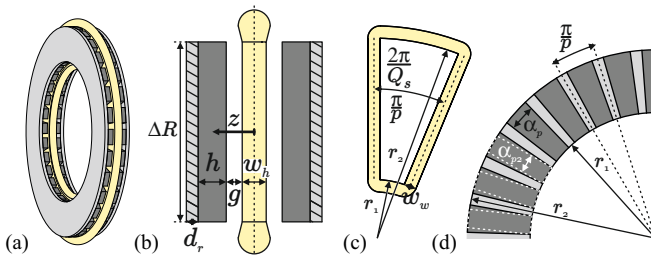


**Fig. 2.36:** Geometrical models of a core-less double rotor single stator axial flux machine (AFM). (a) 3D view of the electro-magnetically active material of the AFM. The AFM consist of an air cored stator winding and two axially magnetized rotor discs with surface mounted permanent magnets. (b) AFM side cut view. (c) Top view of one coil. (d) Top view of rotor disc.

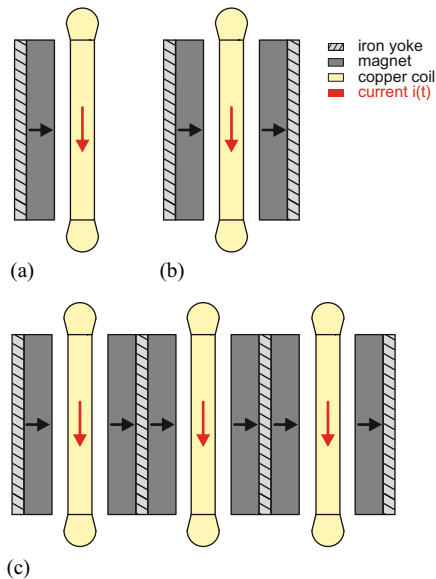


**Fig. 2.37:** Schematic representation of AFM topologies, (a) single-sided machine, (b) double rotor - single stator, (c) multi-stage structure (e.g. 3 stacks).

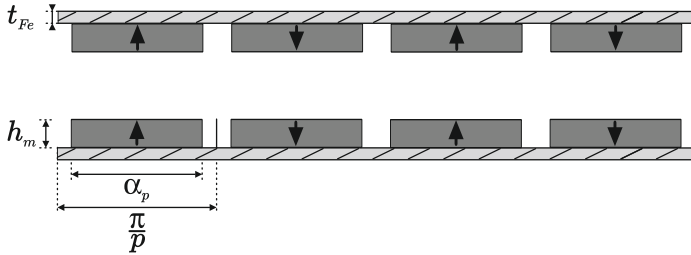


**Fig. 2.38:** Axial magnetization.

allows the flux to flow in a closed path. Hence no stator iron is necessary. But as a consequence the stator is part of the air-gap, which results in a lower air-gap flux density and therefore yields a lower induced voltage compared to iron-cored stator machines. An advantage of this topology, however, is the absence of reluctance forces between the rotor and stator disks, which significantly simplifies the mechanical construction. No iron losses occur in the stator, which would need to be laminated radially further complicating the mechanical construction. However, the air-gap length is increased dependent on the stator thickness, which ultimately makes a good stator design more challenging.

Two different types of magnetization are considered, namely axial magnetization with PMs mounted on rotor iron or a discrete Halbach-array where the rotor iron can be omitted. The magnet arrangement for the common axial magnetization on a rotor iron is depicted in Fig. 2.38. It can be seen that an iron yoke of thickness  $t_{Fe}$  is essential in order to guide the flux in a closed path. The parameters describing the geometrical degrees of freedom are the radius from the center of the machine to the inside edge of the magnet  $r_1$ , the radial length  $\Delta r$  (which defines the radius to the outside edge of the magnets  $r_2 = r_1 + \Delta r$ ), the axial magnet height  $h_m$ , and the width of the magnet (cf. Fig. 2.36). The maximum width of the magnets is limited by the pole pitch, however, it is meaningful for the magnet width to be smaller than the pole pitch  $\frac{\pi}{p}$ . Hence, a parameter  $\alpha_p \leq 1$  is introduced, which describes the pole coverage.

An effective way to increase the air-gap flux density is to employ a discrete Halbach array instead of common axial magnetization. In that case the space between the axially magnetized magnets is filled with additional PMs of proper transverse magnetization. This creates a full

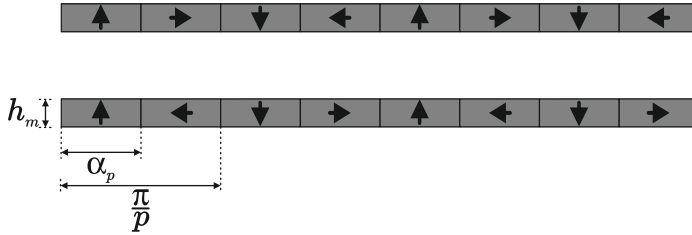


**Fig. 2.39:** Discrete Halbach magnetization.

disk of magnet segments, as depicted in Fig. 2.39. The magnetic field of the transversely magnetized magnets cancels the magnetic field on one side of the magnet disk and amplifies the magnetic field on the other side. As shown in Fig. 2.39, in contrast to the common axial magnetization (non-Halbach), one pole now consists of two magnets, an axially plus a transversely magnetized one per rotor disc. This means, that the pole coverage  $\alpha_p$  has to be redefined as the ratio of an axially magnetized sector to an entire pole for a segmented Halbach configuration. The rest of the geometric dimensions ( $r_1, \Delta r, h_m$ ) are defined the same way as for non-Halbach magnetization.

Multi-stage motors are basically an extension of double rotor - single stator machines, where multiple machines are stacked together to form a single machine. For the application in this thesis only topologies with two or more rotor disks are investigated as it is assumed that they are better suitable for PM generator applications than single-sided topologies. For multi-stage machines certain symmetries can be exploited. In Fig. 2.40 a schematic drawing of one pole pair of a stacked machine is shown, if simply three double rotor single stator machines are attached to each other through their rotor irons. Fig. 2.40 also shows the magnetic equivalent circuit with the reluctances of the permanent magnets,  $R_m$ , the air-gap including the winding,  $R_g$ , and the stator iron,  $R_{Fe} \approx 0$ , where each magnet is a magnetic voltage source with its internal resistance  $R_m$ . It can be seen, that in such an arrangement the magnetic circuits of the different stacks of the AFM are essentially decoupled, i.e. due to symmetries it is sufficient to analyze a single stack electro-magnetically and scale the results by the number of stacks. Furthermore it is evident from the magnetic equivalent circuit, that the iron of the inside rotor discs doesn't guide any flux and can simply be

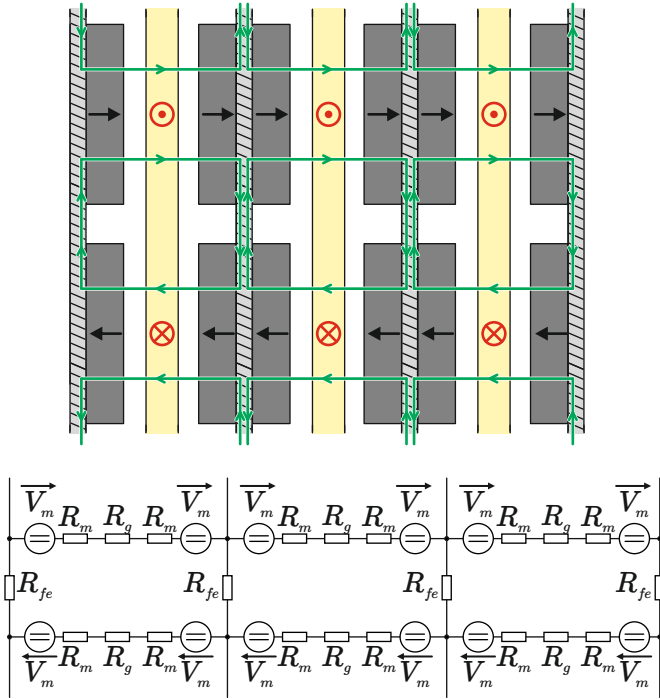


**Fig. 2.40:** Magnetic circuit of one pole pair for a stacked machine with axial magnetization, path of magnetic flux (top), reluctance model (bottom).

omitted. This yields the schematic drawing and equivalent magnetic circuit depicted in Fig. 2.41 and clearly shows, that the magnetic fields in the air-gaps of both structures will be identical. In multi-stage machines with Halbach magnetization it is also sufficient to only analyze one stack electro-magnetically, but no electro-magnetic material can be omitted.

A priori it is not evident, if it is beneficial to construct an axial flux machine as one double rotor AFM or if the magnet and winding material should be segmented into multiple parts for creating a multi-stage AFM. This will clearly depend on the specifications required for the machine. From an electro-magnetic point of view two effects should be considered, which will be explained through thought-experiments.

The first thought-experiment is simple: if a two-stage AFM is built

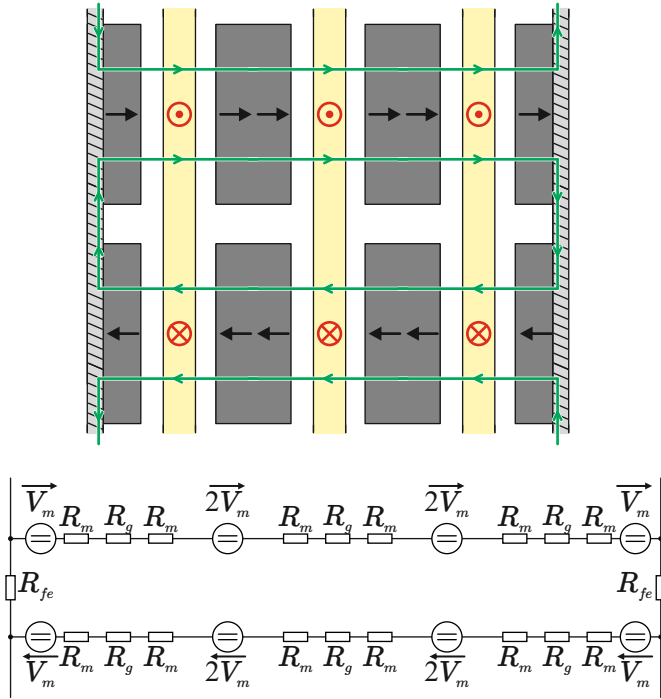


**Fig. 2.41:** Magnetic circuit of one pole pair for a stacked machine with axial magnetization, path of magnetic flux (top), reluctance model (bottom).

using the same amount of material as a single-stage AFM by simply segmenting the copper coils and the magnets, then the total reluctance of the magnetic circuit of the multi-stage AFM will be larger, since two additional (physical) air-gaps are present in the double-stage AFM, compared to the single-stage AFM, i.e. the machine performance will be lower in the multi-stage AFM.

For the second thought experiment, let's assume that the magnet height  $h_m$  and the winding width  $w_w$  are very large and that the distance between the two poles is much smaller than the magnet height, i.e.

$$r_2 \frac{\pi}{p} \ll w_w \text{ and } r_2 \frac{\pi}{p} \ll h_m. \quad (2.65)$$

In such a case there would be essentially no magnetic flux near the

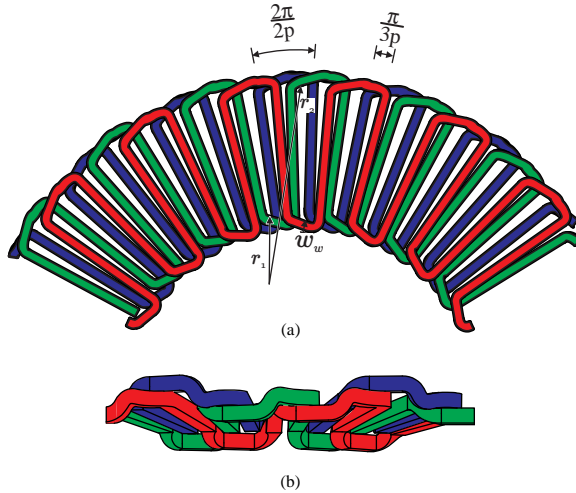


**Fig. 2.42:** Schema of distributed windings, (a) coil arrangement, (b) end-winding connection.

center part of the winding, because the flux path predominately would close radially from one pole to the other, rather than flowing axially from one rotor disc into the other. In such a case it would most likely be beneficial to build a multi-stage machine with the same amount of material as the single-stage machine, because the ratio between the total air-gap distance and the pole pitch distance decreases.

In the stator design the type of winding realization is decisive for the performance of the AFM. Three different types of winding configurations are considered.

In distributed windings, the coils are (as the name already suggest) evenly distributed across the stator disk, which requires the end-windings of the different phases to cross each-other. The phases alternate in tangential stator direction, as indicated by different colors in Fig. 2.42(a). In general, distributed windings are challenging to construct and manufacture. Usually they have to be woven into each other, but in Fig. 2.42, an approach is shown, where all phases can be manufactured as single packets and then be inserted into each other to create the stator assembly.

It is also possible to use concentrated windings in AFMs as depicted

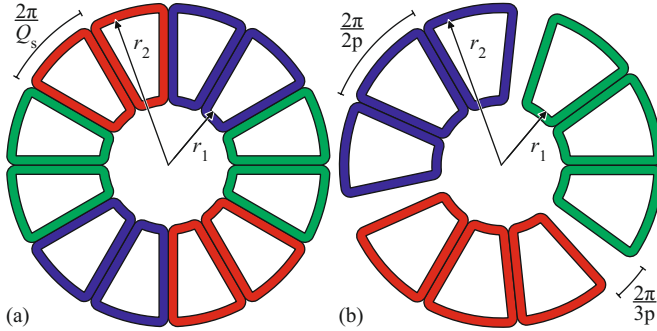


**Fig. 2.43:** Schematic section of possible coil arrangements of two concentrated windings, (a) classical concentrated winding with  $Q_s = 12$ , (b) phase grouped winding with  $Q_s = 9$  and  $p = 5$ .

in Fig. 2.43. In this work two categories of concentrated windings are considered, the classic concentrated winding arrangement, where the coil pitch is defined by the number of coils  $Q_s$  as shown in Fig. 2.43(a), and phase grouped concentrated windings, where the coil pitch is equal to the pole pitch, as illustrated in Fig. 2.43(b). Due to constructive limitations only a subset of concentrated winding arrangements can be configured as phase grouped windings, i.e. the number of coils must be smaller than the number of poles

$$Q_s \stackrel{!}{\leq} 2p. \quad (2.66)$$

Any combinations of pole pairs and number of coils, which can be configured as phase grouped windings could also be realized as classical concentrated windings featuring a pole pitch of  $\frac{2\pi}{Q_s}$ . But because the fundamental winding factor of the phase grouped concentrated windings is equal to 1 and always smaller than 1 for the classical concentrated windings, only the phase grouped configurations are considered.

### 2.4.1 AFM Electro-Magnetic Models

Two types of magnetization and three winding topologies were presented. This enables six different machine implementations, for which analytic electro-magnetic models have been assembled. Similar to the electro-magnetic models of the RFMs the description of the AFMs begins with the magnetic field distribution generated by the rotor, then calculates the back-EMF voltage and finally derives the losses and efficiencies.

For axially magnetized rotor disks, the resulting z-component of the air-gap flux density is given in [24] as

$$B_z(r, \varphi, z) = \mu_0 \sum_{m=1,3,5,\dots}^{\infty} \int_0^{\infty} k A_m(k) J_{mp}(kr) \cos(mp\varphi) \cosh(kz) dk, \quad (2.67)$$

where  $J_{mp}$  is the first kind Bessel function of order  $mp$ . The coefficient  $A_m$  is

$$A_m(k) = \frac{M_m}{k \left( \cosh(k\frac{g}{2}) + \mu_r \cosh(kl) \frac{\sinh(k\frac{g}{2})}{\sinh(kl)} \right)}, \quad (2.68)$$

with

$$M_m = \frac{4k B_{\text{rem}}}{\mu_0 m \pi} \sin\left(\frac{m\pi\alpha_p}{2}\right) \int_{r_1}^{r_2} r J_{mp}(kr') dr', \quad (2.69)$$

where  $B_{\text{rem}}$  is the remanence induction of the permanent magnet material. The computation effort of (2.67) is usually very extensive, because of the improper integration of the Bessel functions. In order to achieve a time efficient implementation, a variable transformation,

$$k = \frac{t}{1-t}, \quad (2.70)$$

is used, which changes the boundaries to  $[0, 1]$  from  $[0, \infty]$  and reduces computation time significantly.

According to [41], the axial component of the field of a disk with

segmented Halbach magnetization can be expressed as

$$B_z(\vec{r}) = \frac{B_{rem}}{4\pi} \sum_{n=0}^{\frac{N_m}{2}-1} (-1)^n \sum_{j=1}^2 (-1)^{j+1} \quad (2.71)$$

$$\left[ \begin{array}{c} [\int_{z_1}^{z_2} \int_{\beta_{1,ax}}^{\beta_{2,ax}} \frac{r \cos(\Phi - \Phi') - r'}{|\vec{r} - \vec{r}'|^3} r' d\Phi' dr']_{r'=r_j} + \\ \\ [\int_{z_1}^{z_2} \int_{r_1}^{r_2} \frac{r \sin(\Phi - \Phi')}{|\vec{r} - \vec{r}'|^3} dr' dz']_{\Phi'=\beta_{j,ax}} - \\ \\ [\int_{r_1}^{r_2} \int_{\beta_{1,tr}}^{\beta_{2,tr}} \frac{r \sin(\Phi - \Phi')}{|\vec{r} - \vec{r}'|^3} r' d\Phi' dr']_{z'=z_j} \end{array} \right] \cdot$$

The angular width of the axially and transversally magnetized sectors are

$$\Delta\beta_{ax} = \frac{4\pi}{N_m} \cdot \alpha_p, \quad (2.72)$$

and

$$\Delta\beta_{tr} = \frac{4\pi}{N_m} \cdot (1 - \alpha_p), \quad (2.73)$$

where  $N_m = 4p$  is the total number of magnets in the Halbach array. Hence the angular positions of the sector boundaries are

$$\begin{aligned} \beta_{1,ax} &= \frac{(4n-1)\pi}{N_m} \\ \beta_{2,ax} &= \frac{(4n-1)\pi}{N_m} + \Delta\beta_{ax} \\ \beta_{1,tr} &= \beta_{2,ax} \\ \beta_{2,tr} &= \beta_{1,tr} + \Delta\beta_{tr}, \end{aligned} \quad (2.74)$$

where  $n$  is an integer and specifies the considered pole pair in the Halbach array. Moreover the axial boundaries are

$$\begin{aligned} z_1 &= 0 \\ z_2 &= h_m. \end{aligned} \quad (2.75)$$

It should be noted that in (2.71), the axial origin is set to be on the surface of the rotor disk, as the formula gives the field distribution for one disk only. Hence  $B_z$  has to be superimposed with the field of the opposite disk (with appropriate coordinates), in order to get the total

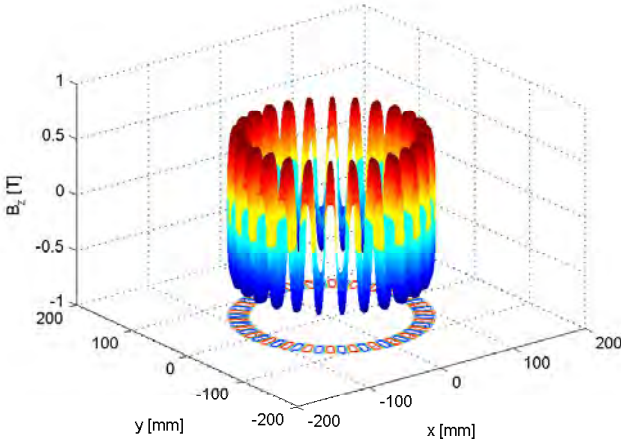


**Fig. 2.44:** Open circuit field in the middle of the air-gap of a Halbach magnetized double rotor AFM with 26 pole pairs.

field in the air-gap of the rotor disks.

An example of the resulting field distribution is shown in Fig. 2.44.

The linked flux and the back-EMF voltage are calculated indirectly through a power balance, i.e. under the assumption that a constant current  $I$  flows in phase  $A$  of the AFM which rotates with a constant rotational speed  $\omega$ . The mechanical power of phase  $A$  is

$$P_{\text{ph},A}(\theta) = u_{\text{ind},A}(\theta) I = T_{\text{ph},A}(\theta) \omega. \quad (2.76)$$

Dividing (2.76) by  $I$  and  $\omega$  we get the linked flux expressed as

$$\Psi_{\text{ph},A}(\theta) = \int u_{\text{ind},A}(\theta) dt = \frac{u_{\text{ind},A}(\theta)}{\omega} = \frac{T_{\text{ph},A}(\theta, I)}{I}. \quad (2.77)$$

In the following, only the tangential component of the torque generated by a sample current  $I$  is considered

$$T_{\varphi}(r, \varphi - \theta, z) = r dF_{\varphi}(r, \varphi - \theta, z) = r \cdot \frac{I \cdot \cos(\varphi)}{w_w \cdot w_h} dB_z(r, \varphi - \theta, z), \quad (2.78)$$

where  $\frac{I \cdot \cos(\varphi)}{w_w \cdot w_h}$  is the radial component of the current density in a coil. This means a simple volume integral of the coil space for different rotor

positions  $\theta$  is required to determine the liked flux and the back-EMF voltage.

For a distributed winding the volume integral is

$$\frac{T_{\text{ph},A}(\theta)}{I} = 2p \int_{-\frac{w_h}{2}}^{\frac{w_h}{2}} \int_{r_1}^{r_2} \int_{\varphi_{\text{coil},s}}^{\varphi_{\text{coil},e}} r \frac{\cos(\varphi)}{w_w w_h} B_z(r, \varphi - \theta, z) dV, \quad (2.79)$$

where  $dV = d\varphi dr dz$  is the infinite decimal size volume, and  $\varphi_{\text{coil},s} = \tan^{-1}(\frac{-w_w}{2r}) + \theta$ , and  $\varphi_{\text{coil},e} = \tan^{-1}(\frac{w_w}{2r}) + \theta$  describe the angular boundaries of the coil.

For phase group windings the volume integral is

$$\frac{T_{\text{ph},A}(\theta)}{I} = \frac{Q_s}{3} \int_{-w_h}^{w_h} \int_{r_1}^{r_2} \int_{\varphi_{\text{coil},s}}^{\varphi_{\text{coil},e}} r \frac{\cos(\varphi)}{w_w w_h} B_z(r, \varphi - \theta, z) dV. \quad (2.80)$$

In case of concentrated windings, the calculation is more complex, since the torque of every coil has to be calculated separately and then added up, because the winding pitch is not equal to a pole pitch, which means the field distribution for all coils is different. For some particular winding configurations periodicities exist and can be exploited.

Once the back-EMF voltage is known, the ohmic losses can be calculated according to (2.44). The phase resistance is estimated as

$$R_{\text{ph},A} = N_{\text{coil}} N_{\text{turns}}^2 \frac{l_{\text{coil}}}{A_{\text{coil}}} \quad \text{with} \quad A_{\text{coil}} = k_{\text{Cu}} w_w w_h, \quad (2.81)$$

where  $N_{\text{coil}}$  is the number of coils per phase and  $l_{\text{coil}}$  is the average length of a coil including its end-windings. The number of coils per phase are  $N_{\text{coil}} = p$  for distributed windings and  $N_{\text{coil}} = \frac{Q_s}{3}$  for concentrated windings. The average coil length is  $l_{\text{coil}} = 2(r_2 - r_1) + l_{\text{end}}$ , where the length of the end-windings is estimated as

$$l_{\text{end}} = 1.5 \cdot \frac{2\pi(r_1 + r_2)}{2p} \quad (2.82)$$

for distributed windings,

$$l_{\text{end}} = \frac{2\pi(r_1 + r_2)}{2p} \quad (2.83)$$

for phase grouped windings, and

$$l_{\text{end}} = \frac{2\pi(r_1 + r_2)}{Q_s} \quad (2.84)$$

for classic concentrated windings. This yields total phase resistances of

$$R_{\text{ph},A,\text{dist}} = p \cdot 2(r_2 - r_1) + 1.5 \pi(r_1 + r_2) \quad (2.85)$$

$$R_{\text{ph},A,\text{ccw}} = \frac{Q_s}{3} \cdot 2(r_2 - r_1) + \frac{1}{3} \pi(r_1 + r_2) \quad (2.86)$$

$$R_{\text{ph},A,\text{pgw}} = \frac{Q_s}{3} \cdot 2(r_2 - r_1) + \frac{Q_s}{2p} \frac{1}{3} \pi(r_1 + r_2). \quad (2.87)$$

The d-axis inductance is also estimated. It is typically low since the stator is iron-less. The estimation assumes a rectangular coil shape and approximates the total d-axis inductance as the series connection of the self inductances per phase:

$$L_d = \begin{cases} p N_{\text{turns}}^2 L_{\text{coil}} & \text{for dist. windings} \\ \frac{Q_s}{3} N_{\text{turns}}^2 L_{\text{coil}} & \text{for conc. windings,} \end{cases} \quad (2.88)$$

where the coil inductance approximation is

$$L_{\text{coil}} = \frac{\mu_0}{\pi} \left( w \log \left( 2 \frac{w}{a} \right) + h \log \left( 2 \frac{h}{a} \right) + 2\sqrt{w^2 + h^2} \right) - \frac{\mu_0}{\pi} \left( w \operatorname{arcsinh} \left( \frac{w}{h} \right) - h \sinh \left( \frac{h}{w} \right) - \frac{7}{4}(w + h) \right), \quad (2.89)$$

with  $h = r_2 - r_1$  as the height of the rectangle. For distributed and phase grouped windings the width of the rectangle is  $w = \frac{r_1 + r_2}{2} \frac{\pi}{p}$  and  $w = \frac{r_1 + r_2}{2} \frac{2\pi}{Q_s}$  for classic concentrated windings. For distributed windings  $a = \frac{w_w}{2}$  and  $a = w_w$  for all types of concentrated windings.

### Losses and Efficiency

In order to calculate the efficiency of a machine, the losses have to be determined for the different operating points. In this context, only operating points #1-3 are of interest. It is sufficient to calculate the losses for the nominal load point #2 and then transform them for the respective torque and speed accordingly. Therefore, the scaling properties of the different types of losses are derived. As only air cored stator machines are considered, all losses are generated in the stator windings, i.e. the armature reaction field is assumed to be low. For this reason, iron and eddy current losses in the rotor are neglected. The winding losses in the stator consist of ohmic and eddy current losses. Since the ohmic losses are calculated according to (2.44) and the torque is linearly dependent on the current, cf. (2.77), the ohmic losses scale with torque,  $T$ , as

$$P_{v,w}(T) = P_{v,w,\#2} \left( \frac{T}{T_{\#2}} \right)^2, \quad (2.90)$$

where  $P_{v,w,\#2}$  are the winding losses at torque  $T_{\#2}$ .

At this point the winding construction is not given, which makes it difficult to correctly estimate the high frequency effects. In order not to completely omit these effects the losses are estimated for the case that the windings are constructed of Litz wire with a strand diameter of 0.2 mm. Hence, the skin effect is neglected. The proximity losses are then scaled with frequency as

$$P_{v,w,prox}(f) = P_{v,w,prox,\#2} \left( \frac{f}{f_{\#2}} \right)^2. \quad (2.91)$$

Finally, the mean efficiency is calculated with (2.1).

### 2.4.2 AFM Thermal Models

As described in Section 2.1 the machines are designed such that they operate at the limits imposed by the electro-magnetic components. As the considered AFMs are iron-less the only electro-magnetic limit is the demagnetization of the magnets due to the stator field, which is less likely to be an implementation limit than thermal considerations. So a second modeling step describes the machine's thermal behaviour, which in return influences important temperature dependent material properties, such as electric conductivity, and therefore influences the torque and losses of the machine. Boglietti [35] outlined the qualities and limitations of different modeling approaches, i.e. finite element method (FEM) simulations, computational fluid dynamics (CFD), and lumped parameter thermal networks (LPTN). As low computational effort is required simplified LPTN are used [36] to calculate the approximate temperatures of the windings and the permanent magnets.

The LPTN for the AFM is shown in Fig. 2.45. The thermal resistance from the stator center to the stator surface is approximated with the thermal resistance in axial direction for a uniform loss distribution

$$R_{\text{wir}} = \frac{1}{8\pi k_{\text{eq}}} \frac{w_h}{\Delta R^2 + 2\Delta R r_1}, \quad (2.92)$$

where  $k_{\text{eq}}$  is the mean thermal conductivity of the stator conductor and epoxy mixture. The other conductive thermal resistances are calculated with the material's thermal conductivity  $k$ , cf. Tab. 2.2. With the disc surface area  $A_{\text{disc}} = \pi(r_2^2 - r_1^2)$ , the conductive thermal resistances are

$$R_{\text{pim}} = \frac{h}{A_{\text{disc}} k_{\text{pm}}} \quad (2.93)$$

and

$$R_{\text{Fe}} = \frac{d_r}{A_{\text{disc}} k_{\text{Fe}}}. \quad (2.94)$$

The convective thermal resistances are expressed as in (2.49). With the convective surface areas of the disc,  $A_{\text{disc}}$ , and perimeter  $A_{\text{perim}} = 2\pi r_2(d_r + h)$ , the heat transfer coefficients may be calculated as in [42], [37].

The heat transfer coefficient at the stator to air-gap boundary is

$$\bar{h}_{c1} = \frac{k_{\text{air}} \overline{\text{Nu}}_{c1}}{R} \quad (2.95)$$

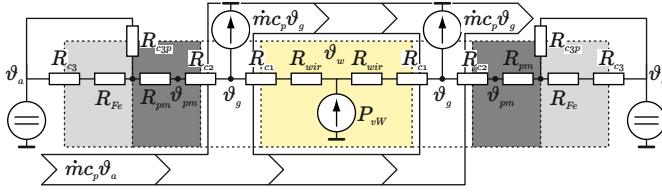


**Fig. 2.45:** LPTN of the AFM, the thermal resistances are:  $R_{c3}$  convective resistance from rotor disc surface to ambient air,  $R_{c3p}$  convective resistance from rotor disc perimeter to ambient air,  $R_{Fe}$  conductive resistance through the iron of the rotor disc,  $R_{pm}$  conductive resistance through the PM of rotor disc,  $R_{c1}$  and  $R_{c2}$  convective resistances at the rotor and stator disc surfaces and  $R_{wir}$  conductive resistance from the middle of the stator to the stator surface.

with

$$\overline{Nu}_{c1} = 0.333 \frac{\dot{V}/2}{\pi \nu_{air} R}, \quad (2.96)$$

where  $R = \frac{r_1+r_2}{2}$  is the mean radius. It is assumed that the same heat transfer coefficient in the air-gap can be used for the stator-to-air and rotor-to-air boundary,  $\bar{h}_{c1} = \bar{h}_{c2}$ .

For the heat transfer coefficient of the outside surface to the outside air,  $\bar{h}_{c3}$ , the (tangential) Reynolds number,

$$Re_{\varphi}(R) = \frac{\omega R^2}{\nu_{air}}, \quad (2.97)$$

is used to assess the flow structure, where  $\omega$  is the discs rotational speed. If  $Re_{\varphi} < 2.8 \cdot 10^5$  the laminar flow heat transfer coefficient,

$$\bar{h}_{c3}^{lam} \approx 0.35 k_{air} \sqrt{\frac{\omega}{\nu_{air}}}, \quad (2.98)$$

is used. If  $Re_{\varphi}(R) > 2.8 \cdot 10^5$ , the turbulent flow heat transfer coefficient,

$$\bar{h}_{c3}^{turb} = \frac{Nu_{c3} k_{air}}{R} \text{ with } Nu_{c3} = 0.0151 Re_{\varphi}^{0.8}, \quad (2.99)$$

is used. The heat transfer coefficient for the rotor radial peripheral edge is,

$$\bar{h}_{c3p} = \frac{k_{air} Nu_{c3p}}{2 r_2} \text{ with } Nu_{c3p} = 0.133 Re_{c3p}^{\frac{2}{3}} Pr^{\frac{1}{3}}, \quad (2.100)$$

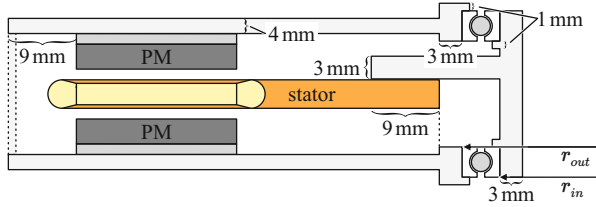


**Fig. 2.46:** Sectional drawing of an AFM including the electromagnetically inactive materials. The stator winding GFRP/CFRP foam core sandwich disc is mounted on a central static hub. The rotor core and permanent magnets are mounted on 4 mm thick aluminum discs, held in place by the bearings and spacer bolts.

where  $Pr$  is the Prandtl number for air and the peripheral Reynolds number is

$$Re_{c3p} = \frac{\omega(2r_2)^2}{\nu_{air}}. \quad (2.101)$$

A volumetric flow rate  $\dot{V} = \dot{m}/\rho$  of the air flowing radially across the stator and rotor magnet surfaces is assumed to be  $\dot{V} = 7 \text{ dm}^3/\text{s}$ , which is a conservative estimate and could be enforced by a small axial fan.

### 2.4.3 AFM Weight Models

Fig. 2.46 shows the model to estimate the structural mass of an AFM. The stator winding is fixed in place with a glass-/carbon-fiber reinforced polymer foam core sandwich disc. The disc connects the stator winding to a central static hub. The static hub is a 3 mm thick hollow cylinder with a 3 mm thick disc interface. The rotor core and the PMs are mounted on 4 mm thick aluminum discs. The attracting forces from the permanent magnets, which pull the two rotor disc together, are held by the bearings and spacer bolts at the outer rim.

### 2.4.4 AFM Optimization and Comparison

As described in Section 2.4 the design space is characterized by the range of free geometric parameters and the considered materials. Tab. 2.2 list the properties of the considered materials. The considered materials are: aluminum and copper windings; neodymium iron boron (NdFeB) magnets, samarium cobalt (SmCo) magnets, and samarium iron nitride bonded (SmFeN) magnets. Tab. 2.13 lists the grid search parameters investigated for the AFM designs.

Fig. 2.47 shows the winding temperatures of the swept AFM Halbach array machine with distributed windings in the  $\gamma$ - $\eta$  plane. Thermally infeasible designs, i.e. winding temperatures  $\theta_W > 125^\circ\text{C}$  or PM temperatures  $\theta_{PM} > 90^\circ\text{C}$ , are colored black. The Pareto Fronts neglecting the thermally dependent losses are superimposed to visualize the loss of efficiency caused by the increased winding temperature.

Parameter	Considered Values (or Designs)
Machine type	Dual rotor with single stator,
Number of stacks	1,2,3
Fill factor	$k_{Cu} = 0.55$ for distr. windings $k_{Cu} = 0.85$ for conc. windings
Air-gap [mm]	1
Cooling flow rate dm <sup>3</sup> /s	7
Magnetization type	Axial with back iron Halbach without iron
Pole pair number	$p = 19 + 1, 2, \dots 7$
Disk inner radius [mm]	$r_1 = 80 + 10 \cdot 0, 1, 2, \dots 5$
Disk inner radius [mm]	$r_2 = r_1 + 5 \cdot 2, 3, \dots 6$
Permanent magnet height [mm]	$h_m = 1, 2, 3, 4, 5$
Pole coverage of axial magnets	$\alpha_p = 0.5, 0.6, 0.7, 0.8$
Winding height [mm]	$w_h = 1, 2, 3, 4$
Winding type	Distributed Classic concentrated Phase grouped concentrated
Number of coils	$Q_s = 36 + 3 \cdot 0, 1, 2, \dots 14$
Fractional coil width	$w_{w,frac} = 0.45 + 0.1 \cdot 0, 1, \dots 4$
Winding material	Copper, aluminum

**Tab. 2.13:** Investigated design space of AFM geometries.

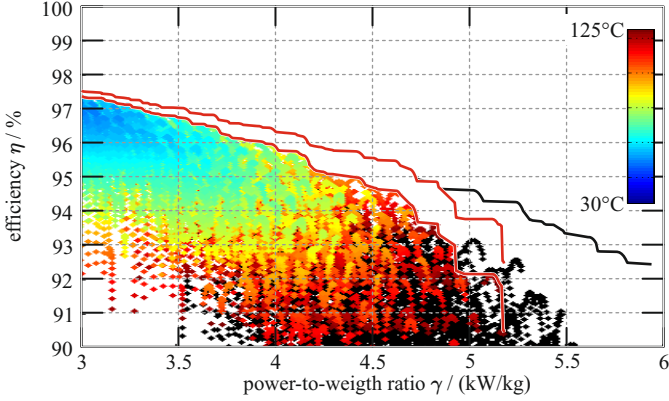


**Fig. 2.47:** Winding temperatures of the AFM Halbach array machine with distributed windings, in the power-to-weight ratio/efficiency plane, i.e.  $\gamma$ - $\eta$  plane. Machines with winding temperatures  $\theta_W > 125^\circ\text{C}$  or PM temperatures  $\theta_{PM} > 90^\circ\text{C}$ , are colored black. The Pareto optimal front, for a winding temperature of only  $\theta_W = 30^\circ\text{C}$ , is superimposed.

The direct search grid can be checked a posteriori, to ensure that the grid ranges cover the relevant design space analog to Section 2.2.4. The comparison of Pareto Fronts is a useful tool to analyse the sensitivity of any of the grid parameters on the overall performance. It can also be used to compare discrete design choices, which can be summarized as:

- ▶ All machine topologies perform best with NdFeB magnets. However, because the eddy current losses in the magnets are neglected, magnet segmentation may be required.
- ▶ For AFM topologies, the performance is always reduced with aluminum (instead of copper) windings. This can be attributed to the reduction of the back EMF for larger air-gaps, e.g. for two AFMs which only differ in winding height,  $w_h$ , such that the winding resistances of an aluminum and a copper winding are equal, the air-gap of the aluminum winding AFM will be larger.
- ▶ The performance of the AFM is not sensitive to the use of rectangular magnets, instead of trapezoidal magnets, which can be attributed to the high number of pole pairs.

- ▶ AFMs with concentrated windings yield a better performance as AFMs with distributed windings, which can be attributed to the shorter end-windings and a higher fill factor of 0.85 versus 0.55.
- ▶ AFMs with phase grouped concentrated windings yield a better performance as the classic concentrated windings.
- ▶ Halbach magnetized rotors significantly increase the performance of the AFM topologies, which can be attributed to the higher air-gap flux density achieved with the Halbach magnetization.
- ▶ If the inverter losses are neglected, all topologies are more efficient when driven with BLAC, rather than BLDC.

## 2.5 AFM Prototype

A design near the Pareto Front is chosen to be implemented as a prototype to verify the design approach. The prototype is a single stator double rotor AFM with segmented Halbach magnetization of the rotor and phase grouped windings. The geometric parameters defining all the geometric degrees of freedom are listed in Tab. 2.14. The expected machine characteristics are listed in Tab. 2.16 and Tab. 2.16. A picture of the CAD design of the prototype machine is shown in Fig. 2.48.

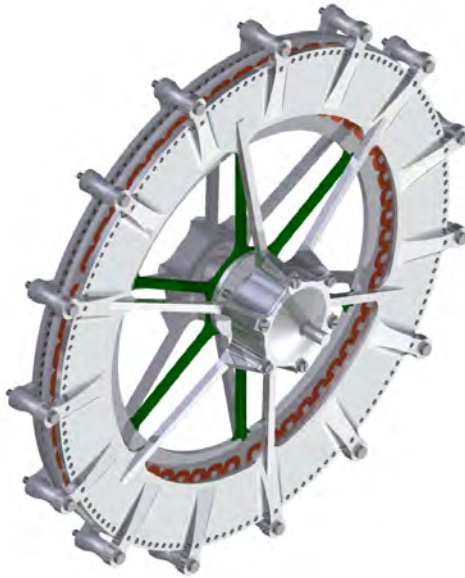


**Fig. 2.48:** Pictures of the CAD design of the AFM prototype. It is a single stator double rotor AFM with segmented Halbach magnetization of the rotor with phase grouped windings.

Degree of Freedom	Variable	Value
Number of pole pairs	$p$	26
Number of coils	$Q_s$	51
Inner disk radius	$r_1$	90 mm
Outer disk radius	$r_2$	115 mm
Air-gap distance	$g$	1 mm
Magnet height	$h_m$	4 mm
Winding height	$w_h$	3 mm
Winding width	$w_w$	3.5 mm

**Tab. 2.14:** Geometric parameters of the AFM prototype.

Derived Weight Component	Variable	Value
Copper winding mass	$m_{Cu}$	332 g
Permanent magnet mass	$m_{PM}$	1005 g
Passive material mass	$m_{passiv}$	734 g

**Tab. 2.15:** Analytic estimation of the required weight for the components of the AFM prototype.

Degree of Freedom	Variable	$N_{turns} = 1$	$N_{turns} = 12.5$
Phase resistance	$R_{ph,A}$	2.6 m $\Omega$	411 m $\Omega$
Direct axis inductance	$L_d$	0.5 $\mu$ H	74 $\mu$ H
Torque constant	$k_T$	0.127 Nm/A <sub>rms</sub>	1.59 Nm/A <sub>rms</sub>
Voltage constant	$k_V$	0.38 V/Hz	4.7 V/Hz

**Tab. 2.16:** Analytically calculated performance parameters of the AFM prototype.

### 2.5.1 Construction and Assembly

Once the number of turns is selected with (2.51), a suitable wire can be selected by dividing the winding width  $w_w$  by the number of turns assuming that a flat wire coil is employed. Attention has to be paid to the isolation and self-bonding layers, which have to be taken into account. With this a wire with copper cross section dimensions of  $2.9 \text{ mm} \times 0.25 \text{ mm}$  results. The coils are wound separately at first to be assembled as a phase grouped winding at a later point in time. This is done by winding the copper wire around a negative of the coil body and pressing it in axial direction. Then a second form with the outer profile of the coil sides is placed to achieve the final angular shape of the coils as shown in Fig. 2.49. The coils have to fit in angular direction. The touching surfaces are made of PTFE, in order not to damage the isolation of the copper wire. Once the coil is pressed into the right shape, the self-bonding layer is melted within 30 s by a 30 A current supplied by a Xantrex DC-supply. After a short period of cooling, the

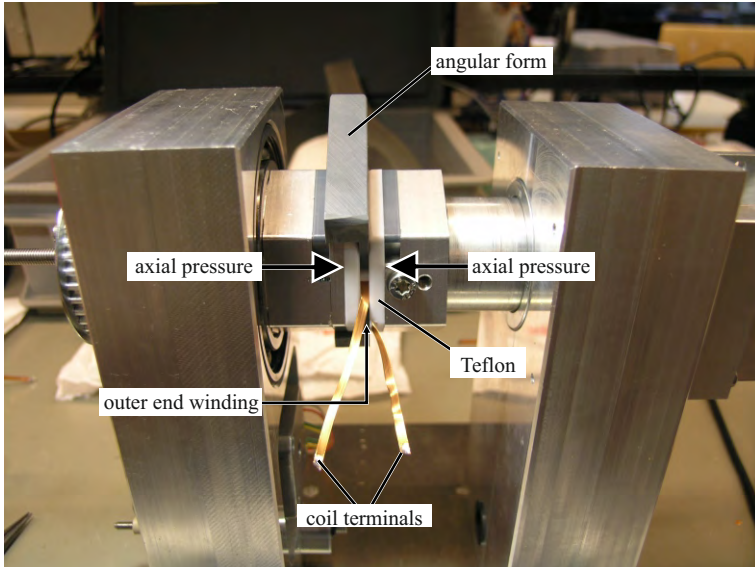


**Fig. 2.49:** Picture of the coil shaping tool used to produce the copper coil for the concentrated windings of the AFM prototype.



**Fig. 2.50:** Picture of two copper coils for concentrated windings of the AFM prototype.

pressure can be released and the winding process is completed. Coil examples are depicted in Fig. 2.50.

The measured phase resistance ( $R_{\text{ph},A} = 404 \text{ m}\Omega$ ) is in good accordance to the analytical result ( $R_{\text{ph},A} = 411 \text{ m}\Omega$ ). Due to tolerances, half a turn was removed from each coil, i.e.  $N_{\text{turns}} = 12.5$ , in order to ensure that the coils can be soldered properly and fit together in angular direction.

To fix the coils in position mechanically, the windings are potted in epoxy. Furthermore, linear Hall sensors are placed in between the phases, in order to determine the rotor position for the control system. In addition, two NTC-thermistors ( $100 \text{ k}\Omega$  at  $25^\circ\text{C}$ ) per phase are mounted on the inner and outer end-winding of the first coil for temperature monitoring. A resin with a high thermal conductivity ( $1.4 \text{ W/mK}$ , Loctite Hysol 9497 [43]) was chosen to ensure an efficient heat transfer from the winding cores to the air-gap. Fig. 2.51 shows a schematic of the potting arrangement.

After the coils are soldered together into complete phases, the phase

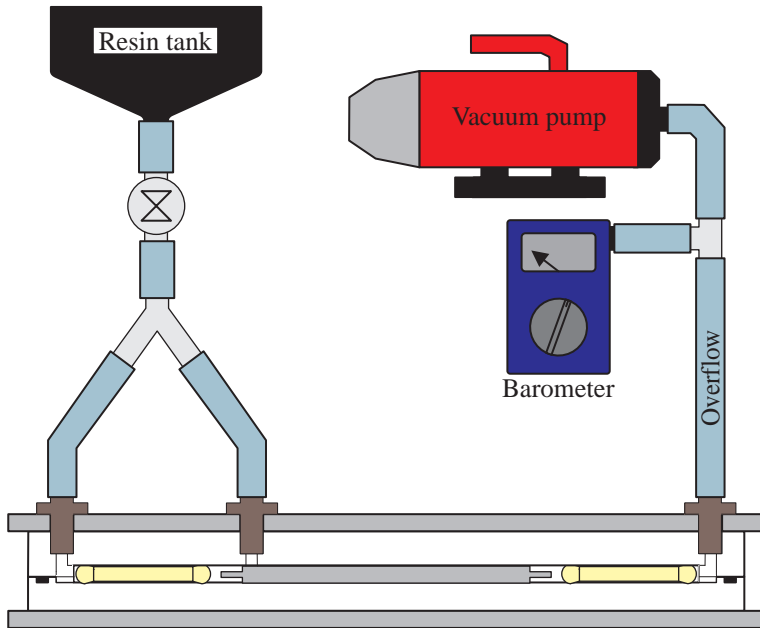


**Fig. 2.51:** Schematic of the setup for potting of the stator of the AFM prototype.

terminals are dipped into a release agent. The windings are placed in a PTFE mold together with an aluminum rim as shown in Fig. 2.52. The mold consists of two halves, which can be closed air-tight. In addition, the mold is placed between aluminum plates in order to achieve a mechanically stiff structure. The bottom mold is shaped such that the positions of the coils are correctly aligned. The top mold features two inlets, one at the inner coil radius and one at the outer radius, which connect to a resin tank through a valve. A vacuum pump is connected to an outlet on the top mold, which is on the opposite side of the inlets.

The vacuum pump, which is attached via an overflow container (or a long hose acting as such) evacuates the air from the mold. Once a vacuum is established inside the potting mold the valve which holds



**Fig. 2.52:** Mould with stator rim and phase group windings.

back the epoxy from the resin tank is opened. The epoxy is then pushed through the mold with 1 atm until it reaches the overflow container at the outlet. At this point the vacuum can be released and the epoxy is continuously pushed into the mold with 1 atm from the inlet and outlet. Finally the epoxy is cured in an oven according to the data sheet instructions. After the resin is cured, the mould can be opened and the stator can be removed. Fig. 2.53 shows the potted stator mounted on the shaft.



**Fig. 2.53:** Potted stator disk mounted on the shaft.

The rotor disks consist of two components, i.e. the aluminum shield and the magnet disk. The magnets are assembled to a Halbach array first and then glued onto the aluminum disk. Fig. 2.54 and Fig. 2.55 show the aluminum rotor shield. The region, where the magnets are glued is indicated in Fig. 2.54. The contact point is marked where spacers connect to the next rotor disk. The shape of these contacts and the indicated stiffeners is determining the axial bending due to the magnetic attractive forces.

The magnetic forces make the assembly of a Halbach array difficult, because the magnets want to align their magnetization. For that reason the magnets are first assembled on a PTFE mold placed on top of an iron plate as shown in Fig. 2.56. The orientation of the Halbach array is such that the flux is concentrated into the iron plate, i.e. where the air-gap will be afterwards. The polarity of the field in a magnet can be

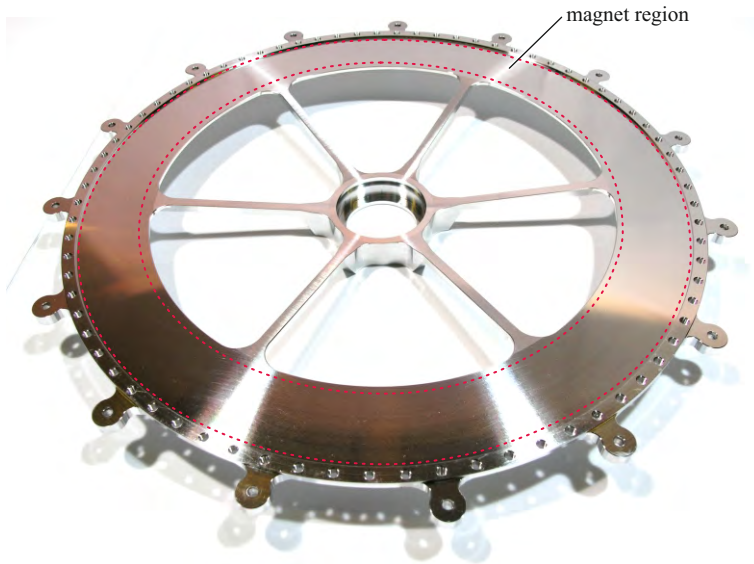


**Fig. 2.54:** Top view of rotor disk.

determined with a Tesla-meter or a compass needle. With this method the magnets with an axial magnetization are attracted to the iron plate and the transversal magnet can be placed in between the axial magnets, which yields a stable assembly. The transversal magnet will unfortunately not be aligned with the axial magnets, because that position doesn't feature the minimum energy state of the system, as shown in Fig. 2.57. This significantly complicates the gluing of the magnets onto the aluminum rotor disk, because a large force is required to press all transversal magnets down and create a flat surface while the magnets are glued on the disc. This was not a priori considered in the mechanical design and it is suggested to add a mechanical fixturing of the magnets to the rotor disks in addition to the adhesive for future designs featuring a segmented Halbach configuration. With the aid of axial magnet dummies, the angular position of the magnets can be checked for every second pole pair. Due to tolerances, some of the magnets had to be ground. Once the Halbach array is correctly assembled, the magnets are ready to be glued onto the aluminum rotor disk.

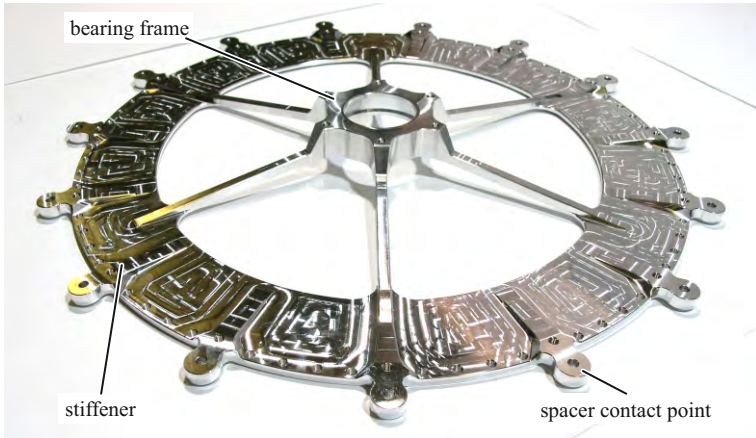


**Fig. 2.55:** Back view of rotor disk.



**Fig. 2.56:** Halbach array assembly.

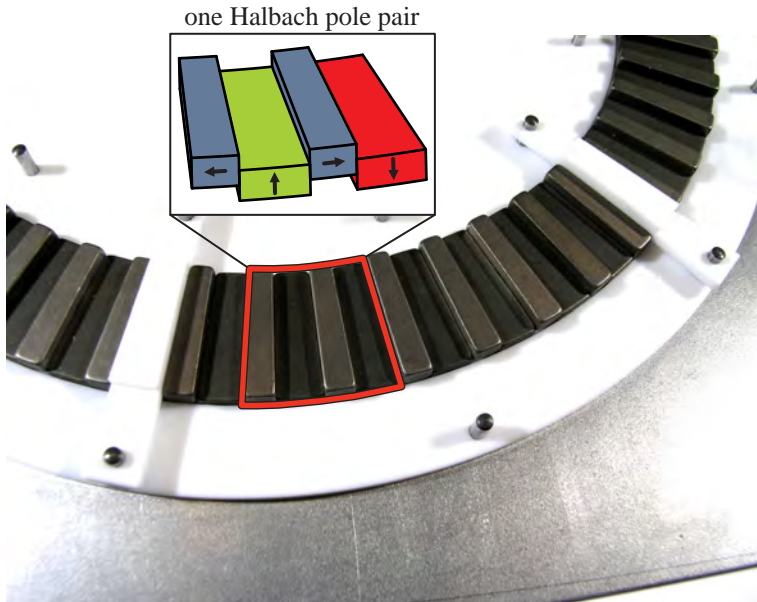


**Fig. 2.57:** One pole pair of the Halbach array.

First a thin layer of adhesive is applied onto the rotor, then the disk is pressed firmly onto the Halbach array with clamps, such that the transversal magnets are pushed down and align with the axial magnets. After a cure time of 24 h, the clamps can be released and the rotor disk with the magnets can be slid off the iron board. Fig. 2.58 shows a completed rotor disk.

After the manufacturing of the single components is completed, the machine can be assembled. The biggest challenge is to handle the strong magnetic attractive forces of the magnets ( $\approx 1.6$  kN in the middle of the air-gap) when the rotor disks approach each other. Hence a proper assembly method was developed to avoid a collision of the magnets. The fully assembled axial flux machine is depicted in Fig. 2.59. The total weight of the AFM prototype is  $m_{\text{tot}} = 2.065$  kg.

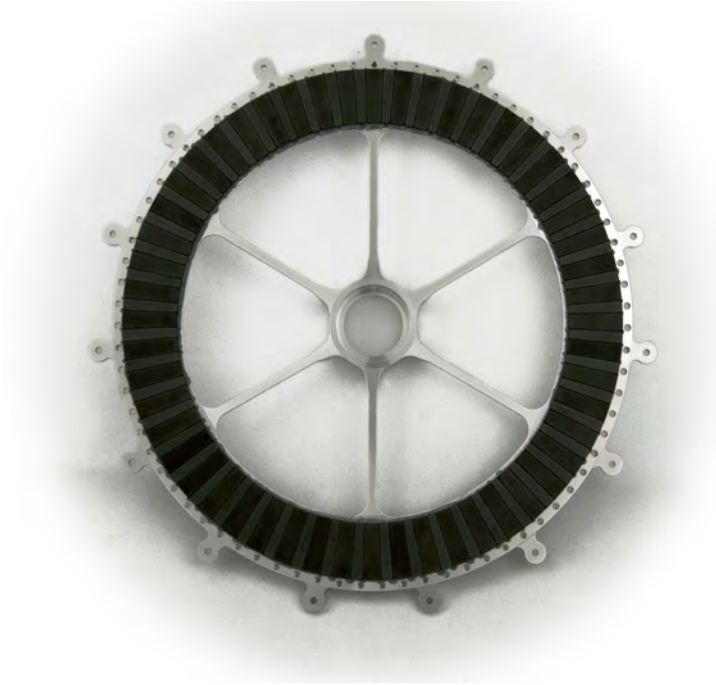


**Fig. 2.58:** Glued rotor disk.



**Fig. 2.59:** Fully assembled Axial Flux Machine.

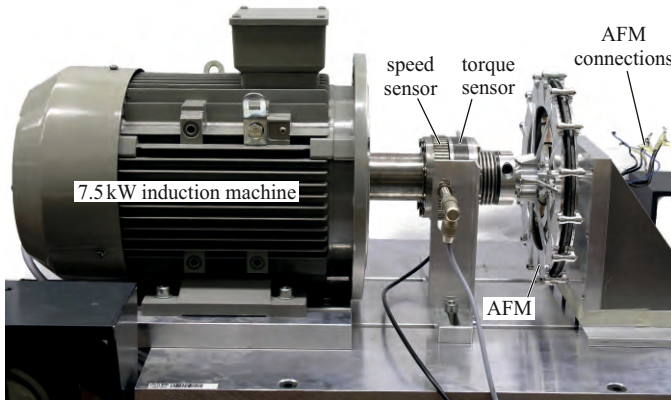


**Fig. 2.60:** Measurement setup of the AFM prototype. An induction machine is driven by an industrial drive and mechanically drives the AFM prototype. A Magtrol TF series torque flange sensor, which also features a speed sensor couples the two machines.

## 2.5.2 Measurement Results

There exist multiple ways to characterize the machine performance. Because of the setup readily available in the lab an induction machine and an industrial drive are used to mechanically drive the AFM prototype. The machines are coupled through a Magtrol TF series torque flange sensor, which also features a speed sensor. The measurement setup is depicted in Fig. 2.60.

The impedances of the stator windings are measured with an Agilent 4294A precision impedance analyzer over a wide range of frequencies. Fig. 2.22 shows the impedances between the star point and the three phases. It can be seen that the impedances of the three phases are identical up to a frequency of  $\approx 1$  MHz. A further measurement is required to determine the mutual inductance. The impedance of phase  $A$  and  $B$  connected in series, such that  $i_A = i_B$ , is also measured. Fig. 2.61 shows the measured inductances and ac-resistances. With the two measurements

$$L_A = L_\sigma + M = 76 \mu\text{H} \quad (2.102)$$

and

$$L_{AB} = L_\sigma + \frac{M}{2} = 76 \mu\text{H}, \quad (2.103)$$

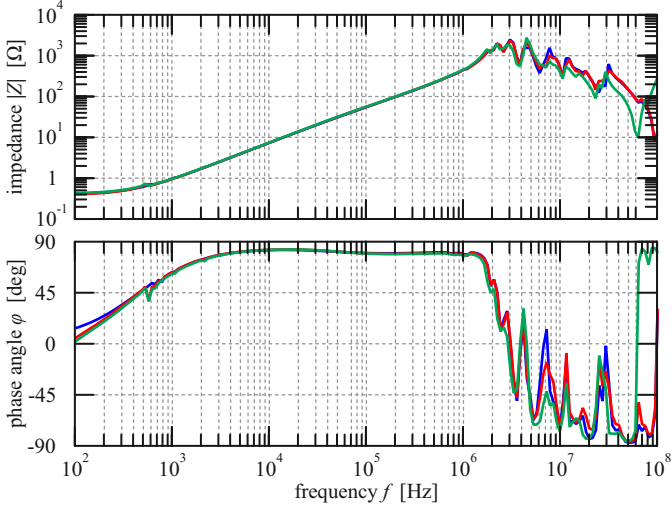


**Fig. 2.61:** Impedance measurement of the stator windings to the star point.

the stray, mutual and d-axis inductance are determined to be

$$L_d = L_\sigma + \frac{3}{2}M = 76 \mu\text{H} \quad (2.104)$$

with

$$L_\sigma = 76 \mu\text{H} \quad (2.105)$$

and

$$M \approx 0 \mu\text{H}. \quad (2.106)$$

It is to be expected that the mutual inductance is  $M \approx 0 \mu\text{H}$ , since the coils of the different phases do not share any common space, hence only the coil at the edges of a phase group is slightly coupled to the adjacent phase. The dc-resistance of the machine phases is obtained with a 4-wire resistance measurement on an Agilent 34410A 6<sup>1/2</sup> digit multimeter to be  $R_s = 404 \text{ m}\Omega$ , which matches very well with the predicted value of  $411 \text{ m}\Omega$ .

It is known in literature that AFMs are challenging structures to assemble, particularly due to strong attractive forces acting on the rotors. Also in this work, some magnets were displaced under large attractive forces during the assembly process. This is attributed to a bending of

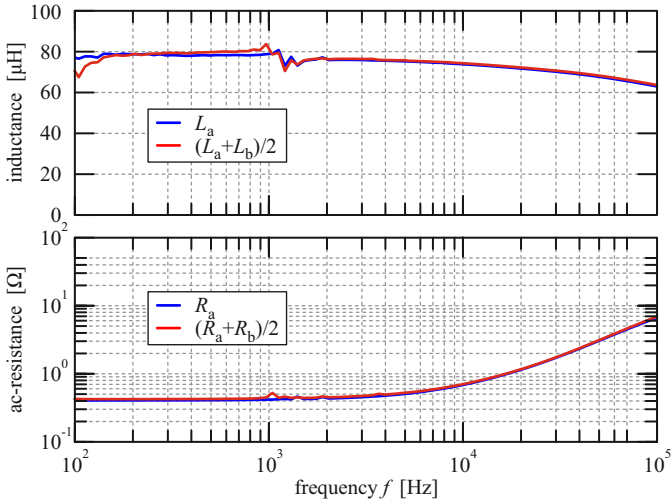


**Fig. 2.62:** Inductance (top) and ac-resistance (bottom) measurement of the stator winding of phase A and the series connection of the stator windings of phases A and B. The d-axis inductance is  $L_d = L_\sigma + \frac{3}{2}M = 76 \mu\text{H}$  with  $L_\sigma = 76 \mu\text{H}$  and  $M \approx 0 \mu\text{H}$ .

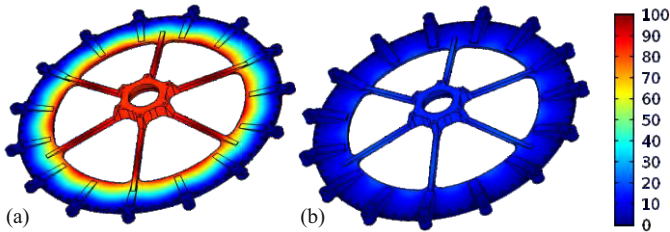


**Fig. 2.63:** Analysis of the influence of the height of structural elements on a bending stress of inner rotor parts. Rotor on the right features ten times lower bending with an increase of the total weight of only 6%.

the rotor disk, which in turn leads to the breaking of the glue holding the magnets. Therefore, in order to proceed with the verification of the design procedure under minimal risk of mechanical failure, the air-gap is increased to 2 mm (from 1 mm) in the following. This, however, is not an unsolvable problem. The rotor bending has been predicted by

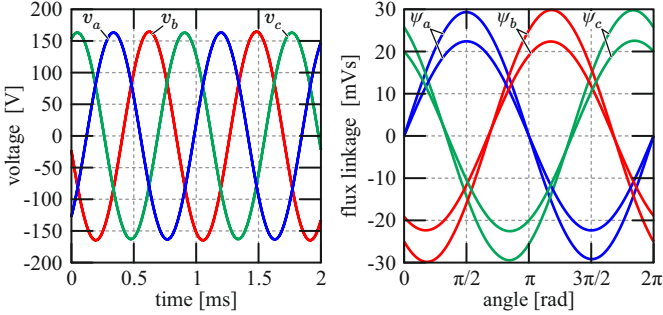


**Fig. 2.64:** Measurement of the phase voltages at 2700 rpm (left). An integration over time yields the flux linkages (right). The amplitude of the flux linkage is  $\hat{\Psi}_{\text{ind},A} = 22.5 \text{ mWb}$  and matches the predicted value of  $22.6 \text{ mWb}$  very well. Experimental results on the air-gap of  $1 \text{ mm}$  resulting in an amplitude value of  $\hat{\Psi}_{\text{ind},A} = 29.1 \text{ mWb}$  are given in the same graph (for reasons of illustration clarity the measured voltages are not depicted for both air-gap values).

the FEM model shown in Fig. 2.63(a), but was tolerated since it did not lead to dangerous stress levels in the solid body. Fig. 2.63(b) depicts structural FEM simulations showing that the rotor bending can be almost eliminated by a slight increase of the height of the 15 structural elements, which results in a mere 6% (128 grams) increase of the overall machine weight. Moreover, surface treating of the rotor disks and the magnets can increase the holding strength of the glue. Regarding the experimental results in the following sections, the only difference that the higher air-gap causes is a decrease of the flux linkage by 23%. Therefore, the results can be scaled to the air-gap of  $1 \text{ mm}$ .

## Flux Linkage

The flux linkage is measured by driving the AFM prototype mechanically without any loads connected on the terminals. In this case the measured phase voltages, shown in Fig. 2.64(a), are equal to the back-EMF voltages and an integration over time yields the flux linkages depicted in Fig. 2.64(b). The amplitude of the flux linkages is  $\hat{\Psi}_{\text{ind},A} = 22.5 \text{ mWb}$  and matches the predicted value of  $22.6 \text{ mWb}$  very well. Experimental results for an air-gap of  $1 \text{ mm}$  resulting in an amplitude value of  $\hat{\Psi}_{\text{ind},A} = 29.1 \text{ mWb}$  are given in the same graph.

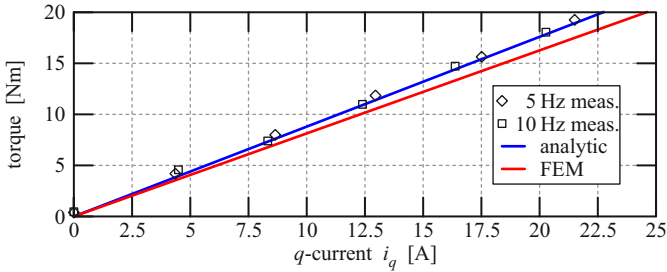


**Fig. 2.65:** Torque dependence on the q-current component measured at different speeds.

### Torque Constant

Under the assumption that the phase currents are in phase with the back-EMF voltage the torque constant can be derived directly from the flux linkage

$$k_T = \frac{T}{\hat{I}_q} = \frac{3}{2} \hat{\Psi}_{\text{ind},A} p = \begin{cases} 0.88 \text{ Nm/A} & \text{for } g = 2 \text{ mm} \\ 1.13 \text{ Nm/A} & \text{for } g = 1 \text{ mm} \end{cases}, \quad (2.107)$$

i.e. it can theoretically be captured by the no-load measurement already presented in Fig. 2.64. Because the AFM prototype is an iron-less machine, the armature reaction flux should only take a minor influence on the available torque. In order to verify this properly the AFM prototype is mechanically driven by the induction machine and loaded electrically with variable three phase resistors. Because the thermal boundary conditions in the test setup are significantly different to the thermal boundary conditions of the AWT application, only transient measurements can be performed. Two synchronized Lecroy HDO4054 oscilloscopes are used to measure the three phase voltages, the three phase currents, and the outputs of the torque and speed sensors. The inductances of the load resistors and the inductance of the machine are causing the phase currents to be out of phase with the back-EMF voltage. Hence, the q-component of the phase currents needs to be extracted from the measurements, since only the q-component of the current produces a net torque. Fig. 2.65 shows the measure torque in dependence of the q-current. It can be seen, that the measurements match the analytic predictions very well.

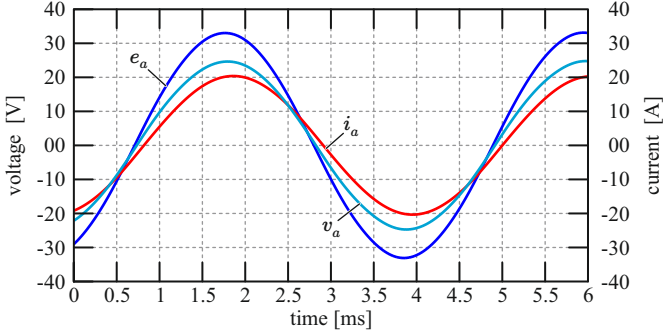


**Fig. 2.66:** Induced voltage  $e_a$ , output voltage  $v_a$  and current  $i_a$  of phase A for nominal current operation at a speed of  $\approx 600$  rpm. The phase shift between the induced voltage  $e_a$  and the current  $i_a$  is predominantly caused by the inductance of the employed load resistor, which in this case is significantly higher than the machine inductance.

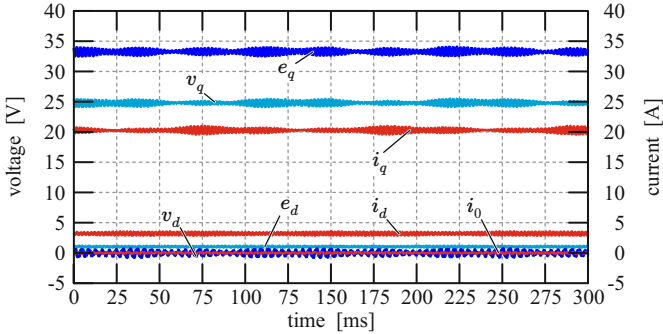


**Fig. 2.67:** D-q components of the phase voltages, currents and back-EMFs for the nominal current operation at the speed of  $\approx 600$  rpm.

The phase voltage  $v_a$  and current  $i_a$  for nominal current operation at a speed of  $\approx 600$  rpm are shown in Fig. 2.66. As all machine parameters are known it is possible to obtain the back-EMF  $e_a$  based on measured voltages and currents. D-q components of the phase voltages, currents and back-EMFs are given in Fig. 2.67. It can be seen that the current d-component has a non-zero value, however, no field-weakening has been observed. Finally, in Fig. 2.68 the torque, speed, and input and output

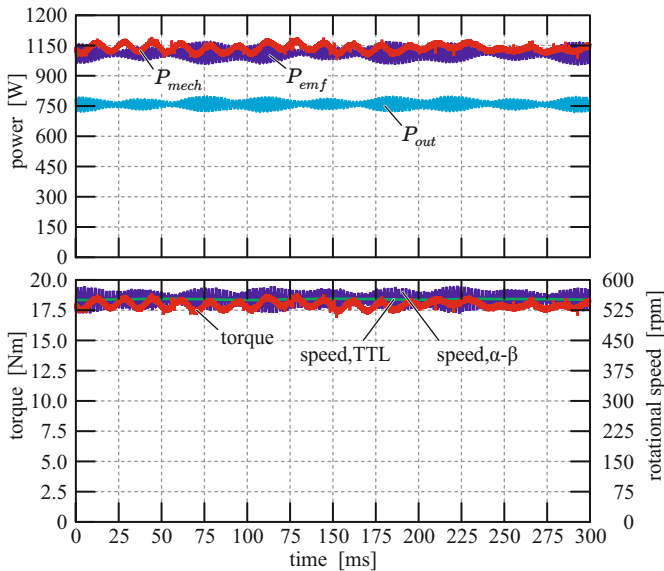


**Fig. 2.68:** Torque, speed, and input and output powers for the nominal current operation at the speed of  $\approx 600$  rpm.

powers are depicted for the same operating point as the one described above.

### No-load Losses

So far only the torque dependent loss components have been identified, i.e. the torque constant and the phase resistance. The sum of the frequency dependent losses is also measured with the test setup. Fig. 2.69 shows torque and the losses of the AFM prototype in dependence of the rotational frequency. In order to get consistent data, the machine is first accelerated to 45 Hz and left to run for 20 min, then the losses are measured consecutively stepping down with 5 Hz steps, because bearing losses are higher at first until the bearing grease has reached its operating temperature, at which point the bearing losses can be significantly lower. The no-load torque shows a linear dependency on the rotational frequency with a small offset, hence the losses can be described as superposition of linear and quadratic loss components.

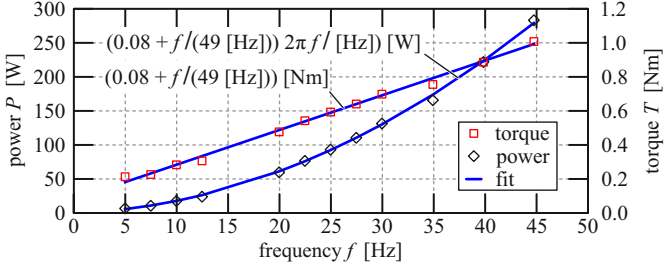


**Fig. 2.69:** Measured torque and losses in dependency of the rotational frequency of the AFM prototype without an electrical load attached.

The no-load torque can be approximated with

$$T_{\text{no-load}}(f_{\text{rot}}) = 80 \text{ mNm} + 20.4 \text{ mNm/Hz} \cdot f_{\text{rot}}, \quad (2.108)$$

where  $f_{\text{rot}}$  is the mechanical rotational frequency. Consequently the losses are approximated as

$$P_{\text{no-load}}(f_{\text{rot}}) = (80 \text{ mNm} + 20.4 \text{ mNm/Hz} \cdot f_{\text{rot}}) \cdot 2\pi f_{\text{rot}}. \quad (2.109)$$

## 2.6 Summary of Chapter

This chapter presented the optimization of electric machines to be employed as motors/generators of an Airborne Wind Turbine. The trade-off between the power-to-weight ratio and the efficiency,  $\gamma$ - $\eta$ , i.e. the Pareto Fronts of different machine topologies are derived and compared. The derivation uses analytical models, which enable the analysis of the whole design space in a computationally efficient manner. The performance of various RFM and AFM topologies are compared and suggest that an internal rotor Halbach array RFM without tooth-tips exhibits the best performance for the given specifications. The analytical results are compared to linear and nonlinear FEM simulations and verify the validity of the analytical optimization approach. An example machine reaches a power-to-weight ratio of  $\gamma \approx 6.2 \text{ kW/kg}$  ( $2.8 \text{ kW/lb}$ ) at an efficiency of  $\eta \approx 95 \%$ . No machine designs with comparable performance have been found in literature or are available in industry.

The main results of this chapter are summarized as follows:

- ▶ Analytical models describing the electro-magnetic, thermal and mechanical behavior of most RFM topologies have been compiled. The analytical models allow for a computationally efficient evaluation of different RFM designs leading to a simple multi-objective optimization.
- ▶ A RFM prototype was designed, built and tested. The measurement results show a good match to the analytical modeling and FEM simulation results.
- ▶ Analytical models describing the electro-magnetic, thermal, and mechanical behavior of double-rotor AFM topologies have been compiled. The analytical models allow for a computationally efficient evaluation of different AFM designs leading to a simple multi-objective optimization.
- ▶ An AFM prototype was designed, built and tested. The measurement results show a good match to the analytical modeling and FEM simulation results.

# 3

## Modeling of Power Electronics for Multi-Objective Optimization

**M**ODELING of power electronics is always a multi-physics problem and can be very difficult, especially once the interactions between the different system components are being taken into account. In this chapter detailed models of the system components will be presented and from that it will be outlined which trade-offs and limitations exist and which degrees of freedom feature a clear optimum. For this thesis the objectives of interest are efficiency/losses, power-to-weight ratio, power density and cost, with the main emphasis on the power-to-weight ratio and the efficiency.

### 3.1 Semiconductors

In terms of power-to-weight ratio and power density the semiconductors barely contribute at all, since the weight and volume of the semiconductors themselves is negligible compared to the total system weight, i.e. the packaging of the semiconductors plays a very important role and will predominantly define the weight and volume contribution. The semiconductors do however have a large impact on the system cost and the system losses and therefore the heat sink weight and volume. Hence, for semiconductors the most important trade-off exists between investment cost and system losses.

Typically the cost for semiconductors monotonically increases with semiconductor size, but the semiconductor losses consist of two parts, conduction losses and switching losses. For MOSFET technology the

conduction losses monotonically decrease with the semiconductor size, while the switching losses monotonically increase with increasing semiconductor size, as will be shown in this section. Furthermore, the switching losses are linearly dependent on the employed switching frequency, while the conduction losses are in a first approximation independent of the switching frequency. Therefore, a MOSFET size exists, which minimizes the total semiconductor losses for a given load and switching frequency. Such an optimization is often called a "chip size optimization". For IGBT technology a similar trade-off between conduction and switching losses exists, but the sensitivities of the conduction and switching losses to semiconductor size are much smaller.

The biggest difference in cost and/or losses will be dependent on the semiconductor technology chosen for the application, e.g. Si-IGBT vs. SiC-MOSFET. Because of this an optimization of the semiconductors to be employed often boils down to a comparison of discrete choices, which are typically very limited.

In general the conduction losses are relatively easy to estimate. Because the conduction characteristics of IGBTs and MOSFETs are fundamentally different, the calculation of the conduction losses needs to be done separately for IGBTs and MOSFETs. The forward voltage drop of a MOSFET can be approximated as

$$v_{ds,cond} = r_{ds,on} i_{ds}, \quad (3.1)$$

which yields the average conduction losses of

$$\bar{P}_{cond,MOSFET} = \frac{1}{T} \int_0^T v_{ds} i_{ds} dt = r_{ds,on} I_{ds,rms}^2, \quad (3.2)$$

that are proportional to the MOSFETs on state resistance  $r_{ds,on}$ . The MOSFETs on state resistance is inversely proportional to the semiconductor size. Hence the conduction losses can be chosen to be arbitrarily low, it's simply a trade-off between conduction losses and acquisition cost (and switching losses, as will be shown later).

For IGBTs this does not hold true. The forward voltage drop of an IGBT is approximated as

$$v_{ce,cond} = V_f + r_{on} i_{ce}, \quad (3.3)$$

therefore the average conduction losses are

$$\bar{P}_{\text{cond,IGBT}} = \frac{1}{T} \int_0^T v_{\text{ce,cond}} i_{\text{ce}} dt = V_f I_{\text{ce,avg}} + r_{\text{on}} I_{\text{ce,rms}}^2. \quad (3.4)$$

Hence, the conduction losses cannot be chosen to be arbitrarily low, because the device specific forward voltage drop  $V_f$  of the IGBT is independent of the semiconductor size, i.e. the losses will always be greater than  $V_f I_{\text{ce,avg}}$ . So the use of IGBTs introduces an efficiency limit independent of acquisition cost and semiconductor size.

As shown above the conduction losses for MOSFETs and IGBTs monotonically decrease with semiconductor size, hence an optimal semiconductor size can only be found once switching losses are also considered. The following subsections will summarize approximations for conduction loss and switching loss calculations, which account for the most important phenomena based on semiconductor physics. The considered phenomena for the switching loss calculations are:

- ▶ losses due to the semiconductors output capacitances;
- ▶ losses due to the reverse recovery currents of (explicit) diodes and/or MOSFETs;
- ▶ losses due to charge stored in IGBTs (which lead to tail currents).

Not considered are losses due to parasitics of circuit layouts and or gate drive specific deficiencies, since these dependencies are not really influenced by the choice in semiconductor, but rather an engineer's challenge to overcome during the design of a converter.

Since the losses due to the parasitics of the circuit layouts are not included in the following switching loss approximations, Section ?? describes the idealized switching waveforms in a 2-level bridge leg based on the assumption of an idealized gate driver. Thereafter, simple approximations for the estimation of the switching loss components as a result of the nonidealities are given, which can be added to the analytic switching losses calculations of the following sections.

The four most common bridge leg topologies are the 2-level, the 3-level T-type, the 3-level NPC, and the 3-level ANPC bridge leg structure depicted in Fig. 3.1. For each of these bridge leg topologies the switching energies of all possible current commutations are analyzed. Together with (3.2) and (3.4) the losses for all possible voltage and

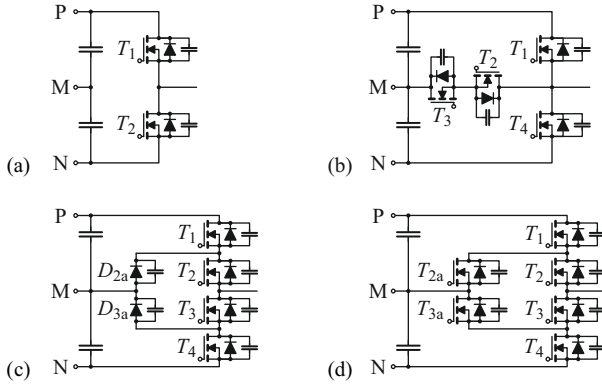


**Fig. 3.1:** The four most common bidirectional bridge leg topologies; (a) 2-level bridge leg, (b) 3-level T-type bridge leg, (c) 3-level NPC bridge leg, (d) 3-level ANPC bridge leg structure.

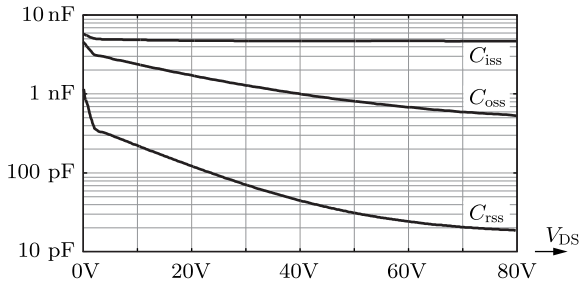


**Fig. 3.2:** Non-linear behavior of parasitic MOSFET capacitances.

current waveforms can then be estimated. Furthermore, using some assumptions, simple expressions for the switching and conduction losses for a 3-phase inverter/rectifier will be derived.

At first some quantities need to be defined. The output capacitance,  $C_{oss}(v)$ , of a semiconductor typically features a non-linear characteristic. An example is shown in Fig. 3.2. If  $C_{oss}(v)$  is known the charge  $Q_{oss}(v)$  and the energy  $E_{oss}(v)$ , which are stored due to this output

capacitance, can be defined as a function of the voltage  $v$  as

$$Q_{\text{oss}}(v) = \int_0^v C_{\text{oss}}(v) \, dv, \quad (3.5)$$

$$E_{\text{oss}}(v) = \int_0^v C_{\text{oss}}(v) \cdot v \, dv. \quad (3.6)$$

Furthermore, the reverse recovery charge  $Q_{\text{rr}}$ , which flows out of a diode that is being switched off, will be required. The reverse recovery charge shows a time dependence, which can be modeled for a PIN-diode according to [44]. The reverse recovery charge is approximated as a worst case to be the total forward bias injected charge  $Q_{\text{rr}} = \tau |I_L|$ . The lifetime  $\tau$  can usually be extracted from the data sheet of the diode or the MOSFET as described in [44].

### 3.1.1 Losses in 2-Level Bridge Legs

Commutation from the positive rail (P) to the negative rail (N) is shown in Fig. 3.3 and follows these sequences:

If the (inductive) load current  $I_L$  flows out of the switching node, it will flow through the output capacitances of  $T_1$  and  $T_2$  after  $T_1$  has been switched off. This charges the output capacitance of  $T_1$  and discharges the output capacitance of  $T_2$ . Switching off  $T_1$  requires some energy  $E_{\text{off},T1}(V_{\text{dc}}, I_L)$ . For MOSFETs the approximation  $E_{\text{off},T1}(V_{\text{dc}}, I_L) \approx 0 \mu\text{J}$  will be used, i.e. it is assumed that the MOSFET can be turned off fast enough, such that current has completely commutated to the output capacitance before the voltage across it has increased enough to become significant. Once the potential of the switching node reaches the negative rail, the diode of  $T_2$  starts to conduct, at which point  $T_2$  can be turned on at zero voltage condition. For IGBTs the approximation  $E_{\text{off},T1}(V_{\text{dc}}, I_L) \approx V_{\text{dc}}\tau_{\text{tail}}|I_L|$  will be used, i.e. the charge,  $Q_{\text{tail}} \approx \tau_{\text{IGBT}}|I_L|$ , stored in the IGBT at turn off is extracted and flows through the dc-link and  $T_1$  at full voltage, which generates losses in  $T_1$ .

If the (inductive) load current  $I_L$  flows into the switching node, it continues to flow to the positive rail through the diode of  $T_1$ . Turning on  $T_2$  commutates the current from the positive rail to the negative rail. Losses according to this commutation can be minimized with an appropriate gate drive and are therefore neglected in a first approximation. The reverse recovery charge  $Q_{\text{rr}} = \tau_{T1}|I_L|$  is extracted from the diode of the device  $T_1$ . In this process the energy  $Q_{\text{rr}} V_{\text{dc}}$  is taken from the dc-link and dissipated. Turning on  $T_2$  short circuits its output capacitance, hence the stored energy  $E_{\text{oss},T2}$  is dissipated in  $T_2$ . Furthermore, the output capacitance of  $T_1$  is charged from the dc-link through  $T_2$ . The total energy flowing out of the dc-link is  $Q_{\text{oss},T1}(V_{\text{dc}}) V_{\text{dc}}$ , but only  $E_{\text{oss},T1}(V_{\text{dc}})$  is stored in  $T_1$  at the end, hence the difference is dissipated in  $T_2$ .

Therefore, the switching energies for the commutation from the positive rail to the negative rail can be expressed as

$$E_{P\downarrow N, I_L > 0} = E_{\text{off},T1}(V_{\text{dc}}, I_L), \quad (3.7)$$

$$\begin{aligned} E_{P\downarrow N, I_L \leq 0} &= \tau_{T1}|I_L| V_{\text{dc}} \\ &+ E_{\text{oss},T2}(V_{\text{dc}}) \\ &+ Q_{\text{oss},T1}(V_{\text{dc}}) V_{\text{dc}} - E_{\text{oss},T1}(V_{\text{dc}}), \end{aligned} \quad (3.8)$$

where  $E_{P\downarrow N, I_L > 0}$  signifies that the load current is flowing out of the

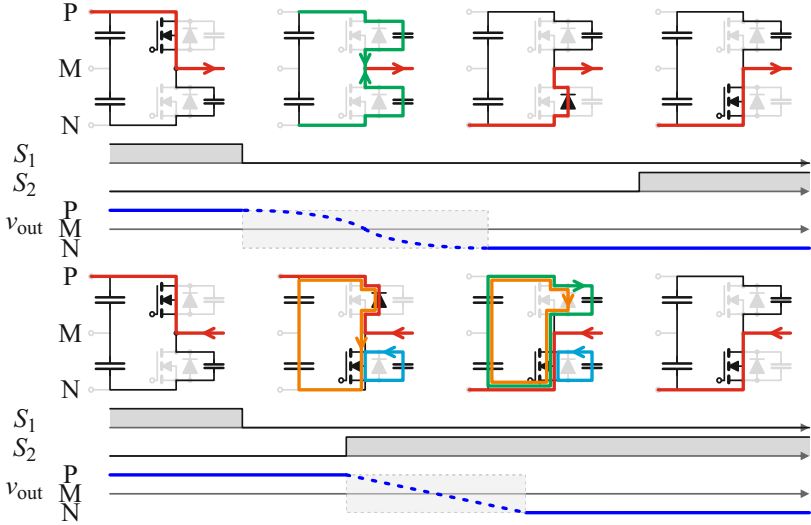


**Fig. 3.3:** Current commutation paths for the switching transitions from the positive rail (P) to the negative rail (N), for currents flowing out of the switching node (top) and currents flowing into the switching node (bottom).

switching node and  $E_{P\downarrow N, I_L \leq 0} \leq 0$  signifies that the load current is flowing into the switching node. The commutation sequences from the negative rail (N) to the positive rail (P) are analog and shown in Fig. 3.4. The switching energies are

$$E_{N\uparrow P, I_L \geq 0} = \tau_{T2} |I_L| V_{dc} + V_{dc} Q_{oss, T2}(V_{dc}) - E_{oss, T2}(V_{dc}) \quad (3.9)$$

$$+ E_{oss, T1}(V_{dc}),$$

$$E_{N\uparrow P, I_L < 0} = E_{off, T2}(V_{dc}, I_L). \quad (3.10)$$

With (3.2), (3.4), and (3.7) – (3.10) the losses for all possible voltage and current waveforms of a 2-level bridge leg can be estimated. However, with the use of some assumptions, the approximations can be simplified. The distribution of the conduction losses between the different switches is a function of the output voltage. However, for a bridge leg of a 3-phase converter the problem becomes symmetric and the opposing switches should be chosen to be the same, i.e.  $T_1 = T_2$ . Let us further assume that output current  $I_L$  is sinusoidal and in phase

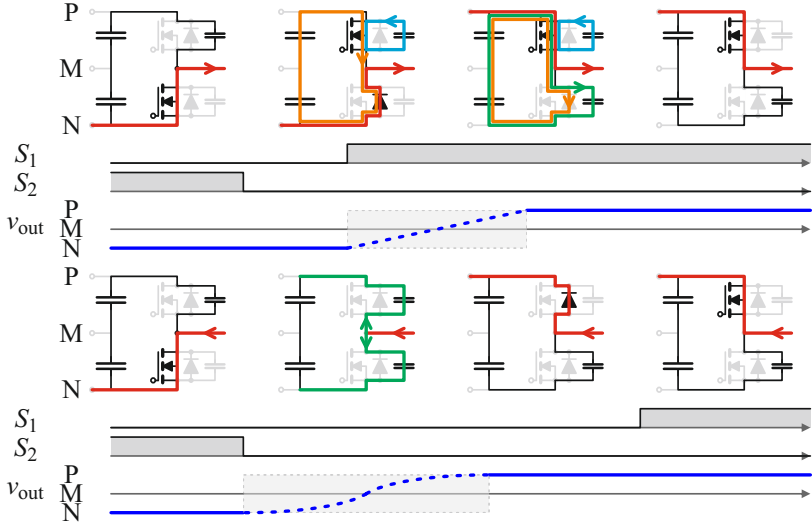


**Fig. 3.4:** Current commutation paths for the switching transitions from the negative rail (N) to the positive rail (P), for currents flowing out of the switching node (top) and currents flowing into the switching node (bottom).

with the fundamental of a sinusoidal output voltage  $v_{out,(1)}$ . In that case the transitions  $E_{P\downarrow N, I_L} > 0$  and  $E_{N\uparrow P, I_L} \geq 0$  occur every switching period while the load current  $I_L > 0$ , i.e. only half the time of a fundamental period. Similarly  $E_{P\downarrow N, I_L} \leq 0$  and  $E_{N\uparrow P, I_L} < 0$  occur every switching period while the load current  $I_L < 0$ . Hence the total switching losses will be

$$P_{sw} = \frac{f_{sw}}{2} (E_{P\downarrow N, I_L} > 0 + E_{N\uparrow P, I_L} \geq 0 + E_{P\downarrow N, I_L} \leq 0 + E_{N\uparrow P, I_L} < 0). \quad (3.11)$$

For MOSFETs the conduction and switching losses of a bridge leg are then described by

$$P_{cond} = r_{ds,on} \bar{I}_{L,rms}^2,$$

$$P_{sw} = f_{sw} \left( \tau_{T1} \frac{2\sqrt{2}}{\pi} I_{L,rms} + Q_{oss,T1}(V_{dc}) \right) V_{dc}.$$

For IGBTs the conduction and switching losses are then described by

$$\begin{aligned}
 P_{\text{cond}} &= V_{f,\text{IGBT1}} I_{\text{IGBT1,avg}} + r_{\text{on,IGBT1}} I_{\text{IGBT1,rms}}^2 \\
 &\quad + V_{f,\text{D1}} I_{\text{D1,avg}} + r_{\text{on,D1}} I_{\text{D1,rms}}^2 \\
 P_{\text{sw}} &= f_{\text{sw}} \left( (\tau_{\text{tail}} + \tau_{\text{T1}}) \frac{2\sqrt{2}}{\pi} I_{\text{L,rms}} + Q_{\text{oss,T1}}(V_{\text{dc}}) \right) V_{\text{dc}},
 \end{aligned}$$

with

$$\begin{aligned}
 I_{\text{IGBT1,avg}} &= \sqrt{2} I_{\text{L}} \left[ \frac{1}{2\pi} + \frac{2\hat{m}}{8} \right], & I_{\text{D1,avg}} &= \sqrt{2} I_{\text{L}} \left[ \frac{2\hat{m}}{8} - \frac{1}{2\pi} \right], \\
 I_{\text{IGBT1,rms}}^2 &= I_{\text{L}}^2 \left[ \frac{1}{4} + \frac{2\hat{m}}{3\pi} \right], & \text{and} & I_{\text{D1,rms}}^2 &= I_{\text{L}}^2 \left[ \frac{2\hat{m}}{3\pi} - \frac{1}{4} \right],
 \end{aligned}$$

where  $\frac{V_{\text{dc}}}{2} \hat{m}$  is the amplitude of the fundamental component of the output voltage with respect to the virtual dc-voltage midpoint potential M, i.e.

$$v_{\text{out}}(\varphi) = \frac{V_{\text{dc}}}{2} \hat{m} \sin(\varphi).$$

Hence  $\hat{m} > 0$  indicates inverter operation and  $\hat{m} < 0$  indicates rectifier operation.

### 3.1.2 Losses in 3-level T-Type Bridge Legs

Commutation from the positive rail (P) to the midpoint rail (M) for a T-type bridge leg is shown in Fig. 3.5 and follows these sequences:

If the (inductive) load current  $I_L$  flows out of the switching node, it will flow through the output capacitances of  $T_1$ ,  $T_2$  and  $T_4$  after  $T_1$  has been switched off. This charges the output capacitance of  $T_1$ , discharges the output capacitance of  $T_2$ , and discharges the output capacitance of  $T_4$  to  $\frac{V_{dc}}{2}$ . Switching off  $T_1$  requires the turn off energy  $E_{off,T1} (\frac{V_{dc}}{2}, I_L)$ . Once the potential of the switching node reaches the midpoint rail, the

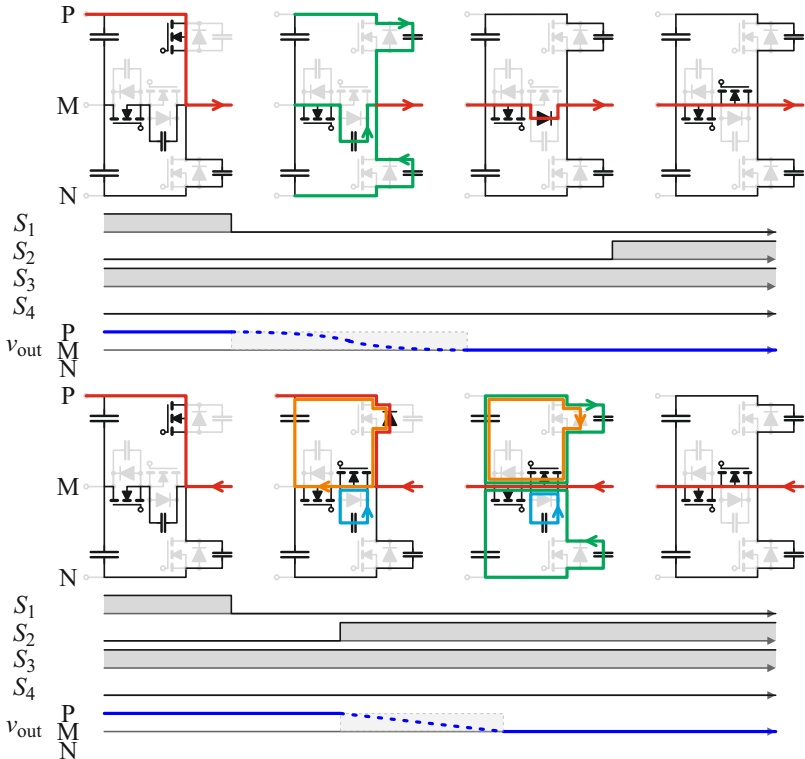


**Fig. 3.5:** Current commutation paths for the switching transitions from the positive rail (P) to the midpoint rail (M) in a T-type bridge leg, for currents flowing out of the switching node (top) and currents flowing into the switching node (bottom).

diode of  $T_2$  starts to conduct, at which point the switch  $T_2$  can be turned on at zero voltage condition.

If the (inductive) load current  $I_L$  flows into the switching node, it continues to flow to the positive rail through the diode of  $T_1$ . Turning on  $T_2$  commutates the current from the positive rail to the midpoint rail. The reverse recovery charge  $Q_{rr} = \tau_{T1}|I_L|$  is extracted from the diode of the device  $T_1$ . In this process the energy of  $Q_{rr} \frac{V_{dc}}{2}$  is taken from the top side dc-link capacitor and dissipated. Turning on  $T_2$  short circuits its output capacitance, hence the stored energy  $E_{oss,T2} \left(\frac{V_{dc}}{2}\right)$  is dissipated in  $T_2$ . The output capacitance of  $T_1$  is charged from the top dc-link capacitor through  $T_2$  and  $T_3$ . The total energy flowing out of the top dc-link capacitor is  $Q_{oss,T1} \left(\frac{V_{dc}}{2}\right) \frac{V_{dc}}{2}$ , but only  $E_{oss,T1} \left(\frac{V_{dc}}{2}\right)$  is stored in  $T_1$  at the end, hence the difference is dissipated. Furthermore, the output capacitance of  $T_4$  is discharged into the bottom dc-link capacitor through  $T_2$  and  $T_3$ . The energy stored in  $T_4$  is reduced from  $E_{oss,T4}(V_{dc})$  to  $E_{oss,T4} \left(\frac{V_{dc}}{2}\right)$ , but the total energy flowing into the bottom dc-link capacitor is only  $[Q_{oss,T4}(V_{dc}) - Q_{oss,T4} \left(\frac{V_{dc}}{2}\right)] \frac{V_{dc}}{2}$ , so the difference in energies must also be dissipated.

Therefore, the switching energies for the commutation from the positive rail to the negative rail can be expressed as

$$E_{P \downarrow M, I_L > 0} = E_{off, T1} \left( \frac{V_{dc}}{2}, I_L \right), \quad (3.12)$$

$$\begin{aligned} E_{P \downarrow M, I_L \leq 0} &= \tau_{T1} |I_L| \frac{V_{dc}}{2} \\ &+ Q_{oss, T1} \left( \frac{V_{dc}}{2} \right) \frac{V_{dc}}{2} - E_{oss, T1} \left( \frac{V_{dc}}{2} \right) \\ &+ E_{oss, T2} \left( \frac{V_{dc}}{2} \right) \\ &- \left[ Q_{oss, T4}(V_{dc}) - Q_{oss, T4} \left( \frac{V_{dc}}{2} \right) \right] \frac{V_{dc}}{2} \\ &+ \left[ E_{oss, T4}(V_{dc}) - E_{oss, T4} \left( \frac{V_{dc}}{2} \right) \right]. \end{aligned} \quad (3.13)$$

The commutation sequences from the negative rail (N) to the midpoint (M) for a T-type bridge leg are analog and shown in Fig. 3.6. The

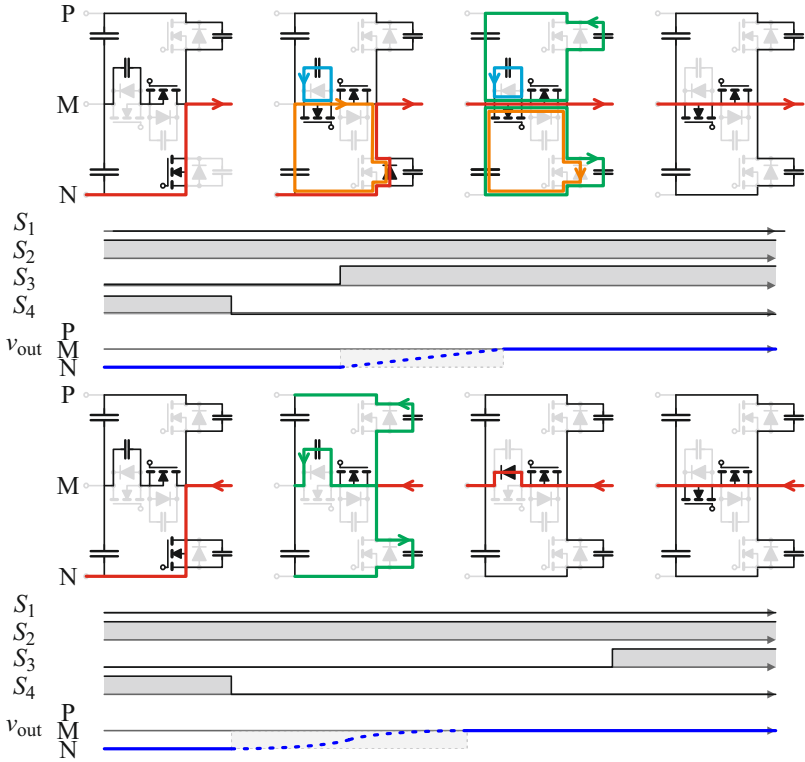


**Fig. 3.6:** Current commutation paths for the switching transitions from the negative rail (N) to the midpoint rail (M) in a T-type bridge leg, for currents flowing out of the switching node (top) and currents flowing into the switching node (bottom).

switching energies are

$$\begin{aligned}
 E_{N \uparrow M, I_L \geq 0} = & \tau_{T4} |I_L| \frac{V_{dc}}{2} \\
 & + Q_{oss, T4} \left( \frac{V_{dc}}{2} \right) \frac{V_{dc}}{2} - E_{oss, T4} \left( \frac{V_{dc}}{2} \right) \\
 & + E_{oss, T3} \left( \frac{V_{dc}}{2} \right) \\
 & - [Q_{oss, T1}(V_{dc}) - Q_{oss, T1} \left( \frac{V_{dc}}{2} \right)] \frac{V_{dc}}{2} \\
 & + [E_{oss, T1}(V_{dc}) - E_{oss, T1} \left( \frac{V_{dc}}{2} \right)], \\
 E_{N \uparrow M, I_L < 0} = & E_{off, T4} \left( -\frac{V_{dc}}{2}, I_L \right).
 \end{aligned} \tag{3.14}$$

$$\tag{3.15}$$

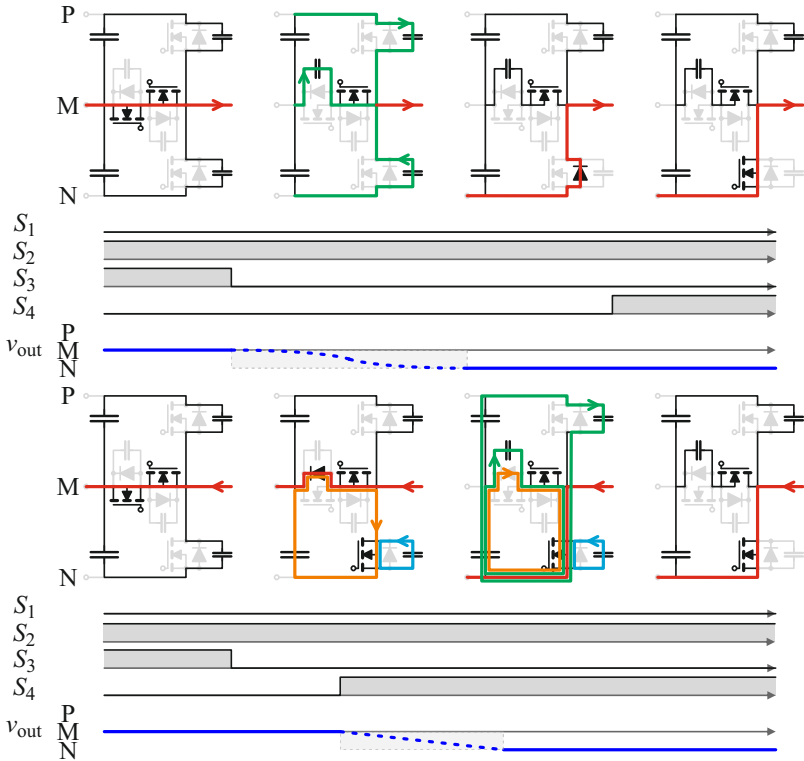


**Fig. 3.7:** Current commutation paths for the switching transitions from the midpoint rail (M) to the negative rail (N) in a T-type bridge leg, for currents flowing out of the switching node (top) and currents flowing into the switching node (bottom).

The commutations away from the midpoint rail are slightly different from the commutations towards the midpoint rail. Commutation from the midpoint rail (M) to the negative rail (N) for a T-type bridge leg is shown in Fig. 3.7 and follows these sequences:

If the (inductive) load current  $I_L$  flows out of the switching node, it will flow through the output capacitances of  $T_1$ ,  $T_3$  and  $T_4$  after  $T_3$  has been switched off. This charges the output capacitances of  $T_1$  and  $T_3$ , while the output capacitance of  $T_4$  is being discharged. Switching off  $T_3$  requires the turn off energy  $E_{off,T3}(\frac{V_{dc}}{2}, I_L)$ . Once the potential of

the switching node reaches the negative rail, the diode of  $T_4$  starts to conduct, at which point the switch  $T_4$  can be turned on at zero voltage condition.

If the (inductive) load current  $I_L$  flows into the switching node, it continues to flow to the midpoint rail through the diode of  $T_3$ . Turning on  $T_4$  commutates the current from the midpoint rail to the negative rail. The reverse recovery charge  $Q_{rr} = \tau_{T3}|I_L|$  is extracted from the diode of the device  $T_3$ . In this process the energy of  $Q_{rr} \frac{V_{dc}}{2}$  is taken from the bottom dc-link capacitor and dissipated. Turning on  $T_4$  short circuits its output capacitance, hence the stored energy  $E_{oss,T4} \left( \frac{V_{dc}}{2} \right)$  is dissipated in  $T_4$ . The output capacitance of  $T_1$  is charged from the dc-link through  $T_4$ . The total energy flowing out of the dc-link is  $[Q_{oss,T1}(V_{dc}) - Q_{oss,T1} \left( \frac{V_{dc}}{2} \right)] V_{dc}$  and  $[E_{oss,T1}(V_{dc}) - E_{oss,T1} \left( \frac{V_{dc}}{2} \right)]$  is stored in  $T_1$  at the end. Furthermore, the output capacitance of  $T_3$  is charged from the bottom dc-link capacitor through  $T_2$  and  $T_4$ . The total energy flowing out of the bottom dc-link capacitor is  $Q_{oss,T3} \left( \frac{V_{dc}}{2} \right) \frac{V_{dc}}{2}$ , but only  $E_{oss,T3} \left( \frac{V_{dc}}{2} \right)$  is stored in  $T_3$  at the end, hence this difference is dissipated.

Therefore, the switching energies for the commutation from the midpoint rail to the negative rail can be expressed as

$$E_{M \downarrow N, I_L > 0} = E_{off,T3} \left( \frac{V_{dc}}{2}, I_L \right), \quad (3.16)$$

$$\begin{aligned} E_{M \downarrow N, I_L \leq 0} = & \tau_{T3}|I_L| \frac{V_{dc}}{2} \quad (3.17) \\ & + [Q_{oss,T1}(V_{dc}) - Q_{oss,T1} \left( \frac{V_{dc}}{2} \right)] V_{dc} \\ & - [E_{oss,T1}(V_{dc}) - E_{oss,T1} \left( \frac{V_{dc}}{2} \right)] \\ & + Q_{oss,T3} \left( \frac{V_{dc}}{2} \right) \frac{V_{dc}}{2} - E_{oss,T3} \left( \frac{V_{dc}}{2} \right) \\ & + E_{oss,T4} \left( \frac{V_{dc}}{2} \right). \end{aligned}$$

The commutation sequences from the midpoint rail (M) to the positive rail (P) for a T-type bridge leg are analog and shown in Fig. 3.8.

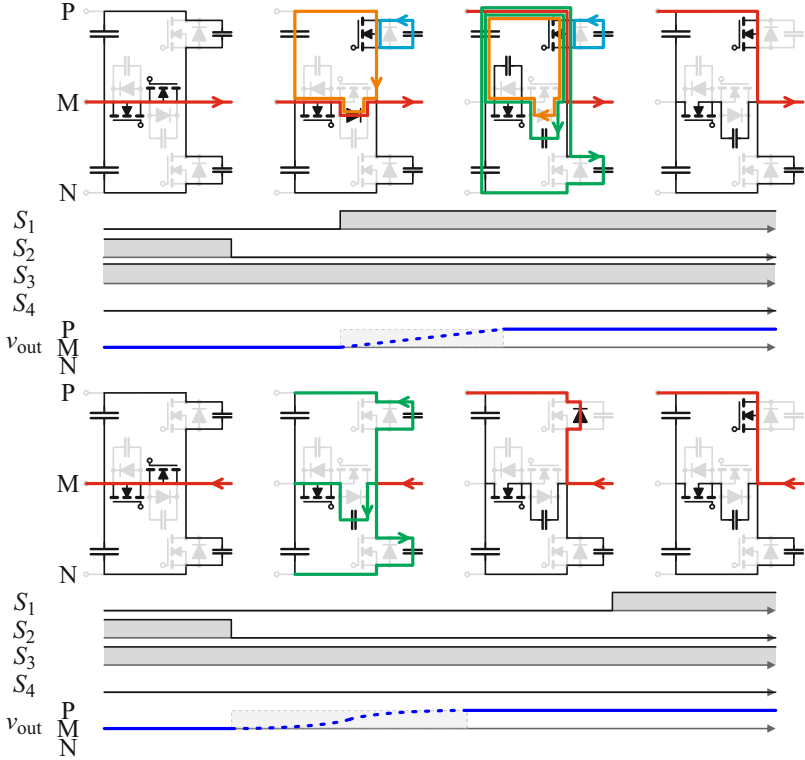


**Fig. 3.8:** Current commutation paths for the switching transitions from the midpoint rail (M) to the positive rail (P) in a T-type bridge leg, for currents flowing out of the switching node (top) and currents flowing into the switching node (bottom).

The switching energies are

$$\begin{aligned}
 E_{M\uparrow P, I_L \geq 0} &= \tau_{T2} |I_L| \frac{V_{dc}}{2} \\
 &\quad + [Q_{oss, T4}(V_{dc}) - Q_{oss, T4}(\frac{V_{dc}}{2})] V_{dc} \\
 &\quad - [E_{oss, T4}(V_{dc}) - E_{oss, T4}(\frac{V_{dc}}{2})] \\
 &\quad + Q_{oss, T2}(\frac{V_{dc}}{2}) \frac{V_{dc}}{2} - E_{oss, T2}(\frac{V_{dc}}{2}) \\
 &\quad + E_{oss, T1}(\frac{V_{dc}}{2}),
 \end{aligned} \tag{3.18}$$

$$E_{M\uparrow P, I_L < 0} = E_{off, T2}(\frac{V_{dc}}{2}, I_L). \tag{3.19}$$

With (3.2), (3.4), and (3.12) – (3.19) the losses for all possible voltage and current waveforms of a 3-level T-type bridge leg can be estimated. However, with the use of some assumptions, the approximations can be simplified. The distribution of the conduction losses between the different switches is a function of the output voltage. However, for a bridge leg of a 3-phase converter the problem becomes symmetric and the opposing switches and diodes should be chosen to be the same, i.e.  $T_1 = T_4$ ,  $D_1 = D_4$ ,  $T_2 = T_3$ , and  $D_2 = D_3$ . Let us further assume that output current  $I_L$  is sinusoidal and in phase with the fundamental of a sinusoidal output voltage  $v_{out,(1)}$ .

For inverter operation only the transitions  $E_{P\downarrow M, I_L} > 0$  and  $E_{M\uparrow P, I_L} \geq 0$  occur every switching period while the load current  $I_L > 0$ , i.e. only half the time of a fundamental period. Similarly  $E_{M\downarrow N, I_L} \leq 0$  and  $E_{N\uparrow M, I_L} < 0$  occur every switching period, while the load current  $I_L < 0$ . Hence the total switching losses in inverter operation will be

$$P_{sw,inv} = \frac{f_{sw}}{2} (E_{P\downarrow M, I_L} > 0 + E_{M\uparrow P, I_L} \geq 0 + E_{M\downarrow N, I_L} \leq 0 + E_{N\uparrow M, I_L} < 0). \quad (3.20)$$

For MOSFETs and inverter operation the switching losses of a bridge leg are described by

$$\begin{aligned} P_{sw,inv} = f_{sw} \cdot ( & [\tau_{T2} \frac{\sqrt{2}}{\pi} I_{L,rms}] V_{dc} \\ & + [Q_{oss,T1}(V_{dc}) - Q_{oss,T1}(\frac{V_{dc}}{2}) + \frac{1}{2} Q_{oss,T2}(\frac{V_{dc}}{2})] V_{dc} \\ & - [E_{oss,T1}(V_{dc}) - 2 E_{oss,T1}(\frac{V_{dc}}{2}) + E_{oss,T2}(\frac{V_{dc}}{2})] ). \end{aligned}$$

But for rectifier operation only the transitions  $E_{P\downarrow M, I_L} \leq 0$  and  $E_{M\uparrow P, I_L} < 0$  occur every switching period while the load current  $I_L < 0$ , i.e. only half the time of a fundamental period. Similarly  $E_{M\downarrow N, I_L} > 0$  and  $E_{N\uparrow M, I_L} \geq 0$  occur every switching period, while the load current  $I_L > 0$ . Hence the total switching losses in rectifier operation will be

$$P_{sw,rec} = \frac{f_{sw}}{2} (E_{P\downarrow M, I_L} \leq 0 + E_{M\uparrow P, I_L} < 0 + E_{M\downarrow N, I_L} > 0 + E_{N\uparrow M, I_L} \geq 0). \quad (3.21)$$

For MOSFETs and rectifier operation the switching losses of a bridge

leg are described by

$$\begin{aligned}
 P_{\text{sw,rec}} = f_{\text{sw}} \cdot ( & [\tau_{\text{T1}} \frac{\sqrt{2}}{\pi} I_{\text{L,rms}}] V_{\text{dc}} \\
 & + [Q_{\text{oss,T1}} \left(\frac{V_{\text{dc}}}{2}\right) - \frac{1}{2} Q_{\text{oss,T1}}(V_{\text{dc}})] V_{\text{dc}} \\
 & - [E_{\text{oss,T1}}(V_{\text{dc}}) - 2 E_{\text{oss,T1}} \left(\frac{V_{\text{dc}}}{2}\right)] ).
 \end{aligned}$$

The conduction losses in the MOSFETs for either operation are

$$P_{\text{cond}} = 2 r_{\text{ds,on,T1}} \overbrace{\frac{4\hat{m}}{3\pi} I_{\text{L,rms}}^2}^{I_{\text{T1,rms}}^2} + 2 r_{\text{ds,on,T2}} \overbrace{\left(1 - \frac{8\hat{m}}{3\pi}\right) I_{\text{L,rms}}^2}^{I_{\text{T2,rms}}^2},$$

where  $\hat{m} > 0$  indicates inverter operation and  $\hat{m} < 0$  indicates rectifier operation.

For IGBTs the switching losses are in inverter operation

$$\begin{aligned}
 P_{\text{sw,inv}} = f_{\text{sw}} \cdot ( & [(\tau_{\text{tail,T1}} + \tau_{\text{T2}}) \frac{\sqrt{2}}{\pi} I_{\text{L,rms}}] V_{\text{dc}} \\
 & + [Q_{\text{oss,T1}}(V_{\text{dc}}) - Q_{\text{oss,T1}} \left(\frac{V_{\text{dc}}}{2}\right) + \frac{1}{2} Q_{\text{oss,T2}} \left(\frac{V_{\text{dc}}}{2}\right)] V_{\text{dc}} \\
 & - [E_{\text{oss,T1}}(V_{\text{dc}}) - 2 E_{\text{oss,T1}} \left(\frac{V_{\text{dc}}}{2}\right) + E_{\text{oss,T2}} \left(\frac{V_{\text{dc}}}{2}\right)] )
 \end{aligned}$$

and in rectifier operation

$$\begin{aligned}
 P_{\text{sw,rec}} = f_{\text{sw}} \cdot ( & [(\tau_{\text{tail,T2}} + \tau_{\text{T1}}) \frac{\sqrt{2}}{\pi} I_{\text{L,rms}}] V_{\text{dc}} \\
 & + [Q_{\text{oss,T1}} \left(\frac{V_{\text{dc}}}{2}\right) - \frac{1}{2} Q_{\text{oss,T1}}(V_{\text{dc}})] V_{\text{dc}} \\
 & - [E_{\text{oss,T1}}(V_{\text{dc}}) - 2 E_{\text{oss,T1}} \left(\frac{V_{\text{dc}}}{2}\right)] ).
 \end{aligned}$$

The conduction losses in the IGBTs and their anti-parallel diodes for inverter operation are

$$\begin{aligned}
 P_{\text{cond}} = 2(V_{\text{f,IGBT1}} I_{\text{IGBT1,avg}} + r_{\text{on,IGBT1}} I_{\text{IGBT1,rms}}^2 \\
 + (V_{\text{f,IGBT2}} + V_{\text{f,D2}}) I_{\text{IGBT2,avg}} \\
 + (r_{\text{on,IGBT2}} + r_{\text{on,D2}}) I_{\text{IGBT2,rms}}^2),
 \end{aligned}$$

with

$$\begin{aligned}
 I_{\text{IGBT1,avg}} = \sqrt{2} I_{\text{L}} \frac{\hat{m}}{4}, & \quad I_{\text{IGBT2,avg}} = \sqrt{2} I_{\text{L}} \left[\frac{1}{\pi} - \frac{\hat{m}}{4}\right], \\
 I_{\text{IGBT1,rms}}^2 = I_{\text{L}}^2 \frac{4\hat{m}}{3\pi}, & \quad \text{and} \quad I_{\text{IGBT2,rms}}^2 = I_{\text{L}}^2 \left[\frac{1}{2} - \frac{4\hat{m}}{3\pi}\right],
 \end{aligned}$$

where  $\hat{m} \in [0, 1]$ , i.e. in inverter operation  $D_1$ , and  $D_4$  never conduct any current. Similarly the conduction losses for rectifier operation are

$$P_{\text{cond}} = 2(V_{f,D1} I_{D1,\text{avg}} + r_{\text{on},D1} I_{D1,\text{rms}}^2 + (V_{f,IGBT2} + V_{f,D2}) I_{IGBT2,\text{avg}} + (r_{\text{on},IGBT2} + r_{\text{on},D2}) I_{IGBT2,\text{rms}}^2),$$

with

$$I_{D1,\text{avg}} = \sqrt{2} I_L \frac{|\hat{m}|}{4}, \quad I_{IGBT2,\text{avg}} = \sqrt{2} I_L \left[ \frac{1}{\pi} - \frac{|\hat{m}|}{4} \right],$$

$$I_{D1,\text{rms}}^2 = I_L^2 \frac{4|\hat{m}|}{3\pi}, \quad \text{and} \quad I_{IGBT2,\text{rms}}^2 = I_L^2 \left[ \frac{1}{2} - \frac{4|\hat{m}|}{3\pi} \right],$$

where  $\hat{m} \in [-1, 0]$ , i.e. in rectifier operation  $T_1$  and  $T_4$  never conduct any current. Omitting  $T_1$  and  $T_4$  from the circuit yields the VIENNA-rectifier.

### 3.1.3 Losses in 3-level NPC Bridge Legs

Commutation from the positive rail (P) to the midpoint rail (M) for a NPC bridge leg is shown in Fig. 3.9 and follows these sequences:

If the (inductive) load current  $I_L$  flows out of the switching node, it will flow through the output capacitances of  $T_1$ ,  $D_{2a}$ ,  $D_{3a}$ ,  $T_3$ , and  $T_4$  after  $T_1$  has been switched off, which requires the turn off energy  $E_{\text{off},T1}(\frac{V_{\text{dc}}}{2}, I_L)$ . This charges the output capacitance of  $T_1$  and discharges the output capacitance of  $D_{2a}$ . Furthermore, the voltage across  $T_3$  and  $T_4$  is reduced from  $V_{\text{dc}}$  to  $\frac{V_{\text{dc}}}{2}$ , this discharges the output capacitances of  $T_3$  and  $T_4$  and charges the output capacitance of  $D_{3a}$ . Once the output capacitances of  $D_{3a}$  and  $T_3$  have reached the same voltage  $\Delta V$  the diode  $D_{2a}$  starts to conduct because the switching node has reached the midpoint potential. At this point the output capacitance of  $T_4$  is discharged to  $\frac{V_{\text{dc}}}{2} - \Delta V$ . Because of the nonlinearity of the output capacitances this problem needs to be solved numerically, where  $\Delta V$  is the solution to

$$Q_{\text{oss},T3}(\frac{V_{\text{dc}}}{2}) - Q_{\text{oss},T3}(\Delta V) \stackrel{!}{=} Q_{\text{oss},D3a}(\Delta V) + Q_{\text{oss},T4}(\frac{V_{\text{dc}}}{2}) - Q_{\text{oss},T4}(\frac{V_{\text{dc}}}{2} - \Delta V). \quad (3.22)$$

At this point the switch  $T_3$  is turned on to ensure that the switching node remains on the midpoint potential in case the output current changes direction during the conduction interval. The turn on of  $T_3$  short circuits the output capacitances of  $T_3$  and  $D_{3a}$ , hence the stored energy  $E_{\text{oss},T3}(\Delta V)$  is dissipated in  $T_3$  and  $E_{\text{oss},D3a}(\Delta V)$  is dissipated in  $D_{2a}$ ,  $T_2$  and  $T_3$ . The output capacitance of  $T_4$  is recharged to  $\frac{V_{\text{dc}}}{2}$  from  $\frac{V_{\text{dc}}}{2} - \Delta V$  through the bottom dc-link capacitor,  $D_{2a}$ ,  $T_2$ , and  $T_3$ . The total energy flowing out of the bottom dc-link is  $[Q_{\text{oss},T4}(\frac{V_{\text{dc}}}{2}) - Q_{\text{oss},T4}(\frac{V_{\text{dc}}}{2} - \Delta V)] \frac{V_{\text{dc}}}{2}$ , but only  $[E_{\text{oss},T4}(\frac{V_{\text{dc}}}{2}) - E_{\text{oss},T4}(\frac{V_{\text{dc}}}{2} - \Delta V)]$  is stored additionally in  $T_4$  at the end, hence the difference must be dissipated.

If the (inductive) load current  $I_L$  flows into the switching node, it continues to flow to the positive rail through the diode of  $T_1$ . Turning on  $T_3$  commutates the current from the positive rail to the midpoint rail. The reverse recovery charge  $Q_{\text{rr}} = \tau_{T1}|I_L|$  is extracted from the diode of the device  $T_1$ . In this process the energy of  $Q_{\text{rr}} \frac{V_{\text{dc}}}{2}$  is taken from the top dc-link capacitor and dissipated. Turning on  $T_3$  short circuits the output capacitances of  $D_{2a}$  and  $T_3$ , hence the stored energy  $E_{\text{oss},T3}(\frac{V_{\text{dc}}}{2})$  is dissipated in  $T_3$  and  $E_{\text{oss},D2a}(\frac{V_{\text{dc}}}{2})$  is dissipated in  $D_{3a}$ ,

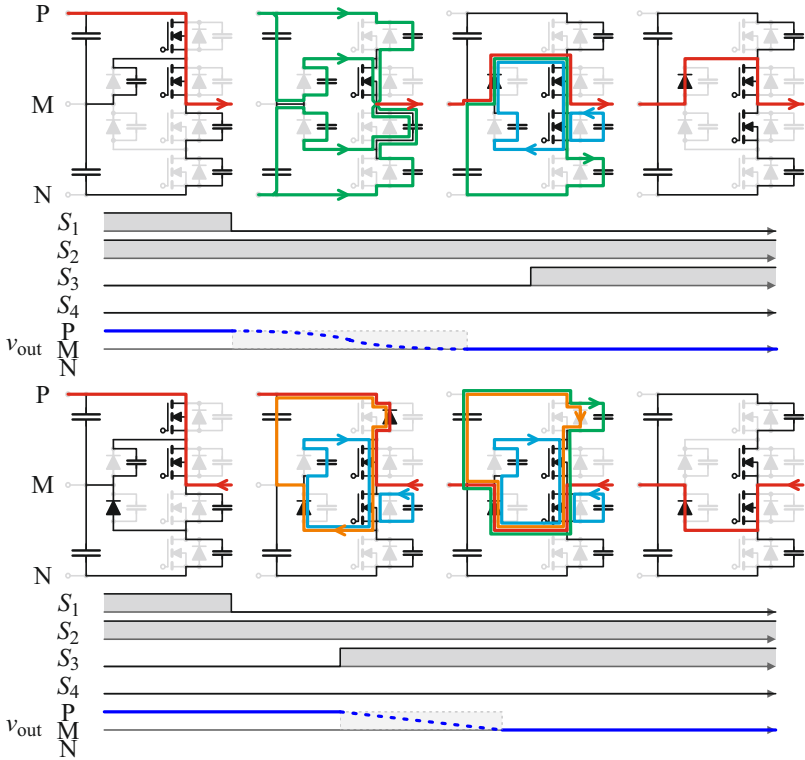


**Fig. 3.9:** Current commutation paths for the switching transitions from the positive rail (P) to the midpoint rail (M) in a NPC bridge leg, for currents flowing out of the switching node (top) and currents flowing into the switching node (bottom).

$T_2$  and  $T_3$ . The output capacitance of  $T_1$  is charged from the top dc-link capacitor through  $T_2$ ,  $T_3$  and  $D_{3a}$ . The total energy flowing out of the top dc-link is  $Q_{oss,T1} \left(\frac{V_{dc}}{2}\right) \frac{V_{dc}}{2}$ , but only  $E_{oss,T1} \left(\frac{V_{dc}}{2}\right)$  is stored in  $T_1$  at the end, hence the difference is dissipated.

Therefore, the switching energies for the commutation from the pos-

itive rail to the negative rail can be expressed as

$$\begin{aligned}
 E_{P\downarrow M, I_L > 0} &= E_{\text{off}, T1} \left( \frac{V_{\text{dc}}}{2}, I_L \right) & (3.23) \\
 &+ E_{\text{oss}, T3}(\Delta V) + E_{\text{oss}, D3a}(\Delta V) \\
 &+ \left[ Q_{\text{oss}, T4} \left( \frac{V_{\text{dc}}}{2} \right) - Q_{\text{oss}, T4} \left( \frac{V_{\text{dc}}}{2} - \Delta V \right) \right] \frac{V_{\text{dc}}}{2} \\
 &- \left[ E_{\text{oss}, T4} \left( \frac{V_{\text{dc}}}{2} \right) - E_{\text{oss}, T4} \left( \frac{V_{\text{dc}}}{2} - \Delta V \right) \right],
 \end{aligned}$$

$$\begin{aligned}
 E_{P\downarrow M, I_L \leq 0} &= \tau_{T1} |I_L| \frac{V_{\text{dc}}}{2} & (3.24) \\
 &+ E_{\text{oss}, T3} \left( \frac{V_{\text{dc}}}{2} \right) + E_{\text{oss}, D2a} \left( \frac{V_{\text{dc}}}{2} \right) \\
 &+ Q_{\text{oss}, T1} \left( \frac{V_{\text{dc}}}{2} \right) V_{\text{dc}} - E_{\text{oss}, T1} \left( \frac{V_{\text{dc}}}{2} \right).
 \end{aligned}$$

The commutation sequences from the negative rail (N) to the midpoint (M) for a NPC bridge leg are analog and shown in Fig. 3.10. The switching energies are

$$\begin{aligned}
 E_{N\uparrow M, I_L \geq 0} &= \tau_{T4} |I_L| \frac{V_{\text{dc}}}{2} & (3.25) \\
 &+ E_{\text{oss}, T2} \left( \frac{V_{\text{dc}}}{2} \right) + E_{\text{oss}, D3a} \left( \frac{V_{\text{dc}}}{2} \right) \\
 &+ Q_{\text{oss}, T4} \left( \frac{V_{\text{dc}}}{2} \right) V_{\text{dc}} - E_{\text{oss}, T4} \left( \frac{V_{\text{dc}}}{2} \right),
 \end{aligned}$$

$$\begin{aligned}
 E_{N\uparrow M, I_L < 0} &= E_{\text{off}, T4} \left( \frac{V_{\text{dc}}}{2}, I_L \right) & (3.26) \\
 &+ E_{\text{oss}, T2}(\Delta V) + E_{\text{oss}, D2a}(\Delta V) \\
 &+ \left[ Q_{\text{oss}, T1} \left( \frac{V_{\text{dc}}}{2} \right) - Q_{\text{oss}, T1} \left( \frac{V_{\text{dc}}}{2} - \Delta V \right) \right] \frac{V_{\text{dc}}}{2} \\
 &- \left[ E_{\text{oss}, T1} \left( \frac{V_{\text{dc}}}{2} \right) - E_{\text{oss}, T1} \left( \frac{V_{\text{dc}}}{2} - \Delta V \right) \right].
 \end{aligned}$$

The commutations away from the midpoint rail are slightly different from the commutations towards the midpoint rail. Commutation from the midpoint rail (M) to the negative rail (N) for a NPC bridge leg is shown in Fig. 3.11 and follows these sequences:

If the (inductive) load current  $I_L$  flows out of the switching node, it will flow through the output capacitances of  $T_2$ ,  $D_{3a}$  and  $T_4$  once  $T_2$  has been switched off. This charges the output capacitances of  $T_2$  and  $D_{3a}$ , while the output capacitance of  $T_4$  is being discharged. Switching off  $T_2$  requires the turn off energy  $E_{\text{off}, T2} \left( \frac{V_{\text{dc}}}{2}, I_L \right)$ . Once the potential of the switching node reaches the negative rail, the diode of  $T_4$  starts to conduct, at which point the switch  $T_4$  can be turned on at zero voltage condition.

If the (inductive) load current  $I_L$  flows into the switching node, it continues to flow to the midpoint rail through  $T_3$  and  $D_{3a}$  when

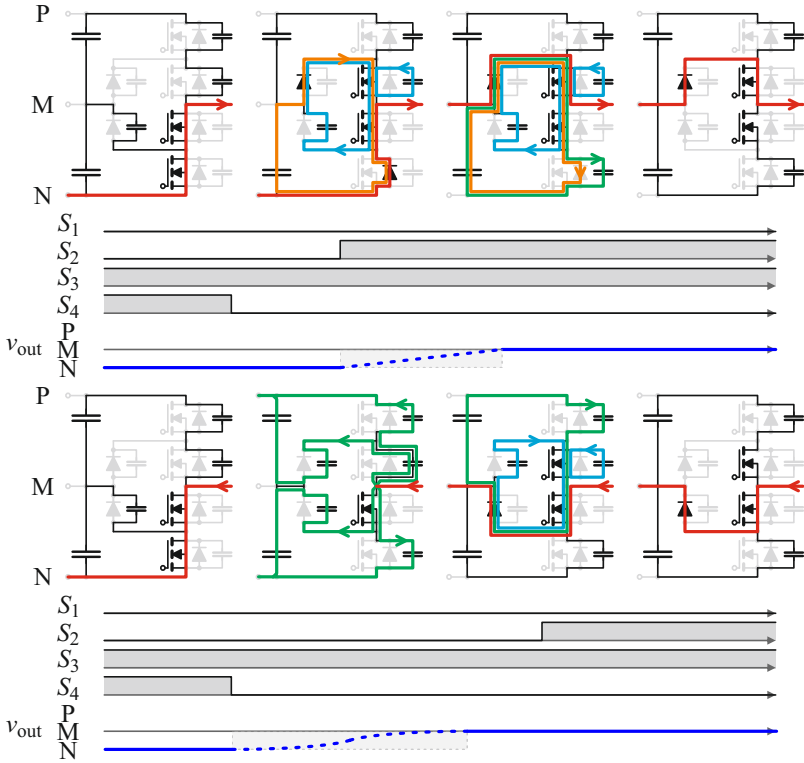


**Fig. 3.10:** Current commutation paths for the switching transitions from the negative rail (N) to the midpoint rail (M) in a NPC bridge leg, for currents flowing out of the switching node (top) and currents flowing into the switching node (bottom).

$T_2$  is turned off at zero voltage switching condition. Turning on  $T_4$  commutates the current from the midpoint rail to the negative rail. The reverse recovery charge  $Q_{rr} = \tau_{D2a}|I_L|$  is extracted from the diode  $D_{3a}$ . In this process the energy of  $Q_{rr} \frac{V_{dc}}{2}$  is taken from the bottom dc-link capacitor and dissipated. Turning on  $T_4$  short circuits its output capacitance, hence the stored energy  $E_{oss,T4} \left( \frac{V_{dc}}{2} \right)$  is dissipated in  $T_4$ . The output capacitance  $T_2$  is charged from the bottom dc-link capacitor through  $D_{2a}$ ,  $T_3$ , and  $T_4$ . The total energy flowing out of the dc-link is  $Q_{oss,T2} \left( \frac{V_{dc}}{2} \right) \frac{V_{dc}}{2}$ , but only  $E_{oss,T2} \left( \frac{V_{dc}}{2} \right)$  is stored in  $T_2$  at the end,

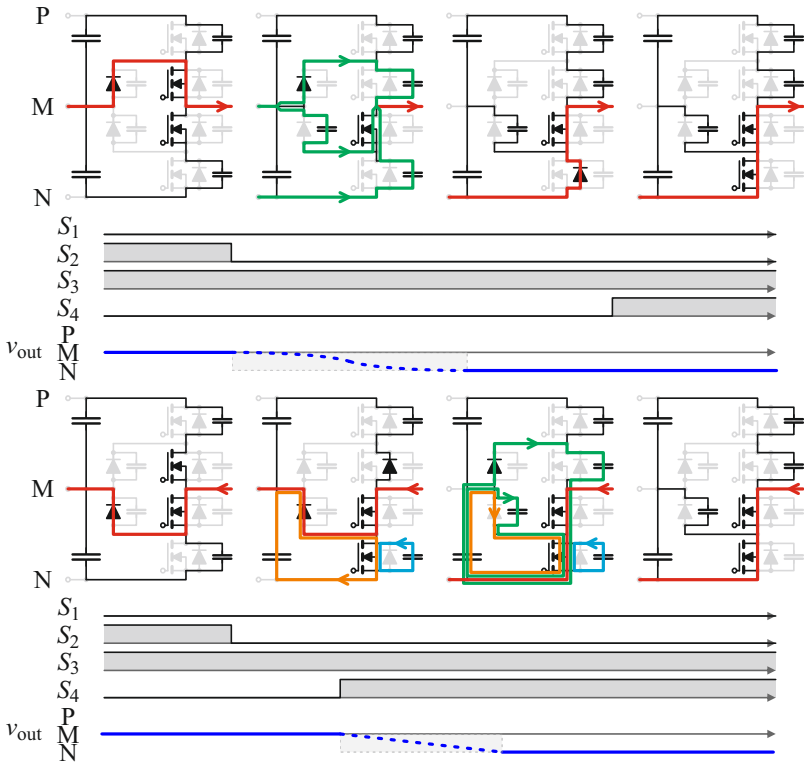


**Fig. 3.11:** Current commutation paths for the switching transitions from the midpoint rail (M) to the negative rail (N) in a NPC bridge leg, for currents flowing out of the switching node (top) and currents flowing into the switching node (bottom).

hence the difference is dissipated. Further, the output capacitance of  $D_{3a}$  is charged from the bottom dc-link capacitor through  $T_4$ . The total energy flowing out of the bottom dc-link capacitor is  $Q_{oss,D3a} \left( \frac{V_{dc}}{2} \right) \frac{V_{dc}}{2}$ , but only  $E_{oss,D3a} \left( \frac{V_{dc}}{2} \right)$  is stored in  $D_{3a}$  at the end, hence this difference is also dissipated.

Therefore, the switching energies for the commutation from the mid-

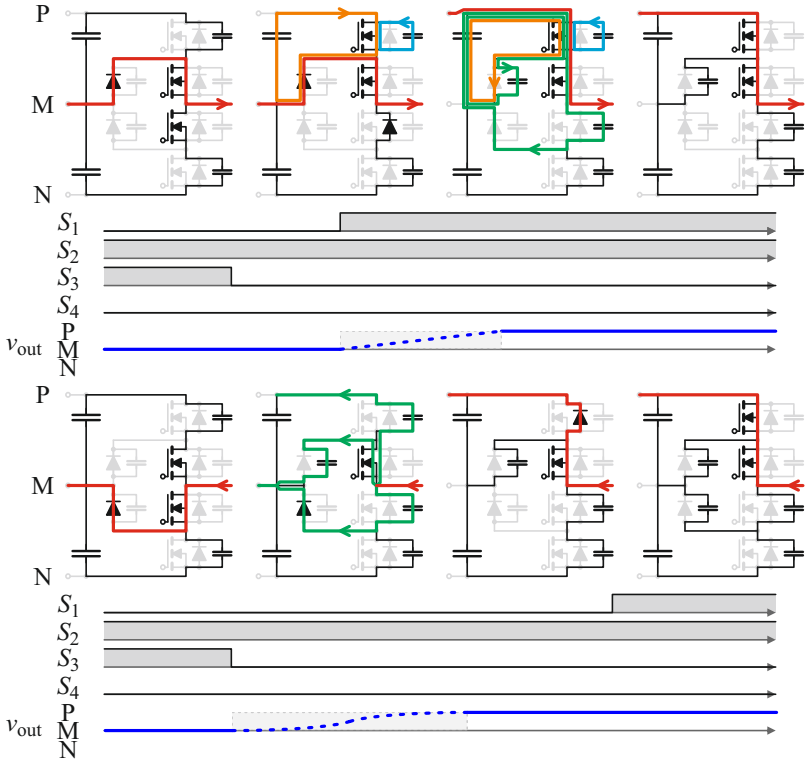


**Fig. 3.12:** Current commutation paths for the switching transitions from the midpoint rail (M) to the negative rail (N) in a NPC bridge leg, for currents flowing out of the switching node (top) and currents flowing into the switching node (bottom).

point rail to the negative rail can be expressed as

$$E_{M \downarrow N, I_L > 0} = E_{\text{off}, T2} \left( \frac{V_{\text{dc}}}{2}, I_L \right), \quad (3.27)$$

$$E_{M \downarrow N, I_L \leq 0} = \tau_{D3a} |I_L| \frac{V_{\text{dc}}}{2} + \left[ Q_{\text{oss}, T2} \left( \frac{V_{\text{dc}}}{2} \right) + Q_{\text{oss}, D3a} \left( \frac{V_{\text{dc}}}{2} \right) \right] \frac{V_{\text{dc}}}{2} - \left[ E_{\text{oss}, T2} \left( \frac{V_{\text{dc}}}{2} \right) + E_{\text{oss}, D3a} \left( \frac{V_{\text{dc}}}{2} \right) \right] + E_{\text{oss}, T4} \left( \frac{V_{\text{dc}}}{2} \right). \quad (3.28)$$

The commutation sequences from the midpoint rail (M) to the pos-

itive rail (P) for a NPC bridge leg are analog and shown in Fig. 3.12. The switching energies are

$$\begin{aligned}
 E_{M\uparrow P, I_L \geq 0} &= \tau_{D2a} |I_L| \frac{V_{dc}}{2} \\
 &+ [Q_{oss, D2a} \left(\frac{V_{dc}}{2}\right) + Q_{oss, T3} \left(\frac{V_{dc}}{2}\right)] \frac{V_{dc}}{2} \\
 &- [E_{oss, D2a} \left(\frac{V_{dc}}{2}\right) + E_{oss, T3} \left(\frac{V_{dc}}{2}\right)] \\
 &+ E_{oss, T1} \left(\frac{V_{dc}}{2}\right),
 \end{aligned} \tag{3.29}$$

$$E_{M\uparrow P, I_L < 0} = E_{off, T2} \left(\frac{V_{dc}}{2}, I_L\right). \tag{3.30}$$

With (3.2), (3.4), and (3.23) – (3.30) the losses for all possible voltage and current waveforms of a 3-level NPC bridge leg can be estimated. However, with the use of some assumptions, the approximations can be simplified. The distribution of the conduction losses between the different switches is a function of the output voltage. However, for a bridge leg of a 3-phase converter the problem becomes symmetric and the opposing switches should be chosen to be the same, i.e.  $T_1 = T_4$ ,  $D_1 = D_4$ ,  $T_2 = T_3$ ,  $D_2 = D_3$ , and  $D_{2a} = D_{3a}$ . Let us further assume that output current  $I_L$  is sinusoidal and in phase with the fundamental of a sinusoidal output voltage  $v_{out,(1)}$ .

For inverter operation only the transitions  $E_{P\downarrow M, I_L > 0}$  and  $E_{M\uparrow P, I_L \geq 0}$  occur every switching period while the load current  $I_L > 0$ , i.e. only half the time of a fundamental period. Similarly  $E_{M\downarrow N, I_L \leq 0}$  and  $E_{N\uparrow M, I_L < 0}$  occur every switching period, while the load current  $I_L < 0$ . Hence the total switching losses in inverter operation will be

$$P_{sw, inv} = \frac{f_{sw}}{2} (E_{P\downarrow M, I_L > 0} + E_{M\uparrow P, I_L \geq 0} + E_{M\downarrow N, I_L \leq 0} + E_{N\uparrow M, I_L < 0}). \tag{3.31}$$

For MOSFETs and inverter operation the switching losses of a bridge leg are described by

$$\begin{aligned}
 P_{sw, inv} &= f_{sw} \cdot \left( [\tau_{T2} \frac{\sqrt{2}}{\pi} I_{L, rms}] V_{dc} \right. \\
 &+ \left[ \frac{1}{2} Q_{oss, T2} \left(\frac{V_{dc}}{2}\right) + \frac{1}{2} Q_{oss, D2a} \left(\frac{V_{dc}}{2}\right) \right. \\
 &\quad \left. + \frac{1}{2} Q_{oss, T1} \left(\frac{V_{dc}}{2}\right) - \frac{1}{2} Q_{oss, T1} \left(\frac{V_{dc}}{2} - \Delta V\right) \right] V_{dc} \\
 &+ \left[ E_{oss, T1} \left(\frac{V_{dc}}{2} - \Delta V\right) + E_{oss, T2}(\Delta V) + E_{oss, D2a}(\Delta V) \right. \\
 &\quad \left. - E_{oss, T2} \left(\frac{V_{dc}}{2}\right) - E_{oss, D2a} \left(\frac{V_{dc}}{2}\right) \right] \left. \right).
 \end{aligned}$$

But for rectifier operation only the transitions  $E_{P\downarrow M, I_L \leq 0}$  and  $E_{M\uparrow P, I_L < 0}$  occur every switching period while the load current  $I_L < 0$ , i.e. only half the time of a fundamental period. Similarly  $E_{M\downarrow N, I_L > 0}$  and  $E_{N\uparrow M, I_L \geq 0}$  occur every switching period, while the load current  $I_L > 0$ . Hence the total switching losses in rectifier operation will be

$$P_{\text{sw,rec}} = \frac{f_{\text{sw}}}{2} (E_{P\downarrow M, I_L \leq 0} + E_{M\uparrow P, I_L < 0} + E_{M\downarrow N, I_L > 0} + E_{N\uparrow M, I_L \geq 0}). \quad (3.32)$$

For MOSFETs and rectifier operation the switching losses of a bridge leg are described by

$$\begin{aligned} P_{\text{sw,rec}} = f_{\text{sw}} \cdot ( & [\tau_{T1} \frac{\sqrt{2}}{\pi} I_{L,\text{rms}}] V_{\text{dc}} \\ & + [\frac{1}{2} Q_{\text{oss},T1} (\frac{V_{\text{dc}}}{2})] V_{\text{dc}} \\ & + [E_{\text{oss},T2} (\frac{V_{\text{dc}}}{2}) + E_{\text{oss},D2a} (\frac{V_{\text{dc}}}{2}) - E_{\text{oss},T1} (\frac{V_{\text{dc}}}{2})] ). \end{aligned}$$

The conduction losses in the MOSFETs for either operation are

$$\begin{aligned} P_{\text{cond}} = 2(r_{\text{ds,on},T1} I_{T1,\text{rms}}^2 + r_{\text{ds,on},T2} I_{T2,\text{rms}}^2 \\ + V_{f,D2a} I_{D2a,\text{avg}} + r_{\text{on},D2a} I_{D2a,\text{rms}}^2), \end{aligned}$$

with

$$\begin{aligned} I_{T1,\text{rms}}^2 &= I_L^2 \frac{4|\hat{m}|}{3\pi}, & I_{D2a,\text{avg}} &= \sqrt{2} I_L \left[ \frac{1}{\pi} - \frac{|\hat{m}|}{4} \right], \\ I_{T2,\text{rms}}^2 &= I_L^2 \frac{1}{2}, \quad \text{and} & I_{D2a,\text{rms}}^2 &= I_L^2 \left[ \frac{1}{2} - \frac{4|\hat{m}|}{3\pi} \right]. \end{aligned}$$

For IGBTs the switching losses are in inverter operation

$$\begin{aligned} P_{\text{sw,inv}} = f_{\text{sw}} \cdot ( & [(\tau_{\text{tail},T1} + \tau_{T2}) \frac{\sqrt{2}}{\pi} I_{L,\text{rms}}] V_{\text{dc}} \\ & + [\frac{1}{2} Q_{\text{oss},T2} (\frac{V_{\text{dc}}}{2}) + \frac{1}{2} Q_{\text{oss},D2a} (\frac{V_{\text{dc}}}{2}) \\ & + \frac{1}{2} Q_{\text{oss},T1} (\frac{V_{\text{dc}}}{2}) - \frac{1}{2} Q_{\text{oss},T1} (\frac{V_{\text{dc}}}{2} - \Delta V)] V_{\text{dc}} \\ & + [E_{\text{oss},T1} (\frac{V_{\text{dc}}}{2} - \Delta V) + E_{\text{oss},T2} (\Delta V) + E_{\text{oss},D2a} (\Delta V) \\ & - E_{\text{oss},T2} (\frac{V_{\text{dc}}}{2}) - E_{\text{oss},D2a} (\frac{V_{\text{dc}}}{2})] ) \end{aligned}$$

and in rectifier operation

$$\begin{aligned} P_{\text{sw,rec}} = f_{\text{sw}} \cdot ( & [(\tau_{\text{tail},T2} + \tau_{T1}) \frac{\sqrt{2}}{\pi} I_{L,\text{rms}}] V_{\text{dc}} \\ & + [\frac{1}{2} Q_{\text{oss},T1} (\frac{V_{\text{dc}}}{2})] V_{\text{dc}} \\ & + [E_{\text{oss},T2} (\frac{V_{\text{dc}}}{2}) + E_{\text{oss},D2a} (\frac{V_{\text{dc}}}{2}) - E_{\text{oss},T1} (\frac{V_{\text{dc}}}{2})] ). \end{aligned}$$

The conduction losses in the IGBTs and their anti-parallel diodes for inverter operation are

$$P_{\text{cond}} = 2(V_{f,\text{IGBT1}} I_{\text{IGBT1,avg}} + r_{\text{on,IGBT1}} I_{\text{IGBT1,rms}}^2 + V_{f,\text{IGBT2}} I_{\text{IGBT2,avg}} + r_{\text{on,IGBT2}} I_{\text{IGBT2,rms}}^2 + V_{f,D2a} I_{D2a,\text{avg}} + r_{\text{on,D2a}} I_{D2a,\text{rms}}^2),$$

with

$$\begin{aligned} I_{\text{IGBT1,avg}} &= \sqrt{2} I_L \frac{\hat{m}}{4}, & I_{\text{IGBT1,rms}}^2 &= I_L^2 \frac{4\hat{m}}{3\pi}, \\ I_{\text{IGBT2,avg}} &= \sqrt{2} I_L \frac{1}{\pi}, & I_{\text{IGBT2,rms}}^2 &= I_L^2 \frac{1}{2}, \\ I_{D2a,\text{avg}} &= \sqrt{2} I_L \left[ \frac{1}{\pi} - \frac{\hat{m}}{4} \right], \quad \text{and} & I_{D2a,\text{rms}}^2 &= I_L^2 \left[ \frac{1}{2} - \frac{4\hat{m}}{3\pi} \right], \end{aligned}$$

where  $\hat{m} \in [0, 1]$ , i.e. in inverter operation  $D_1$ , and  $D_4$  never conduct any current. Similarly the conduction losses for rectifier operation are

$$P_{\text{cond}} = 2(V_{f,D1} I_{D1,\text{avg}} + r_{\text{on,D1}} I_{D1,\text{rms}}^2 + V_{f,\text{IGBT2}} I_{\text{IGBT2,avg}} + r_{\text{on,IGBT2}} I_{\text{IGBT2,rms}}^2 + V_{f,D2a} I_{D2a,\text{avg}} + r_{\text{on,D2a}} I_{D2a,\text{rms}}^2),$$

with

$$\begin{aligned} I_{D1,\text{avg}} &= \sqrt{2} I_L \frac{|\hat{m}|}{4}, & I_{D1,\text{rms}}^2 &= I_L^2 \frac{4|\hat{m}|}{3\pi}, \\ I_{\text{IGBT2,avg}} &= \sqrt{2} I_L \frac{1}{\pi}, & I_{\text{IGBT2,rms}}^2 &= I_L^2 \frac{1}{2}, \\ I_{D2a,\text{avg}} &= \sqrt{2} I_L \left[ \frac{1}{\pi} - \frac{|\hat{m}|}{4} \right], \quad \text{and} & I_{D2a,\text{rms}}^2 &= I_L^2 \left[ \frac{1}{2} - \frac{4|\hat{m}|}{3\pi} \right], \end{aligned}$$

where  $\hat{m} \in [-1, 0]$ , i.e. in rectifier operation  $T_1$  and  $T_4$  never conduct any current.

### 3.1.4 Losses in 3-level ANPC Bridge Legs

Commutation from the positive rail (P) to the midpoint rail (M) for an ANPC bridge leg is shown in Fig. 3.13 and follows these sequences:

If the (inductive) load current  $I_L$  flows out of the switching node, it will flow through the output capacitances of  $T_1$ ,  $T_{2a}$  and  $T_3$  after  $T_1$  has been switched off. This charges the output capacitance of  $T_1$  and discharges the output capacitances of  $T_{2a}$  and  $T_3$ . Switching off  $T_1$  requires the turn off energy  $E_{\text{off},T_1}(\frac{V_{\text{dc}}}{2}, I_L)$ . Once the potential of the switching node reaches the midpoint rail, the diodes of  $T_{2a}$  and  $T_3$  start to conduct, at which point the switches  $T_{2a}$  and  $T_3$  can be turned on at zero voltage condition.

If the (inductive) load current  $I_L$  flows into the switching node, it continues to flow to the positive rail through the diode of  $T_1$ . Turning on  $T_3$  or  $T_{2a}$  commutates the current from the positive rail to the midpoint rail. The reverse recovery charge  $Q_{\text{rr}} = \tau_{T_1}|I_L|$  is extracted from the diode of the device  $T_1$ . In this process the energy  $Q_{\text{rr}} \frac{V_{\text{dc}}}{2}$  is taken from the top dc-link capacitor and dissipated. Turning on  $T_3$  or  $T_{2a}$  short circuits their output capacitances, hence the stored energy  $E_{\text{oss},T_{2a}}(\frac{V_{\text{dc}}}{2}) + E_{\text{oss},T_3}(\frac{V_{\text{dc}}}{2})$  is dissipated in either  $T_{2a}$  or  $T_3$ . The output capacitance of  $T_1$  is charged from the top dc-link capacitor through  $T_{2a}$  or through  $T_2$ ,  $T_3$  and  $T_{3a}$ . The total energy flowing out of the top dc-link is  $Q_{\text{oss},T_1}(\frac{V_{\text{dc}}}{2}) \frac{V_{\text{dc}}}{2}$ , but only  $E_{\text{oss},T_1}(\frac{V_{\text{dc}}}{2})$  is stored in  $T_1$  at the end, hence the difference is dissipated. At this point the other switch ( $T_{2a}$  or  $T_3$ ) can be turned on at zero voltage condition.

Therefore, the switching energies for the commutation from the positive rail to the negative rail can be expressed as

$$E_{P \downarrow M, I_L > 0} = E_{\text{off},T_1}(\frac{V_{\text{dc}}}{2}, I_L) \quad (3.33)$$

$$\begin{aligned} E_{P \downarrow M, I_L \leq 0} &= \tau_{T_1}|I_L| \frac{V_{\text{dc}}}{2} \\ &+ Q_{\text{oss},T_1}(\frac{V_{\text{dc}}}{2}) \frac{V_{\text{dc}}}{2} - E_{\text{oss},T_1}(\frac{V_{\text{dc}}}{2}) \\ &+ E_{\text{oss},T_3}(\frac{V_{\text{dc}}}{2}) + E_{\text{oss},T_{2a}}(\frac{V_{\text{dc}}}{2}). \end{aligned} \quad (3.34)$$

There is one further and important phenomena to be noted here, for the case where the (inductive) load current  $I_L$  flows into the switching node. At the end, when the other switch ( $T_{2a}$  or  $T_3$ ) is turned on at zero voltage condition, a parallel conduction path is provided for the load current, but only the forward voltage drop of the current conducting devices (e.g. of  $T_3$  and  $T_{3a}$ ) is the driving voltage for this current

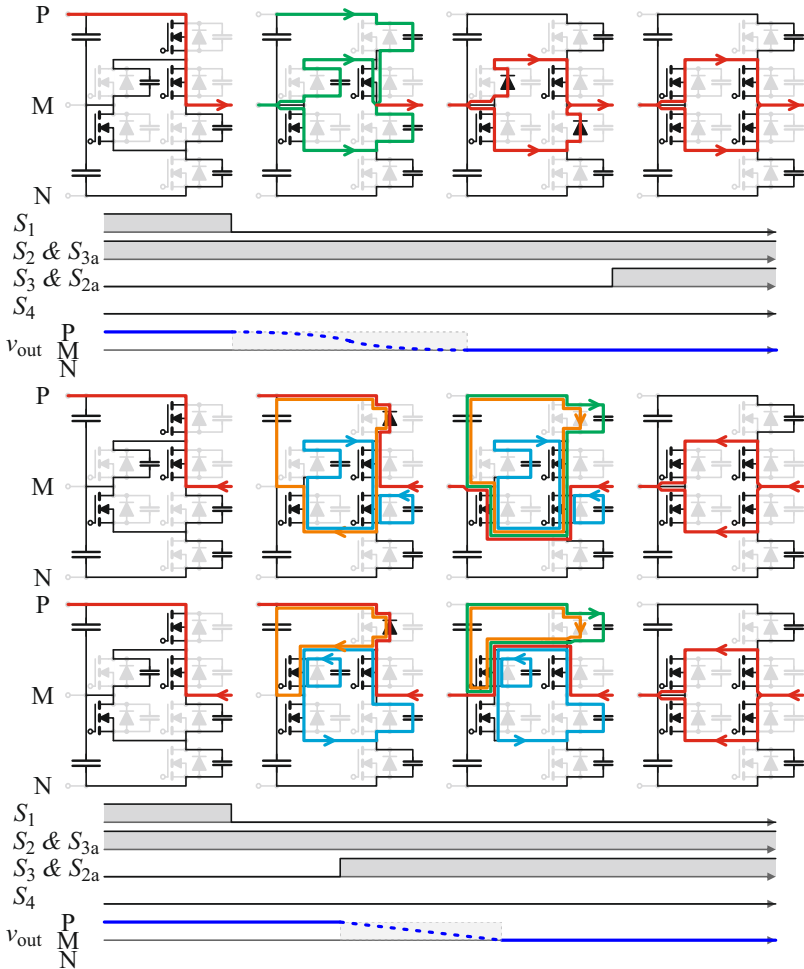


**Fig. 3.13:** Current commutation paths for the switching transitions from the positive rail (P) to the midpoint rail (M) in an ANPC bridge leg, for currents flowing out of the switching node (top) and currents flowing into the switching node (bottom).

commutation. As a consequence the current commutates very slowly to the parallel path and the resulting conduction losses will be somewhere between  $\frac{1}{2}(r_{ds,on,T3} + r_{ds,on,T3a}) I_L^2$  and  $(r_{ds,on,T3} + r_{ds,on,T3a}) I_L^2$ .

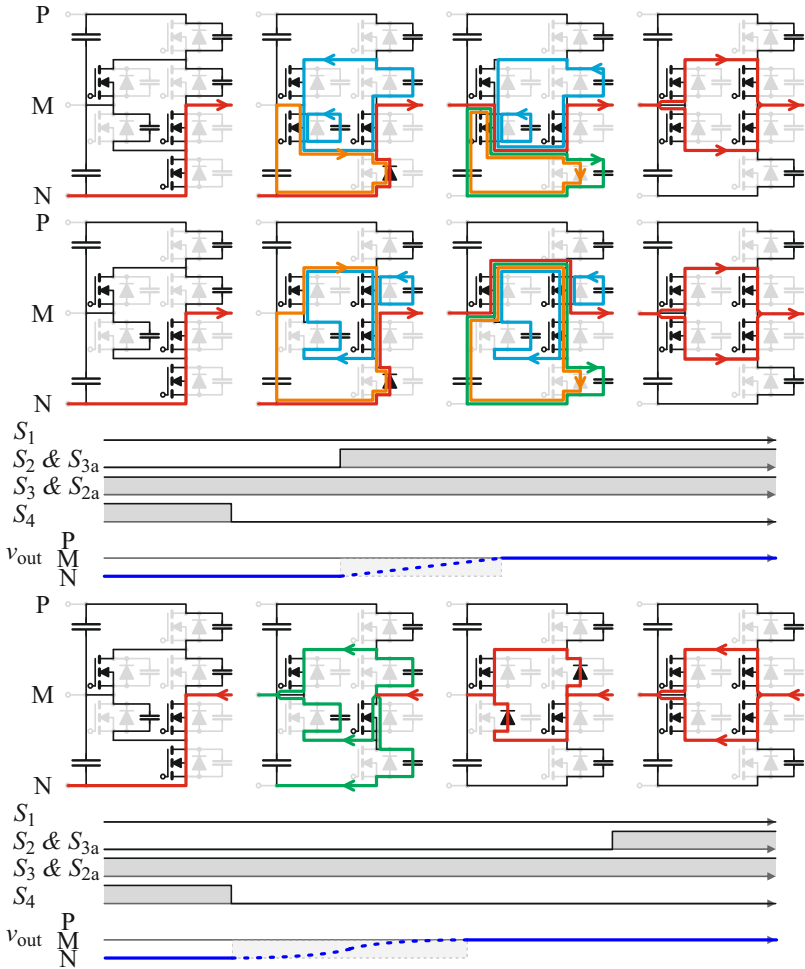


**Fig. 3.14:** Current commutation paths for the switching transitions from the negative rail (N) to the midpoint (M) in an ANPC bridge leg, for currents flowing out of the switching node (top) and currents flowing into the switching node (bottom).

The commutation sequences from the negative rail (N) to the midpoint (M) for an ANPC bridge leg are analog and shown in Fig. 3.14.

The switching energies are

$$E_{N\uparrow M, I_L \geq 0} = \tau_{T4} |I_L| \frac{V_{dc}}{2} \quad (3.35)$$

$$+ Q_{oss, T4} \left( \frac{V_{dc}}{2} \right) \frac{V_{dc}}{2} - E_{oss, T4} \left( \frac{V_{dc}}{2} \right),$$

$$E_{N\uparrow M, I_L < 0} = E_{off, T4} \left( \frac{V_{dc}}{2}, I_L \right). \quad (3.36)$$

The commutations away from the midpoint rail are slightly different from the commutations towards the midpoint rail. Commutation from the midpoint rail (M) to the negative rail (N) for an ANPC bridge leg is shown in Fig. 3.15 and follows these sequences:

If the (inductive) load current  $I_L$  flows out of the switching node, it will flow through the output capacitances of  $T_2$ ,  $T_{3a}$ , and  $T_4$  once  $T_2$  and  $T_{3a}$  have been switched off. This charges the output capacitances of  $T_2$  and  $T_{3a}$ , while the output capacitance of  $T_4$  is being discharged. Switching off  $T_2$  or  $T_{3a}$  requires the turn off energy  $E_{off, T2} \left( \frac{V_{dc}}{2}, I_L \right)$  or  $E_{off, T3a} \left( \frac{V_{dc}}{2}, I_L \right)$  or generally the sum of  $E_{off, T2} \left( \frac{V_{dc}}{2}, I_{T2} \right)$  and  $E_{off, T3a} \left( \frac{V_{dc}}{2}, I_L - I_{T2} \right)$  depending on the synchronization of the switching instances. Once the potential of the switching node reaches the negative rail, the diode of  $T_4$  starts to conduct, at which point the switch  $T_4$  can be turned on at zero voltage condition.

If the (inductive) load current  $I_L$  flows into the switching node, it continues to flow to the midpoint rail through the diode of  $T_2$  or  $T_{3a}$ . Turning on  $T_4$  commutates the current from the midpoint rail to the negative rail. The reverse recovery charge  $Q_{rr} = \tau_{T2} |I_L|$  or  $Q_{rr} = \tau_{T3a} |I_L|$  is extracted from the diode of the device  $T_{3a}$  (or  $T_2$ ). In this process the energy of  $Q_{rr} \frac{V_{dc}}{2}$  is taken from the bottom dc-link capacitor and dissipated. Turning on  $T_4$  short circuits its output capacitance, hence the stored energy  $E_{oss, T4} \left( \frac{V_{dc}}{2} \right)$  is dissipated in  $T_4$ . The output capacitance  $T_2$  is charged from the bottom dc-link capacitor through  $T_{2a}$ ,  $T_3$ , and  $T_4$ . The total energy flowing out of the dc-link is  $Q_{oss, T2} \left( \frac{V_{dc}}{2} \right) \frac{V_{dc}}{2}$ , but only  $E_{oss, T2} \left( \frac{V_{dc}}{2} \right)$  is stored in  $T_2$  at the end, hence the difference is dissipated. Further, the output capacitance of  $T_{3a}$  is charged from the bottom dc-link capacitor through  $T_4$ . The total energy flowing out of the bottom dc-link capacitor is  $Q_{oss, T3a} \left( \frac{V_{dc}}{2} \right) \frac{V_{dc}}{2}$ , but only  $E_{oss, T3a} \left( \frac{V_{dc}}{2} \right)$  is stored in  $T_{3a}$  at the end, hence this difference is also dissipated.

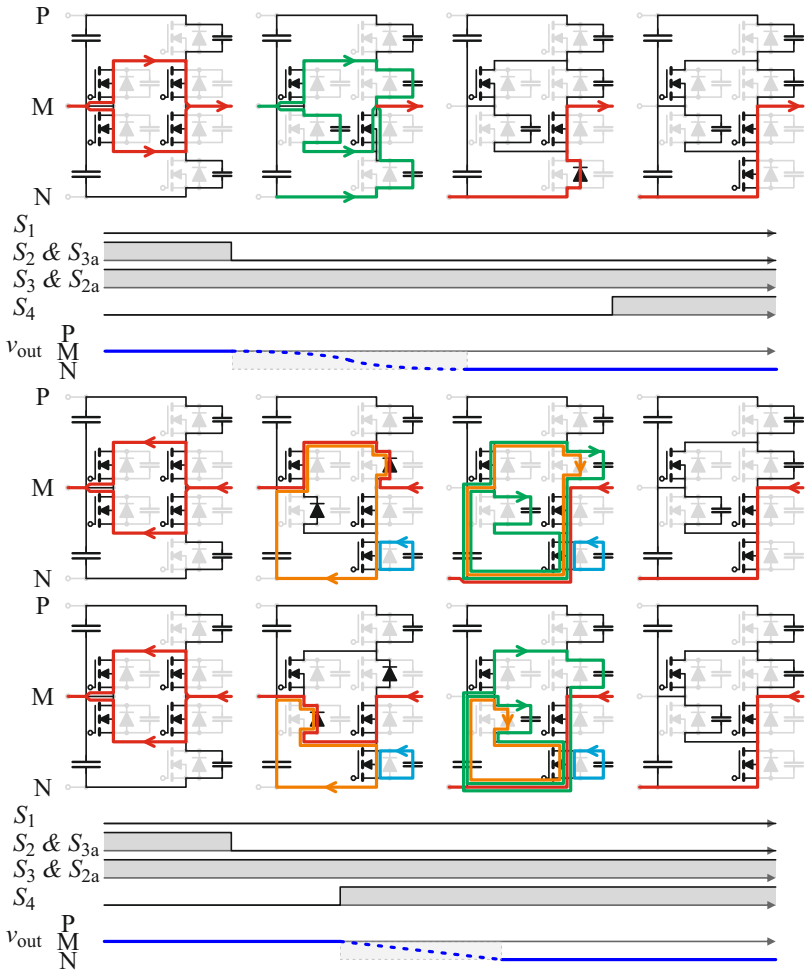


**Fig. 3.15:** Current commutation paths for the switching transitions from the midpoint rail (M) to the negative rail (N) in an ANPC bridge leg, for currents flowing out of the switching node (top) and currents flowing into the switching node (bottom).

Therefore, the switching energies for the commutation from the midpoint rail to the negative rail can be expressed as

$$E_{M\downarrow N, I_L > 0} = E_{\text{off}, T23a} \left( \frac{V_{\text{dc}}}{2}, I_L \right), \quad (3.37)$$

$$\begin{aligned} E_{M\downarrow N, I_L \leq 0} = & \tau_{T23a} |I_L| \frac{V_{\text{dc}}}{2} \quad (3.38) \\ & + Q_{\text{oss}, T2} \left( \frac{V_{\text{dc}}}{2} \right) \frac{V_{\text{dc}}}{2} - E_{\text{oss}, T2} \left( \frac{V_{\text{dc}}}{2} \right) \\ & + Q_{\text{oss}, T3a} \left( \frac{V_{\text{dc}}}{2} \right) \frac{V_{\text{dc}}}{2} - E_{\text{oss}, T3a} \left( \frac{V_{\text{dc}}}{2} \right) \\ & + E_{\text{oss}, T4} \left( \frac{V_{\text{dc}}}{2} \right), \end{aligned}$$

where  $E_{\text{off}, T23a} \left( \frac{V_{\text{dc}}}{2}, I_L \right)$  is the sum of the turn off energies  $E_{\text{off}, T2} \left( \frac{V_{\text{dc}}}{2}, I_{T2} \right)$  and  $E_{\text{off}, T3a} \left( \frac{V_{\text{dc}}}{2}, I_L - I_{T2} \right)$ . The commutation sequences from the midpoint rail (M) to the positive rail (P) for an ANPC bridge leg are analog and shown in Fig. 3.16. The switching energies are

$$E_{M\uparrow P, I_L \geq 0} = \tau_{T32a} |I_L| \frac{V_{\text{dc}}}{2} \quad (3.39)$$

$$\begin{aligned} & + Q_{\text{oss}, T3} \left( \frac{V_{\text{dc}}}{2} \right) \frac{V_{\text{dc}}}{2} - E_{\text{oss}, T3} \left( \frac{V_{\text{dc}}}{2} \right) \\ & + Q_{\text{oss}, T2a} \left( \frac{V_{\text{dc}}}{2} \right) \frac{V_{\text{dc}}}{2} - E_{\text{oss}, T2a} \left( \frac{V_{\text{dc}}}{2} \right) \\ & + E_{\text{oss}, T1} \left( \frac{V_{\text{dc}}}{2} \right), \\ E_{M\uparrow P, I_L < 0} = & E_{\text{off}, T32a} \left( \frac{V_{\text{dc}}}{2}, I_L \right), \quad (3.40) \end{aligned}$$

where  $E_{\text{off}, T32a} \left( \frac{V_{\text{dc}}}{2}, I_L \right)$  is the sum of the turn off energies  $E_{\text{off}, T3} \left( \frac{V_{\text{dc}}}{2}, I_{T3} \right)$  and  $E_{\text{off}, T2a} \left( \frac{V_{\text{dc}}}{2}, I_L - I_{T3} \right)$ .

With (3.2), (3.4), and (3.12) – (3.19) the losses for all possible voltage and current waveforms of a 3-level ANPC bridge leg can be estimated. However, with the use of some assumptions, the approximations can be simplified. The distribution of the conduction losses between the different switches is a function of the output voltage. However, for a bridge leg of a 3-phase converter the problem becomes symmetric and the opposing switches should be chosen to be the same, i.e.  $T_1 = T_4$ ,  $D_1 = D_4$ ,  $T_2 = T_3$ ,  $D_2 = D_3$ ,  $T_{2a} = T_{3a}$ , and  $D_{2a} = D_{3a}$ . Let us further assume that output current  $I_L$  is sinusoidal and in phase with the fundamental of a sinusoidal output voltage  $v_{\text{out},(1)}$ .

For inverter operation only the transitions  $E_{P\downarrow M, I_L > 0}$  and  $E_{M\uparrow P, I_L \geq 0}$  occur every switching period while the load current  $I_L > 0$ , i.e. only half the time of a fundamental period. Similarly  $E_{M\downarrow N, I_L \leq 0}$  and  $E_{N\uparrow M, I_L < 0}$  occur every switching period, while the load current

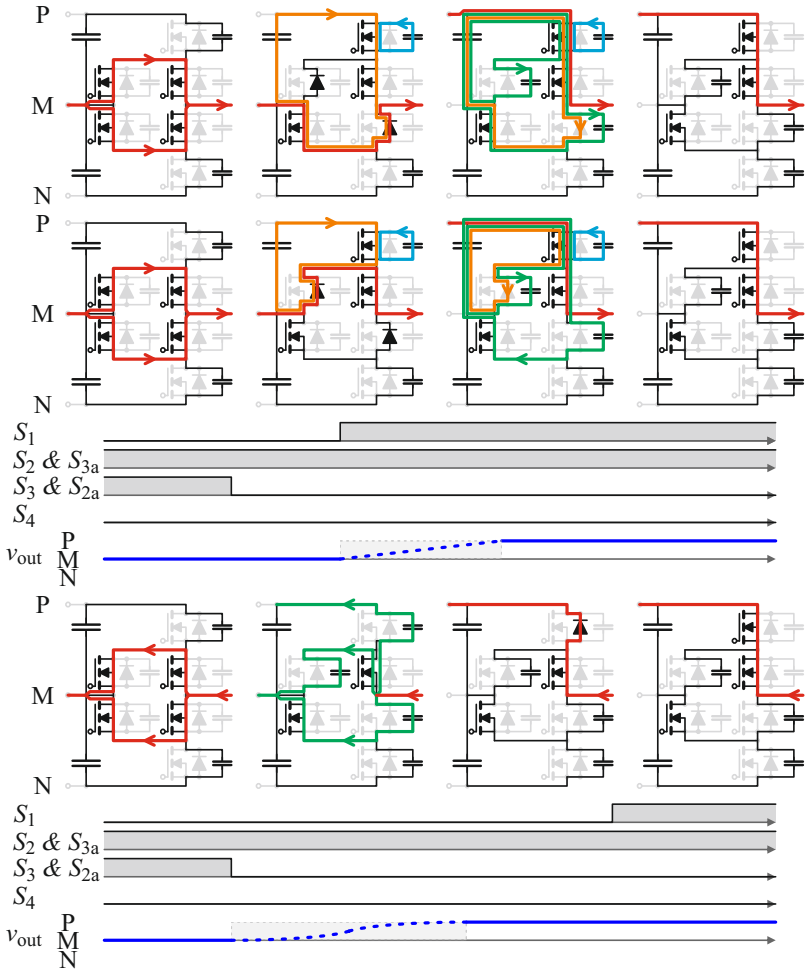


**Fig. 3.16:** Current commutation paths for the switching transitions from the midpoint rail (M) to the positive rail (P) in an ANPC bridge leg, for currents flowing out of the switching node (top) and currents flowing into the switching node (bottom).

$I_L < 0$ . Hence the total switching losses in inverter operation will be

$$P_{sw,inv} = \frac{f_{sw}}{2} (E_{P\downarrow M, I_L > 0} + E_{M\uparrow P, I_L \geq 0} + E_{M\downarrow N, I_L \leq 0} + E_{N\uparrow M, I_L < 0}). \quad (3.41)$$

For MOSFETs and inverter operation the switching losses of a bridge leg are described by

$$\begin{aligned}
 P_{\text{sw,inv}} = & f_{\text{sw}} \cdot \left( [\tau_{\text{T2}} \frac{\sqrt{2}}{\pi} I_{\text{L,rms}}] V_{\text{dc}} \right. \\
 & + \left[ \frac{1}{2} Q_{\text{oss,T2}} \left( \frac{V_{\text{dc}}}{2} \right) + \frac{1}{2} Q_{\text{oss,T2a}} \left( \frac{V_{\text{dc}}}{2} \right) \right] V_{\text{dc}} \\
 & \left. + \left[ E_{\text{oss,T1}} \left( \frac{V_{\text{dc}}}{2} \right) - E_{\text{oss,T2}} \left( \frac{V_{\text{dc}}}{2} \right) + E_{\text{oss,T2a}} \left( \frac{V_{\text{dc}}}{2} \right) \right] \right).
 \end{aligned}$$

But for rectifier operation only the transitions  $E_{\text{P}\downarrow\text{M},I_{\text{L}} \leq 0}$  and  $E_{\text{M}\uparrow\text{P},I_{\text{L}} < 0}$  occur every switching period while the load current  $I_{\text{L}} < 0$ , i.e. only half the time of a fundamental period. Similarly  $E_{\text{M}\downarrow\text{N},I_{\text{L}} > 0}$  and  $E_{\text{N}\uparrow\text{M},I_{\text{L}} \geq 0}$  occur every switching period, while the load current  $I_{\text{L}} > 0$ . Hence the total switching losses in rectifier operation will be

$$P_{\text{sw,rec}} = \frac{f_{\text{sw}}}{2} (E_{\text{P}\downarrow\text{M},I_{\text{L}} \leq 0} + E_{\text{M}\uparrow\text{P},I_{\text{L}} < 0} + E_{\text{M}\downarrow\text{N},I_{\text{L}} > 0} + E_{\text{N}\uparrow\text{M},I_{\text{L}} \geq 0}). \quad (3.42)$$

For MOSFETs and rectifier operation the switching losses of a bridge leg are described by

$$\begin{aligned}
 P_{\text{sw,rec}} = & f_{\text{sw}} \cdot \left( [\tau_{\text{T1}} \frac{\sqrt{2}}{\pi} I_{\text{L,rms}}] V_{\text{dc}} \right. \\
 & + \left[ \frac{1}{2} Q_{\text{oss,T1}} \left( \frac{V_{\text{dc}}}{2} \right) \right] V_{\text{dc}} \\
 & \left. + \left[ E_{\text{oss,T2}} \left( \frac{V_{\text{dc}}}{2} \right) + E_{\text{oss,T2a}} \left( \frac{V_{\text{dc}}}{2} \right) - E_{\text{oss,T1}} \left( \frac{V_{\text{dc}}}{2} \right) \right] \right).
 \end{aligned}$$

The conduction losses in the MOSFETs for either operation are between

$$\begin{aligned}
 P_{\text{cond,max}} = & 2[(r_{\text{ds,on,T1}} + r_{\text{ds,on,T2}}) I_{\text{T1,rms}}^2 \\
 & + (r_{\text{ds,on,T2a}} + r_{\text{ds,on,T2}}) I_{\text{T2a,rms}}^2]
 \end{aligned}$$

and

$$\begin{aligned}
 P_{\text{cond,min}} = & 2[(r_{\text{ds,on,T1}} + r_{\text{ds,on,T2}}) I_{\text{T1,rms}}^2 \\
 & + \frac{1}{2}(r_{\text{ds,on,T2a}} + r_{\text{ds,on,T2}}) I_{\text{T2a,rms}}^2]
 \end{aligned}$$

with

$$I_{\text{T1,rms}}^2 = I_{\text{L}}^2 \frac{4|\hat{m}|}{3\pi} \quad \text{and} \quad I_{\text{T2a,rms}}^2 = I_{\text{L}}^2 \left[ \frac{1}{2} - \frac{4|\hat{m}|}{3\pi} \right].$$

For inverter operation the conduction losses will most likely be closer to  $P_{\text{cond,min}}$  than  $P_{\text{cond,max}}$ , because the commutations towards the mid-point rail are soft. Whereas for rectifier operation the conduction losses will most likely be closer to  $P_{\text{cond,max}}$  than  $P_{\text{cond,min}}$ , because the commutations towards the midpoint rail are hard and the load current has little incentive to commute to the parallel conduction path once it becomes available.

For IGBTs the switching losses are in inverter operation

$$\begin{aligned}
 P_{\text{sw,inv}} = & f_{\text{sw}} \cdot \left( [(\tau_{\text{tail,T1}} + \tau_{\text{T2}}) \frac{\sqrt{2}}{\pi} I_{\text{L,rms}}] V_{\text{dc}} \right. \\
 & + \left[ \frac{1}{2} Q_{\text{oss,T2}} \left( \frac{V_{\text{dc}}}{2} \right) + \frac{1}{2} Q_{\text{oss,T2a}} \left( \frac{V_{\text{dc}}}{2} \right) \right] V_{\text{dc}} \\
 & \left. + \left[ E_{\text{oss,T1}} \left( \frac{V_{\text{dc}}}{2} \right) - E_{\text{oss,T2}} \left( \frac{V_{\text{dc}}}{2} \right) + E_{\text{oss,T2a}} \left( \frac{V_{\text{dc}}}{2} \right) \right] \right).
 \end{aligned}$$

and in rectifier operation

$$\begin{aligned}
 P_{\text{sw,rec}} = & f_{\text{sw}} \cdot \left( [(\tau_{\text{tail,T2}} + \tau_{\text{T1}}) \frac{\sqrt{2}}{\pi} I_{\text{L,rms}}] V_{\text{dc}} \right. \\
 & + \left[ \frac{1}{2} Q_{\text{oss,T1}} \left( \frac{V_{\text{dc}}}{2} \right) \right] V_{\text{dc}} \\
 & \left. + \left[ E_{\text{oss,T2}} \left( \frac{V_{\text{dc}}}{2} \right) + E_{\text{oss,T2a}} \left( \frac{V_{\text{dc}}}{2} \right) - E_{\text{oss,T1}} \left( \frac{V_{\text{dc}}}{2} \right) \right] \right).
 \end{aligned}$$

The conduction losses in the IGBTs and their anti-parallel diodes for inverter operation are

$$\begin{aligned}
 P_{\text{cond}} = & 2(V_{\text{f,IGBT1}} I_{\text{IGBT1,avg}} + r_{\text{on,IGBT1}} I_{\text{IGBT1,rms}}^2 \\
 & + V_{\text{f,IGBT2}} I_{\text{IGBT2,avg}} + r_{\text{on,IGBT2}} I_{\text{IGBT2,rms}}^2 \\
 & + V_{\text{f,D2a}} I_{\text{D2a,avg}} + r_{\text{on,D2a}} I_{\text{D2a,rms}}^2),
 \end{aligned}$$

with

$$\begin{aligned}
 I_{\text{IGBT1,avg}} = & \sqrt{2} I_{\text{L}} \frac{\hat{m}}{4}, & I_{\text{IGBT1,rms}}^2 = & I_{\text{L}}^2 \frac{4\hat{m}}{3\pi}, \\
 I_{\text{IGBT2,avg}} = & \sqrt{2} I_{\text{L}} \frac{1}{\pi}, & I_{\text{IGBT2,rms}}^2 = & I_{\text{L}}^2 \frac{1}{2}, \\
 I_{\text{D2a,avg}} = & \sqrt{2} I_{\text{L}} \left[ \frac{1}{\pi} - \frac{\hat{m}}{4} \right], & \text{and} & I_{\text{D2a,rms}}^2 = & I_{\text{L}}^2 \left[ \frac{1}{2} - \frac{4\hat{m}}{3\pi} \right].
 \end{aligned}$$

where  $\hat{m} \in [0, 1]$ , i.e. in inverter operation  $D_1$ , and  $D_4$  never conduct any current. Similarly the conduction losses for rectifier operation are

$$\begin{aligned}
 P_{\text{cond}} = & 2(V_{\text{f,D1}} I_{\text{D1,avg}} + r_{\text{on,D1}} I_{\text{D1,rms}}^2 \\
 & + V_{\text{f,IGBT2}} I_{\text{IGBT2,avg}} + r_{\text{on,IGBT2}} I_{\text{IGBT2,rms}}^2 \\
 & + V_{\text{f,D2a}} I_{\text{D2a,avg}} + r_{\text{on,D2a}} I_{\text{D2a,rms}}^2),
 \end{aligned}$$

with

$$\begin{aligned} I_{D1,\text{avg}} &= \sqrt{2}I_L \frac{|\hat{m}|}{4}, & I_{D1,\text{rms}}^2 &= I_L^2 \frac{|4\hat{m}|}{3\pi}, \\ I_{IGBT2,\text{avg}} &= \sqrt{2}I_L \frac{1}{\pi}, & I_{IGBT2,\text{rms}}^2 &= I_L^2 \frac{1}{2}, \\ I_{D2a,\text{avg}} &= \sqrt{2}I_L \left[ \frac{1}{\pi} - \frac{|\hat{m}|}{4} \right], & \text{and } I_{D2a,\text{rms}}^2 &= I_L^2 \left[ \frac{1}{2} - \frac{|4\hat{m}|}{3\pi} \right], \end{aligned}$$

where  $\hat{m} \in [-1, 0]$ , i.e. in rectifier operation  $T_1$  and  $T_4$  never conduct any current. It can be seen, that a NPC with IGBTs and an ANPC with IGBTs feature structurally the same conduction losses calculation.

## 3.2 Passive Components

For passive components, i.e. capacitors and inductors, there are not many trade-offs to be considered. Typically weight, and cost increase with volume, whereas the system losses due to the passive components decrease with volume. However, many pitfalls exist, as there are a large number of degrees of freedom and different technologies to choose from, i.e. it may be more important to choose the correct type of technology rather than optimizing the size of the component. E.g., choosing to use foil capacitors, rather than optimizing the number of electrolytic capacitors used in parallel in order to limit the dielectric losses, may yield a much smaller/lighter design. The correct type of technology can often be predicted and well argued a priori. The three main types of capacitors are electrolytic, film, and ceramic capacitors. The electrolytic capacitors feature a high energy density, but also relatively high dielectric losses, which makes them a good choice for transient energy storage purposes. However, the available voltage ratings of electrolytic capacitors are limited to  $\approx 650\text{ V}$ , which disqualifies them for many applications. Film capacitors are available in almost any voltage rating and feature much lower dielectric losses than electrolytic capacitors, but their energy density is much smaller than the energy density of electrolytic capacitors. Finally, ceramic capacitors are also available in almost any voltage rating, while featuring a high energy density and low dielectric losses, but the cost per stored energy is very high and they often feature a strong non-linearity (reduction) of the capacitance with respect to the applied voltage. E.g., the capacitance at rated voltage may be as low as 20% of the rated capacitance.

For magnetic components it also holds true that it may be more important to choose the correct type of technology rather than optimizing the size and geometry of the component itself. A trade-off exists between size and efficiency, i.e. the sum of core and winding losses. The modeling of magnetic components can be very challenging, however, there exist two fundamental limitations for all magnetic components. One of the limitations is the saturation flux density of the soft magnetic material, which may have a significant influence on the size and weight of the component. The other fundamental limitation is thermal, where the minimum possible size of the component will be defined by the chosen thermal boundary conditions and/or heat management. However, efficiency of the component is theoretically unbounded and

only a trade-off between size and efficiency has to be considered.

In this section simple models will be presented to estimate the minimum required weight of passive components in an efficient and easy manner. Although the models are strongly simplified, they describe the basic trade-offs for passive components.

### 3.2.1 Capacitors

The aim of the capacitor weight model is to select a capacitor, which simultaneously fulfills a minimum capacitance requirement  $C_{\min}$ , current carrying capability  $I_{\min}$ , and rated operating voltage  $V_{\min}$ . To that end, lists containing the capacitance  $C$ , current carrying capability  $I$ , rated voltage  $V$ , and associated mass  $m_{\text{cap}}$  are created based on the information provided in the data sheets of manufacturers. For each capacitor in the list the minimum number of parallel capacitors to achieve the capacitance and current rating is determined

$$N_{C,\min} = \left\lceil \frac{C_{\min}}{C} \right\rceil \quad \text{and} \quad N_{I,\min} = \left\lceil \frac{I_{\min}}{I} \right\rceil. \quad (3.43)$$

Consequently the required number of capacitors in parallel and the associated mass in order to satisfy both constraints is

$$N_{\min} = \max(N_{C,\min}, N_{I,\min}) \quad \text{and} \quad m_{\text{tot}} = N_{\min} \cdot m_{\text{cap}}. \quad (3.44)$$

Finally the capacitor, which has the minimum weight  $m_{\text{tot}}$  is selected.

### 3.2.2 Inductive Components

The most common core materials in power electronics are ferrite, amorphous soft magnetic alloys, nanocrystalline soft magnetic alloys or iron powder. The amorphous alloys typically feature the highest saturation flux density ( $B_{\text{sat}} \approx 1.5 \text{ T}$ ) but suffer from relatively high hysteresis losses. The nanocrystalline alloys typically feature a lower (but still high) saturation flux density ( $\approx 1.2 \text{ T}$ ), but significantly lower hysteresis losses. Unfortunately the availability of amorphous and nanocrystalline cut core shapes and sizes is very limited. Ferrite on the other hand is available in all sorts of shapes and sizes, it is relatively cheap and features low hysteresis losses, but its saturation flux density is much lower ( $B_{\text{sat}} < 0.4 \text{ T}$ ). Iron powder is also available in all sorts of shapes

and sizes, it is also very cheap and features a high saturation flux density ( $B_{\text{sat}} \approx 1.2 \text{ T}$ ), but its hysteresis losses are relatively high and it shows a high nonlinearity of its permeability with respect to the applied magnetic flux density in the core.

The best choice of winding technology also highly depends on the application. The most common winding materials are solid copper wire (either as round wire coil or helical coil made of flat wire), litz wire and foil windings. The selection of the winding technology can have an immense impact on the generated losses and the selection thereof is outside the scope of this thesis. Here the reader is referred to [45] for simple models, which account for the losses due to high-frequency effects.

The aim of the magnetic component weight model is to estimate the minimum required weight, with which the magnetic component can be realized. The total losses,  $P_{\text{loss}}$ , composed of winding and core losses, need to be less than the maximum power, which can be dissipated,

$$P_{\text{loss}} = \underbrace{V_w k_w \rho_{\sigma,w} S_{\text{rms}}^2}_{P_{\text{loss,winding}}} + \underbrace{V_c k_c f^\alpha B_f^\beta}_{P_{\text{loss,core}}} \leq Oh\Delta T, \quad (3.45)$$

where  $V_w$ ,  $k_w$ ,  $\rho_{\sigma,w}$  are the total winding volume, packing factor and conductivity,  $S_{\text{rms}}$  is the average conductor current density,  $V_c$  the core volume,  $k_c$ ,  $\alpha$ ,  $\beta$  the Steinmetz parameters,  $B_f$  and  $f$  are the (sinusoidal) magnetic flux density amplitude (ac component) and frequency,  $O$  the surface area of the magnetic component, and  $h\Delta T$  the product of average heat transfer coefficient and difference between the ambient and the component temperature. A very simple way to account for high-frequency effects is to assume a ratio of the ac-resistance to the dc-resistance of  $\frac{r_{\text{ac}}}{r_{\text{dc}}} \approx 2$  for a reasonable design, i.e. it can be accounted for by increasing  $\rho_{\sigma,w}$  by a factor of 2 (in case of a transformer, i.e. missing DC-current component). The parameter  $h\Delta T$  is dependent on the thermal connection to the surrounding environment. In this work  $h\Delta T = 2000 \text{ W/m}^2$  is chosen [46]. The size of the magnetic core must be large enough, such that

$$\Psi_f I_{\text{rms}} \leq \underbrace{B_f A_e}_{\Psi_f / N} \underbrace{S_{\text{rms}} k_w A_{w,\text{eff}}}_{NI_{\text{rms}}} \quad (3.46)$$

holds true, where  $\Psi_f$  is the required flux linkage amplitude,  $I_{\text{rms}}$  the required rms value of the current,  $A_e$  the core cross-sectional area, and

$A_{w,\text{eff}}$  the effective winding cross-sectional area (excluding the space required for the bobbin). The requirements  $\Psi_f$  and  $I_{\text{rms}}$  can be extracted from the circuit simulations. All remaining parameters except for the current density  $S_{\text{rms}}$  can be extracted from material data sheets, available core geometries, and winding geometry considerations. Finally the minimum weight magnetic component, which satisfies the thermal boundary condition is selected.

### 3.3 Cooling System Modeling

The optimization of power electronics with respect to minimum weight is particularly related to the optimization of the cooling system (heat sink plus fan), since the cooling system in a large part contributes to the total converter weight. This has already been outlined in the previous sections, as the selection of semiconductors is primarily a trade-off between acquisition cost and efficiency. The semiconductors introduce some limitations on the maximum possible efficiency, however, the minimum possible efficiency will be characterized by a thermal limit. Similarly the minimum size of the magnetic components will be a consequence of the thermal boundary conditions created by the cooling system design.

An optimization of heat sinks with respect to minimum weight, based on FEM, and a comparison of different materials suitable for low-weight heat sinks are presented in [47]. This optimization, however, considers only natural convection. Furthermore, the heat sink optimization presented in this work can be part of an overall converter optimization procedure and, thus, analytical expressions for the expected thermal resistance (heat sink to ambient), rather than FEM simulation results, are desirable in order to increase the evaluation speed.

Optimization procedures for complete cooling systems with respect to minimum thermal resistance are discussed in [48–51]. Lee, [48], outlines the general optimization problem and the impacts of different parameter variations (e.g. fin thickness) on the resulting thermal resistance values. Holahan, [49], refines the thermal model of the heat sink and includes the fan characteristic (static pressure versus volume flow) in the heat sink optimization. Finally, Drogenik, [50], presents a complete heat sink optimization procedure. The optimizations in [49] and [50] minimize thermal resistance in order to minimize the cooling system volume, the weight of the system is not considered. Ning [51] is the first to present an optimization procedure considering the weight of the complete cooling system, i.e. fan plus heat sink. In [51], however, only heat sink fan arrangements, which allow the air flow to bypass the heat sink, are considered. These arrangements are common in computer electronics cooling, where the airflow produced by the fan is channeled through the housing and only a fraction of the air flows through the heat sink channels. It has been shown in [48] that the lowest thermal resistance is achieved if the air is forced to flow through the heat sink

channels.

This thesis considers arrangements with ducted airflow from the fan through the heat sink channels, which creates a self-contained cooling system, common in cooling solutions for power electronics, and presents an optimization procedure that yields a minimum weight cooling system. It is based on analytical expressions and requires comparably low computational effort. Thus, the proposed procedure can directly be used as part of a complete converter weight optimization routine.

### 3.3.1 Heat Spreading

In general, the conductive thermal resistance of a material can be calculated as

$$R_{\text{th,d}} = \frac{d}{A \cdot \lambda}, \quad (3.47)$$

where  $d$  denotes the thickness,  $A$  the surface and  $\lambda$  the thermal conductivity of the material. However, an additional resistive component has to be considered if the surface area through which the heat flows changes. This additional component is referred to as spreading resistance if the surface area is increased and constriction resistance if the surface area is decreased. E.g. the spreading resistances of both the base plate and the ceramic layer of a semiconductor power module can be modeled using the simple structure shown in Fig. 3.17. It consists of a heat source shown in red with a bottom surface area  $A_s$  and a spreading material shown in light blue with area  $A_{\text{sp}}$ , thickness  $d_{\text{sp}}$  and thermal conductivity  $\lambda_{\text{sp}}$ . The rest of the thermal system shown in dark blue is modeled as a thermal resistance  $R_0$  corresponding to a constant heat transfer coefficient at the bottom surface of the spreading material. It is assumed that all the heat generated by the source is dissipated at the bottom of the cooling system, i.e. the top and the sides of the system are assumed to be adiabatic.

The calculation of the spreading resistance for the geometry in Fig. 3.17 is summarized hereafter. It is based on a paper presented by Lee et al. [52], in which a detailed derivation of the general solution to this problem can be found. This thesis uses the approximative analytical solution also presented in [52], which is reported to deviate less than 10% from the exact solution for typical parameters found in power electronics applications. Furthermore, while [52] presents ex-

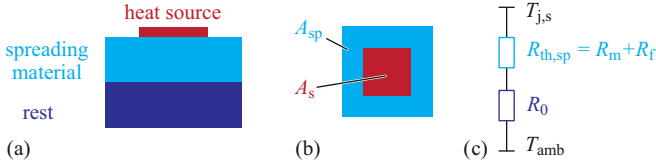


**Fig. 3.17:** Example geometry to calculate the spreading resistance. It consists of a heat source shown in red, a spreading material shown in light blue and the remaining cooling system shown in dark blue. The heat source is characterized by its bottom surface area  $A_s$ , the spreading material by its area  $A_{sp}$ , thickness  $d_{sp}$  and thermal conductivity  $\lambda_{sp}$  and the rest of the system is modeled as a thermal resistance  $R_0$ .

pressions for both maximum and average spreading resistances, only the average value is considered in this thesis.

According to [52] the total thermal resistance of the geometry shown in Fig. 3.17 can be written as

$$R_{th} = R_0 + R_m + R_f, \quad (3.48)$$

where  $R_m$  stands for the conductive resistance in the spreading material which can be calculated with (3.47) and  $R_f$  represents the spreading resistance of the spreading material. It should be noted that the heat source is assumed to have no internal thermal resistance. The thermal resistances can be expressed as

$$R_m = \frac{d_{sp}}{\lambda_{sp} A_{sp}}, \quad (3.49)$$

and

$$R_f = \frac{\Psi}{\lambda_{sp} \cdot \sqrt{A_s}}. \quad (3.50)$$

$\Psi$  is the so called dimensionless constriction resistance [52] and can be approximated by

$$\Psi = \frac{1}{2} \cdot (1 - \epsilon)^{\frac{3}{2}} \cdot \Phi_c, \quad (3.51)$$

where  $\Phi_c$  is

$$\Phi_c = \frac{\tanh(\sigma_c \tau) + \frac{\sigma_c}{B_i}}{1 + \frac{\sigma_c}{B_i} \cdot \tanh(\sigma_c \tau)} \quad (3.52)$$

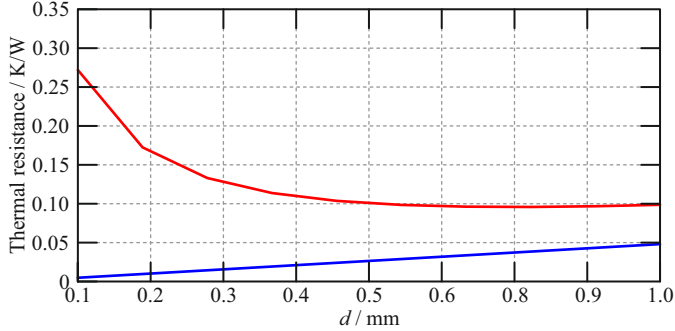


**Fig. 3.18:** Average spreading resistance  $R_{\text{th,sp}}$  in [K/W] of a copper plate as a function of its thickness  $d_{\text{sp}}$  for a given area ratio  $A_{\text{sp}} : A_{\text{s}}$  of 2 and external resistance  $R_0$  of 1K/W (red line). As comparison the material resistance  $R_{\text{th,d}}$  (i.e.  $R_{\text{m}}$ ) in [K/W] is also shown (blue line).

with

$$\epsilon = \sqrt{\frac{A_{\text{s}}}{A_{\text{sp}}}}, \quad \sigma_{\text{c}} = \pi + \frac{1}{\sqrt{\pi} \cdot \epsilon}, \quad \tau = d_{\text{sp}} \cdot \sqrt{\frac{\pi}{A_{\text{sp}}}},$$

and the Biot number,  $B_{\text{i}}$ , defined as

$$B_{\text{i}} = \frac{1}{R_0 \cdot \lambda_{\text{sp}} \cdot \sqrt{\pi A_{\text{sp}}}}. \quad (3.53)$$

Using equations (3.50) - (3.53) the thermal resistance of the spreading layer  $R_{\text{th,sp}} = R_{\text{m}} + R_{\text{f}}$  can be calculated and its dependency on different parameters can be investigated in more detail. The following Figures 3.18 - 3.19 illustrate these dependencies for a CPM2-1200-0025B bare die from Wolfspeed with  $A_{\text{s}} = 4.04 \times 6.44\text{mm}$ , which is placed on a copper base plate with  $\lambda_{\text{sp}} = 400\text{ W/m K}$ .

Fig. 3.18 shows the dependency of the spreading resistance  $R_{\text{th,sp}}$  and the material resistance  $R_{\text{th,d}}$  (i.e.  $R_{\text{m}}$ ) on the base plate thickness  $d_{\text{sp}}$ , which is varied between 0.1mm and 1mm. The area ratio  $A_{\text{sp}} : A_{\text{s}}$  is set to 2 and the external resistance  $R_0$  to 1 W/K.  $R_{\text{th,d}}$  (i.e.  $R_{\text{m}}$ ) increases proportionally to  $d_{\text{sp}}$ , which corresponds to the relationship given in (3.47). The spreading resistance on the other hand decreases with increasing plate thickness for small  $d_{\text{sp}}$ . After reaching a minimum

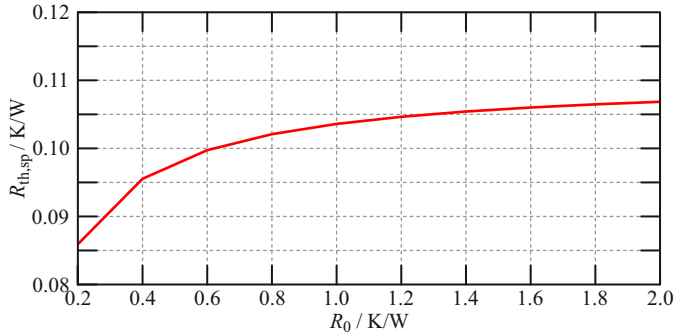


**Fig. 3.19:** Average spreading resistance  $R_{th,sp}$  in [K/W] of a copper plate as a function of the external resistance  $R_0$  for a given area ratio  $A_{sp} : A_s$  of 2 and a plate thickness  $d_{sp}$  of 0.5mm.

at around 0.8mm it starts increasing again and continues to do so more or less at the same rate as  $R_{th,d}$  (i.e.  $R_m$ ) also for thicknesses larger than 1mm. Thus, contrary to the expectation based on the material resistance the spreading resistance can be decreased by increasing  $d_{sp}$  for small plate thicknesses. Similar relations with varying optimal  $d_{sp}$  can be found for other area ratios.

Fig. 3.19 shows how the spreading resistance depends on the external resistance  $R_0$ . The plate thickness is set to 0.5mm and the area ratio to 2. In the examined range of  $R_0 = 0.2 - 2\text{K/W}$   $R_{th,sp}$  increases together with the external resistance and saturates around 0.107K/W.

This shows that the spreading resistance in a base plate of a heat sink can theoretically not be calculated independently from the thermal resistance of the heat sink fins to air. However, as long as the area ratio  $\frac{A_{sp}}{A_s}$  remains small, it typically also holds true that  $R_{th,sp} \ll R_0$  and the influence of spreading on the overall thermal resistance of the cooling system is marginal.

### 3.3.2 Forced Convection

Thermal modeling of a heat sink with fan is a multi-physics problem. The thermal modeling involves three domains: heat conduction in solids, convective heat and mass transfers, and fluid dynamics. Fig. 3.20 illustrates the design process for any forced convection cooling system, considering two heat sinks a and b, which feature different geometries.<sup>1</sup> For a defined heat sink geometry the fluid dynamic system impedance characteristic  $\Delta p_{\text{tot}}(\dot{V})$  is calculated. The impedance characteristic  $\Delta p_{\text{tot}}(\dot{V})$  correlates the static pressure difference between fluid inlet and outlet of the heat sink to the volume flow,  $\dot{V}$ , through the heat sink. The fans, listed in Tab. 3.1, provide a static pressure drop versus volume flow characteristic  $\Delta p_{\text{fan}}(\dot{V})$  (analogous to a non ideal voltage source). The intersection of the two characteristics,

$$\Delta p_{\text{fan}}(\dot{V}) - \Delta p_{\text{tot}}(\dot{V}) = 0, \quad (3.54)$$

defines the volume flow,  $\dot{V}$ , through the heat sink (analogous to a current through a resistor). The thermal resistance characteristic of the heat sink,  $R_{\text{th,S-a}}(\dot{V})$ , may be calculated as a function of the volume flow,  $\dot{V}$ , of the cooling fluid flowing through the system. As the volume flow,  $\dot{V}$ , is obtained from (3.54) and, thus, is known, each cooling system, i.e. a combination of a heat sink and a fan, can be represented by means of an equivalent thermal resistance,  $R_{\text{th,S-a}}$ , that takes the temperature difference between the heat sink interface surface and the cooling fluid at the inlet into account.

Heat conduction and convective heat and mass transfers required for the calculation of  $R_{\text{th,S-a}}(\dot{V})$  are covered first. The fluid dynamics required for the calculation of  $\Delta p_{\text{tot}}(\dot{V})$  will be detailed afterwards.

The proposed optimization procedure presented in this thesis considers a cooling system with heat sink and fan, and extends a conventional heat sink geometry, defined in Fig. 3.21(b), with an air duct, shown in Fig. 3.21(a). It further considers closed heat sink channels in order to avoid a degradation of the heat sink's thermal resistance due to flow bypass [48]. The considered thermal model, depicted in Fig. 3.21(c), assumes equal fin spacing  $s$  and fin thickness  $t$  with  $n$  channels. Therefore, and due to symmetry conditions, only one channel / fin is modeled.

---

<sup>1</sup>The dimensions of the two heat sink geometries are  $\{a,b\}$ :  $n = \{13,9\}$ ,  $c = \{25,36\}$  mm,  $L = 100$  mm,  $b = 40$  mm,  $d = 4$  mm,  $t = 1$  mm (cf. Fig. 3.21).

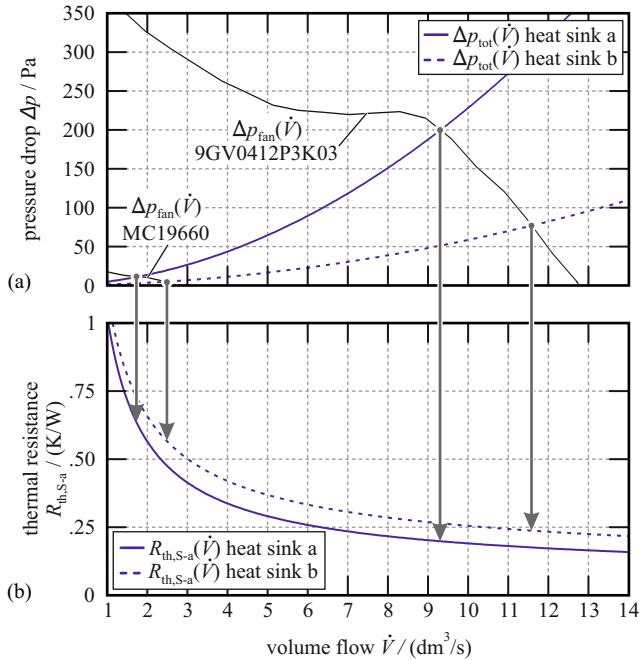


**Fig. 3.20:** Basic cooling system design process: the intersections of the heat sink impedances  $\Delta p_{\text{tot}}(\dot{V})$  of the heat sinks a and b with the characteristic of the selected fan determine the operating points, i.e. the volume flows  $\dot{V}$ , and the equivalent thermal resistances  $R_{\text{th,S-a}}$ . (a) Characteristics of the fans MC19660 and 9GV0412P3K03, and the total system impedances  $\Delta p_{\text{tot}}(\dot{V})$  for two heat sink geometries a and b. (b) Thermal resistance characteristics  $R_{\text{th,S-a}}(\dot{V})$  of the two systems a and b as functions of volume flow  $\dot{V}$ . The heat sink geometries are  $\{a, b\}$ :  $n = \{13, 9\}$ ,  $c = \{25, 36\}$  mm,  $L = 100$  mm,  $b = 40$  mm,  $d = 4$  mm,  $t = 1$  mm (cf. Fig. 3.21).

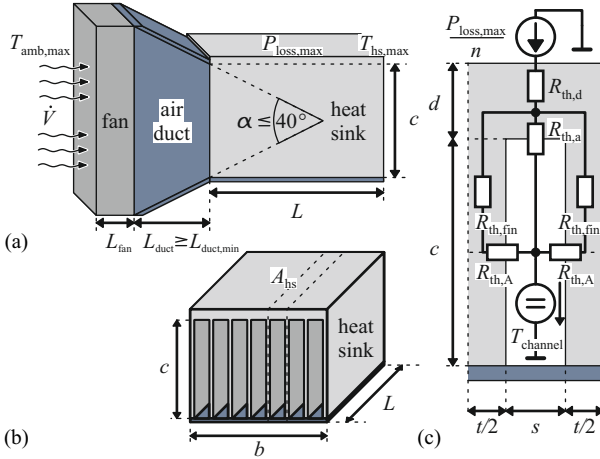


**Fig. 3.21:** (a) Cooling system model allowing for fin length optimization with air duct and bottom plate (made of PVC), which prevents air flow bypass; for the air duct a maximum angle,  $\alpha \leq 40^\circ$ , and a minimum duct length,  $L_{duct} \geq L_{duct,min}$ , is considered. (b) Geometrical model of the heat sink; the dotted lines indicate the symmetry axes used for the thermal model. (c) Heat sink thermal model; due to symmetry properties only two half fins with thicknesses  $t/2$ , left and right channel walls and one channel with height  $c$  and width  $s$  need to be considered [50].

Name	$\frac{P_{fan}}{W}$	$\frac{L_{fan}}{mm}$	$\frac{m_{fan}}{g}$	$\frac{\dot{V}_{max}}{dm^3/s}$	$\frac{\Delta p_{max}}{Pa}$
GM0504PEV2-8.GN	0.4	6	7.5	2.6	20.0
MC19660	0.5	6	7.5	2.8	25.0
BP402012H-W	1.9	20	40.0	4.0	51.7
1608VL-04W-B60-B00	1.6	20	40.0	5.4	99.3
412JHH	3.3	25	50.0	6.7	216.3
9L0412J301	3.7	28	55.0	8.5	205.1
9GA0412P6G001	2.8	20	35.0	7.1	319.2
9GV0412P3K03	10.1	28	50.0	12.7	416.2
1611FT-D4W-B86-B50	11.4	28	49.0	13.8	736.9
1619FT-04W-B86-B50	12.6	48	71.0	14.1	800.0

**Tab. 3.1:** 40 mm  $\times$  40 mm axial fans considered in the optimization.

### Thermal Model

A simple way to model the three dimensional heat conduction problem is to represent the three dimensional structure as a network of thermal resistances. To keep the thermal network as simple as possible the heat sink symmetries can be exploited, resulting in a thermal resistance network as shown Fig. 3.21(c). Solving the resistive network results in a total thermal resistance of

$$R_{\text{th,S-a}} = R_{\text{th,d}} + \frac{1}{n} \frac{(R_{\text{th,fin}} + R_{\text{th,A}})R_{\text{th,a}}}{R_{\text{th,fin}} + R_{\text{th,A}} + 2R_{\text{th,a}}} = R_{\text{th,d}} + R_{\text{th,conv}}; \quad (3.55)$$

radiation is neglected. Based on the assumption of a uniform loss distribution across the heat sink base plate area  $A_{\text{hs}} = bL$ , the thermal resistance  $R_{\text{th,d}}$  is a function of the heat sink geometry and the heat sink material's thermal conductivity  $\lambda_{\text{hs}}$ ,

$$R_{\text{th,d}} = \frac{d}{A_{\text{hs}}\lambda_{\text{hs}}}. \quad (3.56)$$

The temperature in the heat sink channels,  $T_{\text{channel}}$ , and the thermal resistances,  $R_{\text{th,fin}}$ ,  $R_{\text{th,A}}$ , and  $R_{\text{th,a}}$ , depend on the volume flow, the geometry, and the position along the longitudinal axis of the channel. According to [53] and [54], these dependencies can be accurately modeled with the single fluid heat exchanger model that summarizes the thermal resistances,  $R_{\text{th,fin}}$ ,  $R_{\text{th,A}}$ , and  $R_{\text{th,a}}$  in a single convective thermal resistance,

$$R_{\text{th,conv}} = \left[ \rho_{\text{air}} c_{\text{air}} \dot{V} \left( 1 - e^{-\frac{hA_{\text{eff}}}{\rho_{\text{air}} c_{\text{air}} \dot{V}}} \right) \right]^{-1}, \quad (3.57)$$

with the effective convective surface area  $A_{\text{eff}}$  and the fin efficiency  $\eta$  [55],

$$A_{\text{eff}} = n(2c\eta + s)L \text{ and } \eta = \frac{\tanh\left(\sqrt{\frac{2h(t+L)}{\lambda_{\text{hs}}tL}} \cdot c\right)}{\sqrt{\frac{2h(t+L)}{\lambda_{\text{hs}}tL}} \cdot c}, \quad (3.58)$$

and with the average heat transfer coefficient  $h$ , cf. (3.69), being known. The average heat transfer coefficient is predominantly a function of the fluid boundary layer velocity [54]. For viscous flow in ducts this

boundary layer velocity is a function of the average fluid velocity in the duct and the fluid viscosity  $\nu_{\text{air}}$ , which is generally described by means of non-dimensional analysis and the use of the Nusselt number, which represents the ratio of convective to conductive heat transfer [54]. The Nusselt number, however, is a function of average duct velocity, geometry, and the Prandtl number, Pr. Muzychka and Yovanovich have derived an analytical model for the Nusselt number,  $\text{Nu}_{\sqrt{A}}$ , suitable for the parallel plate fin heat sink model, which includes the effect of flow development at the inlet of a duct with arbitrary cross section [56]:

$$\text{Nu}_{\sqrt{A}} = \left[ \left( \frac{C_4 f(\text{Pr})}{\sqrt{z^*}} \right)^m + \left( \left\{ C_1 \left( \frac{f \text{Re}_{\sqrt{A}}}{8\sqrt{\pi}\epsilon^\gamma} \right) \right\}^5 + \left\{ C_2 C_3 \left( \frac{f \text{Re}_{\sqrt{A}}}{z^*} \right)^{1/3} \right\}^5 \right)^{m/5} \right]^{1/m}. \quad (3.59)$$

The required coefficients  $C_1$ ,  $C_2$ ,  $C_3$ ,  $C_4$ ,  $\gamma$ , and functions  $f(\text{Pr})$ ,  $f \text{Re}_{\sqrt{A}}$ ,  $z^*$ ,  $\epsilon$ , and  $m$ , provided in [56], are summarized below.

At the inlet of the heat channel the velocity profile at the boundary layer, i.e. the channel walls, shows a distinct dependency on the position along the longitudinal axis of the channel. As a consequence, the Nusselt number is large at the inlet of the duct, where the boundary layer velocity is large, i.e. the heat transfer coefficient  $h$  will be large. The Nusselt number decreases along the thermal entry length, [54], and settles to a constant value. The model developed in [56] describes this effect and is solved for Uniform Wall Flux (UWF) and Uniform Wall Temperature (UWT) boundary conditions. This model also accounts for the aspect ratio  $\epsilon$  of the heat sink channels and is valid for any aspect ratio  $\epsilon$ , cf. (3.66). The models employed in [50] and [51] are approximations of the Nusselt number for viscous fluid flow between two parallel plates, which are only valid for aspect ratios  $\epsilon \ll 1$ .

The presented investigation assumes UWT, due to the high thermal conductivity of the heat sink material. For UWT boundary conditions the function  $f(\text{Pr})$  is

$$f(\text{Pr}) = \frac{0.564}{[1 + (1.664 \text{Pr}^{1/6})^{9/2}]^{2/9}}, \quad (3.60)$$

and the parameters  $C_1$  and  $C_3$  are

$$C_1 = 3.24 \text{ and } C_3 = 0.409, \quad (3.61)$$

given in [56]. To calculate the average (not local) Nusselt number the parameters  $C_2$  and  $C_4$  are

$$C_2 = 3/2 \text{ and } C_4 = 2. \quad (3.62)$$

The shape parameter is

$$\gamma = -3/10 \quad (3.63)$$

for rectangular ducts. The blending parameter  $m$  is

$$m = 2.27 + 1.65 \text{ Pr}^{1/3}. \quad (3.64)$$

The model of [56] is valid for  $0.1 < \text{Pr} < \infty$ , which is valid for most heat exchanger applications. For the parallel plate fin heat sink the shape functions are

$$z^* = \frac{Ln\nu_{\text{air}}}{\text{Pr} \cdot \dot{V}} \quad (3.65)$$

and

$$\epsilon = \begin{cases} \frac{s}{c} & \text{if } s \leq c \\ \frac{c}{s} & \text{if } s > c. \end{cases} \quad (3.66)$$

The friction factor Reynolds product function,

$$f\text{Re}_{\sqrt{A}} = \left[ \frac{11.8336 \cdot \dot{V}}{Ln\nu_{\text{air}}} + \left( f\text{Re}_{\sqrt{A},\text{fd}} \right)^2 \right]^{1/2} \text{ with} \quad (3.67)$$

$$f\text{Re}_{\sqrt{A},\text{fd}} = \frac{12}{\sqrt{\epsilon}(1 + \epsilon) \left[ 1 - \frac{192}{\pi^5} \epsilon \tanh\left(\frac{\pi}{2\epsilon}\right) \right]} \quad (3.68)$$

describes the effect of the boundary layer velocity profile on the mass transfer [57]. With this and with (3.59) the heat transfer coefficient becomes

$$h = \frac{\text{Nu}_{\sqrt{A}} \lambda_{\text{air}}}{d_h} \text{ with } d_h = \frac{2sc}{s+c} \text{ and } s = \frac{b - (n+1)t}{n}. \quad (3.69)$$

Expression (3.69) enables the total thermal resistance, (3.55), to be calculated as a function of geometry and volume flow.

Fig. 3.22 shows the thermal resistances as functions of the volume flow for a particular heat sink calculated with the model in [50] (green line), the proposed model (red line), and FEM simulation. The FEM simulated thermal resistances are calculated from the maximum base

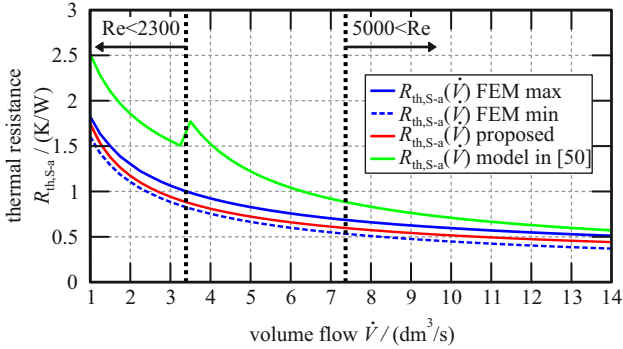


**Fig. 3.22:** Thermal resistance  $R_{\text{th,S-a}}$  as a function of volume flow  $\dot{V}$ : FEM calculated with maximum base plate temperature (at the fluid outlet, solid blue), FEM calculated with minimum base plate temperature (at the fluid inlet, dotted blue), proposed model (red), and model proposed in [50] (green), for a heat sink with dimensions  $n = 5$ ,  $L = 100$  mm,  $b = 40$  mm,  $d = 3$  mm,  $c = 30$  mm,  $t = 1$  mm, cf. Fig. 3.21.

plate temperatures (at the fluid outlet, solid blue line) and the minimum base plate temperatures (at the fluid inlet, dotted blue line). A comparison reveals, that the model in [50] significantly overestimates the thermal resistance for low volume flows. The discontinuity in the model given in [50] is caused by the discrete distinction between laminar and turbulent flow ( $\text{Re} > 2300$ ) and the use of the turbulent flow model within the transition region ( $2300 < \text{Re} < 5000$ ). The distinction between turbulent and laminar flow is essential for fully developed fluid flow. This distinction, however, only becomes valid once the fluid dynamic entry length has been reached, where the fluid flow turns from laminar to turbulent [58]. For the cooling system geometry in Fig. 3.22 the fluid dynamic entry length [54],

$$L_{\text{h}} = \frac{L_{\text{h}}^+}{\sqrt{A}} \text{Re}_{\sqrt{A}} = L_{\text{h}}^+ \frac{\dot{V}}{n\nu_{\text{air}}}, \quad (3.70)$$

with the dimensionless fluid dynamic entry length for laminar flow [54],

$$L_{\text{h}}^+ = 0.0822\epsilon(1 + \epsilon)^2 \left[ 1 - \frac{192\epsilon}{\pi^5} \tanh\left(\frac{\pi}{2\epsilon}\right) \right], \quad (3.71)$$

is  $L_h = 650$  mm at  $Re = 2300$  and  $L_h = 1425$  mm at  $Re = 5000$ . Therefore, turbulent flow will not develop over the whole length  $L = 100$  mm  $\ll L_h$  of the heat sinks presented in this work.

### Fluid Dynamic Model

The sole purpose of the fluid dynamic model is to determine the volume flow  $\dot{V}$ , which is an input of the thermal model [in particular (3.57)] and generated by the selected fan. Literature review reveals that different phenomena affect the relation between the total static pressure drop,  $\Delta p_{\text{tot}}$ , and the volume flow for a given heat sink. All these effects are functions of geometry and average air speed. In [50] only the apparent friction factor,  $f_{\text{app}}$ , is considered and approximated as the friction factor for fully developed fluid flow between two parallel plates, which turns out to insufficiently predict the actual pressure drop and volume flow. The apparent friction factor,  $f_{\text{app}}$ , is approximately the same as the friction factor for fully developed fluid flow if the duct length is greater than 10 times the fluid dynamic entry length,  $L \gtrsim 10L_h$  [54], which, however, is not fulfilled in commonly used heat sink geometries. Improved fluid dynamic models are proposed in [57,59,60]. References [59] and [60] include the effects of sudden contraction at the inlet and sudden expansion at the outlet, based on [58], and the effects of developing fluid flow [57]. In addition, the conservation of momentum needs to be considered, in order to account for the fluid acceleration in the air duct and the heat sink. Respective literature is found in [58,61–63].

The total cooling system static pressure drop is the sum of all the pressure drop contributions expressed as functions of the volume flow,

$$\Delta p_{\text{tot}}(\dot{V}) = \Delta p_{\text{hs}}(\dot{V}) + \Delta p_{\text{duct}}(\dot{V}) + \Delta p_{\text{acc}}(\dot{V}), \quad (3.72)$$

with  $\Delta p_{\text{hs}}$ ,  $\Delta p_{\text{duct}}$ , and  $\Delta p_{\text{acc}}$  denoting the static pressure drop due to fluid friction of the heat sink,  $\Delta p_{\text{hs}}$ , due to fluid friction of the air duct,  $\Delta p_{\text{duct}}$ , and due to frictionless fluid flow acceleration,  $\Delta p_{\text{acc}}$ , respectively.

The pressure drop  $\Delta p_{\text{hs}}$ ,

$$\Delta p_{\text{hs}}(\dot{V}) = \left( f_{\text{app}}(\dot{V}) \frac{L}{d_h} + K_{\text{se}} + K_{\text{sc}} \right) \cdot \frac{\rho}{2} \bar{U}_{\text{hs}}^2(\dot{V}), \quad (3.73)$$

consists of the friction factors for sudden contraction and sudden ex-

pansion [58, 59, 62],

$$K_{\text{se}} = \left(1 - \frac{d_h^2}{D_h^2}\right)^2 = \left(1 - \left(1 - \frac{(n+1)t}{b}\right)^2\right)^2, \quad (3.74)$$

$$K_{\text{sc}} \approx 0.42 \left(1 - \frac{d_h^2}{D_h^2}\right) = 0.42 \left(1 - \left(1 - \frac{(n+1)t}{b}\right)^2\right), \quad (3.75)$$

and the apparent friction factor for viscous fluid flow in ducts with arbitrary cross sections [57],

$$f_{\text{app}}(\dot{V}) = \frac{f\text{Re}_{\sqrt{A}}(\dot{V})}{\text{Re}_{\sqrt{A}}(\dot{V})} = \frac{n\nu_{\text{air}}\sqrt{cs}}{\dot{V}} \cdot f\text{Re}_{\sqrt{A}}(\dot{V}). \quad (3.76)$$

Noteworthy to mention at this point is the importance of the friction factor Reynolds product,  $f\text{Re}_{\sqrt{A}}(\dot{V})$  [cf. (3.67)]. The friction factor Reynolds product appears in both the thermal, (3.59), and the fluid dynamic models, (3.73), because it describes the interactions between the fluid in motion and the channel walls. An increase in  $f\text{Re}_{\sqrt{A}}(\dot{V})$  denotes an increase in mass transfer, which results in a greater heat transfer, i.e.  $\text{Nu}_{\sqrt{A}}$  increases, but also an increase of the friction at the channel walls. Consequently, a direct tradeoff between heat transfer and required pressure drop exists, as an increased mass transfer simultaneously increases the heat transfer coefficient,  $h$ , and the apparent friction factor  $f_{\text{app}}$ , cf. (3.69) and (3.76).

The pressure drop  $\Delta p_{\text{duct}}$ ,

$$\Delta p_{\text{duct}}(\dot{V}) = \left(f_{\text{app,duct}}(\dot{V}) \frac{L_{\text{duct}}}{\bar{d}_{\text{h,duct}}} \frac{1}{4} + K_{\text{venturi}}\right) \cdot \frac{\rho}{2} \bar{U}_{\text{duct}}^2(\dot{V}), \quad (3.77)$$

consists of the apparent friction factor for the average duct hydraulic diameter,  $f_{\text{app,duct}}$  [57], and the friction factor for a Venturi nozzle  $K_{\text{venturi}}$  [58],

$$f_{\text{app,duct}}(\dot{V}) = \frac{\nu_{\text{air}}\sqrt{b(b+c)}}{\sqrt{2}\dot{V}} \cdot \left[\frac{11.8336\dot{V}}{L_{\text{duct}}\nu_{\text{air}}} + \left(f\text{Re}_{\sqrt{A},\text{fd}}\right)^2\right]^{1/2}, \quad (3.78)$$

$$\bar{d}_{\text{h,duct}} = \frac{2b(b+c)}{3b+c}, \quad L_{\text{duct}} = \max\left[\frac{b-c}{2\tan(\alpha)}, L_{\text{duct,min}}\right], \quad (3.79)$$

$$\epsilon_{\text{duct}} = \frac{b+c}{2c}, \text{ and } K_{\text{venturi}} \approx 0.2. \quad (3.80)$$

A minimal air duct length  $L_{\text{duct,min}}$  is recommended, since the commonly used assumption that the fan produces an evenly distributed laminar inflow pattern cannot be true, because no air can flow through the hub of the fan. The air flow and pressure distributions produced by the fan require a certain air duct length to form the assumed inflow conditions. The influence of this fan system effect, however, is poorly documented, but commercially available products reveal its importance, e.g. the only difference between the cooling aggregates LA 6 and LA V 6, manufactured by Fischer Elektronik, is a 3 cm air duct between the fan and heat sink but this air duct reduces the thermal resistance by approximately 13%. This work considers a minimal duct length of  $L_{\text{duct,min}} = 3$  cm, in order to reduce the degradation of the fan static pressure drop characteristic,  $\Delta p_{\text{fan}}$ , due to fan system effects. The friction factor for the Venturi nozzle  $K_{\text{venturi}}$  is a function of the air duct shape and increases with the duct angle  $\alpha$ ,  $K_{\text{venturi}} \in [0.04, 0.5]$  [58]. In this work an air duct angle of  $0 \leq \alpha \leq 40^\circ$  is considered, and thus, the contribution of  $\Delta p_{\text{duct}}$  to the total static pressure drop,  $\Delta p_{\text{tot}}$ , is small. However, without an air duct, i.e. if the fan is directly mounted to the heat sink, the static pressure drop generated by the fan may be considerably reduced.

The average velocities of the cooling fluid are given as functions of the volume flow,

$$\bar{U}_{\text{hs}}(\dot{V}) = \frac{\dot{V}}{nsc} \quad \text{and} \quad \bar{U}_{\text{duct}}(\dot{V}) = \frac{\dot{V}}{bc}, \quad (3.81)$$

where  $\bar{U}_{\text{hs}}(\dot{V})$  is the average velocity in the channels and  $\bar{U}_{\text{duct}}(\dot{V})$  is the velocity at the output of the duct.

Conservation of momentum for the cooling fluid flowing through the air duct and heat sink [58, 61–63], gives the pressure drop for the frictionless fluid flow acceleration,

$$\Delta p_{\text{acc}}(\dot{V}) = \left[ \frac{1}{A_{\text{min}}^2} - \frac{1}{A_{\text{src}}^2} \right] \frac{\rho}{2} \dot{V}^2 = \left[ \frac{1}{(nsc)^2} - \frac{1}{b^4} \right] \frac{\rho}{2} \dot{V}^2, \quad (3.82)$$

where  $A_{\text{min}}$  is the minimum cross-sectional area the fluid flows through and  $A_{\text{src}}$  is the cross-sectional area of the pressure source, i.e. the fan.

Fig. 3.23 (a) shows the contributions of the different effects causing the total cooling system static pressure drop for an example cooling

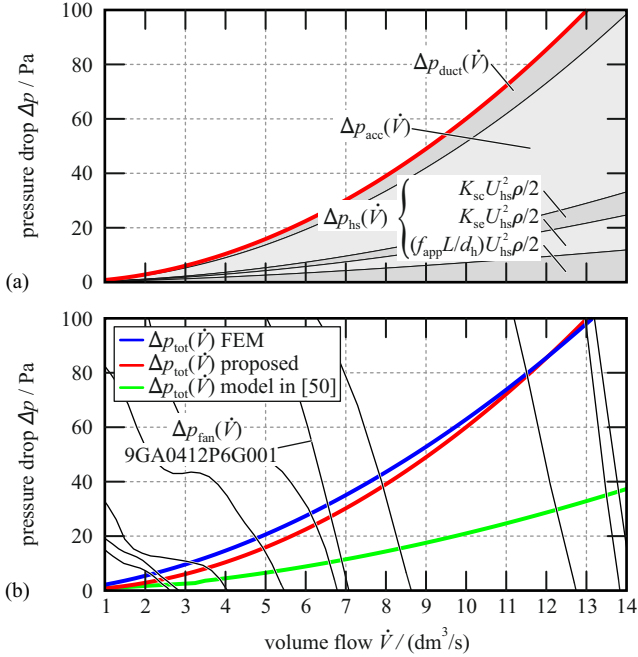


**Fig. 3.23:** Cooling system static pressure drop  $\Delta p_{\text{tot}}$  as a function of volume flow  $\dot{V}$ : (a) the shaded areas from bottom to top show the contributions of apparent friction factor  $f_{\text{app}}$ , sudden expansion  $K_{\text{se}}$ , sudden contraction  $K_{\text{sc}}$ , conservation of momentum  $\Delta p_{\text{acc}}$ , and the friction of the air duct  $\Delta p_{\text{duct}}$ ; (b) FEM simulation results (blue), proposed model (red), and model in [50] (green). The solid black lines denote the static pressure drop characteristics of the fans listed in Tab. 3.1. The heat sink dimensions are:  $n = 5$ ,  $L = 100$  mm,  $b = 40$  mm,  $d = 3$  mm,  $c = 30$  mm,  $t = 1$  mm.

system with dimensions:  $n = 5$ ,  $L = 100$  mm,  $b = 40$  mm,  $d = 3$  mm,  $c = 30$  mm,  $t = 1$  mm. The shaded areas from bottom to top are the contributions of the following effects: apparent friction  $f_{\text{app}}$ , sudden expansion  $K_{\text{se}}$ , sudden contraction  $K_{\text{sc}}$ , conservation of momentum  $\Delta p_{\text{acc}}$ , and friction of the duct  $\Delta p_{\text{duct}}$ .

Fig. 3.23 (b) shows the total static pressure drop as a function of the volume flow calculated with the proposed fluid dynamic model (red line), the fluid dynamic model in [50] (with fitting factor  $k$ , green line),

and FEM simulation results (blue line).

### Experimental Verification

The results obtained with the proposed thermal and fluid dynamic model and the model in [50] are compared to FEM simulation results and to experimental results, in order to present the improvements achieved with the analytical model. Based on the assumption that the most accurate calculations of thermal resistance, volume flow, and pressure drop are feasible with FEM simulations, a large number of FEM simulations is used as basis for the evaluation.

The utilized 3-D FEM simulation software is COMSOL Multiphysics. Exploiting all symmetries only half a fin and half a channel is modeled. The Conjugate Heat Transfer (ntif) module is used with air and aluminum provided in the standard library. The boundary conditions for the fluid dynamic problem are: “no slip” at the heat sink channel wall, “symmetry” at the channel midplane, “symmetry” in the air duct at the channel midplane and the fin midplane, “Pressure, no viscous stress” at the channel outlet, and “laminar inflow” enforcing a flow rate of  $\dot{V}/(2n)$  at the fan inlet. The boundary conditions for the heat transfer in solids are: a “total heat flux” of  $80\text{ W}/(2n)$  at the base plate surface, “symmetry” at the channel midplane, “symmetry” at the fin midplane, an “inflow heat flux” of  $0\text{ W}/\text{m}^2$  with an external temperature of  $30\text{ }^\circ\text{C}$  at the fan inlet, and the “outflow” at the channel outlet. The mesh settings are: “Physics-controlled mesh” with a “Coarse” element size. The study is a “Parametric sweep” of the parameter volume flow  $\dot{V} \in [1, 14]\text{ dm}^3/\text{s}$ , with a linear step size of  $0.25\text{ dm}^3/\text{s}$ . From the “Parametric sweep” the heat sink system characteristics  $\Delta p_{\text{tot}}(\dot{V})$  and  $R_{\text{th,S-a}}(\dot{V}) = (T_{\text{hs,max}} - 30\text{ }^\circ\text{C})/80\text{ W}$  are extracted, where  $T_{\text{hs,max}}$  is the maximum temperature on the base plate surface.

The fluid dynamic models, which determine the operating point of the fan, are needed to evaluate the thermal model, in particular (3.57), and are discussed first. Figs. 3.24 and 3.25 show the operating points calculated for all combinations of all 10 considered fans in Tab. 3.1 and 72 different heat sink geometries with parameters in the range of  $L \in [60\text{ mm}, 100\text{ mm}]$ ,  $n \in [5, 13]$ ,  $c \in [10\text{ mm}, 37\text{ mm}]$ ,  $b = 40\text{ mm}$ ,  $t = 1\text{ mm}$ , and  $\dot{V} \in [1\text{ dm}^3/\text{s}, 14\text{ dm}^3/\text{s}]$ , i.e. 720 different cooling systems. The operating point is determined by equalizing the cooling system static pressure drop and the fan characteristic (the fan characteristics are obtained from data sheets).

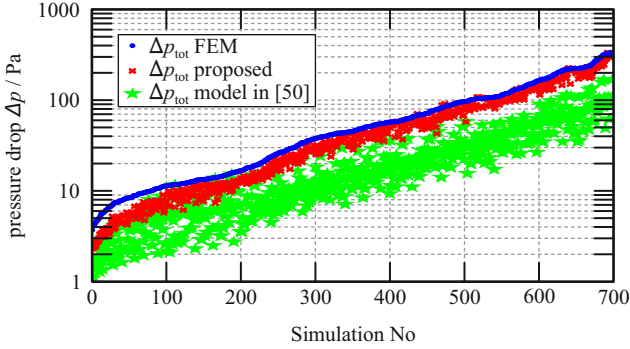


**Fig. 3.24:** Comparison of the total static pressure drop  $\Delta p_{\text{tot}}$  at the operating points of the fans listed in Tab. 3.1. The geometry parameters of the considered cooling systems are in the range of  $L \in [60 \text{ mm}, 100 \text{ mm}]$ ,  $n \in [5, 13]$ ,  $c \in [10 \text{ mm}, 37 \text{ mm}]$ ,  $b = 40 \text{ mm}$ ,  $t = 1 \text{ mm}$ . Blue dots: FEM simulation results, green dots: results calculated with the cooling system model in [50], and red crosses: proposed cooling system model.

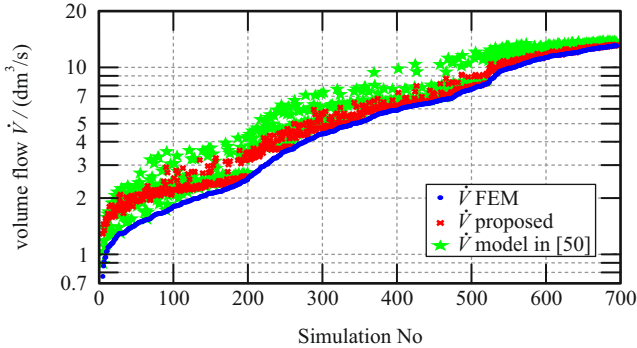


**Fig. 3.25:** Comparison of the static volume flows  $\dot{V}$  at the operating points of the fans listed in Tab. 3.1. The geometry parameters of the considered cooling systems are in the range of  $L \in [60 \text{ mm}, 100 \text{ mm}]$ ,  $n \in [5, 13]$ ,  $c \in [10 \text{ mm}, 37 \text{ mm}]$ ,  $b = 40 \text{ mm}$ ,  $t = 1 \text{ mm}$ . Blue dots: FEM simulation results, green dots: results calculated with the cooling system model in [50], and red crosses: proposed cooling system model.

In Figs. 3.24–3.27 and Fig. 3.29 the results of the FEM simulations are marked with blue dots, the results of the proposed model with red crosses and the results of the model in [50] with green stars. For a better graphic representation the results in Figs. 3.24–3.27 are sorted in different orders, such that the blue line (FEM simulation results) is monotonic.

Fig. 3.24 shows a high correlation for the pressure drop of the proposed model and the FEM simulation with a mean deviation of

$$\sigma_{\Delta p_{\text{tot}}} = \frac{1}{k} \sum_{i=1}^k \frac{|\Delta p_{\text{tot,FEM},i} - \Delta p_{\text{tot,model},i}|}{\Delta p_{\text{tot,FEM},i}} = 21\%, \quad (3.83)$$

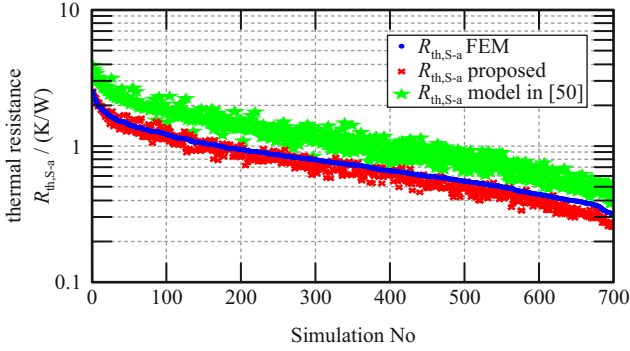
( $k = 720$ ), whereas the previous cooling system model of [50] gives a mean deviation of  $\sigma_{\Delta p_{\text{tot}}} = 64.3\%$ .

Fig. 3.25 shows the volume flows determined at the calculated operating points. The mean deviations between simulated and calculated results are 14.6% for the proposed model and 24.7% for the model detailed in [50].

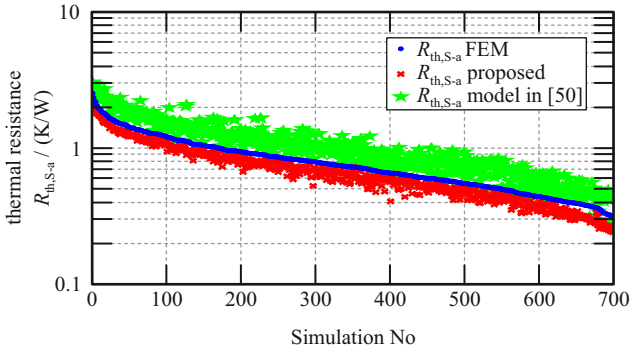
Fig. 3.26 depicts the expected thermal resistances if the operating points are determined based on the pressure drop versus volume flow characteristics obtained by means of FEM simulations. This facilitates a direct comparison of the 3 thermal models and excludes the interaction of the fluid dynamic and thermal models. The mean deviations between simulated and calculated results are 9.9% for the proposed model and 45.7% for the previous model [50].

Fig. 3.27, finally, compares the expected thermal resistances of the combined fluid dynamic and thermal models. The mean deviations are 15% for the proposed model and 30.3% for the previous model [50].

Twelve experimental cooling systems, listed in Tab. 3.2, are used to verify the theoretical considerations presented above. The twelve cooling systems consist of three different heat sinks featuring the same base plate thicknesses,  $d = 3$  mm, and fin thickness,  $t = 1$  mm. The heat sinks differ in length, fin length, and number of channels  $\{L, c, n\} = \{\{60 \text{ mm}, 37 \text{ mm}, 8\}, \{60 \text{ mm}, 25 \text{ mm}, 9\}, \{80 \text{ mm}, 37 \text{ mm}, 13\}\}$ . The thermal resistances are measured for each combination of the 3 heat sinks and 4 different fans (GM0504PEV2-8.GN, MC19660, 9GA0412P6G001, 1611FT-D4W-B86-B50) to obtain twelve cooling systems.



**Fig. 3.26:** Comparison of the thermal resistance values  $R_{\text{th},S-a}$  at the operating points of the fans, listed in Tab. 3.1, being determined by the FEM fluid dynamic model. The geometry parameters of the considered cooling systems are in the range of  $L \in [60 \text{ mm}, 100 \text{ mm}]$ ,  $n \in [5, 13]$ ,  $c \in [10 \text{ mm}, 37 \text{ mm}]$ ,  $b = 40 \text{ mm}$ ,  $t = 1 \text{ mm}$ . Blue dots: FEM simulation results, green dots: results calculated with the cooling system model in [50], and red crosses: proposed cooling system model.



**Fig. 3.27:** Comparison of the thermal resistance values  $R_{\text{th},S-a}$  at the operating points of the fans, listed in Tab. 3.1, being determined by the corresponding fluid dynamic models. The geometry parameters of the considered cooling systems are in the range of  $L \in [60 \text{ mm}, 100 \text{ mm}]$ ,  $n \in [5, 13]$ ,  $c \in [10 \text{ mm}, 37 \text{ mm}]$ ,  $b = 40 \text{ mm}$ ,  $t = 1 \text{ mm}$ . Blue dots: FEM simulation results, green dots: results calculated with the cooling system model in [50], and red crosses: proposed cooling system model.

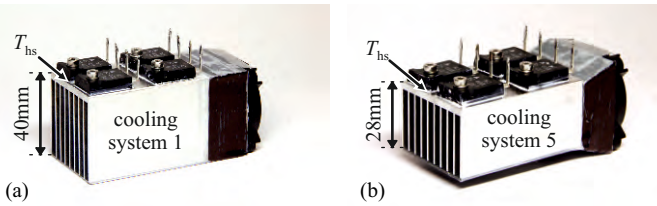


**Fig. 3.28:** Pictures of the realized cooling systems.  $T_{hs}$  indicates the location for the temperature measurement.

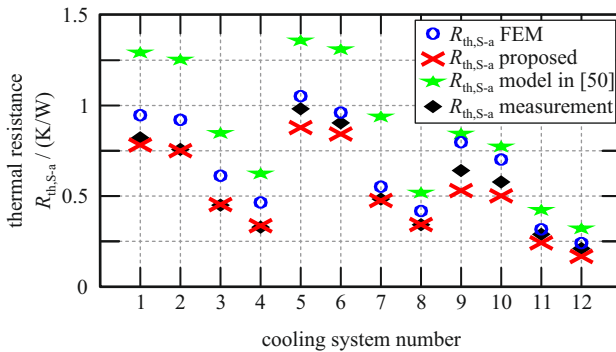


**Fig. 3.29:** Comparison of measurements (black diamonds) to the results obtained from FEM simulations (blue dots), the cooling system model given in [50] (green stars), and the proposed cooling system model (red crosses), [cf. Tab. 3.2].

Four  $100\ \Omega$  resistors are mounted to the base plates of each heat sink in order to provide defined heat fluxes. The base plate temperatures,  $T_{hs}$ , are measured at the surfaces as indicated in Figs. 3.28(a) and (b) with type-K thermocouples. The cooling system is mounted on a hollow cardboard box and covered with thermally insulating material to reduce measurement errors due to heat conduction to the supporting table, natural convection, and radiation.

Fig. 3.29 summarizes the results obtained from measurements, FEM simulations, the proposed analytical model, and the model detailed in [50]. The mean deviations are 19.5% for FEM, 8% for the new model, and 58% for the model of [50].

heat sink dimensions			
Fin length $c$	37 mm	25 mm	37 mm
Heat sink length $L$	60 mm	60 mm	80 mm
Number of channels $n$	8	9	13
40 mm $\times$ 40 mm axial fan	cooling system number		
GM0504PEV2-8.GN	1	5	9
MC19660	2	6	10
9GA0412P6G001	3	7	11
1611FT-D4W-B86-B50	4	8	12

**Tab. 3.2:** Experimental cooling systems ( $d = 3$  mm,  $t = 1$  mm).

### 3.3.3 Cooling System Optimization

The algorithm of the optimization procedure, illustrated in Fig. 3.30, yields a minimum weight cooling system and, additionally, satisfies design and manufacturability constraints. Its main input parameters are a list of considered fans, the required base plate area,  $A_{\text{hs}}$ , and the maximum allowable thermal resistance of the cooling system,

$$R_{\text{th,S-a,max}} = \frac{T_{\text{hs,max}} - T_{\text{amb,max}}}{P_{\text{loss,max}}}, \quad (3.84)$$

with maximum base plate temperature of the heat sink,  $T_{\text{hs,max}}$ , maximum ambient temperature specified,  $T_{\text{amb,max}}$ , and maximum thermal flux transmitted to the heat sink's base plate,  $P_{\text{loss,max}}$ .

The thickness of the base plate is set to the minimum possible value in order to achieve a low weight of the heat sink. In this work the minimum thickness is  $d = 3$  mm in order to facilitate sufficient mechanical stability and depth for the M3 threads that are needed to mount the components onto the heat sink. Despite the thin base plate, a constant and homogeneous temperature  $T_{\text{hs,max}}$  all over the surface of the base plate is considered, due to the high thermal conductivity material, i.e. aluminum, employed. Moreover, the components mounted to the heat sink are assumed to cover large parts of the available surface, as shown in Figs. 3.28(a) and (b), in order to achieve a well-balanced distribution of the thermal flux across the surface of the base plate. The procedure detailed in [50] sets the width  $b$  of the heat sink equal to the width of the fan employed. The air duct allows for a variable fin length

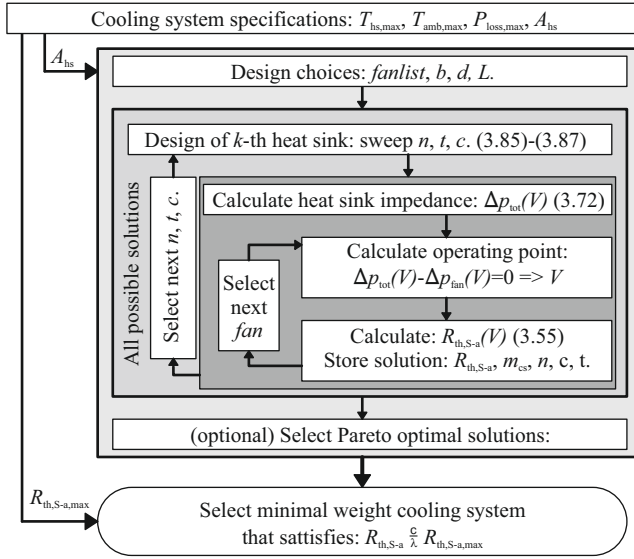


**Fig. 3.30:** Proposed cooling system optimization procedure for minimum weight cooling system that satisfies  $R_{th,S-a} \leq R_{th,S-a,max}$ . The calculated weight  $m_{cs}$  is the sum of the weight of all the components, i.e. heat sink, fan, air duct, and bottom plate.

$c$  and adds an additional degree of freedom. The presented procedure considers a height of the heat sink,  $c+d$ , equal to or less than the height of the fan. The total area requirement of all components (including any additional space for placement, e.g. due to isolation requirements), defines the length of the heat sink,  $L = A_{hs}/b$ .

Thus, the variables remaining for optimization are: the number of channels,  $n$ , the fin thickness,  $t$ , and the fin length,  $c$ , which are constrained by the manufacturing technology available. The presented cooling systems are manufactured with CNC-machines and, thus, a minimum fin thickness of 1 mm and a minimum channel width,  $s$ , of 1 mm apply.

In an initial step, the optimization procedure selects a list of fans. The fan list consists of fans with equal widths and contains the fan's width, height, weight, and pressure drop characteristic. Further, the geometry parameters defined by the fan, i.e.  $b$  and  $L$ , are set. In a

second step, an outer loop sweeps all possible heat sink geometries given by

$$1 \leq n \leq \left\lfloor \frac{b - t_{\min}}{s_{\min} + t_{\min}} \right\rfloor, \quad (3.85)$$

$$t_{\min} \leq t \leq \frac{b - ns_{\min}}{n + 1}, \quad (3.86)$$

$$c_{\min} \leq c \leq b - c, \quad (3.87)$$

where  $c_{\min}$  can be chosen arbitrarily. With the heat sink and duct geometries defined, the fluid dynamic system impedance characteristic  $\Delta p_{\text{tot}}(\dot{V})$  is calculated. An inner loop calculates the operating point of the fan, the resulting thermal resistance  $R_{\text{th,S-a}}$ , and the total weight  $m_{\text{cs}}$  of the particular combination of heat sink, fan, air duct and bottom plate. The solutions are stored in a solution database.

To reduce storage space of the solution database all suboptimal solutions are excluded, i.e. all solutions which feature non-minimal thermal resistances  $R_{\text{th,S-a}}$  for a given mass  $m_{\text{cs}}$  are excluded. The algorithm, finally, picks that particular entry of the result database, which features minimum weight and satisfies  $R_{\text{th,S-a}} \leq R_{\text{th,S-a,max}}$ . This entry represents the optimal cooling system design [within the constraints and accuracies resulting from the list of considered fans, cf. Tab. 3.1, and the accuracies due to limited resolutions of the sweeps (3.86) and (3.87)].

### Improvements achieved with variable fin length

The cooling system of Fig. 3.21(a) adds an air duct between the fan and the heat sink and, thus, allows a variable fin length of the heat sink. An air duct built of light weight materials can be beneficial, because a reduction of the fin length reduces the weight of the heat sink, decreases the average thermal resistance of the fin,  $R_{\text{th,fin}}$ , and increases the velocity of the air inside the channels, which, in turn increases the heat transfer coefficient  $h$  between the aluminum channel walls and the air. A reduction of the fin length, however, reduces the effective surface of the fins, which counteracts the decrease of the thermal resistance between the fins and the air. The air duct, finally, causes an additional pressure drop and a slight increase of the total weight and the volume of the cooling system. With the model presented in this thesis the impact

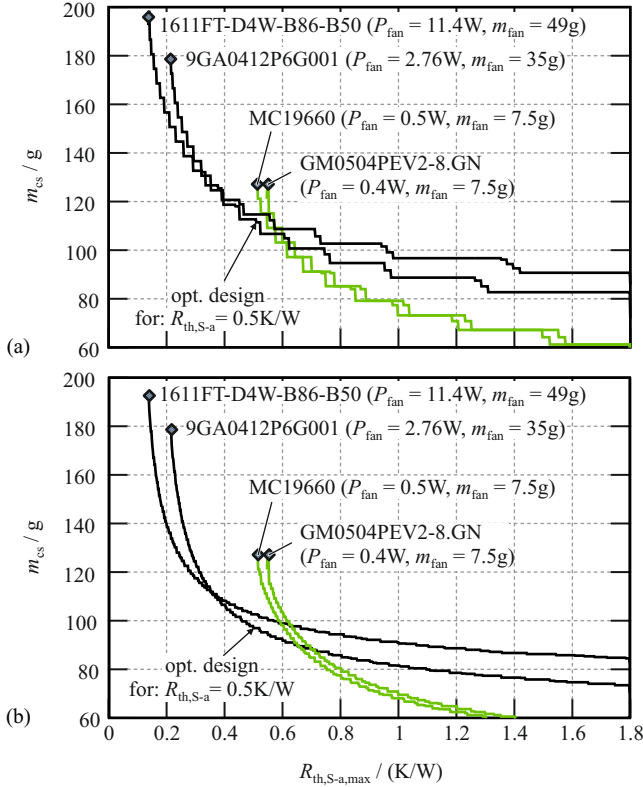


**Fig. 3.31:** Optimization results for  $R_{th,S-a,max} \in [0, 1.8]$  K/W considering 4 fans,  $A_{hs} = 40$  mm x 60 mm, and  $d = 3$  mm: (a) Fin length constrained to  $c = 37$  mm. (b) Optimal fin length selected.

of a variable fin length on the thermal resistances of the heat sink can be easily analyzed.

Fig. 3.31 (a) depicts the total weights of optimized cooling systems with  $A_{hs} = 40$  mm x 60 mm, a constant fin length of  $c_{min} = 37$  mm for 4 different fans, and different values of  $R_{th,S-a,max}$ ; steps occur in the plots as a result of the discrete number of channels,  $n$ . According to these results, the low power fans (MC19660 and GM0504PEV2-8.GN) yield lighter cooling systems for  $R_{th,S-a,max} > 0.6$  K/W due to the lower weights of the fans. These fans, however, fail to realize cooling systems

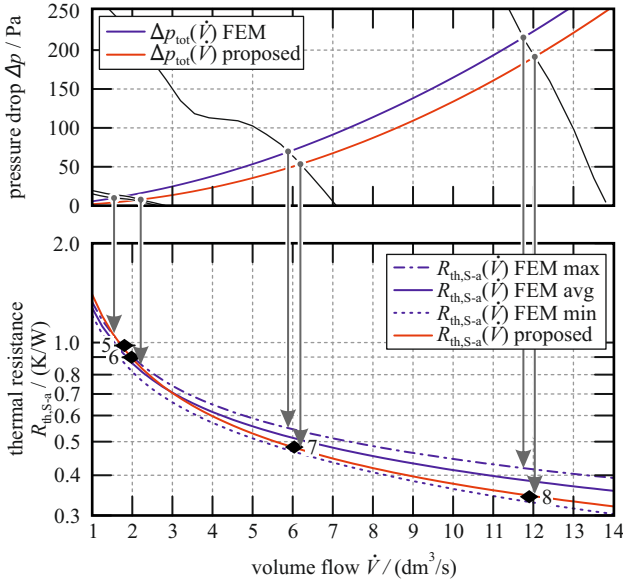
with low thermal resistances, i.e. no solutions result for  $R_{\text{th,S-a,max}} < 0.5 \text{ K/W}$ , due to limited air flow capabilities. The fans 9GA0412P6G001 ( $P_{\text{fan}} = 2.76 \text{ W}$ ) and 1611FT-D4W-B86-B50 ( $P_{\text{fan}} = 11.4 \text{ W}$ ) cause the total weight to increase for  $R_{\text{th,S-a,max}} > 0.6 \text{ K/W}$  and are, thus, better suited for low maximum thermal resistances,  $R_{\text{th,S-a,max}} < 0.6 \text{ K/W}$ .

Fig. 3.31 (b) shows the total weights of the same cooling systems with the optimal fin lengths being selected. The extended cooling system model clearly indicates the combination of heat sink and fan, which results in the minimum weight cooling system, e.g. the 9GA0412P6G001 fan is the optimal combination for  $0.35 \text{ K/W} < R_{\text{th,S-a,max}} < 0.65 \text{ K/W}$ . A comparison of Figs. 3.31 (a) and (b) reveals the weight reduction achievable with the extended cooling system model, e.g. for  $R_{\text{th,S-a,max}} = 0.5 \text{ K/W}$  the total weight is reduced by 14 % (97 g instead of 113 g).

According to the results attained in this section the proposed model is considerably better suited for weight optimization than the previous model in [50], as it more accurately models the behaviour of the fluid dynamic and thermal characteristics,  $\Delta p_{\text{tot}}(\dot{V})$  and  $R_{\text{th,S-a}}(\dot{V})$ . The fluid dynamic model includes the most important phenomena, i.e. fluid friction at the walls, sudden contraction, sudden expansion, and conservation of momentum. The main improvements of the thermal model are: the use of a single fluid heat exchanger model (3.57) (instead of a convective model [50]), the use of a fin efficiency model (3.58), and the use of the Nusselt number model (3.59), developed in [56].

The measurement results demonstrate a very good matching of calculated, FEM simulated, and measured results for the realized cooling systems. The great difference between the calculation of the thermal resistance,  $R_{\text{th,S-a}}$ , by means of FEM simulations and analytical modeling, lies in the computational time required to achieve an optimization result: the analytical model requires less than 20 seconds on a personal computer to evaluate 2000 geometries with the 10 fans listed in Tab. 3.1, whereas FEM simulations often require hours to determine the results for a single geometry. The accuracies of the thermal resistances,  $R_{\text{th,S-a}}$ , calculated with the proposed thermal model are found to be similar to the accuracies of the results obtained from thermal 3-D FEM simulations if both, thermal model and FEM simulation, are conducted for the same (predetermined) volume flow. With thermal 3-D FEM simulations, however, additional details may be obtained, e.g. hot spot temperatures on the heat sink's interface surface.<sup>2</sup>

<sup>2</sup>If required, the proposed thermal model can be extended with respect to heat



**Fig. 3.32:** Comparison of measured cooling systems 5–8, (black diamonds), cf. Tab. 3.2, to the thermal and fluid dynamic characteristics,  $\Delta p_{\text{tot}}(\dot{V})$  and  $R_{\text{th,S-a}}(\dot{V})$ , attained with FEM simulation results and the proposed cooling system model.

Fig. 3.32 shows the pressure drop and thermal characteristics,  $\Delta p_{\text{tot}}(\dot{V})$  and  $R_{\text{th,S-a}}(\dot{V})$ , of the measured cooling systems 5–8, cf. Tab. 3.2, obtained by 3-D FEM simulation and the analytical model. As FEM simulation results provide a temperature distribution instead of thermal resistances, the maximum, mean, and minimal temperatures on the heat sink’s interface surface are translated into equivalent thermal resistances. For the cooling systems 5 and 6 the FEM simulated and the calculated thermal resistance characteristics,  $R_{\text{th,S-a}}(\dot{V})$  (the blue and the red curves in Fig. 3.32), are almost identical. The differences between the FEM simulated and the calculated thermal resistance values for the cooling systems 5 and 6, shown in Fig. 3.29, can be explained by differences in simulated and calculated pressure drops  $\Delta p_{\text{tot}}(\dot{V})$ , which lead to different volume flows and thermal resistances. The thermal resis-

spreading effects, e.g. using the approach presented in [52].

tances,  $R_{\text{th,S-a}}(\dot{V})$ , of the cooling systems employing the fans MC19660 and GM0504PEV2-8.GN, i.e.  $\{1, 2, 5, 6, 9, 10\}$ , are found to be particularly sensitive to minor errors in the estimations of  $\Delta p_{\text{tot}}(\dot{V})$ . For these systems, a change of the fan speed of  $\pm 10\%$ , which is achieved by changing the supply voltage by  $\pm 10\%$ , considerably changes the resulting thermal resistance. The thermal resistance measured for cooling system number 6, for example, would match the FEM simulation result if the rotational speed of the corresponding fan, MC19660, is 10% lower; if this fan rotates 10% faster, the measurement would match the calculated result.<sup>3</sup>

Fig. 3.32 shows that the calculation of the volume flow is less sensitive on an error of the calculated or simulated pressure drop for cooling system 7, since, at the intersection point, the slope of the characteristic of the corresponding fan,  $d[\Delta p_{\text{fan}}(\dot{V})]/d\dot{V}$ , is greater than for the cooling systems 5 and 6. The same holds for cooling system 8. This can be explained based on the fan affinity laws, since, for a given fan diameter (which is the same for all fans considered in this work), the volume flow increases linearly with the revolution speed and the pressure drop increases quadratically with the revolution speed [64].

According to the results obtained from 3-D FEM simulations the cooling systems 7 and 8 (volume flows between  $\dot{V} = [5, 12]\text{dm}^3/\text{s}$ ) and for  $P_{\text{loss}} = 80\text{ W}$ , the differences between the base plate temperatures near the outlet,  $T_{\text{hs,max}}$ , and near the inlet,  $T_{\text{hs,min}}$ , are in the range  $T_{\text{hs,max}} - T_{\text{hs,min}} = [6.3, 6.8]^\circ\text{C}$ . The corresponding maximum temperature rises of the heat sink,  $T_{\text{hs,max}} - T_{\text{amb}} = [47.2, 33.1]^\circ\text{C}$ , decrease by approximately 21% if the volume flow increases from  $5\text{ dm}^3/\text{s}$  to  $12\text{ dm}^3/\text{s}$ . Thus, for heat sinks with comparably low thermal resistance,  $R_{\text{th,S-a}}$ , achieved by means of a high volume flow, heat spreading effects may have a considerable impact on the total thermal resistance and should be considered, e.g. according to [52]. Including the effect of heat spreading, i.e. replacing  $R_{\text{th,d}}$  with the expressions in [52], yields a change in the total thermal resistance  $R_{\text{th,S-a}}$  from  $0.98\text{ K/W}$  to  $1.02\text{ K/W}$  (cooling system 5) and from  $0.341\text{ K/W}$  to  $0.368\text{ K/W}$  (cooling system 8). At  $P_{\text{loss}} = 80\text{ W}$  this is a temperature difference of  $T_{\text{hs,max}} - T_{\text{hs,min}} = 3.5^\circ\text{C}$  for both realized cooling systems 5 and 8.

---

<sup>3</sup>For the underlying calculations the fan characteristic has been scaled according to the fan affinity laws [64].

The cooling systems attained with the proposed optimization procedure (Fig. 3.30) and the optimization procedure presented in [51] are compared with respect to the total weights, by applying the procedure to the case study provided in [51]. Using the fan MC25060V1 in combination with a ducted heat sink featuring the dimensions  $b = 25$  mm,  $d = 4$  mm,  $c = 12$  mm,  $n = 8$ ,  $t = 1$  mm, and  $L = 20$  mm, only 19.1 g is required to achieve a thermal resistance of 2.5 K/W, whereas the cooling system of [51] requires 31.3 g, i.e. 64 % more weight.

Finally, a comparison of a selected experimental cooling system with  $R_{\text{th,S-a}} = 0.98$  K/W and  $m_{cs} = 75$  g to commercially available products, of equivalent thermal resistance  $R_{\text{th,S-a}} \approx 1$  K/W, e.g. miniature cooling aggregate LAM 4 with heat sink dimensions of 40 mm  $\times$  40 mm  $\times$  60 mm and total weight  $m_{cs} = 157$  g, reveals a weight reduction of 52 %.

## 3.4 Summary of Chapter

This chapter presented models for multi-objective optimization of power electronics covering first the analytical derivations of the losses in semi-conductors for different types of bridge leg configurations. Furthermore, simple models for minimum weight design of passive components have been presented. Finally, a new cooling system model has been developed and verified, and a novel cooling system optimization procedure has been presented and the monotonic trade-off between the required thermal resistance of the cooling system and its weight has been outlined.

The main results of this chapter are summarized as follows:

- ▶ Analytical equations for the conduction and switching loss of different bridge leg configurations are derived for arbitrary waveforms. The bridge-leg configurations are: the 2-level, the 3-level T-type, the 3-level NPC, and the 3-level ANPC.
- ▶ From the analytical equations for arbitrary waveforms, simplified analytical equations for the conduction and switching losses of 3-phase inverters/rectifiers are derived for all above mentioned bridge leg configurations.
- ▶ Simple models for the selection of passive components, i.e. capacitors, inductors and transformers, which yield a minimum weight solution are summarized.
- ▶ A new cooling system model is developed and experimentally verified.
- ▶ A cooling system optimization procedure is presented and it is shown that a reduction of the cooling system weight of more than 50 % can be achieved compared to off-the-shelf products.



# 4

## Electric Machine Drive Design Considerations

**T**HE OPTIMIZATION of the motors/generators in Chapter 2 has shown that the operating voltage of the drive can be freely selected. As long as the insulation between the windings and the stator is sufficient the number of turns can be chosen to suit the inverter employed. For the AWT application and its electrical system the obvious question is: Which operating voltage should be chosen in order to minimize the overall weight of the electrical system? This question is predominantly answered by the choice of semiconductors available on the market. However, in general a high bus voltage on the AWT is preferred to reduce conduction losses and/or the weight of the wiring inside the AWT. Too high voltages require special high-voltage cables and connectors, which would add significant weight to the electrical system. Here a good trade-off is provided for a bus voltage of  $\approx 800$  V. This chapter will outline, why a 2-level voltage source inverter with 1.2 kV SiC-MOSFETs, as shown in Fig. 4.1, is a good choice for the AWT system.

Section 4.1 compares 3-phase VSIs featuring SiC-MOSFET and Si-IGBT technology arranged in the different bridge leg configurations previously presented in Chapter 3. The optimal matching of motor/generator and inverter combination is described in Section 4.2. Finally, a hardware prototype is presented to demonstrate the achievable power-to-weight ratio.

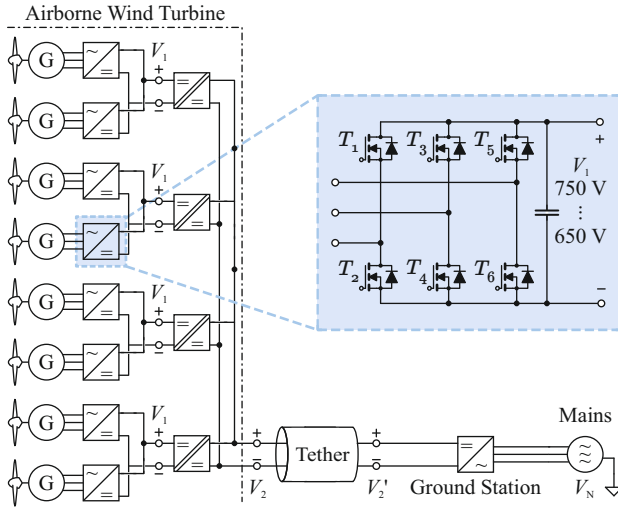


**Fig. 4.1:** Electrical system of the Airborne Wind Turbine (AWT); four bi-directional dc-dc converters are linking eight generators with bidirectional voltage source rectifiers, port voltage  $V_1$ , to a tether ( $\approx 1$  km), port voltage  $V_2$ . The ground station, i.e. bi-directional dc-ac converter, connects the tether to the three-phase grid.

## 4.1 VSI Topology Comparison

According to Section 3.3 the trade-off between the maximum semiconductor losses required to be dissipated and the cooling system weight is monotonic. Hence, as a first approximation only the semiconductors and their losses can be considered to be the most relevant variable, which characterizes both the efficiency and the power-to-weight ratio of the inverter.

With the models described in Section 3.1 the losses in the semiconductors for different switches and topologies can be easily estimated with little effort. A standard approach would be the use of IGBTs, because of their low price, especially compared to newer technologies such as SiC-MOSFETs. A calculation of the worst case losses occurring at the operating points #1–3 (cf. Tab. 2.1) for a 2-level voltage source inverter with IGBT technology yields Tab. 4.1. At this point a minimum required switching frequency of 20 kHz is assumed, due to

Total W	Conduction W	Switching W	Device(s) parallel	Device Name
357	57	301	4x	IKW15N120H3
357	55	303	5x	IKW15N120H3
359	60	299	3x	IKW15N120H3
364	68	296	2x	IKW15N120H3
384	90	294	1x	IKW15N120H3
419	46	373	2x	IKW40N120H3
422	55	367	1x	IKW40N120H3

**Tab. 4.1:** Calculation of the worst case losses occurring at the operating points #1–3 (cf. Tab. 2.1) for a 2-level voltage source inverter with IGBT technology for different semiconductor switches for a dc-link voltage of  $V_{dc} = 800$  V, a semiconductor junction temperature of  $T_j = 125$  °C, and  $f_{sw} = 20$  kHz switching frequency.

the high fundamental frequency of the motor/generator, i.e. 1.9 kHz at operating point #3. The potential benefits of an even higher switching frequency will be addressed in Section 4.2.2. A quick look at Tab. 4.1 shows that even with a discrete chip size optimization the switching losses for the 2-level voltage source inverter (VSI) with 1.2 kV IGBTs and a dc-link voltage of  $\approx 800$  V are the most significant loss contribution. For reducing the switching losses a different topology has to be used.

A calculation of the worst case losses occurring at the operating points #1–3 for a 3-level T-type VSI with IGBT technology yields Tab. 4.2. The results above the horizontal line include a discrete chip size optimization. The results below the horizontal line are single device solutions, i.e. no parallel devices are considered. A comparison of Tab. 4.1 and 4.2 shows that the switching losses of the 3-level T-type VSI are lower by  $\approx 50$  % compared to the 2-level VSI, because the switched voltage is reduced to  $\frac{V_{dc}}{2}$  from  $V_{dc}$  (cf. Section 3.1.1 and 3.1.2). However, the conduction losses are significantly increased because the forward voltage drop across  $T_2$  and  $T_3$  in series is approximately twice as large as the forward voltage drop across  $T_1$  (and  $T_4$ ), which are of the same type as the devices employed in the 2-level VSI. An alternative topology is the 3-level ANPC VSI, which allows the use of IGBTs with blocking voltages smaller than 1.2 kV, i.e. 600 V.

A calculation of the worst case losses occurring at the operating

Total	Cond.	Switch.	Device(s)	Device(s)
W	W	W	$T_1$	$T_2$
256	109	147	5x IKW15N120H3	5x IKZ50N65EH5
257	110	147	5x IKW15N120H3	3x IKZ50N65EH5
257	109	147	5x IKW15N120H3	4x IKZ50N65EH5
257	110	147	5x IKW15N120H3	4x IKZ50N65ES5
257	109	147	5x IKW15N120H3	5x IKZ50N65ES5
258	110	147	5x IKW15N120H3	3x IKZ50N65ES5
259	112	147	4x IKW15N120H3	4x IKZ50N65EH5
259	112	147	4x IKW15N120H3	5x IKZ50N65EH5
259	112	147	4x IKW15N120H3	5x IKZ50N65ES5
259	112	147	5x IKW15N120H3	2x IKZ50N65EH5
259	112	147	5x IKW15N120H3	2x IKZ50N65ES5
260	113	147	4x IKW15N120H3	3x IKZ50N65EH5
260	113	147	4x IKW15N120H3	3x IKZ50N65ES5
260	113	147	4x IKW15N120H3	4x IKZ50N65ES5
307	126	182	1x IKW40N120H3	1x IKZ50N65ES5
309	127	182	1x IKW40N120H3	1x IKZ50N65EH5
310	164	146	1x IKW15N120H3	1x IKZ50N65ES5
312	165	146	1x IKW15N120H3	1x IKZ50N65EH5
314	132	182	1x IKW40N120H3	1x IKW50N65F5

**Tab. 4.2:** Calculation of the worst case losses occurring at the operating points #1–3 (cf. Tab. 2.1) for a 3-level T-type voltage source inverter with IGBT technology for different semiconductor switches for a dc-link voltage of  $V_{dc} = 800$  V, a semiconductor junction temperature of  $T_j = 125$  °C, and  $f_{sw} = 20$  kHz switching frequency. The results above the horizontal line include a discrete chip size optimization. The results below the horizontal line are single device solutions, i.e. no parallel devices are considered. The switching losses including a discrete chip size optimization show that the influence of the output capacitance of the IKW15N120H3 IGBT is negligible compared to the influence of the tail current losses.

points #1–3 for a 3-level ANPC VSI with IGBT technology yields Tab. 4.3. A comparison of Tab. 4.2 and 4.3 reveals that the switching losses of the 3-level ANPC VSI are reduced to about a third of the switching losses of the 3-level T-type VSI, because the time constants for the reverse recovery losses and the tail current losses of the 650 V IGBTs are significantly smaller than the time constants of the 1.2 kV

IGBTs. However, the conduction losses of the ANPC VSI are even higher than the conduction losses of the T-type VSI, since always two devices connected in series are conducting the load current. The 3-level NPC VSI is not considered here, because the conduction losses are approximately the same as the conduction losses of the ANPC VSI, while the switching losses are higher for the NPC VSI than for the ANPC VSI.

In summary it can be stated that, if Si-IGBT technology is used, the optimal choice of topology is most significantly influenced by the employed switching frequency. The obvious choices are:

- ▶ The 2-level VSI, if the switching frequency is low and the output power/current is large.
- ▶ The 3-level ANPC, if the switching frequency is high and the output power/current is small.

In the intermediate area, e.g. if the switching frequency is not low and the output power/current is not small, the 3-level T-type VSI inverter also needs to be considered as a possible optimal choice of topology.

Although, the conduction characteristics for IGBTs and MOSFETs are fundamentally different (cf. equations (3.4) and (3.2)), similar conclusions can be drawn for VSIs, which employ SiC-MOSFET technology. A calculation of the worst case losses occurring at the operating points #1–3 (cf. Tab. 2.1) for a 2-level voltage source inverter with SiC-MOSFET technology yields Tab. 4.4. The results above the horizontal line include a discrete chip size optimization. The results below the horizontal line are single device solutions, i.e. no parallel devices are considered.

Tab. 4.4 shows two relations: First, at 20 kHz switching frequency the conduction losses are the more significant loss contribution for single device designs and secondly an increase of the semiconductor chip size monotonically decreases the conduction losses while monotonically increasing the switching losses due to the increasing output capacitance. This yields an optimal configuration for a given switching frequency, i.e. a higher switching frequency yields an optimal design with a smaller semiconductor chip size. A comparison of Tab. 4.4 with Tabs. 4.1–4.3 shows that both conduction and switching losses are significantly reduced by the use of 1.2 kV SiC-MOSFETs.

Total W	Cond. W	Switch. W	Device(s)		Device(s)		Device(s)	
			$T_1$	$T_2$	$T_2$	$T_{2a}$		
177	130	47	5x IKZ50N65NH5	5x IKW50N65F5	3x IKZ50N65EH5			
177	130	47	5x IKZ50N65NH5	5x IKW50N65F5	5x IKZ50N65EH5			
178	132	46	3x IKZ50N65NH5	5x IKW50N65F5	3x IKZ50N65EH5			
178	131	47	3x IKZ50N65NH5	5x IKW50N65F5	5x IKZ50N65EH5			
178	131	48	5x IKZ50N65NH5	5x IKZ50N65EH5	3x IKZ50N65EH5			
178	130	49	5x IKZ50N65NH5	5x IKZ50N65EH5	5x IKZ50N65EH5			
179	132	47	3x IKZ50N65NH5	5x IKZ50N65EH5	3x IKZ50N65EH5			
179	131	48	3x IKZ50N65NH5	5x IKZ50N65EH5	5x IKZ50N65EH5			
179	132	47	3x IKZ50N65NH5	5x IKZ50N65NH5	3x IKZ50N65EH5			
179	131	48	3x IKZ50N65NH5	5x IKZ50N65NH5	5x IKZ50N65EH5			
179	132	46	5x IKZ50N65NH5	3x IKW50N65F5	3x IKZ50N65EH5			
179	132	47	5x IKZ50N65NH5	3x IKW50N65F5	5x IKZ50N65EH5			
179	130	48	5x IKZ50N65NH5	5x IKZ50N65NH5	3x IKZ50N65EH5			
179	130	49	5x IKZ50N65NH5	5x IKZ50N65NH5	5x IKZ50N65EH5			
180	134	45	3x IKZ50N65NH5	3x IKW50N65F5	3x IKZ50N65EH5			
200	157	43	1x IKZ50N65NH5	1x IKW50N65F5	1x IKZ50N65EH5			
201	157	44	1x IKZ50N65NH5	1x IKZ50N65EH5	1x IKZ50N65EH5			
201	157	45	1x IKZ50N65NH5	1x IKZ50N65NH5	1x IKZ50N65EH5			
203	160	43	1x IKZ50N65NH5	1x IKW50N65F5	1x IKZ50N65ES5			
204	160	44	1x IKZ50N65NH5	1x IKZ50N65EH5	1x IKZ50N65ES5			
204	144	60	1x IKZ50N65NH5	1x IKZ50N65ES5	1x IKZ50N65EH5			
204	160	45	1x IKZ50N65NH5	1x IKZ50N65NH5	1x IKZ50N65ES5			
205	162	43	1x IKZ50N65NH5	1x IKW50N65F5	1x IKW50N65F5			
206	163	43	1x IKZ50N65NH5	1x IKW50N65F5	1x IKZ50N65NH5			

**Tab. 4.3:** Calculation of the worst case losses occurring at the operating points #1–3 (cf. Tab. 2.1) for a 3-level ANPC voltage source inverter with IGBT technology for different semiconductor switches for a dc-link voltage of  $V_{dc} = 800$  V, a semiconductor junction temperature of  $T_j = 125^\circ\text{C}$ , and  $f_{sw} = 20$  kHz switching frequency. The results above the horizontal line include a discrete chip size optimization. The results below the horizontal line are single device solutions, i.e. no parallel devices are considered.

Total W	Conduction W	Switching W	Device(s) parallel	Device Name
53	23	31	2x	SCT3022KL
54	22	32	3x	SCT3030KL
54	21	33	4x	SCT3040KL
55	28	27	3x	SCT3040KL
56	15	41	3x	SCT3022KL
56	16	40	4x	SCT3030KL
56	17	39	5x	SCT3040KL
57	33	25	2x	SCT3030KL
60	33	27	5x	SCT3080KL
61	13	48	5x	SCT3030KL
63	11	52	4x	SCT3022KL
63	42	21	2x	SCT3040KL
65	45	20	1x	SCT3022KL
65	41	24	4x	SCT3080KL
69	25	44	2x	C2M0025120D
65	45	20	1x	SCT3022KL
80	49	31	1x	C2M0025120D
82	65	17	1x	SCT3030KL
99	83	15	1x	SCT3040KL
124	96	27	1x	C2M0040120D

**Tab. 4.4:** Calculation of the worst case losses occurring at the operating points #1–3 (cf. Tab. 2.1) for a 2-level voltage source inverter with SiC-MOSFET technology for different semiconductor switches for a dc-link voltage of  $V_{dc} = 800$  V, a semiconductor junction temperature of  $T_j = 125$  °C, and  $f_{sw} = 20$  kHz switching frequency. The results above the horizontal line include a discrete chip size optimization. The results below the horizontal line are single device solutions, i.e. no parallel devices are considered.

A calculation of the worst case losses occurring at the operating points #1–3 for a 3-level T-type and ANPC VSI with SiC-MOSFET technology yield Tab. 4.5 and 4.6. A comparison of Tab. 4.4, 4.5, and 4.6 shows that the switching losses of the 3-level VSIs are reduced compared to the 2-level VSI, because the switched voltage is reduced to  $\frac{V_{dc}}{2}$  from  $V_{dc}$  (cf. Section 3.1.1, 3.1.2, and 3.1.4). Contrary to the behavior seen with IGBTs, the conduction losses can also be reduced for both the T-type and the ANPC VSI. However, the reduction in conduction losses

Total W	Cond. W	Switch. W	Device(s) $T_1$	Device(s) $T_2$
30	17	13	3x SCT3022KL	3x SCT3017AL
31	18	13	3x SCT3022KL	3x SCT3022AL
31	21	10	3x SCT3030KL	3x SCT3017AL
32	22	10	2x SCT3022KL	3x SCT3017AL
33	23	10	2x SCT3022KL	3x SCT3022AL
33	20	13	3x SCT3022KL	3x SCT3022KL
33	20	13	3x SCT3022KL	2x SCT3017AL
33	23	10	3x SCT3030KL	3x SCT3022AL
34	21	13	3x SCT3022KL	3x C2M0025120D
34	21	13	3x SCT3022KL	3x SCT3030AL
34	24	10	3x SCT3030KL	3x SCT3022KL
34	26	9	3x SCT3040KL	3x SCT3017AL
35	18	17	3x C2M0025120D	3x SCT3017AL
58	51	7	1x SCT3022KL	1x SCT3017AL
62	55	7	1x SCT3022KL	1x SCT3022AL
65	53	12	1x C2M0025120D	1x SCT3017AL
67	60	7	1x SCT3022KL	1x SCT3022KL
69	57	12	1x C2M0025120D	1x SCT3022AL

**Tab. 4.5:** Calculation of the worst case losses occurring at the operating points #1–3 (cf. Tab. 2.1) for a 3-level T-Type voltage source inverter with SiC-MOSFET technology for different semiconductor switches for a dc-link voltage of  $V_{dc} = 800$  V, a semiconductor junction temperature of  $T_j = 125$  °C, and  $f_{sw} = 20$  kHz switching frequency. The results above the horizontal line include a discrete chip size optimization. The results below the horizontal line are single device solutions, i.e. no parallel devices are considered.

is achieved through the use of a much larger semiconductor chip size and is accompanied by high investment costs. For single device designs the total losses for all 3 topologies are similar, only the distribution between conduction and switching losses is different.

Total W	Cond. W	Switch. W	Device(s)		Device(s)		Device(s)	
			$T_1$	$T_2$	$T_2$	$T_{2a}$		
30	17	14	3x SCT3017AL	5x SCT3017AL	5x SCT3017AL	3x SCT3017AL		
30	16	14	3x SCT3017AL	3x SCT3017AL	5x SCT3017AL	4x SCT3017AL		
30	15	15	3x SCT3017AL	3x SCT3017AL	5x SCT3017AL	5x SCT3017AL		
31	20	11	2x SCT3017AL	2x SCT3017AL	5x SCT3017AL	3x SCT3017AL		
31	19	12	2x SCT3017AL	2x SCT3017AL	5x SCT3017AL	4x SCT3017AL		
31	19	13	2x SCT3017AL	2x SCT3017AL	5x SCT3017AL	5x SCT3017AL		
31	18	13	3x SCT3017AL	3x SCT3017AL	5x SCT3017AL	2x SCT3017AL		
31	15	16	4x SCT3017AL	4x SCT3017AL	5x SCT3017AL	3x SCT3017AL		
31	14	17	4x SCT3017AL	4x SCT3017AL	5x SCT3017AL	4x SCT3017AL		
31	13	17	4x SCT3017AL	4x SCT3017AL	5x SCT3017AL	5x SCT3017AL		
32	22	11	2x SCT3017AL	2x SCT3017AL	5x SCT3017AL	2x SCT3017AL		
32	18	14	3x SCT3017AL	3x SCT3017AL	4x SCT3017AL	3x SCT3017AL		
32	17	14	3x SCT3017AL	3x SCT3017AL	4x SCT3017AL	4x SCT3017AL		
70	62	8	1x SCT3017AL	1x SCT3017AL	1x SCT3017AL	1x SCT3017AL		
75	67	8	1x SCT3017AL	1x SCT3017AL	1x SCT3017AL	1x SCT3022KL		
76	68	8	1x SCT3017AL	1x SCT3017AL	1x SCT3017AL	1x C2M0025120D		
80	72	9	1x SCT3022KL	1x SCT3022KL	1x SCT3017AL	1x SCT3017AL		
84	76	8	1x SCT3017AL	1x SCT3017AL	1x SCT3022KL	1x SCT3017AL		
85	76	9	1x SCT3022KL	1x SCT3022KL	1x SCT3017AL	1x SCT3022KL		
87	77	9	1x SCT3022KL	1x SCT3022KL	1x SCT3017AL	1x C2M0025120D		
88	74	13	1x C2M0025120D	1x SCT3017AL	1x SCT3017AL	1x SCT3017AL		
89	80	8	1x SCT3017AL	1x SCT3017AL	1x C2M0025120D	1x SCT3017AL		
89	81	9	1x SCT3017AL	1x SCT3022KL	1x SCT3022KL	1x SCT3022KL		

**Tab. 4.6:** Calculation of the worst case losses occurring at the operating points #1–3 (cf. Tab. 2.1) for a 3-level ANPC voltage source inverter with SiC-MOSFET technology for different semiconductor switches for a dc-link voltage of  $V_{dc} = 800$  V, a semiconductor junction temperature of  $T_j = 125$  °C, and  $f_{sw} = 20$  kHz switching frequency. The results above the horizontal line include a discrete chip size optimization. The results below the horizontal line are single device solutions, i.e. no parallel devices are considered.

In summary it can be stated that the optimal choice of topology, in case of using SiC-MOSFET technology, is also most significantly influenced by the employed switching frequency. The obvious choices are:

- ▶ The 2-level VSI, if the switching frequency is low and the output power/current is large.
- ▶ The 3-level T-type converter, if the switching frequency is high and the output power/current is small.

The 3-level ANPC features higher conduction and switching losses than the T-type converter at a dc-link voltage of  $\approx 800$  V, but would allow for a configuration with higher dc-link voltage if only devices with blocking voltages of 1.2 kV are used. In either case the losses of the single device designs of  $\approx 65$  W are small for all 3 topologies and choosing a 2-level voltage source inverter due to the smallest investment costs and the highest reliability is well justified.

## 4.2 Inverter and Machine Interactions

Once the design choices for the inverter topology and the motor/generator have been made some parameters can be optimized in order to arrive at the most efficient combination of motor/generator and inverter. The number of turns of the machine coils and the employed switching frequency most significantly influence the losses of the machine and inverter combination.

### 4.2.1 Optimal Number of Turns

The motor/generator operation requires a defined amount of current in the coil, i.e. sum of the currents of the turns of the coil, to produce the required torque. Hence the current loading of the drive is reduced with an increasing number of turns of the motor/generator, i.e. the higher the number of turns the lower the conduction and switching losses of the inverter for a given dc-link voltage. However, there is a limit imposed by the speed range of the motor/generator. For the highest rotational frequency of the motor/generator the induced voltage needs to remain low enough, such that the voltage rating of the inverter components is

not exceeded, which yields considering (2.51)

$$N_{\text{turns}} \leq \left\lfloor \frac{V_{\text{dc-link,max}}}{\sqrt{3} \hat{u}_{\text{ind},A,\text{max}}} \right\rfloor,$$

where  $V_{\text{dc-link,max}}$  is the dc-link voltage when the maximum peak voltage per turn  $\hat{u}_{\text{ind},A,\text{max}}$  is induced. Because operating point # 6 only occurs when the drivetrain for one of the propellers fails, a maximum dc-link voltage of  $V_{\text{dc-link,max}} = 1130 \text{ V}$  is chosen to be acceptable for the short time required to land the AWT for maintenance, since the motor/generator isn't actively driven in this operating point. With the maximum induced peak back-EMF voltage of  $\hat{u}_{\text{ind},A,\text{max}} = 54.2 \text{ V}$  at 7100 rpm this yields

$$N_{\text{turns}} \leq 12.$$

## 4.2.2 Optimal Switching Frequency

Once the number of turns of the motor/generator coils is chosen the machine inductances and the voltage constant are known and the machine/drive current waveforms can finally be calculated. Calculating the current waveforms and attributed conduction losses only based on the calculated values of the inductance and dc-resistance will yield relatively accurate current waveforms, but inaccurate high-frequency conduction losses. However, if a measurement of the machine impedance over frequency is available (e.g. Fig. 2.22), the high-frequency conduction losses can be accounted for. Fig. 4.2 shows the conduction losses in the RFM prototype and losses of the 2-level VSI prototype for operating point #2 (cf. Tab. 2.1) in dependency of the switching frequency of the VSI.

A Fourier transform of the inverter voltage waveform (10 ns resolution) is divided by the impedance measurement of the RFM prototype  $Z_A(f)$  (cf. Fig. 2.22) and yields the Fourier transform of the current waveform  $\sum_{n=1}^{n=\infty} i_A(n f_{\text{fund}})$ . The conduction losses of the machine are then calculated as

$$P_{\text{cond,RFM}} = \sum_{n=1}^{n=\infty} \Re[Z_A(n f_{\text{fund}})] i_A(n f_{\text{fund}}) i_A^*(n f_{\text{fund}}), \quad (4.1)$$

where  $i^*$  is the complex conjugate of  $i$ . A frequency dependency of the on state resistance of the power semiconductors is not considered.

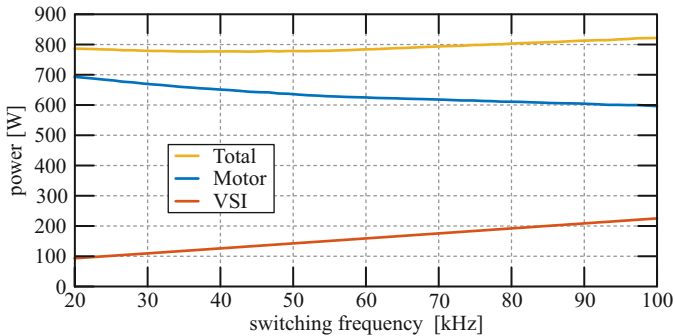


**Fig. 4.2:** Conduction Losses in the RFM prototype and losses of the 2-level VSI prototype for operating point #2 (cf. Tab. 2.1) in dependency on the switching frequency of the VSI. The conduction losses are decreasing with increasing switching frequency due to a decreasing current ripple and the losses of the VSI increase with increasing switching frequency due to switching losses. The total system losses are showing a flat optimum at  $\approx 45$  kHz.

Fig. 4.2 shows that the conduction losses in the RFM prototype decreasing with increasing switching frequency due to a decreasing current ripple and the losses of the VSI increasing with increasing switching frequency due to increasing switching losses. The total system losses are showing a flat optimum at  $\approx 45$  kHz.

### 4.3 Hardware Prototype

The 2-level VSI topology is chosen to be implemented with a CCS050M-12CM2 power module from Cree. This 1.2 kV SiC-MOSFET module features a low on-state resistance  $r_{ds,on}$  of 25 m $\Omega$  at a junction temperature of 25  $^{\circ}$ C. While the body diode of the MOSFET has a comparatively high forward voltage drop, its reverse recovery charge is small as to be expected from SiC devices. Additional high-performance SiC Schottky diodes are included inside the package. While the package is relatively heavy at 180 g, it features an isolated base-plate and a junction-to-baseplate thermal resistance of 0.43  $^{\circ}$ K/W per die. Furthermore, at the time it was one of the only packages, which provided a Kelvin source-pins for the MOSFET gate drives, allowing high  $\frac{di}{dt}$  values to be achieved during switching.

The hardware prototype shown in Fig. 4.3 features:

- ▶ Auxiliary power supply: Required for supplying the low-voltage components of the inverter directly from the DC-link voltage.
- ▶ Startup power supply: Required for driving the auxiliary power supply before it can supply itself.
- ▶ 5V/12V/15V voltage regulators: Required for supplying the control logic, the gate drive circuitry, the control electronics, the cooling system fan, etc.
- ▶ Gate drive power supplies: Isolated DC/DC power supplies providing the voltages for the gate drives.
- ▶ Isolated gate drivers: Required for operating the power MOS-FETs.
- ▶ DSP/FPGA: Control logic of the inverter.
- ▶ Current and voltage measurement circuitry for protection and control. The voltage measurement is performed with the internal ADC of the DSP and voltage divider. The phase currents are measured using the *CDS4050* magnetoresistive sensor from *Sensitec*.
- ▶ DC-link capacitance consisting of electrolytic capacitors with balancing circuit, foil capacitors and ceramic capacitors.
- ▶ Heat sink and fan for dissipating the losses that occur in the power semiconductors (overdimensioned such that a power loss of 300 W at the semiconductor junction is acceptable).

The DC-link capacitance is split into 3 parts. The first part is required for providing the energy storage for load ramps. It consists of two series connected aluminum electrolytic capacitors providing 120  $\mu\text{F}$  each. Due to its reduced height and long life time, the capacitors of type *LGX2H121MELA35* from *Nichicon* are selected. Since electrolytic capacitors have significant series resistance (ESR), the current ripple of the electrolytic capacitors should be small. This is achieved by adding an 10  $\mu\text{H}$  inductor in series to the capacitors, which provides sufficient impedance at switching frequency to block most of the ripple current

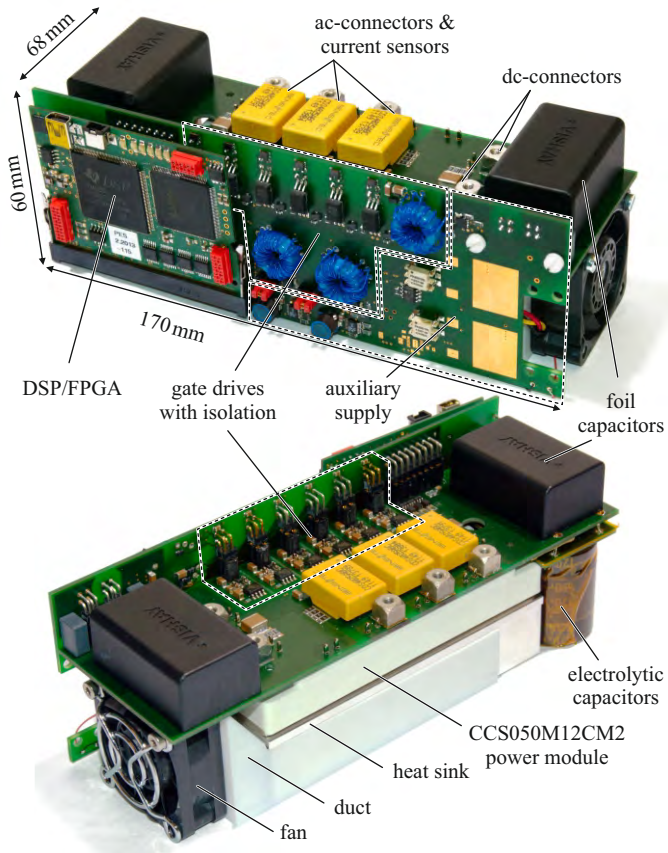


**Fig. 4.3:** Picture of the 12.5 kW converter prototype, (a) front view, (b) rear view. The total system weight is 661 g. The achieved power-to-weight ratio is 18.9 kW/kg and the power density is 18 kW/dm<sup>3</sup>.

from the electrolytic capacitors. Furthermore, the voltage of the mid-point of the series connection of the electrolytic capacitors must be balanced. This is achieved using the circuit presented in [65]. The ripple current is buffered using foil capacitors. Since the module has two DC-link terminals, the DC-link stray inductance can be minimized by using foil capacitors on either side of the module. Based on the weight, capacitance and ripple current capabilities, capacitors of type

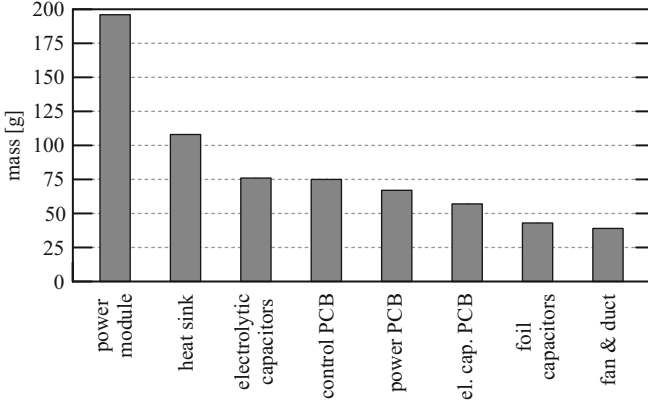


**Fig. 4.4:** Weight distribution of the inverter components. The total inverter weight is 661 g.

*MKP1848S55010JP2C* from *Vishay* are selected. The commutation loop inductance is minimized by adding two ceramic capacitors directly to the DC-link terminals of the module. The capacitors provide a capacitance of  $0.1 \mu\text{F}$  and are rated to a voltage of 1.5 kV with X7R dielectric. However, the actual capacitance is voltage dependent and expected to be around 20 nF at rated voltage. Oscillations between the capacitors may occur due to the series inductances of the devices. In order to damp these oscillations, resistors with total resistance of  $5\Omega$  are added in series to the ceramic capacitors. Simulations conducted with GeckoCircuits suggest that this measure is sufficient for damping the oscillations which may occur between the ceramic and the foil capacitors.

The heat sink is dimensioned such that a power loss of 300 W is acceptable. Accordingly, the admissible thermal resistance between heat sink base plate and the ambient is

$$R_{\text{th,heat-sink-to-amb}} = \frac{130^\circ - \frac{P_v}{6} R_{\text{th,junc-to-heat-sink}} - 25^\circ}{P_v} = 0.25^\circ\text{K/W},$$

with  $P_v = 300 \text{ W}$  and  $R_{\text{th,junction-to-heat-sink}} = 0.62^\circ\text{K/W}$ . The selected cooling system features an aluminum heat sink, a duct, and the 1.92 W fan *9GA0412G7001*. It features a thermal resistance of  $0.305^\circ\text{K/W}$  at a weight of 133 g.

The weight distribution of the inverter is shown in Fig. 4.4. The total weight of the inverter is 661 g which evaluates to a power-to-weight ratio of 18.9 kW/kg. The boxed volume of the inverter is slightly below 0.7 dm<sup>3</sup> leading to a volumetric power density of 18 kW/liter.

## 4.4 Summary of Chapter

The main results of this chapter are summarized as follows:

- ▶ The losses of different 3-phase inverter/rectifier topologies are compared for the required set of specifications. Furthermore, the use of SiC-MOSFET versus Si-IGBT technology is comparatively evaluated.
- ▶ The optimal number of turns per coil of the motor/generator is described.
- ▶ The optimal switching frequency of the converter in order to achieve the highest efficiency of the motor/generator and drive combination is described.
- ▶ A 2-level VSI with SiC-MOSFETs is designed and built. The achieved power-to-weight ratio is 18.9 kW/kg and shows only a small weight contribution of the VSI to the total weight of the AWT.

# 5

## Tether (Transmission Cable)

**T**HE FOLLOWING description is based on [1] which also considers the conceptualization and multi-objective optimization of the electrical system of an airborne wind turbine (AWT). The tether represents a key element of an AWT power generation system. It retains the airborne part of the AWT system, i.e. the power kite, to the ground and provides the electric link between the kite's local power network and the ground-based power and control station, which is connected to the LV or MV grid. The requirements of the tether are demanding. Its desired properties can be summarized as follows:

- ▶ Sufficiently high tensile strength and flexibility at a low weight to minimize the impact on the power kite's flight performance.
- ▶ Failsafe transmission of electric power under repetitive mechanical strain to allow for high operational reliability and minimum maintenance.
- ▶ Resistance to environmental impacts such as UV irradiation, rain, or air pollutants in combination with water (leading to acid) to enhance the system lifetime.

Based on the requirements, three main components of the tether can be identified: a functional part that provides the tensile strength, two or multiple electric conductor(s), and a rugged outer protection jacket. The tether is comparable with a custom rugged and light-weight power transmission cable, where the most critical property is the weight. By

investigating the materials of commercial power cables, it is found that the conductors, which are typically made of copper (Cu) or aluminum (Al), have the highest share of the weight. Thus, the cross-sectional area of the conductors should be minimized to obtain a light-weight tether. This can be achieved by increasing the operating voltage, in this case the dc voltage level. However, a higher operating voltage requires also a thicker insulation, which may ultimately lead to a higher weight again. This trade-off is the starting point of the following analysis.

To begin with, the tether construction has to be defined. One option is a design with coaxial electrical conductors at the tether's center. Synthetic fibers would then surround the conductors and provide the physical strength necessary to withstand the pull of the kite system at a low weight. The disadvantage with a center aligned conductor (e.g. made of copper litz wire) is that the copper may yield under load. When the tensile force is relaxed, all parts of the tether behave elastically and retract apart from the copper, which is ductile and not elastic above 0.4% strain. The excess conductor length after ductile deformation has nowhere to go, and thus buckles and is likely to form a kink. A significantly better design is to use wire conductors that are arranged in a helical path around a center-aligned strain relief core. This provides the wire conductors some axial compliance when the cable is under tension or when load cycles are applied. A schematic cross section of the selected tether assembly (available e.g. from [66]) is depicted in Fig. 5.1. An alternative highly flexible cable construction, which is not further investigated here, is described in [67, 68].

The strain relief core is fabricated from aramid (Kevlar) fibers providing a tensile strength  $\beta_{ts,Ar} = 3.6 \text{ kN/mm}^2$ . Six copper or aluminum litz wires with cross-linked polyethylene insulation are considered for the conductors. An additional insulation layer could be added by wrapping an insulator material around the conductors. The outer tether protection jacket is implemented using a combination of elastomer and synthetic fiber layers (e.g. Hytrel thermoplastic elastomer and Vectran fibers manufactured by DuPont). The material data of the tether is summarized in Tab. 5.1.

Firstly, the tensile strength of the tether needs to be determined. For that purpose it is assumed that the power kite is operated as shown in Fig. A.5. The maximum force of the tether  $F_{Th,max}$  can then be

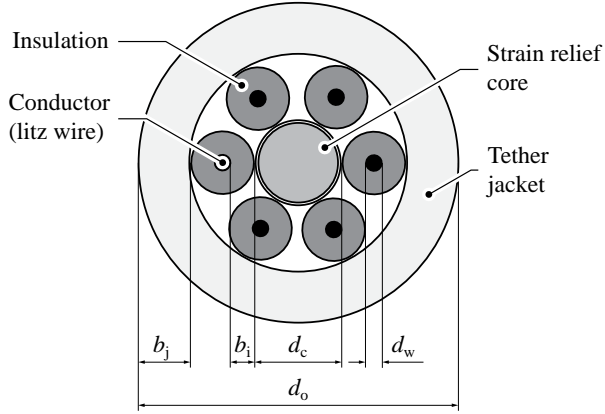


**Fig. 5.1:** Cross section of the tether depicted in [1], showing its assembly with a center-aligned strain relief core, six litz wire conductors with insulation arranged around the core, and the tether protection jacket. An additional insulation layer could be wrapped around all conductors.

estimated by

$$F_{\text{Th,max}} = \frac{1}{2} c_{\text{LK}} \rho A_{\text{K,eff}} v_{\text{W,r}}^2 \frac{v_{\text{W,r}}}{\sqrt{v_{\text{W,r}}^2 - v_{\text{W}}^2}} \quad (5.1)$$

(see Appendix, [1]). Considering an effective kite wing area of  $A_{\text{K,eff}} = 25 \text{ m}^2$  including the mounting of the generator/motor units, the maximum tether force yields to  $F_{\text{Th,max}} \approx 22.5 \text{ kN}$ . (The density of air is assumed with  $\rho = 1.225 \text{ kg/m}^3$ , the lift coefficient of the kite wing with  $c_{\text{LK}} = 1.2$ , the wind speed with  $v_{\text{W}} = 10 \text{ m/s}$ , and the relative wind speed acting upon the kite wing with  $v_{\text{W,r}} = 33.4 \text{ m/s}$ ; see [1]) The required diameter of the aramid core  $d_c$ , including a safety factor of three, can then be calculated to

$$d_c = \sqrt{\frac{3 \cdot 4 F_{\text{Th,max}}}{\beta_{\text{ts,Ar}} \pi}} \approx 5 \text{ mm} . \quad (5.2)$$

Next, the thickness of the cross-linked polyethylene conductor insulation  $b_i$  needs to be expressed as a function of the insulation voltage  $V_i$ .

Property	Value	Description
$\beta_{ts,Ar}$	3.6 kN/mm <sup>2</sup>	Tensile strength of aramid (Kevlar)
$\rho$	1.225 mg/cm <sup>3</sup>	Density of air
$\rho_{Al}$	2.8 g/cm <sup>3</sup>	Density of aluminum
$\rho_{Ar}$	1.45 g/cm <sup>3</sup>	Density of aramid (Kevlar)
$\rho_{Cu}$	8.9 g/cm <sup>3</sup>	Density of copper
$\rho_{PE}$	0.92 g/cm <sup>3</sup>	Density of cross-linked polyethylene
$\rho_j$	1.3 g/cm <sup>3</sup>	Density of the tether jacket
$\sigma_{Al}$	$3.5 \cdot 10^7$ S/m	Conductivity of aluminum
$\sigma_{Cu}$	$5.96 \cdot 10^7$ S/m	Conductivity of copper
$b_i$	1.3 mm	Thickness of the litz wire insulation
$b_j$	3 mm	Thickness of the tether jacket
$d_c$	5 mm	Strain relief core diameter
$d_w$	1.5 mm	Litz wire diameter
$d_o$	19.2 mm	Outer tether diameter
$F_{Th,ts}$	70 kN	Tensile strength of the tether
$l_{Th}$	1000 m	Tether length
$m'_{Th}$	0.32 kg/m	Specific mass of the tether
$V'_{Th,1}$	$\leq 8$ kV	Tether voltage at the AWT system
$C'_{Th}$	100 pF/m	Specific tether capacitance
$L'_{Th}$	360 nH/m	Specific tether inductance
$R'_{Th}$	9 m $\Omega$ /m	Specific tether resistance

**Tab. 5.1:** Tether material data and parameter overview, [1].

The required relation is given by

$$b_i = 0.0144 \frac{\text{mm}}{\text{kV}^2} \cdot V_i^2 + 0.1694 \frac{\text{mm}}{\text{kV}} \cdot V_i + 0.40 \text{ mm} , \quad (5.3)$$

and is determined based on the insulation layer thickness of commercial MV power cables for transportation systems [69]. The thickness of the tether protection jacket  $b_j$  is assumed with 3 mm and is kept constant

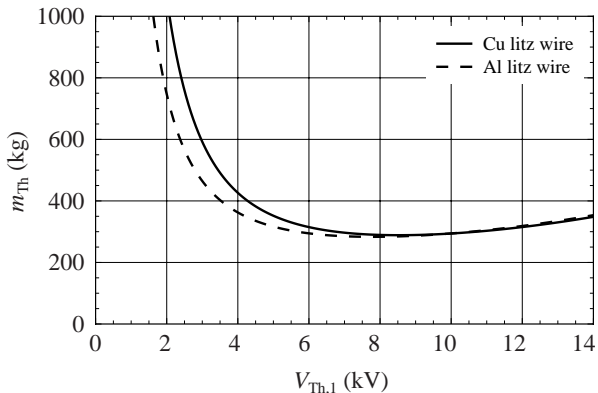


**Fig. 5.2:** Tether mass versus tether dc voltage for copper (Cu) and aluminum (Al) litz wire conductors, for a fixed tether efficiency  $\eta_{\text{Th}} = 98.5\%$  (1.5 kW conduction losses at a power input of 100 kW), [1].

within the considered tether parameter range. In order to determine the ohmic losses, the litz wire resistance  $R_w$  at  $20^\circ\text{C}$  is modeled as a function of the wire diameter  $d_w$  and the wire length  $l_w$  using the data from [70],

$$R_w = \frac{1.7877 \cdot 10^6}{\sigma} \frac{1}{\text{m}} \cdot l_w \cdot \left( \frac{d_w}{\text{mm}} \right)^{-2.017} \quad [\sigma] = \frac{S}{m}; \quad (5.4)$$

$l_w$  is assumed with the length  $l_{\text{Th}}$  of the tether. The remaining design variables of the tether are the litz wire diameter  $d_w$  and the dc voltage of the tether, e.g.  $V_{\text{Th},1}$  at the connection point to the AWT. The tether is now fully parameterized and the optimal tether voltage can be determined by varying  $V_{\text{Th},1}$ . Thereby, the resulting wire resistance of the tether  $R_{\text{Th}}$  is adapted such that the tether efficiency

$$\eta_{\text{Th}} = \frac{P_{\text{Th},1} V_{\text{Th},1}^2 - P_{\text{Th},1}^2 R_{\text{Th}}}{P_{\text{Th},1} V_{\text{Th},1}^2} \geq 97\% \quad R_{\text{Th}} = \frac{2}{3} R_w \quad (5.5)$$

remains constant and above a predefined minimum value. The ground-based power station with a dc bus voltage  $V_{\text{Th},2}$  ensures that the positive and negative bus is referenced to the ground potential by  $\pm V_{\text{Th},2}/2$ . This enables to design the conductor-to-ground insulation for  $V_{\text{Th},2}/2$  only. The six conductors of the tether are alternately connected to the positive and negative bus to reduce the resultant tether inductance.

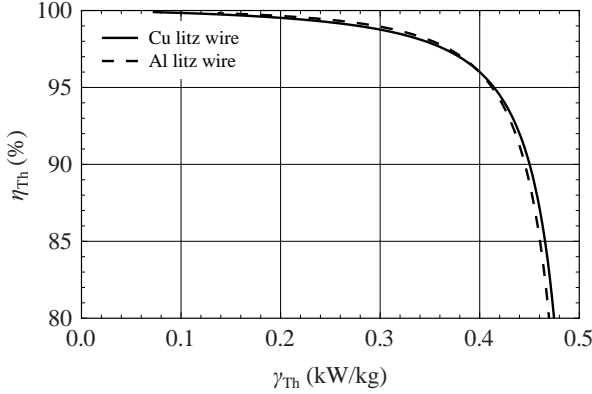


**Fig. 5.3:** Efficiency versus power-to-weight ratio of the tether for copper (Cu) and aluminum (Al) litz wire conductors at a tether dc voltage of 8 kV, [1].

Fig. 5.2 shows the relation between the tether weight and tether dc voltage for copper and aluminum litz wire conductors, assuming a tether efficiency of  $\eta_{\text{Th}} = 98.5\%$ . This corresponds to 1.5 kW conduction losses at a tether input power from the AWT system of  $P_{\text{Th},1} = 100$  kW and a tether length of  $l_{\text{Th}} = 1000$  m. The optimal dc voltage of the tether leading to the lowest weight is approximately 8 kV as can be seen from Fig. 5.2. Aluminum wire conductors do not lead to a weight reduction. Thus, the tether is designed for a maximum nominal operating voltage of 8 kV using copper litz wires. The resulting tether parameters are given in Tab. 5.1. The outer tether diameter equals to  $d_o = 19$  mm, requires a litz wire diameter of  $d_w = 1.5$  mm (corresponding to AWG 16), and has a specific mass of  $m'_{\text{Th}} = 0.32$  kg/m.

Finally, in Fig. 5.3 the tether efficiency is plotted versus the achievable power-to-weight ratio  $\gamma_{\text{Th}}$ , which is given by

$$\gamma_{\text{Th}} = \frac{P_{\text{Th},1} V_{\text{Th},1}^2 - P_{\text{Th},1}^2 R_{\text{Th}}}{V_{\text{Th},1}^2 m_{\text{Th}}} . \quad (5.6)$$

These characteristics will be used later for the overall AWT power generation system optimization and indicate that the power-to-weight ratio should be selected below 0.4 kW/kg for the considered tether design. Beyond 0.4 kW/kg, the copper cross section becomes too small leading to a steep drop in efficiency, and the tether weight is then mainly determined by the non-conductive materials, [1].

# 6

## Multi-Objective Optimization of the All-SiC 8kV/700V DAB

**T**HE greatest challenge with respect to the realization of the electric system of the considered AWT, with a total maximum input power of 100 kW, is to achieve a lightweight tether, and lightweight generators as well as power converters. From related investigations detailed above the electrical system depicted in Fig. 6.1 emerges, which uses low-voltage (LV) generators and inverters, operated from a dc bus voltage ranging from 650 V to 750 V, dc–dc converters that convert the LV dc bus voltage to a high tether voltage of up to 8 kV, the tether itself, and the ground station. The AWT system considers four identical dc–dc converters for safety reasons. With the proposed electrical system structure a failure of any on-board power conversion system component will result at most in the loss of two propulsion systems. In case of a system malfunction, six propellers provide sufficient propulsion to safely land the AWT for maintenance. Furthermore, each dc–dc converter is

	AWT	DC–DC Converter	Converter Cell
Input voltage	$650 \text{ V} < V_1 < 750 \text{ V}$		
Output voltage	$6.9 \text{ kV} < V_2 < 8 \text{ kV}$		$1733 \text{ V} < V_{2,i} < 2 \text{ kV}$
Rated power	100 kW	25 kW	6.25 kW
Allowable weight	25 kg	6.25 kg	1.65 kg

**Tab. 6.1:** Specifications for the AWT dc–dc transmission system.

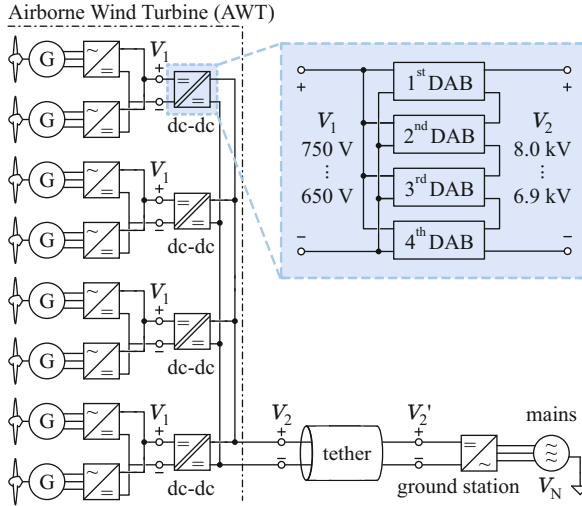


**Fig. 6.1:** Electrical system of the Airborne Wind Turbine (AWT). Four bi-directional dc–dc converters link eight voltage source rectifiers to a power transmission tether ( $\approx 1$  km). The ground station, i.e. a bi-directional dc–ac converter, connects the tether to the three-phase grid. Four single converter cells form a bi-directional dc–dc converter with a dc port voltage  $V_2$  of up to 8 kV.

composed of four single converter cells that are arranged in an input series output parallel (ISOP) structure, i.e. the cells are connected in parallel on the low-voltage side and in series on the high-voltage side in order to reduce the maximum tether side port voltage of each converter cell to 2 kV. The complete electrical system needs to allow for bi-directional energy transfer at rated power in order to enable the startup of the AWT. These and further considerations yield the specifications for the dc–dc transmission system summarized in Tab. 6.1. Each converter cell is essentially a dual active bridge (DAB) converter with a full bridge (FB) circuit on the low-voltage side (dc port voltage  $V_1$ ), a high-frequency (HF) transformer and inductor, and a neutral point clamped (NPC) circuit on the high-voltage side (dc port voltage  $V_{2,i}$ , Fig. 6.2).

A literature research on *lightweight power electronic converters* re-

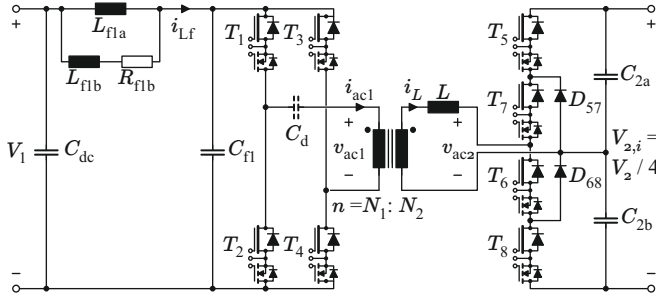


**Fig. 6.2:** Modified dual active bridge (DAB) converter topology used to realize a single cell of the bi-directional dc–dc converter. The rated output power is 6.25 kW, the maximum MV–side port voltage is 2 kV, and the maximum allowed weight is 1.65 kg.

veals current publications to focus on three main topics:

1. *Semiconductors:* Highly efficient power converters, and converters operated at high temperatures [71–75]. The high efficiency and temperature operation reduces the system weight predominately by reducing the cooling system requirements.
2. *Lightweight magnetic components:* Multi-physics modeling and design optimization of transformers and inductors in reference to geometric optimization, magnetic material properties, medium/high-frequency operation and high-voltage isolation stress analysis [76–82].
3. *Cooling systems:* Optimizations that yield cooling systems which feature minimal weight for a required thermal resistance [47, 51].

However, so far no fully functional design of a lightweight converter system that, including a comprehensive description of all relevant interactions of different converter components and further aspects has been presented. No experimental verification of the achievable performance in terms of a power-to-weight ratio in kW/kg (or kW/lb) for a 2 kV/700 V isolated bidirectional dc–dc converter exist. Because the weight of a fully functional power electronics converter provides the only meaningful measure, any weight optimized converter must include, besides it’s main functionality, also the auxiliary supply, considerations

on analysis of the stability of the control over the specified operating range, which involves considerations on the input filter design, e.g. the size and weight of capacitor  $C_{dc}$  (cf. Fig. 6.2) depends on the design of the control and associated delay time, which in turn depends on the hardware implementation of the control circuitry.

This chapter presents a comprehensive overall design method for the realization of a weight-optimized a 2 kV/700 V DAB converter. In this context, the design procedures for the remaining converter components that are required for the converter operation and the integration into the final electrical AWT system, e.g. gate drivers, digital control, filters, and auxiliary power supplies are thoroughly explained.

The weight optimization of a power converter not only involves the weights of the power components themselves but also the components' dissipated losses, since the weight of the cooling system increases with increasing losses and may substantially contribute to the total converter weight. For this reason, the presented weight optimized design is performed as multi-objective optimization and takes, besides the actual components' weights, the losses of the converter components and the associated weight of the optimized cooling system into account. The task of minimizing the weight of the complete DAB converter system is split into the subtasks listed below.

1. Selection of a suitable *switching frequency* that allows for a light-weight converter realization.
2. Efficient operation of the DAB and *calculation of a corresponding turns ratio  $n$  and inductance  $L$*  in Section 6.1.1.
3. Selection of *most suitable power semiconductors*, cf. Section 6.1.2.
4. Analytical multi-objective optimization of the *DAB transformer and inductor* in Section 6.1.3.
5. Weight optimization of the *cooling system* in Section 6.1.4.
6. Realization of *filter networks* (Section 6.1.5).
7. Implementation of the *control circuitry*: consideration of aspects related to the converter weight (Section 6.2).
8. Lightweight *auxiliary power supplies and startup* procedure (Section 6.3).

The switching frequency denotes a key design parameter: at very low switching frequencies, heavy passive components and, at very high switching frequencies, high switching losses, core losses, and HF losses result. In this work it has been assumed that the sensitivity of the final converter weight with respect to the switching frequency is relatively low for a switching frequency close to the optimal switching frequency (flat optimum). For this reason the complete AWT system has initially been optimized for six different switching frequencies ( $f_s = 50$  kHz, 80 kHz, 100 kHz, 125 kHz, 160 kHz, and 200 kHz), using simplified models and practice-oriented assumptions; the obtained results suggest a switching frequency of approximately 100 kHz. With the determined switching frequency the remaining items 2) to 8) of the list can be processed in the given sequence in order to optimize the DAB converter with respect to minimum weight. Finally, Section 6.4 presents experimental results demonstrating the achieved performance of 4.28 kW/kg (1.94 kW/lb) of a prototype system.

## 6.1 Minimum Weight DAB Power Converter

This section details the design or the selection of power components suitable for a lightweight power converter, i.e. power semiconductors, HF transformer and inductor, and the components of the filter networks. Prior to this, however, the converter's turns ratio,  $n$ , and HF inductance,  $L$ , need to be determined in order to allow for the calculation of all operating point dependent voltage and current waveforms the DAB converter is subject to.

### 6.1.1 Optimal Converter Operation, optimal $n$ and $L$

The investigated DAB converter is operated most efficiently at  $V_1 \approx V_{2,i}/2$  with the conventional phase shift modulation (CPM) scheme [83]. Thus, the turns ratio of the DAB transformer is

$$n = \frac{V_1}{V_{2,i}/2} = \frac{750 \text{ V}}{1 \text{ kV}} = 0.75. \quad (6.1)$$

The CPM scheme needs to be slightly modified, since the MV-side NPC converter requires a minimum freewheeling time of 250 ns in or-

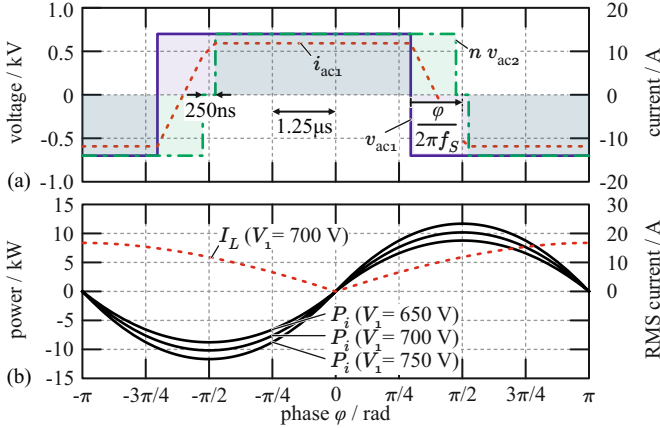


**Fig. 6.3:** (a) Voltage and current waveforms calculated for a single DAB converter ( $V_1 = 700$  V,  $V_{2,i} = 1.9$  kV,  $P_i = 6.25$  kW/ $\eta_{\text{exp}}$ ,  $\eta_{\text{exp}} = 95\%$ ,  $n = 0.75$ ,  $L = 107$   $\mu$ H,  $f_s = 100$  kHz); the NPC converter on the MV-side requires a freewheeling time of 250 ns. (b) Power transfer characteristics of the DAB (cf. [83]),  $V_1/V_{2,i} = 0.375 = \text{constant}$ ; maximum power transfer is achieved for  $\varphi = \pm\pi/2$ ; the dashed line depicts the rms inductor current  $I_L(\varphi)$  at nominal operation.

der to ensure an equal distribution of the blocking voltages across the switches  $T_5 \dots T_8$  [75]. With this, the voltage and current waveforms depicted in Fig. 6.3(a) result, i.e. a maximum duty cycle of the NPC converter of  $D_2 = (0.5 - 250 \text{ ns} \cdot f_s) = 0.475$  results. The corresponding maximum allowable DAB inductance,  $L$ , for a maximum duty cycle of the NPC converter and the specified rated power, is determined with

$$L = \frac{\min(V_1 V_{2,i})}{4 n f_s \frac{P_{i,\text{max}}}{\eta_{\text{exp}}}} \left[ \frac{\varphi_{\text{max}}}{\pi} \left( 1 - \frac{\varphi_{\text{max}}^2}{\pi^2} \right) - \left( \frac{1}{2} - D_2 \right)^2 \right] = 107 \mu\text{H}, \quad (6.2)$$

calculated for  $P_{i,\text{max}} = 6.25$  kW, a conservative value of the expected efficiency<sup>1</sup>,  $\eta_{\text{exp}} = 95\%$ , and the maximum steady state phase angle  $\varphi_{\text{max}} = \pi/4$  (in order to maintain a good controllability at low output

<sup>1</sup>For a more accurate estimation of the expected efficiency, the efficiency needs to be part of the converter optimization, i.e.  $\eta_{\text{exp}}$  is a result of each particular

Property	Value	Description
$\max(I_{ac1})$	12.2 A	Max. rms transformer current, LV-side
$\max(I_L)$	9.2 A	Max. rms transformer current, MV-side
$\max(I_{L,\text{peak}})$	10.2 A	Max. peak inductor current
$\max(I_{T_1})$	8.65 A	Max. rms current in switches $T_1 \dots T_4$
$\max(I_{T_5})$	6.5 A	Max. rms current in switches $T_5 \dots T_8$
$\max(I_{C1})$	7.0 A	Max. rms capacitor current of $C_{f1}$
$\max(I_{C2})$	5.0 A	Max. rms capacitor current of $C_{2a}$ and $C_{2b}$

**Tab. 6.2:** Transformer, capacitor and semiconductor currents of a single DAB converter module with  $P_i = 6.25 \text{ kW}/\eta_{\text{exp}}$  and  $\eta_{\text{exp}} = 95\%$ .

power, typically  $\varphi_{\text{max}} \in [\pi/4, \pi/3]$ ). With known values of  $n$  and  $L$  the characteristic converter currents can be calculated using the methods presented in [83]. These currents are summarized in Tab. 6.2.

### 6.1.2 Power Semiconductors

SiC power semiconductors are considered to be most suitable with respect to low losses and, subsequently, low weights of the heat sinks required for active cooling. For the *MV-side NPC converter*, normally-on SiC JFETs in a TO-247 package with breakdown voltages of 1700 V and low on-state resistances of 150 m $\Omega$  at 125°C are selected. Each SiC JFET is connected in series to a low-voltage p-channel Si MOSFET (FDMS6681Z,  $R_{DS,\text{on}} = 3.2 \text{ m}\Omega$ ), and a gate driver especially dedicated to SiC JFETs operates both devices (here Infineon’s 1EDI30J12CP EiceDriver is used), to gain normally-off properties. The *LV-side full bridge converter* employs SiC JFETs with breakdown voltages of 1200 V and on-state resistances of 100 m $\Omega$  at 125°C. Again, one low-voltage p-channel MOSFET (FDMS6681Z,  $R_{DS,\text{on}} = 3.2 \text{ m}\Omega$ ) is connected in

---

converter design. However, relatively little impact of a minor change of  $\eta_{\text{exp}}$ , e.g. from 95 % to 97.5 %, on the final losses and total weight is expected and, therefore,  $\eta_{\text{exp}} = 95\%$  is maintained throughout the whole converter design procedure. The conservative value of 95 % is selected in order to take a slight safety margin for the required cooling system into account.

series to each JFET and the 1EDI30J12CP EiceDriver is used.<sup>2</sup>

### Considered weight

The weight attributed to the power semiconductors is equal to the sum of the weights of the eight JFETs, p-channel MOSFETs, and gate drivers, and the belonging PCB. This weight does not include the cooling systems' weights, which are separately considered in Section 6.1.4.

The total weight of all JFETs and p-channel MOSFETs is  $m_{\text{semi}} = 48.8 \text{ g}$  and the PCB and connector's weight is  $49 \text{ g}$ . The total weight of all gate drivers is  $m_{\text{drv}} = 24 \text{ g}$ . This includes eight 1EDI30J12CP EiceDriver devices, the connected SMD resistors and capacitors, and the corresponding part of the PCB with an estimated total surface of  $500 \text{ mm}^2$  (for the two layer PCB with a height of  $1.6 \text{ mm}$  an average density of  $2.24 \text{ g/cm}^3$  is assumed).

### Conduction and switching losses

For the optimization of the cooling system, presented in Section 6.1.4, the losses generated by the converter's semiconductors need to be known. The considered loss model accounts for conduction and switching losses.

The conduction losses are calculated based on the on-state channel resistance at an assumed junction temperature of  $125^\circ\text{C}$ ,

$$P_{T_{1,2,3,4},\text{cond}} = 4 \cdot R_{\text{DS,on,I}} I_{T_{1,2,3,4},\text{rms}}^2 = 4 \cdot R_{\text{DS,on,I}} \frac{I_{\text{ac1,rms}}^2}{2}, \quad (6.3)$$

$$P_{T_{5,6,7,8},\text{cond}} = 4 \cdot R_{\text{DS,on,II}} I_{T_{5,6,7,8},\text{rms}}^2 = 4 \cdot R_{\text{DS,on,II}} \frac{I_{L,\text{rms}}^2}{2}, \quad (6.4)$$

with  $R_{\text{DS,on,I}} = 100 \text{ m}\Omega$  and  $R_{\text{DS,on,II}} = 150 \text{ m}\Omega$ .

In the realized converter prototype each previously used cascode circuit of a JFET and an n-channel MOSFET, cf. [75], is replaced by a series connection of a JFET and a p-channel MOSFET in order to reduce

---

<sup>2</sup>No competitive SiC MOSFETs have been available at the time when the design of the investigated converter has started. Meanwhile, competitive  $1200 \text{ V}$  MOSFETs are available. Thus, the SiC JFETs of the LV-side full bridge could be replaced by SiC MOSFETs (e.g. C2M0025120D manufactured by CREE), which would lower the losses at full load by approximately  $20 \text{ W}$  and increase the full load efficiency by  $0.3 \%$ . Thus, some further weight reduction is feasible with SiC MOSFETs, since the series-connected low-voltage p-channel MOSFETs are not required. The lower losses, furthermore, would allow for a slight reduction of the weight of the heat sink.

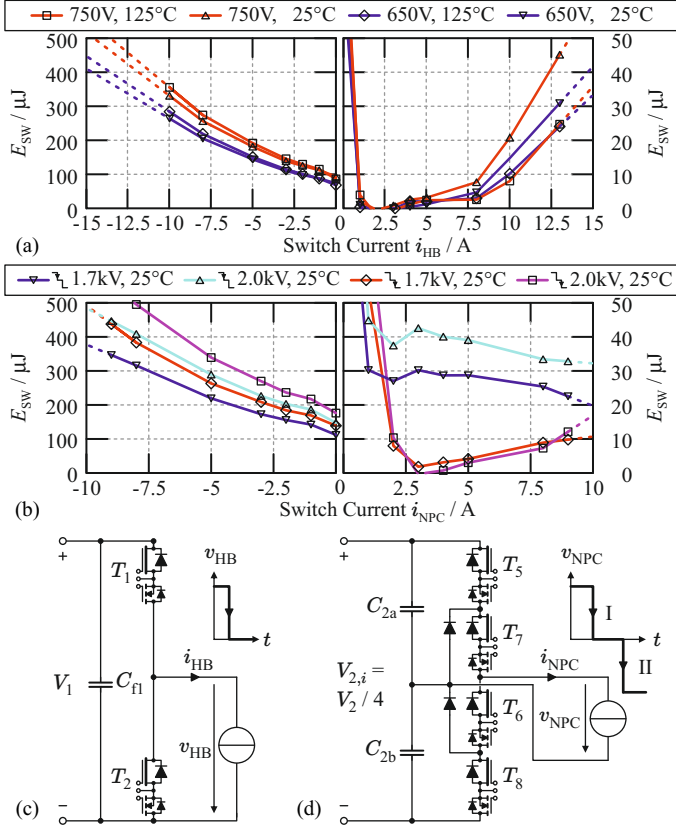
the effective output capacitance of each power switch and to achieve a further reduction of the switching losses. As already mentioned, dedicated gate drivers featuring direct drive technology (1EDI30J12CP manufactured by Infineon) ensure normally-off properties of the power switches. The corresponding switching losses have been measured according to [75] (double pulse measurement) on the final converter PCB in order to account for the implications of parasitic components, e.g. the inductance of the commutation loop. The JFETs have been thermally connected to a heat plate to enable switching loss measurements at different junction temperatures ( $T_j = 25^\circ\text{C}$  and  $125^\circ\text{C}$  are considered). Different switching operations result for the half bridge (HB) and the NPC converters, due to structural differences of these circuits, cf. Section 3.1. In summary, the switching losses of a HB converter, depicted in Fig. 6.4(a), thus only depend on the instantaneous port voltage,  $V_1$ , and output current,  $i_{\text{HB}}$ . The switching losses of the NPC converter, Fig. 6.4(b), additionally depend on the previous states of the switches  $T_5$ ,  $T_6$ ,  $T_7$ , and  $T_8$ : for the NPC converter, different switching losses result if  $v_{\text{ac},2}$  switches from  $\pm V_{2,i}$  to zero (edge with label I in Fig. 6.4(d)) or if  $v_{\text{ac},2}$  switches from zero to  $\pm V_{2,i}$  (edge II).

Fig. 6.4(a) presents the switching losses measured for the full bridge converter at  $V_1 = 650\text{ V}$  and  $750\text{ V}$  and  $T_j = 25^\circ\text{C}$  and  $125^\circ\text{C}$ . For positive currents  $i_{\text{HB}}$  the condition for ZVS is, theoretically, fulfilled and for negative currents  $i_{\text{HB}}$  hard switching occurs. According to these results, low switching losses of less than  $10\ \mu\text{J}$  can be achieved for  $1\text{ A} < i_{\text{HB}} < 8\text{ A}$ .

Fig. 6.4(b) depicts the results obtained for the NPC converter. Similar switching losses are measured for the HB and the NPC converter if the switching operation labeled I in Fig. 6.4(d) is present. For  $2\text{ A} < i_{\text{NPC}} < 10\text{ A}$  increased switching losses result for edge II, due to residual turn-on losses.

In Fig. 6.4(a) and (b) there is a rapid increase in the switching energies when the current is approaching zero. For currents  $0 < i_{\text{HB}} < 1\text{ A}$  and  $0 < i_{\text{NPC}} < 2\text{ A}$  the semiconductor's effective output capacitances are incompletely charged or discharged during the dead time intervals, i.e. residual drain to source voltages remain for the MOSFETs that are turned on after the dead time intervals elapsed and, as a consequence, hard switching operations with turn-on losses result [84].

The switching losses generated by the switches  $T_1 \dots T_4$  and  $T_5 \dots T_8$



**Fig. 6.4:** Measured SiC JFET switching energies with the (1EDI30J12CP) and external gate resistances  $\{R_{off}, R_{on}\} = \{1\ \Omega, 2.6\ \Omega\}$  being used. (a) Infineon IJW120R070T1 1.2 kV/70 m $\Omega$  in a half bridge configuration, (b) Infineon sample 1.7 kV/100 m $\Omega$  in a NPC configuration. (c) and (d) Circuit diagrams used to measure the switching energies in (a) and (b), respectively.

are calculated with

$$P_{T_{1,2,3,4,sw}} = 2f_s [E_{sw}(V_1, i_{HB1}, T_j) + E_{sw}(V_1, i_{HB2}, T_j)], \quad (6.5)$$

$$P_{T_{5,6,7,8,sw}} = 2f_s [E_{sw,I}(V_{2,i}, i_{NPC1}, T_j) + E_{sw,II}(V_{2,i}, i_{NPC2}, T_j)], \quad (6.6)$$

respectively;  $i_{HB1}$ ,  $i_{HB2}$ ,  $i_{NPC1}$ , and  $i_{NPC2}$  denote the instantaneous switch currents at switching, i.e.  $i_{HB1}$  denotes the current switched by

$T_1$  and  $T_2$ ,  $i_{HB2}$  the current switched by  $T_3$  and  $T_4$ ,  $i_{NPC1}$  the current switched by  $T_5$  and  $T_6$ , and  $i_{NPC2}$  the current switched by  $T_7$  and  $T_8$ , cf. Fig. 6.2 and Fig. 6.4(c) and (d). The switching energies are, in case of negative slopes of the voltages  $v_{HB}$  and  $v_{NPC}$ , evaluated for currents  $i_{HB}$  and  $i_{NPC}$  flowing in the directions defined in Fig. 6.4(c) and (d), respectively. The switching energies for positive and negative voltage slopes are equal, since, in steady state operation, only the signs of the bridges' output voltages and currents change during the second half of the switching period.

### 6.1.3 Optimization of the DAB Transformer and Inductor

The optimal design of the HF transformer and the inductor  $L$ , with respect to minimum weight and losses, requires an extensive optimization procedure. In a first step, the transformer and inductor setup is defined according to Fig. 6.5 in order to establish a scalable geometrical transformer and inductor model: Fig. 6.5(a) depicts the top view of the proposed configuration and Fig. 6.5(b) details the core window and defines the respective geometric properties. The transformer and the inductor employ  $n_{tr,core}$  and  $n_{ind,core}$  stacked E-cores, respectively, the LV winding is located close to the inner core leg, the MV winding is placed around the LV winding and encloses the transformer and the inductor cores, and the center core leg of the inductor employs an air gap to achieve the required converter inductance. Insulation with a thickness of 2 mm encloses the MV winding and a 0.2 mm thick insulation encloses the LV winding to achieve the isolation requirements. The copper foils and the heat pipes depicted in Fig. 6.5 are used to transport the dissipated heat from the windings and the core to the heat sink, which is placed on top of the configuration shown in Fig. 6.5(a). Moreover, an aluminum plate with a thickness of 3 mm is mounted to the bottom of the transformer and the inductor; it extracts the core losses from the bottom sides and uses the heat pipes depicted in Fig. 6.5(a) to transport the heat to the heat sink.

The employed design procedure calculates the weights and the losses of transformer and inductor for a high number of different designs. In order to reduce the computation time some constant design parameters, as listed in Tab. 6.3, are used. The remaining design parameter space is given with:

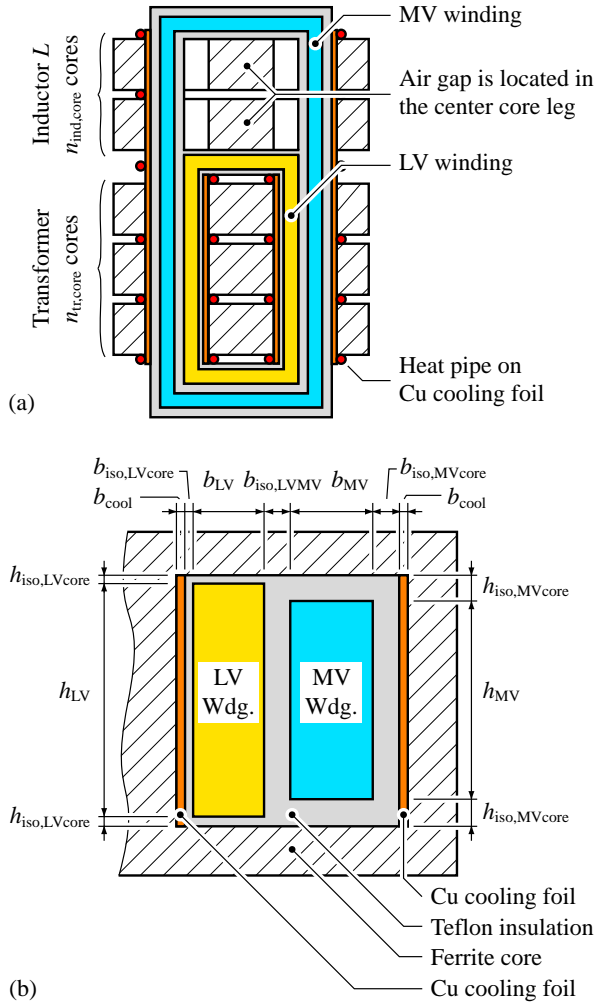


**Fig. 6.5:** (a) Transformer setup with  $n_{tr,core} = 3$  and  $n_{ind,core} = 2$  as seen from top (cross-sectional drawing); the LV winding is located inside and encloses the 3 transformer cores; the MV winding is located around the LV winding due to the isolation requirements and encloses all 5 cores; the copper cooling foils and the heat pipes are used to extract copper and core losses and transport the losses to an external heat sink. (b) Cross-sectional drawing of the transformer winding window (front view); this Figure defines the geometric properties listed in Tab. 6.3.

Property	Value	Description
$B_{\text{tr,peak}}$	200 mT	Peak allowable flux density, transformer
$B_{\text{ind,peak}}$	200 mT	Peak allowable flux density, inductor
$k_{\text{tr}}$	0.85	Max. fill factor, transformer
$k_{\text{ind}}$	0.75	Max. fill factor, ind. (unusable space at air gap)
$b_{\text{iso,LVcore}}$	0.2 mm	Insulation width between LV wdg. and core
$b_{\text{iso,LVMV}}$	2 mm	Insulation width between LV and MV wdgs.
$b_{\text{iso,MVcore}}$	2 mm	Insulation width between MV wdg. and core
$b_{\text{cool}}$	0.3 mm	Thickness of the copper foil used for cooling
$h_{\text{iso,LVcore}}$	0.2 mm	Insulation height between LV wdg. and core
$h_{\text{iso,MVcore}}$	2 mm	Insulation height between MV wdg. and core
$d_{\text{heat pipe}}$	3.0 mm	Diameter of the heat pipe

**Tab. 6.3:** Parameters used for the transformer design.

$$\begin{aligned}
 \vec{N}_1 &= [5 \ 6 \ 7 \ 8 \ 9 \ 10 \ 11 \ \dots \ 39 \ 40]^T, \\
 \vec{N}_2 &= \text{round}(\vec{N}_1 \cdot 1 \text{ kV}/750 \text{ V}), \\
 \vec{n}_{\text{tr,core}} &= [1 \ 2 \ 3 \ 4 \ 5 \ 6 \ 8 \ 10 \ 12 \ 14 \ 16 \ 18 \ 20]^T, \\
 \vec{n}_{\text{ind,core}} &= [1 \ 2 \ 3 \ 4 \ 5 \ 7 \ 10]^T, \\
 \vec{a}_{\text{LVMV}} &= [0.75 \ 1.0 \ 1.25]^T, \\
 \vec{c}_{\text{tr}} &= [\text{E30}/15/7 \ \text{E32}/16/9 \ \text{E42}/21/20 \ \text{E55}/28/21 \\
 &\quad \text{E65}/32/27 \ \text{E70}/33/32 \ \text{UI93}/76/30 \ \text{UU93}/76/30]^T, \\
 \vec{c}_{\text{ind}} &= \vec{c}_{\text{tr}}
 \end{aligned} \tag{6.7}$$

( $N_1$  the number of turns of the LV winding,  $N_2$  the number of turns of the MV winding,  $a_{\text{LVMV}}$  determines the ratio of the width of the LV winding and the width of the MV winding:  $a_{\text{LVMV}} = b_{\text{LV}}/b_{\text{MV}}$ ;  $\vec{c}_{\text{tr}}$  and  $\vec{c}_{\text{ind}}$  contain the considered E-cores). This parameter space still yields 78624 different designs. In order to reduce the number of

stored design results, the employed design procedure, which is outlined in Fig. 6.6, conducts some tests, which are detailed below.

1. Does the MV winding, whose size is defined by the transformer core, fit into the selected inductor core?
2. Is the total weight of the selected cores reasonably low (e.g. less than 2.5 kg)?
3. Is the total weight of transformer and inductor reasonably small?
4. Is the peak flux density in the cores below a reasonable value (e.g. less than 200 mT at a switching frequency of 100 kHz)?
5. Is the total weight (transformer + inductor + heat sink) below a reasonable value?

The winding losses  $P_{\text{tr,wdg}}$  and  $P_{\text{ind,wdg}}$  of the transformer and the inductor are calculated with the respective rms currents and the ac winding resistances at a copper temperature of 100°C. The windings employ litz-wires due to the HF operation, whereas a single strand copper diameter of  $d_c = 0.071$  mm was found to yield the lowest resistance at  $f_S = 100$  kHz. The core losses of the employed N87 ferrite material are approximately determined with the Steinmetz equation,

$$P_{\text{tr,core}} \approx V_{\text{tr,core}} k f_S^\alpha B_{\text{tr,peak}}^\beta \quad \text{and} \quad P_{\text{ind,core}} \approx V_{\text{ind,core}} k f_S^\alpha B_{\text{ind,peak}}^\beta, \quad (6.8)$$

whereas  $V_{\text{tr,core}}$  and  $V_{\text{ind,core}}$  denote the core volumes of the transformer and the inductor, respectively;  $B_{\text{tr,peak}}$  and  $B_{\text{ind,peak}}$  are the respective peak flux densities;  $k$ ,  $\alpha$ , and  $\beta$  are the Steinmetz parameters. At a core temperature of  $T_{\text{core}} = 25^\circ\text{C}$  the core losses are higher than the losses at an elevated core temperature of  $T_{\text{core}} = 100^\circ\text{C}$ . In order to account for increased core losses during the startup phase of the converter  $T_{\text{core}} = 25^\circ\text{C}$  is considered.

The result of the transformer and inductor design is shown in Fig. 6.7. There, each point denotes the total weight and the total dissipated power calculated for a set of input parameters; the red points denote results with a total power loss density  $p_{\text{total}}$  of less than  $1.2 \text{ W/cm}^2$  ( $p_{\text{total}}$  is the total dissipated power per available surface of the cooling foil shown in Fig. 6.5) and the gray points yield  $p_{\text{total}} \geq 1.2 \text{ W/cm}^2$ .

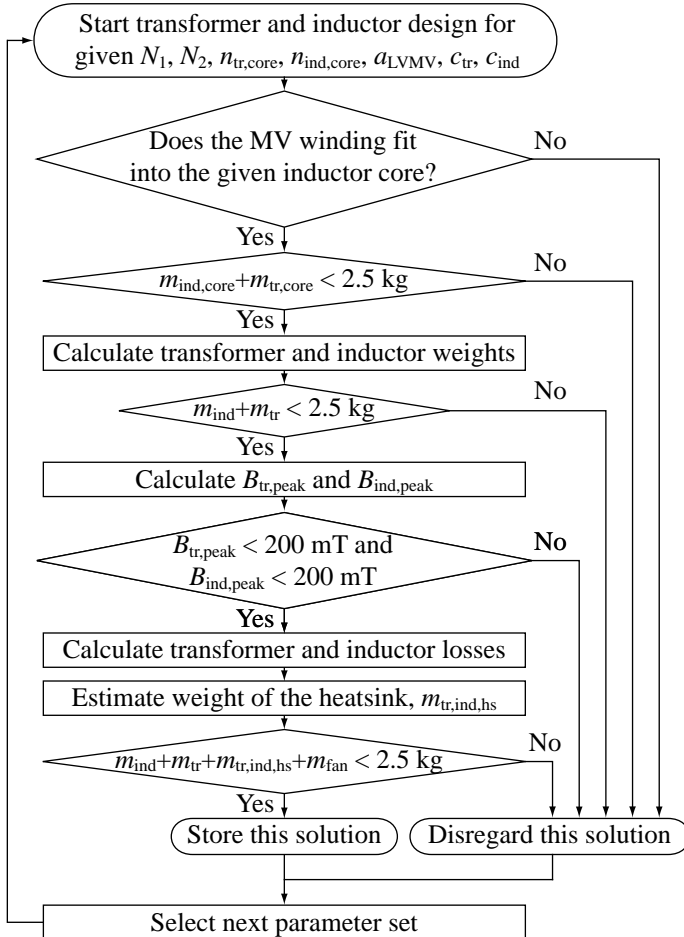


**Fig. 6.6:** Flowchart showing the procedure employed to design the HF transformer and the inductor of the DAB. With this design procedure the results shown in Fig. 6.7 are calculated.

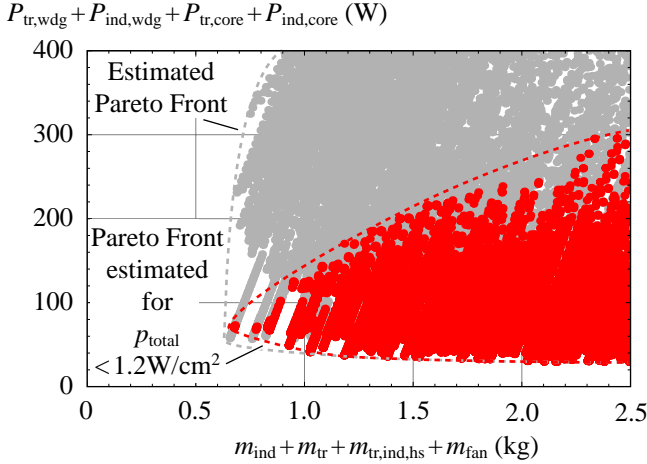


**Fig. 6.7:** Result of the transformer and inductor design; each point denotes the total weight and the maximum dissipated power calculated for a set of input parameters obtained from (6.7). The red points denote a total power loss density  $p_{total}$  of less than  $1.2 \text{ W/cm}^2$  (total dissipated power per available surface of the cooling foil shown in Fig. 6.5) and the gray points are the remaining results with  $p_{total} \geq 1.2 \text{ W/cm}^2$ . The dashed lines denote the estimated Pareto Fronts for  $p_{total} < 1.2 \text{ W/cm}^2$  (red) and  $p_{total} \geq 1.2 \text{ W/cm}^2$  (gray).

The dashed lines in Fig. 6.7 denote the estimated Pareto Fronts for  $p_{total} < 1.2 \text{ W/cm}^2$  (red) and  $p_{total} \geq 1.2 \text{ W/cm}^2$  (gray). According to the depicted Pareto Fronts, a loss reduction is possible by increasing the weight; however, due the side conditions considered in Fig. 6.6, also the maximum losses are limited at a certain weight. The design results for the most lightweight transformer and inductor design with  $p_{total} < 1.2 \text{ W/cm}^2$  are listed in Tab. 6.4. The maximum copper temperatures are calculated for minimum input and output voltages:  $T_{tr,wdg,MV,max} = 149^\circ\text{C}$  and  $T_{tr,wdg,LV,max} = 135^\circ\text{C}$  inside the MV winding and the LV winding, respectively. The maximum temperatures at nominal operation are  $T_{tr,wdg,MV,max} = 131^\circ\text{C}$  and  $T_{tr,wdg,LV,max} = 120^\circ\text{C}$ .

The configuration of the optimized DAB transformer and inductor is depicted in Fig. 6.8(a). The used insulation material is epoxy resin in order to eliminate the creepage path between the adjacent trans-

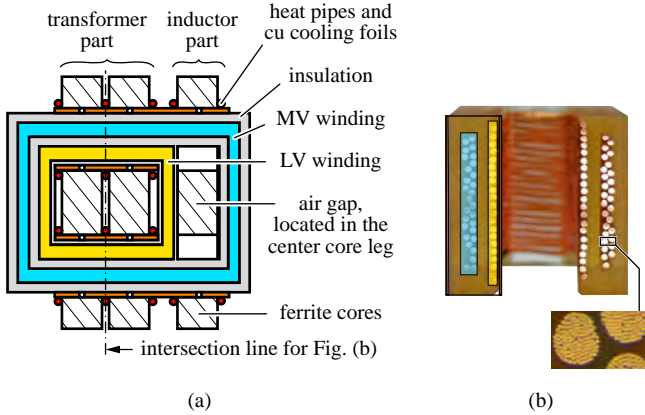


**Fig. 6.8:** (a) Configuration of the optimized DAB transformer and inductor; (b) picture of a cross sectional cut through the realized transformer windings showing the HF litz-wires being embedded in the epoxy resin, which is used for isolation; the turns ratio is  $n = N_{LV}/N_{MV} = 21/28$ , both HF litz-wires are  $200 \times 71 \mu\text{m}$ . The magnified image in the lower right corner enables a detailed view on the embedded HF litz wire.

former windings and between the windings and the core. The MV-side winding is surrounded with 2 mm thick epoxy resin and is considered to withstand dc voltages of more than 10 kV [85–88]. Fig. 6.8 (b) depicts a cross sectional view through the LV- and MV-side transformer windings, embedded in epoxy resin, and shows that the HF litz-wires could be suited into the available space. The weight of the realized DAB transformer and inductor, inclusive copper plates and heat pipes, is 522 g.

#### 6.1.4 Minimum Weight Cooling System

The DAB converter requires a cooling system with three separate heat sinks to dissipate the heat generated by the JFETs of the NPC and FB converters and to actively cool the HF transformer and inductor. Due to the ISOP structure of the dc-dc converter system, cf. Fig. 6.1, voltages of up to 4.75 kV are present between the LV and MV-sides of the first and the fourth DAB converter. Therefore, the galvanic isolation between the MV-side heat sink and all LV-side components, including

Transformer core:	2 stacked E42/21/20 core sets
Inductor core:	single E42/21/20 core set
Number of turns:	$N_{LV} = 21, N_{MV} = 28$
Employed HF litz wire, LV-side:	$200 \times 0.071$ mm
Employed HF litz wire, MV-side:	$200 \times 0.071$ mm
Inductor air gap length:	$l_{\text{air}} = 3.3$ mm

**Tab. 6.4:** Parameters of the DAB transformer and inductor.

the heat sink used to cool the HF transformer and inductor, of which the core is referred to the potential of the minus port of the LV-side, needs to be designed accordingly. Furthermore, the heat sink used for the switches of the FB converter is thermally isolated from the heat sink used to cool the magnetic components, because these heat sinks are operated on different temperatures.<sup>3</sup>

The design of the cooling system is based on previously calculated maximum losses given in [75],<sup>4</sup> which are

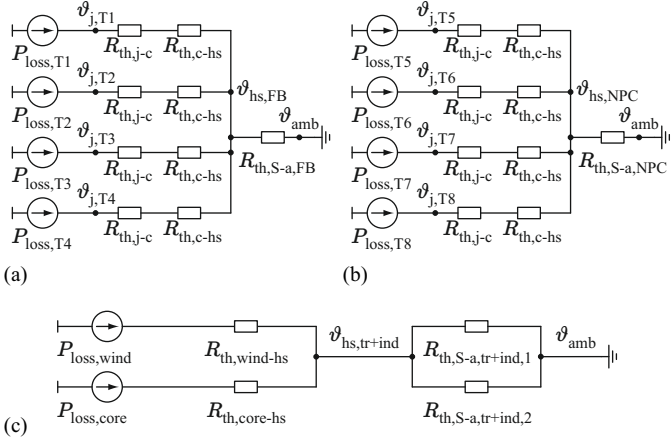
$$P_{\text{loss,FB}} = 57 \text{ W}, P_{\text{loss,NPC}} = 50 \text{ W}, P_{\text{loss,mag}} = 80 \text{ W}.$$

Fig. 6.9 depicts the equivalent thermal networks for all three cooling systems. The thermal networks depicted in Fig. 6.9(a) and Fig. 6.9(b) consider one heat source per JFET, the corresponding junction to case thermal resistances,  $R_{\text{th,j-c}}$ , the thermal resistances of the isolating thermal interfaces,  $R_{\text{th,c-hs}}$ , and the thermal resistances of the heat sinks themselves. For reliability junction temperatures are limited to 120 °C. With this, the thermal resistances given in Fig. 6.9, and the losses listed in [75], the worst case base plate temperatures of the heat sinks required

---

<sup>3</sup>In case of a common heat sink for the LV-side FB converter and the magnetic components, the LV-side semiconductors would heat up the magnetic components additionally.

<sup>4</sup>The revision of the switching loss measurements, using the direct drive technology, presented in 6.1.2 has been carried out with the final converter setup, which already required the fully functional cooling system. For this reason, the achieved reduction of the switching losses was unknown at the time the cooling system has been designed.



**Fig. 6.9:** Thermal networks of the 3 cooling systems: (a) LV-side semiconductors, (b) MV-side semiconductors, and (c) transformer and inductor.

for the FB and NPC converters are

$$\vartheta_{hs,max,FB} = 120^{\circ}\text{C} - 14.25\text{ W} \times 0.94\text{ K/W} = 106^{\circ}\text{C}, \quad (6.9)$$

$$\vartheta_{hs,max,NPC} = 120^{\circ}\text{C} - 12.5\text{ W} \times 0.94\text{ K/W} = 108^{\circ}\text{C}, \quad (6.10)$$

respectively. With a maximum allowed operating ambient temperature of  $\vartheta_{amb,max} = 40^{\circ}\text{C}$  the thermal resistance required for the two heat sinks are calculated according to

$$R_{th,S-a,max,FB} = \frac{\vartheta_{hs,max,FB} - \vartheta_{amb,max}}{4 \times 14.25\text{ W}} = 1.17\text{ K/W}, \quad (6.11)$$

$$R_{th,S-a,max,NPC} = \frac{\vartheta_{hs,max,NPC} - \vartheta_{amb,max}}{4 \times 12.5\text{ W}} = 1.37\text{ K/W}. \quad (6.12)$$

A similar calculation is conducted for the heat sink used to cool the HF transformer and inductor, which leads to the corresponding base plate temperature and the required thermal resistance of the heat sink,

$$\vartheta_{hs,max,mag} = 77^{\circ}\text{C}, \quad (6.13)$$

$$R_{th,S-a,max,tr+ind} = \frac{\vartheta_{hs,max,mag} - \vartheta_{amb,max}}{80\text{ W}} = 0.46\text{ K/W}. \quad (6.14)$$

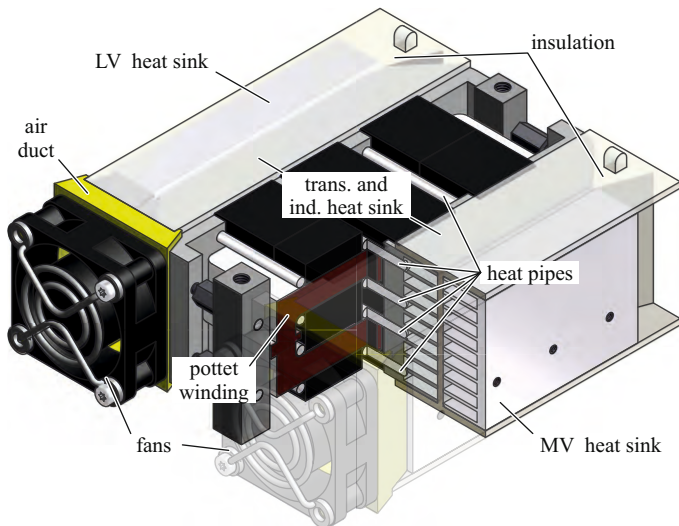


**Fig. 6.10:** CAD model of the final cooling system configuration. Heat pipes from the transformer and inductor connect to heat sinks on both sides. Thermal and electrical insulation separates the heat sinks for the LV- and MV-side semiconductors from the heat sinks cooling the transformer and inductor.

In the quest for achieving a minimum weight DAB converter different heat sink configurations have been investigated and the configuration depicted in Fig. 6.10, which employs four heat sink halves has been identified to be most suitable with respect to minimum weight. Two heat sink halves are used to cool the HF transformer and inductor (due to the comparably low value of  $R_{th,S-a,max,tr+ind}$ , i.e. a relatively high cooling capability required) and the remaining two halves cool the HB and NPC converters, respectively. The heat sink used to cool the magnetic components requires a base plate size of  $A_{hs,tr+in} = 40 \text{ mm} \times 80 \text{ mm}$  to accommodate all heat pipes and ferrite cores. The same base plate size is used for the remaining two heat sink halves in order to allow for a simplified construction of the DAB converter and to allow for sufficiently large distances between adjacent JFETs due to voltage isolation requirements.

Fig. 6.11 presents the minimum cooling system weights, calculated with the optimization algorithm detailed in Section 3.3.3, for different

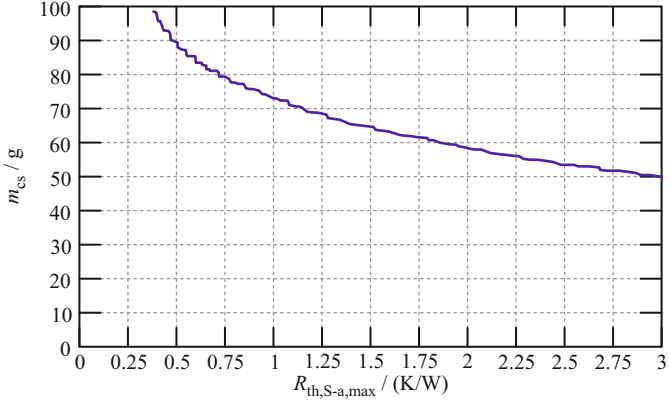


**Fig. 6.11:** Minimum cooling system weights, calculated with the optimization algorithm detailed in Section 3.3.3, for different base plate to ambient thermal resistances of the different cooling system halves, i.e.  $m_{cs} = m_{\text{heat sink halve}} + (m_{\text{fan}} + m_{\text{duct}} + m_{\text{iso}})/2$ . Only the 40 mm x 40 mm fans in Tab. 6.5 are considered.

Name	$\frac{P_{fan}}{W}$	$\frac{L_{fan}}{mm}$	$\frac{m_{fan}}{g}$	$\frac{\dot{V}_{max}}{dm^3/s}$	$\frac{\Delta p_{max}}{Pa}$
GM0504PEV2-8.GN	0.4	6	7.5	2.6	20.0
MC19660	0.5	6	7.5	2.8	25.0
BP402012H-W	1.9	20	40.0	4.0	51.7
1608VL-04W-B60-B00	1.6	20	40.0	5.4	99.3
9GA0412G7001	2.0	15	28.0	6.0	192.0
9GA0412P6G001	2.8	20	35.0	7.1	319.2
412JHH	3.3	25	50.0	6.7	216.3
9L0412J301	3.7	28	55.0	8.5	205.1
9GV0412P3K03	10.1	28	50.0	12.7	416.2
1611FT-D4W-B86-B50	11.4	28	49.0	13.8	736.9
1619FT-04W-B86-B50	12.6	48	71.0	14.1	800.0

**Tab. 6.5:** 40 mm x 40 mm axial fans considered in the optimization.

base plate to ambient thermal resistances of the different cooling system halves, i.e.  $m_{cs} = m_{\text{heat sink halve}} + (m_{\text{fan}} + m_{\text{duct}} + m_{\text{iso}})/2$ ; this optimization considers the fans listed in Tab. 6.5. Because the airflows through the heat sinks are coupled, only symmetric heat sink geometries

	MV-side NPC	LV-side FB	Transformer and ind.
$R_{\text{th,S-a}}$	0.97 K/W	0.97 K/W	$1/2 \times 0.97 \text{ K/W}$
$m_{\text{cs}}$	75 g	75 g	150 g
$n$	9	9	9
$c$	12 mm	12 mm	12 mm
fan	9GA0412G7001	9GA0412G7001	9GA0412G7001
power	$1/2 \times 2 \text{ W}$	$1/2 \times 2 \text{ W}$	2 W
$L$	80 mm	80 mm	80 mm
$b$	40 mm	40 mm	40 mm
$t$	1 mm	1 mm	1 mm
$d$	3 mm	3 mm	3 mm

**Tab. 6.6:** Cooling system properties that feature symmetric heat sinks for all three cooling systems.

are considered, i.e. the heat sinks cooled by one fan feature the same pressure drop characteristics. The properties of the resulting minimum weight cooling systems are listed in Tab. 6.6. The total weight of the cooling system is

$$m_{\text{cs,total}} = m_{\text{cs,FB}} + m_{\text{cs,tr+ind}} + m_{\text{cs,NPC}} = (75 + 2 \times 75 + 75) \text{ g} = 300 \text{ g}. \quad (6.15)$$

### 6.1.5 Design of the Filter Networks

The dc–dc converter is part of a generator / drive system, i.e. power electronic converters are connected to both sides. The DAB converter, therefore, is not required to fulfill specific conducted electromagnetic compatibility standards. Still, filter networks are needed in order to allow for proper converter operation and to enable the DAB converter cells to be embedded in the ISOP structure depicted in Fig. 6.1.<sup>5</sup> Fig. 6.2 depicts the employed filter networks and the list given below motivates the need for the different filter components.

- ▶ The capacitors  $C_{f1}$ ,  $C_{2a}$ , and  $C_{2b}$  are part of the converter topology, provide low inductive commutation loops, and stabilize the supply voltages of the bridges.
- ▶ The network formed with  $L_{f1a}$ ,  $L_{f1b}$ , and  $R_{f1b}$  enables the straightforward paralleling of different DAB converter cells on the LV–side ( $L_{f1b}$  and  $R_{f1b}$  introduce damping at the resonance frequency). For this reason the LV–side port currents of each converter cell,  $i_{Lf}$  in Fig. 6.2, are separately measured and controlled, cf. Section 6.2.
- ▶ The capacitor  $C_{dc}$  is used for energy storage. In the ISOP configuration depicted in Fig. 6.1, a single capacitor is used for four DAB converter cells together. The capacitance of this single dc capacitor then is equal to four times the dc capacitance of a single cell. In case of stand-alone testing of a single cell, e.g. for the purpose of verifying the operability and the achieved efficiency of a single cell (which is the case in this work)  $C_{dc}$  is populated on the PCB of a single DAB converter cell.

The emphasis of the filter design is to achieve reliable converter operation. No analytical weight optimization is carried out, because of the relatively little contributions of the weights of both filters to the total weight of a single DAB converter cell, i.e. total weights of 93 g and 59 g and relative weight contributions of 6% and 4% result for the MV and LV–side filters, respectively. Tab. 6.7 lists the weights of the employed LV filter component.

---

<sup>5</sup>On the MV–side, four 25 kW DAB converter systems, each composed of four single DAB converter cells, are operated in parallel. Therefore, each 25 kW DAB converter system requires a decoupling inductance with a damping network, cf. LV–side filter network depicted in Fig. 6.2, at the corresponding MV–side dc port. For each of these networks a weight of 70 g is estimated, which is less than the additionally allowed weight of 400 g, cf. Section 6.4.

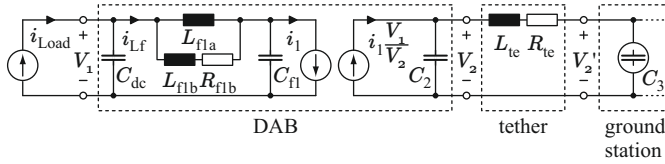


**Fig. 6.12:** Equivalent circuit of the AWT power electronic system, including the simplified circuit model of the DAB presented in [89].

The presented design approach employs the simplified dynamic DAB converter model developed in [89] and the networks connected to the LV- and MV-sides. Fig. 6.12 depicts the considered network, which consists of two current sources to model the innermost part of the DAB converter. It shows a LV-side C-L-C filter with damping network, and, on the MV-side, the equivalent filter capacitance,  $C_2$ , and the equivalent circuits of the tether and the ground station, i.e. the rectifier / inverter system located on the ground, that are relevant for a single DAB converter cell. For the ground station no weight limitation applies and, for this reason, a sufficiently large dc-link capacitance  $C_3$  at the ground station is assumed, which provides a stabilized direct voltage. Thus, in the simplified network depicted in Fig. 6.12, the ground station is replaced by a direct voltage source.

### MV Side Filter

The MV-side of the DAB converter system depicted in Fig. 6.12 is connected to the ground station by means of the tether, which, in terms of simplified electrical properties, is a 1 km long cable with a series resistance of  $9\ \Omega$  and a series inductance of  $360\ \mu\text{H}$ .<sup>6</sup> The network of Fig. 6.12 corresponds to a single DAB converter cell, and

$$L_{te} = 360\ \mu\text{H} \text{ and } R_{te} = 9\ \Omega \quad (6.16)$$

applies, since, on the MV-side, four DAB converter systems are connected in parallel and each of the four converter systems itself is com-

<sup>6</sup>Wave propagation effects are not considered in this work, since the critical frequency related to wave propagation effects calculated for this cable is greater than 100 kHz. Thus, the critical frequency is considerably greater than the bandwidth of the closed current control loop, which is less than 10 kHz, and the corresponding maximum achievable excitation frequency.

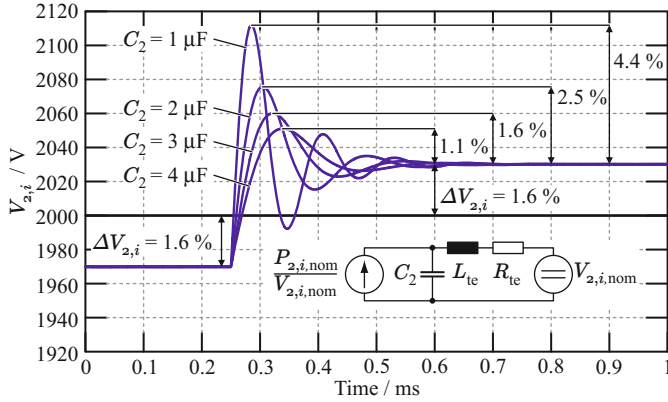


**Fig. 6.13:** Transient response of the MV-side filter voltage  $V_{2,i}$  to a step, in the dc-dc converters transferred power, from  $-P_{\text{nom}}$  to  $P_{\text{nom}}$  for different equivalent capacitances  $C_2$ . The ground station is assumed to be an ideal voltage source. The MV-side of the DAB is a controlled current source [89] and the tether provides a damped inductance of  $360 \mu\text{H}$  with a series resistance of  $9 \Omega$ .

posed of four DAB converter cells that are connected in series, cf. Fig. 6.1. Based on these considerations and with the given converter circuit depicted in Fig. 6.2, the values of the capacitances  $C_{2,a} = C_{2,b}$  constitute the only possible degree of freedom related to the design of the MV-side filter.

Fig. 6.13 shows the transient response of the MV-side filter voltage  $V_{2,i}$  due to a worst-case stepwise change of the MV-side current source. The worst-case is considered to be present if the ground station generates the maximum voltage,  $V_2' = 8 \text{ kV}$  (or, when referring to a single DAB converter,  $V_{2,i}' = 2 \text{ kV}$ ), since any transient voltage change may lead to overvoltage situations at the MV dc ports of the DAB converters. Furthermore the maximum possible current change is considered, which, for  $V_2' = V_{2,i,\text{max}}$ , gives a stepwise change from  $-P_{\text{nom}}/V_{2,i,\text{max}}$  to  $P_{\text{nom}}/V_{2,i,\text{max}}$ . From the results depicted in Fig. 6.13 a capacitance value  $C_2 = 3 \mu\text{F}$  is selected, which, in combination with  $L_{\text{te}}$  gives a characteristic impedance of

$$Z_0 = \sqrt{\frac{L_{\text{te}}}{C_2}} = 11 \Omega > R_{\text{te}} = 9 \Omega \quad (6.17)$$

and a sufficiently damped voltage response results. With this, a maximum instantaneous absolute voltage overshoot (transient + static overvoltage) of 64 V results, which can be easily handled by all MV-side power components that are subject to this overvoltage condition.

Due to the required capacitor rms current of 5 A and the capacitor voltage of up to 1 kV, only film capacitors have been considered for  $C_{2a}$  and  $C_{2b}$ . Each capacitor is implemented with two B32774D1305K 3  $\mu\text{F}/1300\text{ V}/4\text{ A}$  capacitors operated in parallel in order to achieve  $C_{2a} = C_{2b} = 6\ \mu\text{F}$ .

### LV-Side Filter

According to Section 6.2.3, the worst-case dynamic situation is present if the inverters perform a stepwise change of the output current with maximum possible amplitude, e.g. from motor mode at rated power to generator mode at rated power, while the operating mode of the DAB converter system remains unchanged, e.g. the DAB converter system continues to provide energy to the machine inverters at rated power. In this case a superordinate on-board power management unit coordinates the energy flow, i.e. immediately tells the DAB converter system to change the direction of energy flow. Depending on the realization of this power management unit, however, a certain time delay may occur, which is the time between the instant a transient change at an inverter port occurs until the connected DAB converter system adapts to the new situation. In the meantime the dc capacitors need to buffer the energy whereas  $V_1$  may not exceed a maximum voltage of  $V_{1,\max} = 810\text{ V}$  in order to protect the power electronic switches of the DAB converters and the machine inverters. With a digitally controlled system, a time delay of  $T_{\text{delay}} = 50\ \mu\text{s}$  is assumed to be reasonable. Thus, in case of a worst-case dynamic situation, the maximum charge absorbed by the sum of the capacitances  $C_{\text{dc}} + C_{\text{fl}}$  is

$$\Delta Q = \frac{T_{\text{delay}} 2P_{i,\max}}{V_{1,\max} \eta_{\text{exp}}} = 877\ \mu\text{C}, \quad (6.18)$$

which yields the condition

$$C_{\text{dc}} + C_{\text{fl}} > \frac{\Delta Q}{\Delta V_{1,\text{trans}}} = \frac{877\ \mu\text{C}}{810\text{ V} - 750\text{ V}} = 14.6\ \mu\text{F} \quad (6.19)$$

for  $C_{\text{dc}} + C_{\text{fl}}$ . Since  $C_{\text{fl}}$  is subject to high rms currents, cf. Tab. 6.2, it is implemented with suitable film capacitors. The considered converter

prototype operates two  $2\ \mu\text{F} / 1100\ \text{V}$  film capacitors (B32774D0205 manufactured by EPCOS) in parallel. These film capacitors allow for a reasonable steady state voltage ripple, approximately determined with

$$\Delta V_{\text{Cfl}} \leq \frac{\sqrt{2} \max(I_{\text{C1}})}{2\pi 2f_s C_{\text{fl}}} \approx 2\ \text{V}. \quad (6.20)$$

Aluminum electrolytic capacitors are selected for the realization of  $C_{\text{dc}}$ , due to the better capacitance to weight ratio compared to film capacitors and since  $C_{\text{dc}}$  is subject to comparably low capacitor rms currents. Thus, for a single DAB converter cell,  $C_{\text{dc}}$  is realized with two UCYW6220MHD  $22\ \mu\text{F} / 420\ \text{V}$  capacitors in series. The maximum allowable rms current is  $2 \times 285\ \text{mA} = 570\ \text{mA}$  (factor 2 due to HF operation) for this capacitor at  $2f_s = 200\ \text{kHz}$ .

$L_{\text{fla}}$ ,  $L_{\text{flb}}$ , and  $R_{\text{flb}}$  limit the rms current that  $C_{\text{dc}}$  is subject to. In this work,  $I_{\text{Lf}} \leq 250\ \text{mA}$ , i.e. a current less than one half of  $C_{\text{dc}}$ 's maximum allowable rms current, is considered to be a useful assumption, since this leaves sufficient remaining capacitor current capability for the connected machine inverters and allows for comparably small and lightweight components  $L_{\text{fla}}$ ,  $L_{\text{flb}}$ , and  $R_{\text{flb}}$ , cf. Tab. 6.7. In the stopband of the filter the ratio between  $I_{\text{Cf}}$  and  $I_{\text{Lf}}$  is approximately determined with the fundamental frequency approach,

$$\frac{I_{\text{Cdc}}}{I_{\text{Cf}}} \approx \left| \frac{-j(2\pi 2f_s C_{\text{fl}})^{-1}}{j2\pi 2f_s (L_{\text{fla}} || L_{\text{flb}}) + R_{\text{Cdc}} - j(2\pi 2f_s C_{\text{fl}})^{-1}} \right|. \quad (6.21)$$

Note that the FB converter operates the filter at a fundamental frequency of  $2f_s$ . Furthermore, the dc capacitance is replaced by its equivalent series resistance, due to  $2\pi 2f_s C_{\text{dc}} \ll R_{\text{Cdc}}$ . With (6.21)

$$L_{\text{fla}} || L_{\text{flb}} \approx 4.5\ \mu\text{H} \quad (6.22)$$

applies in order to keep  $|I_{\text{Cdc}}/I_{\text{Cfl}}|$  below  $250\ \text{mA}/7\ \text{A}$ . For the filter a maximum resonance rise of 1.5 dB is tolerated, which, according to [90], yields

$$L_{\text{fla}} = 10\ \mu\text{H}, \quad L_{\text{flb}} = 8.2\ \mu\text{H}, \quad \text{and} \quad R_{\text{flb}} = 1.35\ \Omega. \quad (6.23)$$

Symbol	Value	Description	Component	Weight
$L_{\text{com},1}$	40 nH	Half bridge commutation loop inductance	2x TO-247 case, PCB	
$C_b$	100 nF	Commutation loop damping capacitance	2x C4532X7R2J1-04K230KA	2x 304 mg
$R_b$	0.5 $\Omega$	Commutation loop damping	2x 1206 resistor	160 mg
$L_{\text{com},2}$	10 nH	Inductance half bridge to $C_{\text{fl}}$	PCB	
$C_{\text{fl}}$	4.0 $\mu\text{F}$	Full bridge filter capacitance	2x B32774D0205K	18 g
$L_{\text{Cfl}}$	12.5 nH	Equivalent series inductance	$\frac{1}{2}$ x B32774D0205K	
$C_{\text{dc}}$	11.0 $\mu\text{F}$	Input filter capacitance	$\frac{1}{2}$ x UCYW6220MHD	8 g
$R_{\text{Cdc}}$	1.50 $\Omega$	Equivalent series resistance	2x UCYW6220MHD	
$L_{\text{fla}}$	10.0 $\mu\text{H}$	Input filter inductance	T60-26D core with $N=14$ and AWG 16	12.7 g
$L_{\text{flb}}$	8.2 $\mu\text{H}$	Input filter $R$ - $L$ damping inductance	T50-70B core with $N=17$ and AWG 18	3.7 g
$R_{\text{flb}}$	1.35 $\Omega$	Input filter $R$ - $L$ damping resistance	2x 1206 SMD resistors	160 mg
		Interconnections	PCB and connectors	15.6 g

**Tab. 6.7:** LV filter components of the DAB.

## 6.2 Control: Concept and Implementation

At this point, all main power components have been designed or selected. A fully operational DAB converter, however, requires additional circuitries for digital control and auxiliary power supplies, which also add to the total weight. Section 6.2.1 details the concept employed for the digital control of four DAB converter cells operated in the ISOP structure. Due to the required galvanic isolation, additional circuit components, i.e. optical transmitters, optical receivers, and fibers, are needed to establish digital signalling paths between the LV- and MV-sides. Section 6.2.2 details the implemented circuit, which requires solely six such signal paths in order to achieve low weight. The design of the digital controllers is given in 6.2.3.

### 6.2.1 ISOP Structured DAB Control Concept

The ground station controls the voltage applied to the tether at the ground,  $V_2'$ , cf. Fig. 6.1, which defines the voltage at the MV-side dc port of the DAB converter system according to the discussion presented in Section 6.1.5. The DAB can adjust the tether current, since the ground station adapts to the actual tether current. Thus, at the MV dc port, the DAB converter system is free to control the actual operating power by means of current control. This property, in combination with the bidirectional power transfer capability, renders the DAB converter system to be the ideal component regarding the stabilization of the LV-side direct voltage,  $V_1$ .

Fig. 6.14 shows the block diagram for the control of one DAB converter system (out of four), which consists of four series-connected DAB converter cells and features a total power of 25 kW. The below list summarizes the functionalities of the different blocks.

- ▶ The power management unit determines the set values for the current controllers of all DAB converter cells in order to control the LV-side dc bus voltage,  $V_1$ . The calculation of the reference current  $I_{1,\text{ref}}$ , in addition, includes the dc port currents of both machine inverters in order to reduce the required energy buffering capability of  $C_{\text{dc}} + C_{\text{fl}}$ , cf. Section 6.1.5.
- ▶ A master and slave control strategy is chosen to balance the output voltages of all four DAB converter cells: the master module controls the input voltage  $V_1$  and the slave modules ensure an

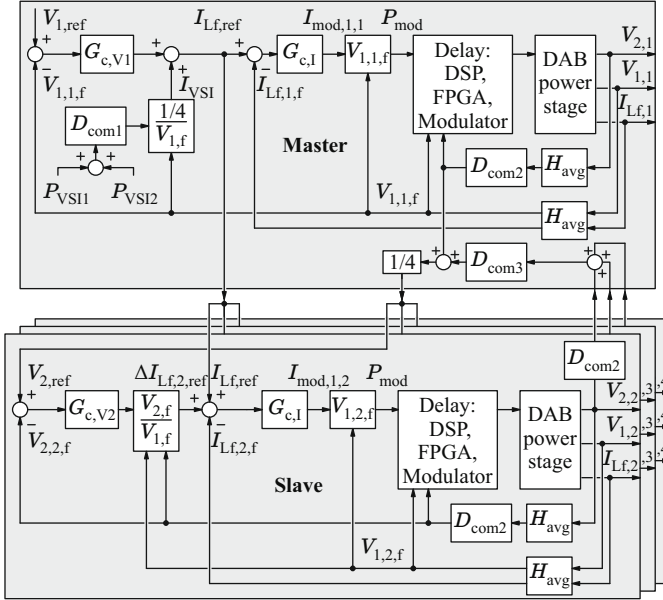


**Fig. 6.14:** Master and slave control block diagram of the dc–dc converter with a feed forward of the instantaneous power requirements of the machine inverters  $P_{VSI1}$  and  $P_{VSI2}$ .

equal distribution of the output voltage  $V_{2,i} = V_{2,ref} = (1/4)V_2$ . The master module provides the reference value  $V_{2,ref}$  to the slave modules as reference, such that each slave module can adjust its own transferred power, in order to balance the series-connected dc-links.

- The current control loop of each converter cell is realized on the LV-side and according to [89].

## 6.2.2 ISOP Structured DAB Controller Implementation

Fig. 6.15 depicts the block diagram of the implemented digital control hardware. Each converter cell incorporates a microcontroller (TMS320-F28335), which handles the communication between the connected con-

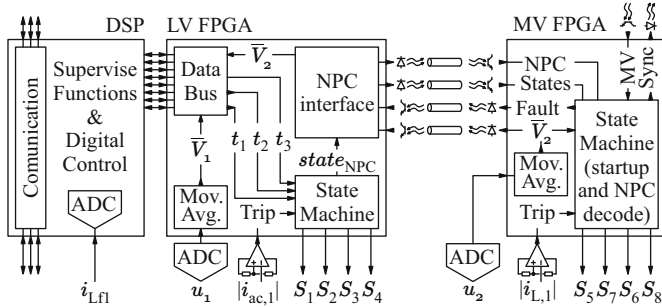


**Fig. 6.15:** Schematic drawing of the control hardware implementation on each DAB converter cell.

verter cells and the LV-side FPGA, monitors currents and voltages, implements the digital control, and calculates the switching times  $t_1$ ,  $t_2$ , and  $t_3$  for minimum transformer rms current according to [83]. The FPGA on the LV-side (LFXP2-5E-5TN14C) runs a state machine that generates the gate signals for the LV-side FB converter and determines the current state of the MV-side NPC converter, which is 0, 1, 2, or 3 (for  $v_{ac2} = -V_{2,i}$ , 0,  $V_{2,i}$ , or to turn all switches off due to a fault on the LV-side, respectively). The state of the NPC converter is transferred to a second FPGA located at the MV-side (LCMXO2-640HC-4TG100I) by means of two optical fibres (2 bits). This second FPGA generates the gate signals for the HV-side NPC converter. The control of both, the HB and the LV converters, considers dead time intervals with durations of 120 ns.

The proposed implementation requires two further optical communication lines between LV- and MV-sides, to transmit the value of the actual port voltage,  $V_{2,i}$ , using a RS232 protocol with a baud rate of 2.5 MBaud and to signalize a fault by reason of an instantaneous overcurrent.<sup>7</sup> Finally, a daisy chain connection of all four series-connected DAB converter cells is achieved with another two optical communication lines. These are needed for an initial synchronization of all four NPC converters and to quickly signalize a fault condition between the

<sup>7</sup>Two protection circuits compare the absolute values of the transformer currents on the LV- and MV-side,  $|i_{ac,1}|$  and  $|i_{L,1}|$ , to maximum set values. The respective FPGA signals a fault in case of an instantaneous overcurrent situation, which turns off the DAB converter system within less than one microsecond.

different converter cells.

The total weight of the digital control circuitry (including PCB, optical transmitters, receivers, and fibres) is 133 g (for one DAB converter cell), the total weight of the optical transmitters, receivers, and fibres is 24.6 g.

### 6.2.3 ISOP Structured DAB Controller Design

The presented controller design is conducted in continuous time and, for this reason, the bilinear transformation with sampling interval  $T_0$

$$z \rightarrow \frac{2 + sT_0}{2 - sT_0} \text{ and } s \rightarrow \frac{2}{T_0} \frac{z - 1}{z + 1}, \quad (6.24)$$

is used to approximately convert transfer functions between the discrete and the continuous time domains [91].

According to the simplified dynamic model given in [89], the DAB converter can be replaced by the two controlled current sources and the respective filter networks depicted in Fig. 6.12. The modulator current  $I_{\text{mod},1,i}$  simultaneously controls both, LV- and MV-side, current sources  $I_{\text{LF},i}$  and  $I_2$ . The considered simplified dynamic DAB converter model, thus, disregards interactions between LV- and MV-sides. The most influential component of the transfer function of the DAB converter without filter networks,  $G_{\text{DAB},0} = I_{\text{LF},i}/I_{\text{mod},1,i}$ , identified in [89] is the time delay introduced by the digital control system,  $T_c = 50 \mu\text{s}$ ,

$$G_{\text{DAB},0}(s) = \frac{I_{\text{LF},i}}{I_{\text{mod},1,i}} = e^{-sT_c}, \quad (6.25)$$

and the total open loop transfer function of a DAB converter cell,  $G_{i,\text{ol}}(s)$ , is

$$G_{i,\text{ol}}(s) = \frac{I_{\text{Lf1},i}}{I_{\text{mod},1,i}} = \frac{Z_{\text{Cf1}}}{Z_{\text{Lf1}} + Z_{\text{Cf1}}} G_{\text{DAB},0}, \text{ with} \quad (6.26)$$

$$Z_{\text{Lf1}} = \frac{sL_{\text{f1a}}(R_{\text{f1b}} + sL_{\text{f1b}})}{sL_{\text{f1a}} + (R_{\text{f1b}} + sL_{\text{f1b}})}, \text{ and } Z_{\text{Cf1}} = \frac{1}{sC_{\text{f1}}}.$$

The transfer functions of the PI-controllers are [89]

$$G_c = K_p \frac{z - (1 - T_c/T_i)}{z - 1} \stackrel{z \rightarrow s}{=} K_p \left( 1 - \frac{T_c}{2T_i} + \frac{1}{sT_i} \right), \quad (6.27)$$

with gain  $K_p$ , integral time constant  $T_i$ , and controller update period time  $T_c$ . The discrete time transfer function of a moving average filter of filter order  $N_s$  is

$$H_{\text{avg}} = \frac{1}{N_s} \sum_{k=0}^{N_s-1} \frac{1}{z^k} \stackrel{z \rightarrow s}{=} \frac{1}{N_s} \sum_{k=0}^{N_s-1} \left( \frac{2 - sT_s}{2 + sT_s} \right)^k, \quad (6.28)$$

where  $N_s = 8$  and  $T_s = 1.25 \mu\text{s}$  apply in this work. Hence, the voltages  $V_1$ ,  $V_{2,i}$  and the filter currents  $I_{Lfi,i}$  are sampled and averaged eight times within each switching period.

In order to achieve a high bandwidth of the current controller, and because the transfer function  $G_{\text{DAB}}$  is essentially a second order low pass filter with a time delay, the current controllers are designed with the optimum amount method with a selected phase margin of  $\varphi_I = 60^\circ$ . For this, the corner frequency of the current controller's transfer function,  $f_{i,I} = 1/(2\pi T_{i,I})$ , is set equal to the frequency, where  $G_{i,ol}$  shows maximum resonant gain,

$$\left| G_{i,ol}(s) \left( j \frac{2\pi}{T_{i,I}} \right) \right| = \max |G_{\text{DAB}}|. \quad (6.29)$$

The current controller gain  $K_{p,I}$  is adjusted to achieve a phase margin of  $\varphi_I = 60^\circ$  at the cross overfrequency  $\omega_{\varphi,I}$  of the loop gain,

$$F_{o,I} = G_{c,I} G_{\text{DAB}} H_{\text{avg}}, \quad (6.30)$$

by solving

$$\angle [F_{o,I}(j\omega_{\varphi,I}) |_{K_{p,I} \rightarrow 1}] \stackrel{!}{=} \varphi_I - \pi \quad (6.31)$$

in order to determine  $\omega_{\varphi,I}$  and, subsequently,

$$|F_{o,I}(j\omega_{\varphi,I})| \stackrel{!}{=} 1 \quad (6.32)$$

to determine  $K_{p,I}$ . The loop gain for the voltage controller used to control  $V_1$  then becomes

$$F_{o,V1} = G_{c,V1} G_{i,cl} H_{\text{avg}} \quad \text{with} \quad G_{i,cl} = \frac{F_{o,I}}{1 + F_{o,I}}, \quad (6.33)$$

where  $G_{cl,I}$  is the transfer function of the closed current control loop. Fig. 6.16 depicts all resulting open- and closed-loop gains.

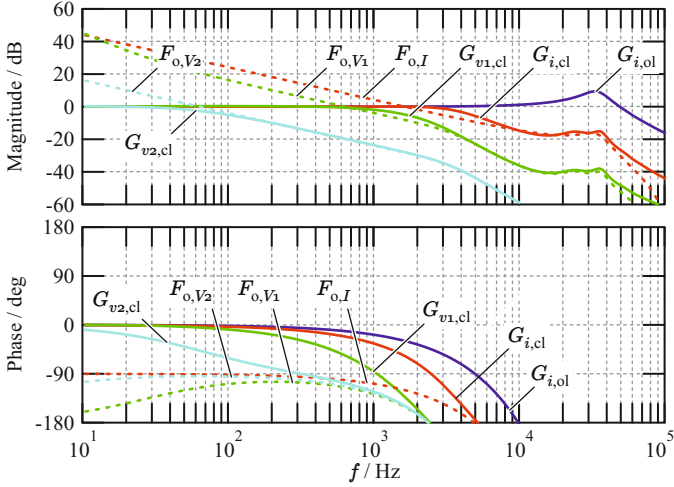


**Fig. 6.16:** Bode plots of the plant's transfer function  $G_{\text{DAB}}$ , the open loop gains  $F_{o,I}$ ,  $F_{o,V1}$ , and  $F_{o,V2}$ , and the closed-loop transfer functions  $G_{cl,I}$ ,  $G_{cl,V1}$ , and  $G_{cl,V2}$ .

The voltage controller of  $V_1$  stabilizes the voltage of the dc bus on the LV-side and, for this purpose, alters the reference current  $I_{1,\text{ref}}$ . This voltage controller is designed with the symmetric optimum method [89], for a phase margin of  $\varphi_{V1} = 60^\circ$ . With this, the controller parameters  $K_{p,V1} = 44.1 \text{ mA/V}$  and  $T_{i,V1} = 5.83 \text{ ms}$  result.

Finally, the voltage controllers for the MV-side voltages of the slave modules,  $V_{2,2}$ ,  $V_{2,3}$ , and  $V_{2,4}$  need to be designed. The MV-side filter capacitors realize a capacitive voltage divider, which enables voltage balancing in case of time varying output currents, i.e. alternating currents. These voltage controllers, therefore, need to compensate unbalancing due to slowly varying output current deviations of the different modules. For this reason, the respective closed-loop bandwidths can be set to a comparably low value,

$$\omega_{\varphi,V2} = \omega_{\varphi,V2,2} = \omega_{\varphi,V2,3} = \omega_{\varphi,V2,4} = \omega_{\varphi,V1}/10, \quad (6.34)$$

i.e. an order of magnitude below  $\omega_{\varphi,V1}$  is selected, cf. Fig. 6.16, in order to avoid interactions between the voltage controller used to stabilize  $V_1$  and the MV-side voltage controllers. The controllers are designed

$G_{c,I}$ for $I_{f,1}$	$G_{c,V1}$ for $V_1$	$G_{c,V2}$ for $V_{2,i}$
$K_{p,I} = 0.293$	$K_{p,V1} = 44.1 \text{ mA/V}$	$K_{p,V2} = 3.2 \text{ mA/V}$
$T_{i,I} = 28.6 \text{ } \mu\text{s}$	$T_{i,V1} = 5.83 \text{ ms}$	$T_{i,V2} = 58.3 \text{ ms}$
$\frac{\omega_{\varphi,I}}{2\pi} = 1.64 \text{ kHz}$	$\frac{\omega_{\varphi,V1}}{2\pi} = 640 \text{ Hz}$	$\frac{\omega_{\varphi,V2}}{2\pi} = 64 \text{ Hz}$

**Tab. 6.8:** dc–dc converter control parameters.

according to the symmetric optimum method for a phase margin of  $\varphi_{V1} = 60^\circ$ . Tab. 6.8 summarizes the resulting controller parameters.

## 6.3 Auxiliary Power Supplies and Startup

Two auxiliary power supplies, situated at the LV- and MV-sides, respectively, provide power to the belonging control, measurement, and gate driver circuits. Section 6.3.1 details the design and implementation of these auxiliary power supplies, which are based on a resonant LLC converter topology, achieve low switching losses (ZVS), high switching frequencies, and low weight. Section 6.3.2, finally, outlines the startup of auxiliary and main power converters and presents the corresponding timing diagram.

### 6.3.1 Auxiliary Power Supplies

Each DAB converter cell employs two auxiliary power supplies, to separately provide power to all MV-side and all LV-side system components.

- ▶ The MV-side auxiliary power supply provides power to:
  - MV-side gate drives,
  - MV-side control and measurement circuitry.
- ▶ The LV-side auxiliary power supply provides power to:
  - LV-side gate drives,
  - LV-side control and measurement circuitry,
  - cooling system fans.

Both auxiliary power supplies are equipped with startup circuitries and feature self-supply capabilities, according to [92].

#### MV-side

The MV-side auxiliary supply provides three output voltages (12 V, 5 V, and 3.3 V) from an input voltage of up to 2 kV. The total required output power is 3 W. From an initial investigation of different topologies [92,93] the integrated LLC resonant converter topology depicted in Fig. 6.17, which is a modified version of the converter presented in [92], has been identified to allow for a low-weight realization, due to negligible switching losses (ZVS), a single magnetic component ( $L_\sigma$  and

$L_\mu$  are integrated into the transformer), a reduced primary-side transformer voltage of  $\pm(1/2)V_{2,i}$ , and the need for only two MOSFETs and two gate drivers.

The realized LLC resonant converter essentially realizes a constant voltage transfer ratio, i.e. the output voltage changes proportional to the input voltage. Thus, three output-side buck converters are connected in series to the LLC converter, according to Fig. 6.17, to provide stable output voltages. The half bridge is operated with fixed duty cycle, dead time intervals, and frequency. Fig. 6.18 illustrates transformer voltage and current waveforms and the corresponding gate signals attained from an electric circuit simulation of the final MV-side auxiliary power supply, cf. Tab. 6.10.

A high switching frequency is desired in order to achieve a low transformer weight. The selected converter topology features ZVS properties and, thus, negligible switching losses can be achieved if MOSFETs are used (Si-MOSFETs are readily available for blocking voltages up to 4.5 kV, cf. Tab. 6.9). A half bridge circuit realized with MOSFETs, however, only achieves very low switching losses if the input current of the resonant network,  $i_1$  in Fig. 6.17, completely charges and discharges the MOSFETs' parasitic capacitances during the dead time interval  $T_{\text{dead}}$  [94], which requires a minimum charge  $Q_{\text{ZVS,min}}$ ,

$$\begin{aligned}
 Q_{\text{ZVS,min}}(V_{2,i}) &= \int_0^{V_{2,i}} [C_{\text{oss}}(v_{\text{HB}}) + C_{\text{oss}}(V_{2,i} - v_{\text{HB}})] dv_{\text{HB}} \\
 &+ \int_0^{V_{2,i}} \left[ C_{\text{Tr},1} \left( \frac{V_{2,i}}{2} - v_{\text{HB}} \right) + C_{\text{PCB}} \left( \frac{V_{2,i}}{2} - v_{\text{HB}} \right) \right] dv_{\text{HB}}. \quad (6.35)
 \end{aligned}$$

Thus, the input current  $i_1$  of the resonant network needs to provide sufficient charge  $Q_{\text{ZVS}}$  during the dead time interval,

$$Q_{\text{ZVS}} = \int_0^{T_{\text{dead}}} i_1(t) dt = \int_0^{T_{\text{dead}}} \frac{N_2}{kN_1} i_2(t) + i_\mu(t) dt \geq Q_{\text{ZVS,min}}. \quad (6.36)$$

The auxiliary power converter is designed such that ZVS is maintained even in the case of no-load. For this reason, the magnetizing inductance of the HF transformer is appropriately designed and facilitates ZVS by means of the magnetizing current,  $i_\mu(t)$ , independent of

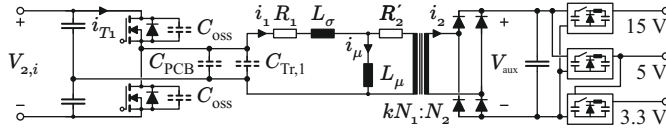


**Fig. 6.17:** Equivalent circuit of the proposed two-stage MV auxiliary supply, implemented for each DAB converter cell. A transformer connected to a split dc-link and a half bridge, which is operated with constant duty cycles and provides an approximately constant voltage conversion ratio,  $V_{\text{aux}} \approx V_{2,i}/57.4$ . The second stage regulates the required auxiliary voltages using low-voltage buck converters.

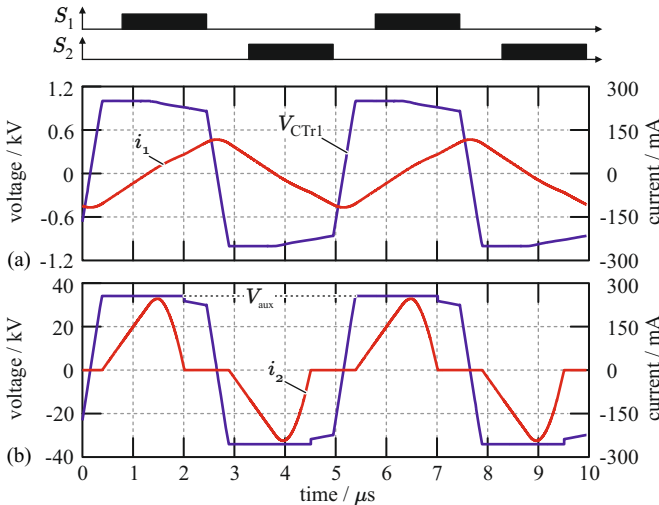


**Fig. 6.18:** Transformer voltage and current waveforms of the designed LLC converter with the half bridge being operated with fixed duty cycles, dead time intervals, and frequency (a) at the primary-side and (b) at the secondary-side of the transformer for  $V_{2,i} = 2 \text{ kV}$  and  $P_{\text{aux}} = 3 \text{ W}$ .

the load condition. Furthermore,

$$i_{\mu}(t) \approx i_1(t) \quad (6.37)$$

is assumed, since initial design results reveal that the magnetizing currents needed to achieve ZVS at the targeted high switching frequency

are, for all three MOSFETs listed in Tab. 6.9, considerably higher than the currents needed to provide the output power. In addition, a comparably long relative duration of the dead time interval of

$$T_{\text{dead}} = \frac{1}{6} \frac{1}{f_s} \quad (6.38)$$

provides sufficient time for the resonant voltage transition to complete, in particular with regard to the estimation of the maximum feasible switching frequency, which is estimated in the following.

Due to the long relative dead time (6.38) the waveform of the transformer magnetizing current,  $i_\mu(t)$ , is approximated with a sinusoidal waveform,

$$i_\mu(t) \approx I_{\mu,\text{peak}} \sin(2\pi f_s t), \quad (6.39)$$

cf. Fig. 6.18. With this and (6.36) the charge  $Q_{\text{ZVS}}$  can be calculated,

$$Q_{\text{ZVS}} = \int_{-1/(12f_s)}^{1/(12f_s)} I_{\mu,\text{peak}} \cos(2\pi f_s t) dt = \frac{I_{\mu,\text{peak}}}{2\pi f_s}. \quad (6.40)$$

Subsequently, under the assumption that  $Q_{\text{ZVS}} = Q_{\text{ZVS},\text{min}}$  and with (6.37)–(6.39) the conduction losses of the MOSFETs,

$$P_{\text{T,loss}} = R_{\text{ds,on}} I_{\text{T,rms}}^2 = R_{\text{ds,on}} I_{\mu,\text{peak}}^2 \frac{4\pi - 3\sqrt{3}}{24\pi}, \quad (6.41)$$

can be calculated, which are limited to

$$P_{\text{T,loss,max}} = \frac{T_j - T_{\text{amb}}}{R_{\text{th,j-c}} + R_{\text{th,c-a}}} \approx \frac{80^\circ\text{C}}{60\text{K/W}} \approx 1.3\text{W} \quad (6.42)$$

per MOSFET, since passive cooling without additional heat sink is considered [95]. The maximum switching frequency is obtained from (6.40) and (6.41), by eliminating  $I_{\mu,\text{peak}}$ , for  $Q_{\text{ZVS}} = Q_{\text{ZVS},\text{min}}$ ,

$$f_s \leq \sqrt{\frac{6 P_{\text{T,loss,max}}}{\pi(4\pi - 3\sqrt{3})}} \frac{1}{\sqrt{R_{\text{ds,on}} Q_{\text{ZVS},\text{min}}}}. \quad (6.43)$$

Tab. 6.9 summarizes the characteristic values for three Si-MOSFETs with blocking voltages of 4.5 kV and for  $C_{\text{Tr},1} = 2\text{pF}$  and  $C_{\text{PCB}} = 3\text{pF}$ . Based on this result the switch IXTA02N450HV is selected. However,

Device	$R_{ds,on}$ @ 125 °C	$Q_{oss}$ @ 2 kV	$Q_{ZVS,min}$ @ 2 kV	$f_{s,max}$	weight
IXTA02N450HV	1500 $\Omega$	33.4 nC	43.4 nC	345 kHz	2.5 g
IXTT1N450HV	160 $\Omega$	131.6 nC	141.6 nC	324 kHz	4.0 g
IXTL2N450	40 $\Omega$	438.2 nC	448.2 nC	205 kHz	8.0 g

**Tab. 6.9:** Characteristic values determined for three different Si-MOSFETS with maximum drain source voltages of 4.5 kV.

$N_1 = 180$	$N_2 = 7$	$k = 89.3 \%$
$R_1 = 21 \Omega$	$L_\mu = 7.46 \text{ mH}$	$L_\sigma = 1.89 \text{ mH}$
$R'_2 = 30 \Omega$	$C_{Tr,1} = 2 \text{ pF}$	$C_{PCB} = 3 \text{ pF}$

**Tab. 6.10:** Parameters of the equivalent circuit of the MV-side auxiliary supply's HF transformer depicted in Fig. 6.19 and 6.20.

a reduced final switching frequency of  $f_s = 200 \text{ kHz}$ , well below the calculated theoretical maximum frequency of  $f_{s,max} = 345 \text{ kHz}$  is selected, since (6.43) is an approximation and neglects turn-off losses and conduction losses due to the load current.

According to (6.40) and (6.41) the peak value of the magnetizing current is bounded to

$$2\pi f_s Q_{ZVS,min} < I_{\mu,peak} < \sqrt{\frac{24\pi}{4\pi - 3\sqrt{3}} \frac{P_{T,loss,max}}{R_{ds,on}}} \quad (6.44)$$

$$55 \text{ mA} < I_{\mu,peak} < 94 \text{ mA},$$

which requires a transformer primary inductance of

$$L_1 = L_\sigma + L_\mu = \frac{V_{2,i}/2}{I_{\mu,peak}} \frac{1}{2\pi f_s} \in [8.45 \text{ mH}, 14.5 \text{ mH}]. \quad (6.45)$$

In order to adjust the primary inductance independently of the number of primary turns and yield a great number of degrees of freedom, stacked E-core transformer designs with an air gap in the magnetic

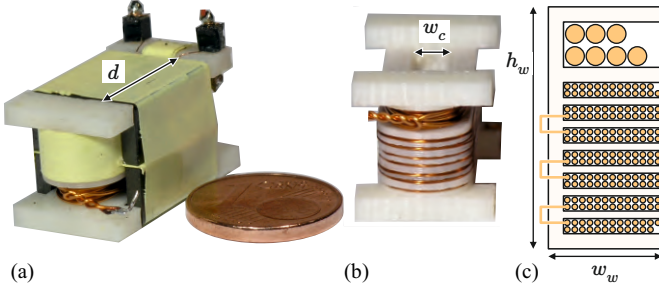


**Fig. 6.19:** (a) MV-side auxiliary transformer with four E 13/7/4 N87 core pairs next to a one cent (Euro) coin; (b) photograph of the 3D printed bobbin, with 180 turns of 0.1 mm diameter and 7 turn of 0.45 mm diameter enameled copper wire; (c) Schematic drawing of the chosen winding topology which features a low primary winding capacitance  $C_{Tr,1}$  [96].

path are considered. The winding topology is chosen, such that a small parasitic primary winding capacitance results [96]. Fig. 6.19 shows the implemented MV auxiliary transformer and a schematic drawing of the winding topology.

For a given core cross-sectional area  $A_c$  the number of primary turns must be

$$N_1 \geq \frac{V_{2,i}/2}{4 f_s A_c B_{\max}}, \quad (6.46)$$

with the maximum flux density  $B_{\max} = 150$  mT for the considered ferrite cores. In order to calculate the number of secondary turns, the leakage inductance  $L_\sigma$  needs to be estimated first to determine the transformer coupling

$$k = \sqrt{\frac{L_\mu}{L_\mu + L_\sigma}}. \quad (6.47)$$

The number of secondary turns is chosen, such that the transformer output voltage does not exceed the maximum tolerated auxiliary dc-link voltage  $V_{\text{aux,max}} = 36$  V provided to the auxiliary buck converters under no load conditions, cf. Fig. 6.17,

$$N_2 = \frac{V_{2,i}/2}{k N_1} \cdot V_{\text{aux,max}}. \quad (6.48)$$

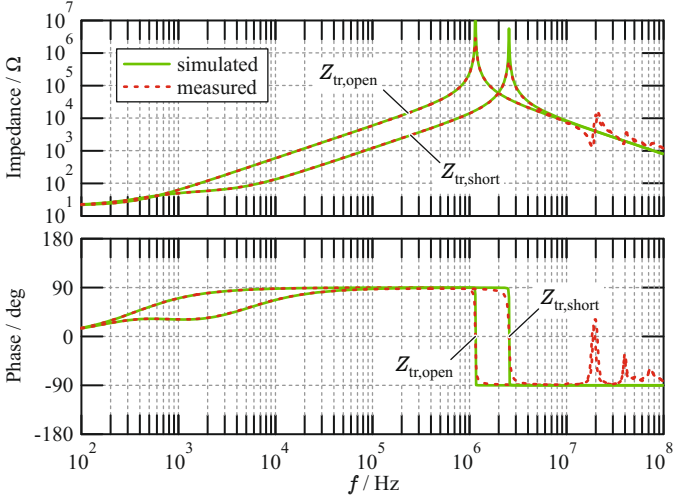


**Fig. 6.20:** Measured and simulated impedance of the MV auxiliary transformer seen from the primary-side terminals with secondary-side open,  $Z_{tr,open}$ , and short circuited,  $Z_{tr,short}$ , terminals.

The leakage inductance is estimated as

$$L_{\sigma} \approx \mu_0 \left( \underbrace{N_1^2 \frac{2}{3} \frac{d h_w}{w_w}}_{\text{inside core}} + \underbrace{N_1^2 \frac{\pi (w_w + 2w_c)^2}{16 h_w}}_{\text{outside core}} \right), \quad (6.49)$$

with the height  $h_w$  and width  $w_w$  of the core's winding window, the width of the core center leg  $w_c$ , and the depth of the E-core stack  $d$ .

The chosen transformer consists of four E 13/7/4 N87 core pairs, a 3D printed bobbin, 180 turns of 0.1 mm diameter and 7 turns of 0.45 mm diameter enameled copper wire. The equivalent circuit parameters are listed in Tab. 6.10. They were obtained with a least squares fit of the transformer model impedance and the impedances measured with the Agilent 4294A precision impedance analyzer. Fig. 6.20 shows the measured and simulated impedances of the MV auxiliary transformer seen from the primary-side terminals with the secondary-side terminals open and short circuited.

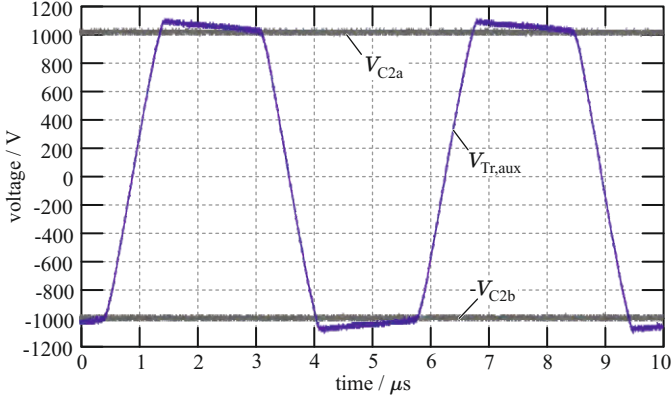


**Fig. 6.21:** Voltage waveform at rated input voltage of  $V_{2,i} = 2\text{ kV}$  and  $P_{\text{aux}} = 3\text{ W}$ . The smooth transitions of the auxiliary transformer voltage waveform show that the ZVS conditions are fulfilled.

Fig. 6.20 shows that the chosen equivalent circuit, cf. Fig. 6.17, models the transformer behavior well for frequencies below 1 MHz.

Fig. 6.21 depicts the measured ac voltage applied to the transformer of the MV-side auxiliary power supply and the voltages across  $C_{2a}$  and  $C_{2b}$  at  $V_{2,i} = 2\text{ kV}$ . The shown smooth transitions of the auxiliary transformer voltage indicate that zero-voltage turn-on is achieved.<sup>8</sup>

The point of load buck converters depicted in Fig. 6.17 are designed for an operating input voltage range of  $V_{\text{aux}} \in [16\text{ V}, 36\text{ V}]$ , which maps to a useful operating input voltage range of the MV-side auxiliary power supply of

$$V_{2,i} \approx 2 \frac{kN_1}{N_2} \frac{L_\sigma + L_\mu}{L_\mu} V_{\text{aux}} \in [1\text{ kV}, 2\text{ kV}]. \quad (6.50)$$

The load dependency of  $V_{\text{aux}}$  is negligible, as long as

$$\frac{N_2}{kN_1} i_2(t) \ll i_\mu(t), \quad (6.51)$$

i.e.  $V_{\text{aux}}$  is not load dependent in this work. Tab. 6.11 summarizes all weights of the MV-side auxiliary power supply components.

<sup>8</sup> It is to be mentioned here that the input capacitance of the differential probe, which was used to measure the auxiliary transformer voltage, adds approximately 7 pF to  $C_{\text{Tr},1}$  and  $C_{\text{PCB}}$ .

Component	Weight	Component	Weight
2×4.5 kV Switches	5 g	2× R10 Gate transformers	2 g
2× SLF7055 Inductors	1.6 g	4× E 13/7/4 N87 Core pairs	8 g
PCB	8 g	Components and connectors	9.4 g
Total weight 34 g			

**Tab. 6.11:** Summary of the MV auxiliary supply components.

Component	Weight	Component	Weight
2×1.2 kV Switches	8 g	2× R10 Gate transformers	2 g
3× SLF7055 Inductors	2.4 g	4× E 13/7/4 N87 Core pairs	8 g
PCB	7 g	Components and connectors	4.6 g
Total weight 32 g			

**Tab. 6.12:** Summary of the LV auxiliary supply components.

## LV-Side

The same converter topologies and the same power supply structures are selected for the LV and the MV auxiliary power supplies, cf. Fig. 6.17. However, devices with a lower  $\sqrt{R_{ds,on}}Q_{oss}$  product (cf. (6.43)) are available for the LV-side, due to the lower input voltage requirements,  $V_1 \in [650 \text{ V}, 750 \text{ V}]$ , and thus the design of the LV-side supply is less challenging. Tab. 6.12 summarizes all weights of the LV-side auxiliary power supply components.

### 6.3.2 Startup

The ground station provides initial power to the AWT system and gradually increases the voltage  $V_2$  with a maximum voltage slope of  $(dV/dt)_{\max} = 200 \text{ V/ms}$  in order to avoid overvoltage at the MV port of the dc-dc converter system. This initial power is used to successively start the dc-dc converter system and the inverters, i.e. the connected machine inverters are deactivated during this time interval, to avoid any unnecessary load. With the power system of the AWT being fully

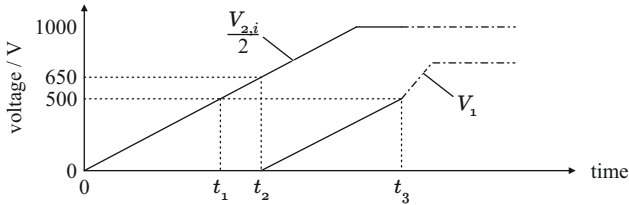


**Fig. 6.22:** Timing diagram of the DAB startup sequence.

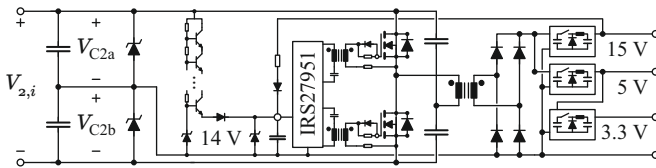


**Fig. 6.23:** Equivalent circuit of the additional circuitry facilitating a smooth startup of the system. The TVS diodes clamp the voltages across  $C_{2a}$  and  $C_{2b}$  in order to protect the NPC dc-link capacitors and semiconductor switches. The linear regulator, implemented as a series connection of bipolar transistors, [65], provides the initial power and is turned off when the 15 V buck converter provides its regulated output voltage.

functional, the AWT system can be lifted from the ground to the operational altitude, where it transitions into the generation trajectory, i.e. switches from motor to generator mode of operation.

The below list summarizes how the dc-dc converter system is started and Fig. 6.22 illustrates the corresponding timing diagram.

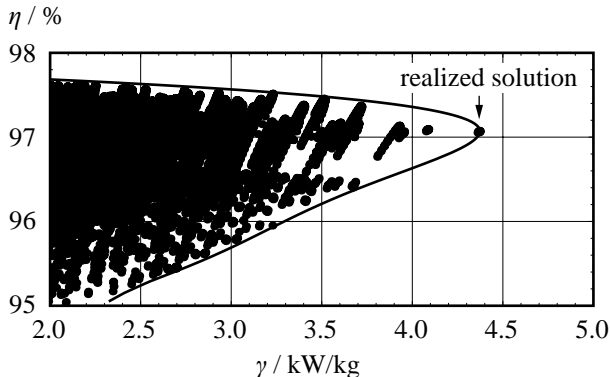
1.  $V_{2,i}/2 < 500 \text{ V}$  ( $0 < t < t_1$  in Fig. 6.22): a linear regulator, realized with 12 bipolar transistors (FCX605TA) connected in series [65], supplies the IRS27951 self-oscillating IC of the MV-side auxiliary power supply continuously. The converter system is designed such that the linear regulator does not overheat for  $V_{2,i} < 1 \text{ kV}$ . Furthermore, unequal voltages  $V_{C_{2a}}$  and  $V_{C_{2b}}$  result due to unequal currents being drawn from  $C_{2a}$  and  $C_{2b}$ . TVS diodes with clamping voltages of 1.2 kV, cf. Fig. 6.23, are used to prevent critical overvoltage situations.

2.  $500\text{ V} < V_{2,i}/2 < 650\text{ V}$  ( $t_1 < t < t_2$  in Fig. 6.22): above 1 kV the 15 V point of load (POL) buck converter provides a stable output voltage to the MV-side auxiliary supply. Thus, the auxiliary power supply operates in the self sustainable mode and the linear regulator is turned off. All three POL converters depicted in Fig. 6.23 provide stable output voltages.
3.  $V_{2,i}/2 > 650\text{ V}$  (startup mode of the DAB converter,  $t_2 < t < t_3$  in Fig. 6.1 and 6.2): active operation of the MV-side NPC converters, passive diode rectifier operation of the LV-side full bridge. The FPGAs located at the DAB converters' MV-sides communicate with each other to achieve a synchronous start at  $t = t_3$  and, thereafter, linearly increase the duty ratios  $D_2$  from 0 to 0.475 within 2s. With this strategy, the LV-side dc-link voltage,  $V_1$ , is built up at a limited maximum tether rms currents of 1 A.
4.  $V_1 > 500\text{ V}$  ( $t_4 < t$  in Fig. 6.22): all LV-side auxiliary power supplies and the complete circuitries needed for the digital control are started up and self sustaining. The main microcontrollers initiate the respective DAB converters in order to make them ready for closed-loop control.

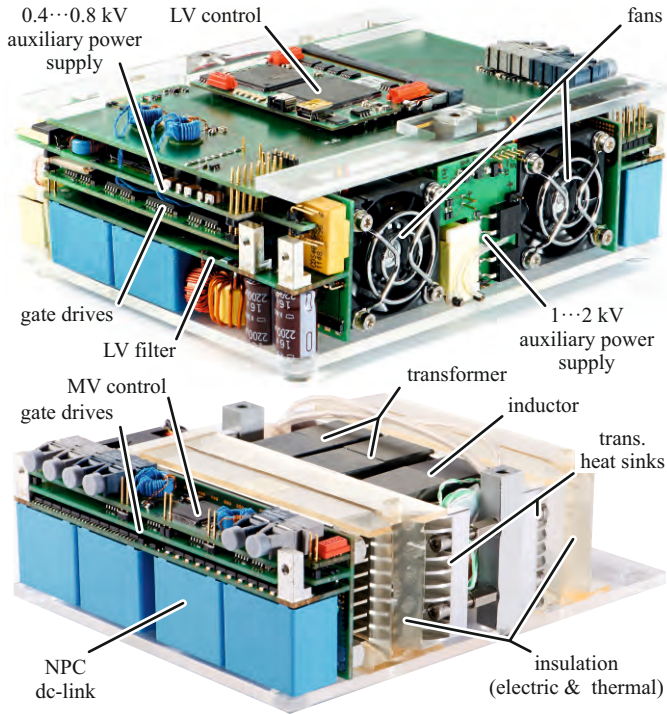
## 6.4 Hardware Prototype

Fig. 6.24 depicts the Pareto Front determined for a single DAB converter cell. Based on this Pareto Front the design point which leads to the maximum power-to-weight ratio of 4.35 kW/kg, at a calculated efficiency of 97.1%, has been selected for hardware implementation. The corresponding realized converter prototype is shown in Fig. 6.25. The total weight of this 6.25 kW converter system is 1.46 kg, its power-to-weight ratio is 4.28 kW/kg (1.94 kW/lb), and the power density is 5.15 kW/dm<sup>3</sup>. This leaves a margin of 100 g per cell, with respect to the specifications listed in Tab. 6.1, to facilitate the interconnections and eventually required additional filter components, cf. Section 6.1.5.

Fig. 6.26 (a) and (b) illustrate the partitioning of the DAB weight by function and materials, respectively. According to Fig. 6.26 (a), the total weight of transformer, inductor, and cooling system is approximately 60% of the total system weight. This result confirms the strong impact of these components' weights on the total system weight and justifies the selected optimization strategy. The DAB converter system, however, also requires the remaining converter parts, of which the weights of the remaining circuits add up to 29% and structural elements, e.g.



**Fig. 6.24:** Pareto Front calculated for a single DAB converter cell; the different dots depicted in this graph correspond to different designs of the HF transformer and inductor. The presented hardware prototype is a realization of the right-most design point which leads to the maximum feasible power-to-weight ratio of 4.35 kW/kg at a calculated efficiency of 97.1%.



**Fig. 6.25:** Photograph of the 6.25 kW converter prototype, (a) front view, (b) rear view without the LV-side components. The total system weight is 1.46 kg. The achieved power-to-weight ratio is 4.28 kW/kg and the power density is 5.15 kW/dm<sup>3</sup>.

screws, add up to 11 % of the total weight.

According to Fig. 6.26 (b), the transformer core and winding account for 31 % and 5 % of the total system weight, respectively. Furthermore, the weight needed for the transformer cooling system accounts for 14 % of the total weight.

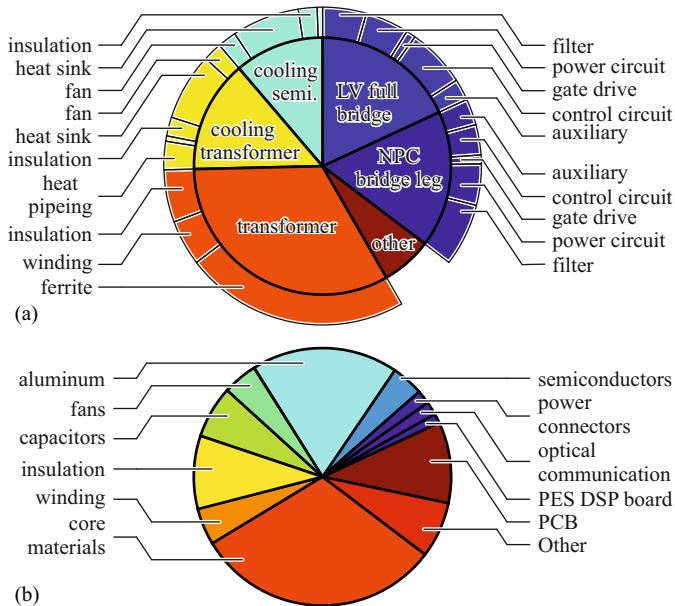


**Fig. 6.26:** Pie charts of the partitioning of the DAB weight by (a) function and (b) materials. The total system weight is 1.46 kg.

### 6.4.1 Efficiency and Temperature Measurements

Fig. 6.27 shows the measured voltage and current waveforms at nominal load, Fig. 6.28 depicts the measurement setup. A series and parallel interconnection of four 600 V/10 A dc power supplies (Xantrex XDC 600-10) provides sufficient voltage and current to the LV-side of the DAB converter. The 1 mH inductor decouples the dc power supplies from the DAB converter in order to prevent parasitic oscillations between the output capacitors of the dc power supplies and the LV-side dc-link. A Yokogawa WT3000 precision power analyzer measures the dc input and output powers. The DAB converter controls the output voltage to  $V_{2,i} = 2V_1/n$ . An adjustable resistive load, attached to the positive and negative terminals of the MV-side dc-link, is used to set the requested output power. The converter has reached thermal equilibrium in every single measurement point. Fig. 6.29 summarizes the obtained loss and efficiency measurement results. The converter achieves a maximum

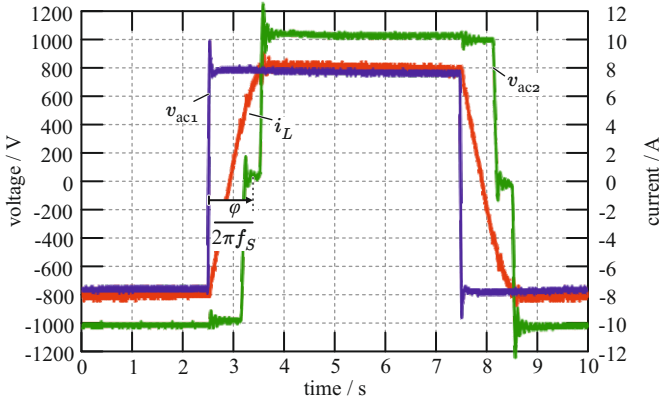


**Fig. 6.27:** Measured voltage and current waveforms at nominal load.

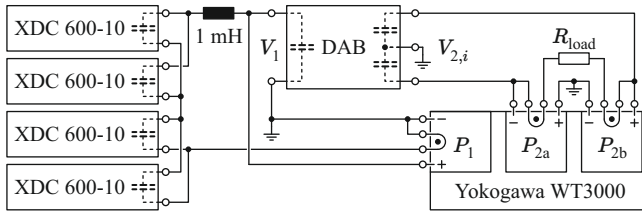


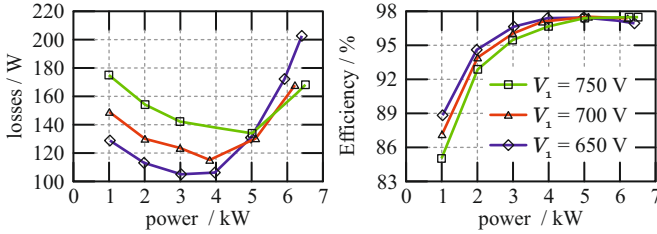
**Fig. 6.28:** Schematic of the measurement setup with four Xantrex XDC 600-10 dc-power supplies and a Yokogawa WT3000 precision power analyzer.

efficiency of 97.5 % at  $V_1 = 700$  V and  $P_{2,i} = 5$  kW.

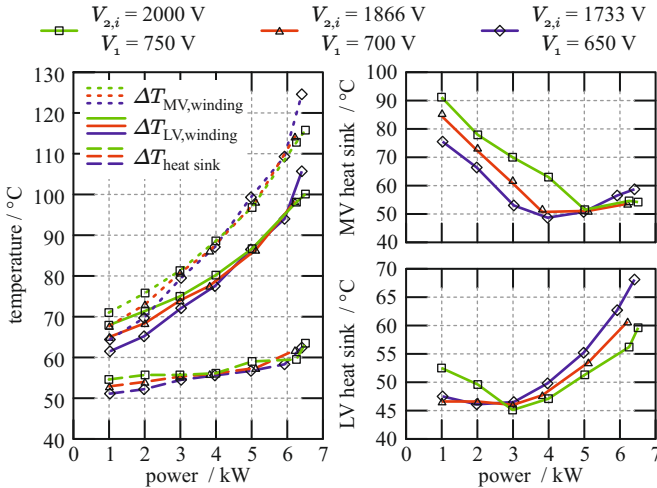
Fig. 6.30 depicts the measured temperature rises of the four heat sink halves and the hot spots of the MV- and LV-side transformer windings<sup>9</sup> with respect to an ambient air temperature of 40 °C. The temperature measurements are carried out with K-type thermo-couples and Fluke 187 multimeters.

Fig. 6.30 illustrates the dependency of the loss allocation with varying load  $P_2$ . For the LV-side FB the losses are to be attributed predominantly to conduction losses while the contribution of the ZVS losses is

<sup>9</sup>The winding hot spots are assumed to be in the middle of the inductor end turns of the MV-side winding and inside the end turns of the LV-side winding on the opposite side of the transformer.



**Fig. 6.29:** Measured losses and efficiency of the DAB converter cell prototype. All operating points feature the voltage conversion ratio  $V_{2,i} = 2V_1/n$ .



**Fig. 6.30:** Measured temperatures of the DAB converter cell prototype. The temperatures are scaled to 40 °C ambient temperature. All operating points feature the voltage conversion ratio  $V_{2,i} = 2V_1/n$ .

comparably small at the switching frequency of 100 kHz. The measured ZVS losses and corresponding temperature rises are well below the values originally estimated. This difference can be attributed to the use of the dedicated JFET EiceDriver 1EDI30J12CP instead of a JFET n-channel MOSFET cascade configuration as in [75]. The same holds true for the ZVS losses at the MV-side NPC bridge leg. However, for loads below  $P_2 = 3\text{ kW}$  the switching losses, due to residual turn-on

or partial ZVS losses of the NPC bridge leg are considerably larger than the losses at the rated power of  $P_2 = 6.25$  kW. In this work, the maximum temperature rise of the MV-side heat sink (at  $P_2 = 1$  kW and  $V_{2,i} = 2$  kV) is approximately  $50^\circ\text{C}$  and significantly exceeds the allowed temperature rise of  $40^\circ\text{C}$ . However, with further control efforts the losses at low transferred powers can be reduced, e.g. through power cycling strategies. For the transformer and inductor the total losses approximately double from  $P_2 = 1$  kW to full output power  $P_2 = 6.25$  kW, which shows an approximately even distribution between the core and winding losses. For the magnetic component the measured MV winding hot spot temperature is most sensitive to the transferred power. This result is to be expected and underlines the need for an active cooling system that reduces the thermal resistance of the MV winding, which is engulfed by a 2 mm layer of electric insulation.

The power consumption of the MV-side auxiliary power supply is approximately 7 W and the LV-side auxiliary power supply requires an input power of approximately 12 W, since it also provides power to the two fans for the cooling system.

At the designed operating point,  $V_1 = 650$  V,  $V_{2,i} = 1733$  V, and  $P_{2,i} = 6.25$  W the calculated and the measured efficiencies are 97.3% and 97%, respectively.

## 6.4.2 Cost Decomposition

Besides the weight and the efficiency of the converter, the cost is an important parameter for industry. For this reason a cost estimation based on the methods and models presented in [97] is performed. The results are summarized in Fig. 6.31. The analysis yields material costs at a production volume of more than 5'000 converters of approximately 350 € per DAB converter cell, i.e. 56 €/kW.

The contribution of the passive power components to the total material costs is 8.2%, i.e. the filter components and the transformer and inductor; the contribution of the DAB power semiconductors is 23.5%, i.e. JFETs, p-channel MOSFET, SiC diodes and protective TVS diodes; and the cooling system contributes with 6.1%, where the majority of the costs are attributed to the two fans. According to the result of this estimation these power components add up to 38% of the total costs. The remaining part, 62% of the material costs, is attributed to ICs and electronics, which enable the operation and the control of the

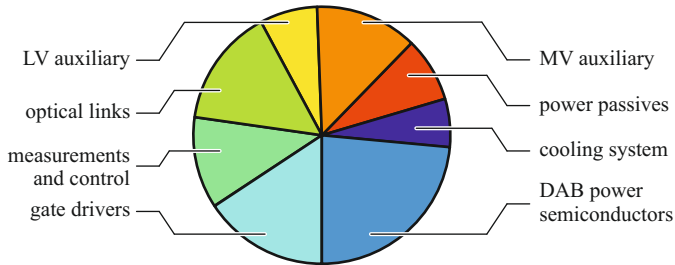


**Fig. 6.31:** Cost decomposition of the DAB converter cell prototype. The material costs at a production volume of more than 5'000 converters is approximately 350 € per DAB converter cell, i.e. 56 €/kW. Housing and connectors are not considered. Power passives consist of the filter components and the transformer and inductor. The DAB power semiconductors consist of the JFETs, p-channel MOSFETs, SiC diodes and protective TVS diodes. The cost estimation is based on the methods and models presented in [97]. A price of 7 € per JFET is assumed.

converter. The contribution of the gate driver components is 15.7% and predominantly consists of the eight dedicated JFET EiceDriver ICs and four MAX13256 transformer driver ICs utilised for the isolated gate driver supplies. Fig. 6.31 further reveals that the material costs for the MV auxiliary supply (12.9%) is almost double the costs of the LV auxiliary supply (7.2%), because of the more expensive high-voltage MOSFETs. The remaining 26% cover all electronics required for the measurements, control, and communication, including the printed circuit boards (1.7%) and, with 14.9%, the fiber optic transmitters and receivers (HFBR-1522Z and HFBR-2522Z), which are required due to the high isolation requirements of the converter's ISOP structure, significantly contribute to the cost of the electronics. The cost decomposition reveals that an optimization for minimum converter weight minimizes the material cost of the passive components and invests in power semiconductors, which feature minimal losses and reduce the cooling system weight, regardless of the power semiconductor cost.

## 6.5 Summary of Chapter

A comprehensive conceptualization and design of a weight-optimized all-SiC 2kV/800 V DAB for an Airborne Wind Turbine (AWT) is presented. Experimental results validate the calculated converter performance: the realized converter prototype achieves a power-to-weight ratio of 4.28 kW/kg (calculated: 4.35 kW/kg) at a weight of 1.46 kg and a power density of 5.15 kW/dm<sup>3</sup>; the efficiency is 97 % (at  $V_1 = 650$  V and  $P_{\text{out}} = 6.25$  kW; calculated: 97.3 %). The realized DAB converter cell fulfills the required specifications (cf. Tab. 6.1) and hence confirms the feasibility of the proposed AWT electrical system structure.

The weight of the cooling system and the transformer and inductor is approximately 60 % of the total system weight. This result confirms the strong impact of the weights of these components on the total system weight and justifies the reason for the weight optimization to focus on these components.

The switching losses are decreased through the evolution of SiC technology, i.e. due to the JFET direct drive technology. This and the fact, that the transformer core material accounts for 31 % of the total system weight, suggests that a DAB operated at a higher switching frequency may have the potential for a further weight reduction.

The MV winding is the first component to reach its thermal limit, in spite of the fact, that the transformer cooling system accounts for 14 % of the total system weight. Due to this reason, different transformer topologies, which do not engulf the winding with a large thermal insulation, may allow for a further weight reduction.

The presented comprehensive weight optimized design of the 6.25 kW DAB converter cell, used as part of a 25 kW ISOP structured dc–dc converter, considers multi-objective optimization and takes, besides the actual components' weights, the losses of the converter components and the associated weight of the required optimized cooling system into account. Furthermore, also the weights of the additional circuitries required for the converter operation and the integration into the final electrical AWT system, i.e. gate drivers, digital control, filters, and auxiliary power supplies, are considered. The converter design detailed in this work, thus, points out the technological limits the DAB converter is subject to and is not limited to the considered AWT application.

# 7

## Conclusion

**T**HIS WORK presented the configuration of power electronics converters for the implementation of a 100 kW airborne wind turbine (AWT), where the major aspect is the trade-off between power-to-weight ratio (kW/kg) and efficiency. The greatest challenge with respect to the realization of the electric system of the AWT was to achieve light-weight generators, power converters, and a light-weight cable.

The multi-objective optimization of the electrical machine required for the AWT system was detailed. An optimization was performed and yielded that a RFM Halbach inrunner design reaching a power-to-weight ratio of,  $\gamma \approx 6.3$  kW/kg, at an efficiency of  $\eta \approx 95\%$  performs best for the AWT application. A prototype RFM was designed, built and tested. The measurement results matched the predicted values and verified the employed design procedure.

A voltage source inverter (VSI) was designed and built, which achieved a power-to-weight ratio of 18.9 kW/kg. This shows that the weight contribution of the VSI to the total weight of the AWT is small. The VSI was designed according to the previously detailed modeling of power electronics for multi-objective optimization. The description of the modeling focuses on analytical semiconductor loss calculations and the optimization of forced convection cooling systems, composed of fans and parallel plate fin heat sinks. A new analytical cooling system model was introduced and verified. It was shown that a weight reduction of  $\approx 50\%$  can be achieved compared to commercially available products.

The fundamentals of the tether design were explained and motivated the design, the implementation, and the experimental verification of a minimum weight input series output parallel (ISOP) structured dual

active bridge (DAB) converter for the AWT system. Furthermore, the design included all necessary considerations to realize a fully functional prototype, i.e. it also considered the auxiliary supply, the control for stable operation of the system, and the startup and shutdown procedure. Experimental results validate the proposed design procedure. The prototype features a power-to-weight ratio of 4.28 kW/kg (1.94 kW/lb) and achieves a maximum full-load efficiency of 97.5 %.

The weight optimization of components is of uttermost importance not only for AWTs but for airborne applications in general, since each additional kilogram of weight carried in an aircraft increases the fuel consumption by 2900 liter kerosene per year [98]. With respect to a power converter not only the weight of the power components but also efficiency plays a major role, since the weight of the converter's cooling system increases with increasing losses and, most often, substantially contributes to the total converter weight; from practical experience it is estimated that 1 kW of losses involves 10 kg of secondary cooling equipment [99]. For this reason the presented design procedures have to be seen in a more general context as guideline for the realization of lightweight power converters for airborne applications.

# Appendix





# Basics of Aerodynamics of Conventional Wind Turbines and Power Kites

**T**HE following is based on [1] and included here for the sake of completeness to briefly illustrate the fundamental mathematical relationships for the calculation of a wind turbine's rotor blade swept area  $A_T$  (Section A.1) and the power generation of rotor blades (Section A.2) and power kites (Section A.3) in greatly simplified form. This conveys on the one hand an insight into the physical relationships and shows on the other hand, taking a 100 kW system as an example, that the surface area of a kite intended for an Airborne Wind Turbine (AWT) can be approximately the same as the surface area of the rotor blades of a conventional two-blade wind turbine.

## A.1 Conventional Wind Turbines

The kinetic energy of an axial air flow is transformed into torque-forming tangential force through the rotor blades of a windmill. According to Lanchester and Betz, the calculation of the maximum achievable power for a given rotor blade swept area  $A_T$  can be replaced by a partially air-permeable actuator disc [2, 100] and the power flow can be considered in a tubular air flow as shown in Fig. A.1. The pressure in front of the disc will increase in relation to the ambient pressure, i.e. the kinetic energy of the air will be reduced, respectively the flow cross-section widened and a force applied to the turbine disc. The re-

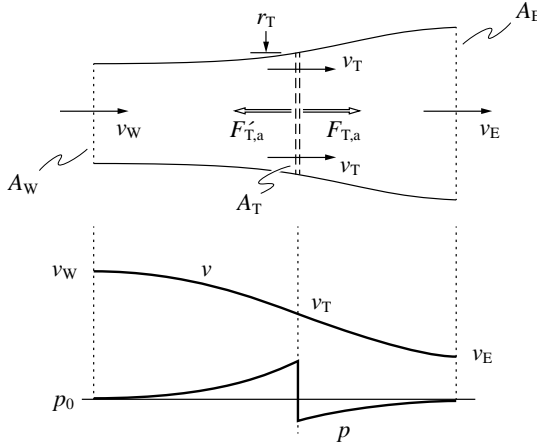


**Fig. A.1:** Setup considered for the derivation of Betz' Law (airflow tube with turbine replaced by actuator disk); wind speed and pressure profile.

removal of energy from the disc causes a steep reduction of the pressure. At a later stage, due to the further reduction of the air speed, the air flow once again reaches the ambient pressure and finally through the absorption of the kinetic energy from the surrounding air again attains the original wind speed  $v_W$ . In contrast to the pressure, the speed, assuming constant air density on the basis of the same mass flow per second through all cross-sections,

$$\dot{m} = \rho A_W v_W = \rho A_T v_T = \rho A_E v_E , \quad (\text{A.1})$$

shows a continuous development. This provokes the question, which terminal velocity of the air  $v_E$  results in maximum turbine power. In this connection it is worth noting that  $v_E = 0$  is not an optimum value, as then the air behind the wind turbine cannot leak away, i.e. the flow of additional air would be impaired.

The force acting on the turbine disc results from the conservation of momentum

$$F_{T,a} = \dot{m} (v_W - v_E) \quad (\text{A.2})$$

and thereby the power generated from the airflow according to the principle of virtual displacement is

$$P_T = F_{T,a} v_T = \dot{m} (v_W - v_E) v_T . \quad (\text{A.3})$$

Furthermore, we have for the power according to the principle of conservation of energy

$$P_T = \frac{1}{2} \dot{m} (v_W^2 - v_E^2) . \quad (\text{A.4})$$

For this reason follows by a combination of (A.3) and (A.4)

$$v_T = \frac{1}{2} (v_W + v_E) , \quad (\text{A.5})$$

i.e. the air speed on the disc is the same as the average of the initial and terminal velocities. The optimal speed  $v_E$  can now by use of (A.1) in (A.4),

$$P_T = \frac{1}{2} \rho A_T v_T (v_W^2 - v_E^2) = \frac{1}{4} \rho A_T (v_W + v_E) (v_W^2 - v_E^2) , \quad (\text{A.6})$$

be calculated in the form of a simple extreme value problem

$$\frac{dP_T}{dt} = 0 \longrightarrow v_{E,i} = \frac{1}{3} v_W . \quad (\text{A.7})$$

This results in a maximum achievable power from the wind (Betz Limit, indicated by an index  $i$ )

$$P_{T,i} = c_{P,i} \frac{1}{2} \rho A_T v_W^3 = c_{P,i} P_W \quad \text{with} \quad c_{P,i} = \frac{16}{27} \approx 0.59 , \quad (\text{A.8})$$

whereby  $c_{P,i}$  denotes the power coefficient for the Betz Limit. Accordingly, 59% of the power  $P_W$  of undisturbed wind flowing through the area  $A_T$  with speed  $v_W$  can be used.

The power that can be generated increases only linear with the area  $A_T$ , however with the third power of the wind speed  $v_W$ ; therefore, an increase of  $v_W$  by only 25% already results in a doubling of the turbine output.

Combining (A.1), (A.2) and (A.7) we now have for the axial force  $F_{T,i,a}$  acting on the tower of a windmill

$$F_{T,a,i} = \rho A_T \frac{4}{9} v_W^2 = \frac{3}{2} \frac{P_{T,i}}{v_W} , \quad (\text{A.9})$$

i.e. accordingly

$$F_{T,a,i} v_W = \frac{3}{2} P_{T,i} . \quad (\text{A.10})$$

In simple terms only 2/3 of the energy that would be necessary to push the turbine disc with a speed of  $-v_W$  against still air can be gained. This observation is of importance for the calculation of the AWT in Section A.3.

The turbine area  $A_T$  is determined by

$$A_T = r_T^2 \pi . \quad (\text{A.11})$$

In the case of a real turbine, however, only a part of the entire area  $A_T$  effectively generates power. Here, for an approximate estimate, it can be considered that within an inner circle having the radius  $r_T/2$ , no power can be generated, i.e. the actual turbine area is only  $3/4A_T$ . The turbine output then is

$$P_T = \frac{3}{4} P_{T,i} = \frac{2}{9} \rho A_T v_W^3 . \quad (\text{A.12})$$

This represents using 44% of  $P_W$  [cf. (A.8)] and coincides with practically achieved values. The turbine area necessary to generate power  $P_G$  is thus

$$A_T = \frac{P_G}{\frac{2}{9} \rho v_W^3} . \quad (\text{A.13})$$

In axial direction the resultant force is

$$F_{T,a} = \frac{3}{4} F_{T,a,i} + c_W \frac{1}{2} \rho \frac{A_T}{4} v_W^2 = \left( 1 + \frac{3}{8} c_W \right) \frac{3}{2} \frac{P_T}{v_W} \approx \frac{3}{2} \frac{P_T}{v_W} , \quad (\text{A.14})$$

whereby the aerodynamic resistance caused by the inner, non-active part of the turbine is considered. Assuming an aerodynamically-favorable design of the non-active part ( $c_W = 0.2$  typ.) this portion can, however, be neglected in respect of the axial force resulting from the turbine effect.

## A.2 Geometrical Dimensions of the Rotor Blades of CWTs

The greatly simplified arrangement of a twin blade turbine with a concentrated force acting on a mean radius  $r_B$  shown in Fig. A.2 is used to calculate the blade surface  $A_B$  and/or the geometrical dimensions of the rotor blades. Furthermore, the analysis of the air flow will be

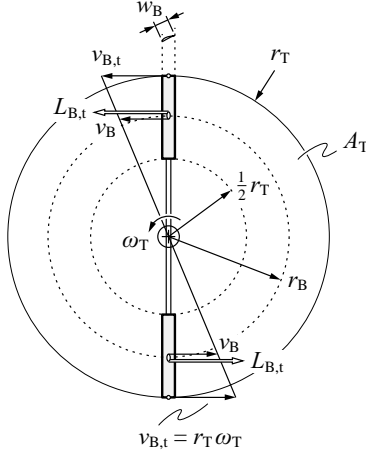


**Fig. A.2:** Turbine swept area and blade area.

limited to this radius. In contrast, a more accurate calculation would require a dissection of the rotor blades into a large number of small radial sections [101].

It should be noted that twin blade turbines are used industrially up to about 100 kW (the same as the rated power of the AWT system considered in this paper). For higher power levels the propellers are equipped with three rotor blades which provide a better balance of the masses, a more uniform torque generation (lee of the tower) and reduced rotational speed.

An important aspect when dimensioning wind turbines is the tip speed ratio

$$\lambda_T = \frac{r_T \omega_T}{v_W} \quad (\text{A.15})$$

that is selected, based on experience from turbine construction [102] as

$$\lambda_{T,\text{opt}} \approx \sqrt{\frac{80}{z_B}} \quad (\text{A.16})$$

( $z_B$  indicates the number of rotor blades). It is clear in the aim for an optimal tip speed ratio that for too low rotational speed  $\omega_T$  and/or tip speed of the turbine rotor blades, the area  $A_T$  is passed over too slowly, in other words the wind can pass through without hindrance

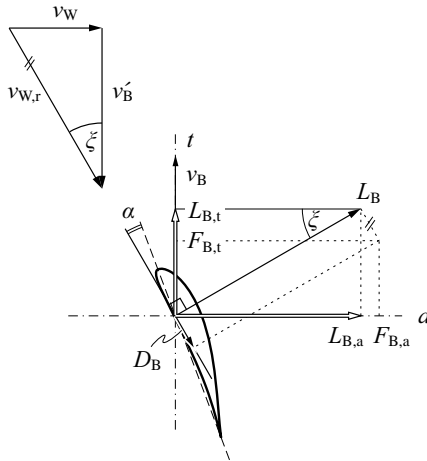


**Fig. A.3:** Velocity components and forces acting on the blade of a CWT.

and/or without extraction of a large amount of energy. At too high a speed the rotor blades can, in the limiting case, block the air stream which once again results in a low energy extraction. Furthermore, at too high  $\omega_T$  a rotating rotor blade reaches the turbulent air left behind the preceding blade resulting in high aerodynamic resistance and/or losses.

For the conversion of the wind energy advantageously the lift  $L_B$  acting orthogonally to the wind speed  $v_{W,r}$  observed from the rotor blade, is employed (cf. Fig. A.3). The lift generated depends essentially on the direction of the relative wind to the rotor blade chord line, i.e. the angle of attack  $\alpha$ . Increasing  $\alpha$  results in increased lift  $L_B$  until finally a strong increase in drag and last of all turbulent air currents result (pp. 60–61 in [2]). Due to the increasing peripheral speed  $v_B$ , caused by the increasing radius, the blade pitch angle is changed over the radius for real turbines.

The effective air flow results in a lift  $L_B$  and drag  $D_B$  acting on the rotor blade

$$L_B = c_{LB} \frac{1}{2} \rho A_B v_{W,r}^2 \quad D_B = c_{DB} \frac{1}{2} \rho A_B v_{W,r}^2, \quad (\text{A.17})$$

with  $c_{LB} = 1 \dots 1.5$  and  $c_{DB} = 0.05 \dots 0.1$  (lift-to-drag ratio  $c_{LB}/c_{DB} =$

15 typ.) for an appropriately shaped blade profile and an optimal angle of attack. Accordingly, the drag effect of  $D_B$  can be disregarded in the following.

The effective wind speed follows with the tangentially directed rotor blade speed

$$v_B = \frac{3}{4} r_T \omega_T = \frac{3}{4} \lambda_T v_W \quad (\text{A.18})$$

as

$$v_{W,r} = \sqrt{v_W^2 + v_B^2} = v_W \sqrt{1 + \frac{9}{16} \lambda_T^2}. \quad (\text{A.19})$$

The force component acting in the blade's direction of rotation is thus

$$L_{B,t} = L_B \sin \xi = L_B \frac{v_W}{v_{W,r}} = c_L \frac{1}{2} \rho A_B v_W^2 \sqrt{1 + \frac{9}{16} \lambda_T^2}, \quad (\text{A.20})$$

and we have with reference to Fig. A.3

$$\frac{L_{B,t}}{L_{B,a}} = \frac{v_W}{v_B} \longrightarrow L_{B,t} v_B = L_{B,a} v_W. \quad (\text{A.21})$$

This well shows the power conversion by the rotor blade from the axial wind direction into a torque-forming tangential component.

The wind speed on the rotor blades was assumed to be  $v_W$  for the previous calculations. However, as can be derived from (A.8), only a wind speed of  $2/3 v_W$  reaches the turbine disc [cf. (A.5) and (A.7)]. It is thus necessary to reduce the tangential force, calculated according to (A.20), to  $2/3 L_{B,t}$ , for the torque generation. As a result it will be clear that also the full axial force  $F_{B,a}$  according to (A.14) corresponds with  $3/2 P_T$  and not directly with  $P_T$ .

In summary, we have for an output power  $P_G$  (referenced to the turbine shaft) to be generated by the turbine,

$$P_G = z_B \frac{2}{3} L_{B,t} v_B = z_B \frac{1}{4} c_L \rho A_B v_W^3 \lambda_T \sqrt{1 + \frac{9}{16} \lambda_T^2} \quad (\text{A.22})$$

( $z_B$  denominates the number of rotor blades), which allows to calculate the required rotor blade area  $A_B$  and/or the rotor blade width

$$w_B = \frac{A_B}{\frac{1}{2} r_T} \quad (\text{A.23})$$

as  $r_T$  is determined by (A.11) and (A.12).

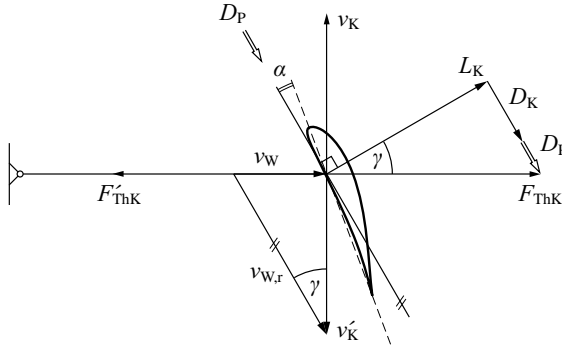


**Fig. A.4:** Velocity components and forces acting on the power kite of an AWT (turbines not shown, cf. Fig. A.5).

### A.3 Crosswind Power Kite Modeling

A crosswind kite moves transversal to the wind in the same manner as the rotor blade of a windmill, i.e. the aerodynamic area  $A_K$  converts wind energy to move the kite against the aerodynamic resistance. It is assumed that the kite retaining cable lies parallel to the wind, whereby the motion is orthogonal to  $v_W$  (cf. Fig. A.4) and  $v_K$  shows a constant value, i.e. no acceleration forces occur, for the sake of simplicity in the following observations. In reality, this situation is given only in sections of the kite figure-of-eight flight trajectory.

For the lift  $L_K$  and drag  $D_K$  acting upon the kite we have

$$L_K = c_{LK} \frac{1}{2} \rho A_K v_{W,r}^2 \quad D_K = c_{DK} \frac{1}{2} \rho A_K v_{W,r}^2. \quad (\text{A.24})$$

In case wind turbines are mounted on the kite according to [3] (cf. Fig. A.5), i.e. an Airborne Wind Turbine (AWT) is created, a counteracting force takes effect, in addition to the aerodynamic drag, which reflects the energy generated by the turbine for a wind speed  $v_{W,r}$ . In addition to  $D_L$  and  $D_P$  the lift must also support the weight  $G_K$  of the kite itself as well as that of the retaining cable (tether)  $G_{Th}$  and causes a tensile loading of the tether. Within the terms of a basic overview,  $G_K$  and  $G_{Th}$  will not be considered here [3]. Therefore, the forces  $L_K$ ,  $D_K$  and  $D_P$  combine to a resulting force acting in the direction of the tether.

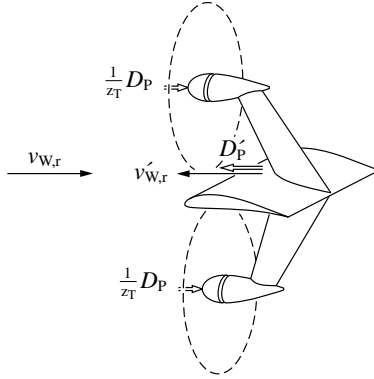


**Fig. A.5:** Schematic representation of an AWT section (power kite wing carrying wind turbines, cf. Fig. 1.2).

The aerodynamic quality of an aerofoil respectively a kite is determined by the lift-to-drag ratio which is itself dependent on the angle of attack  $\alpha$  (cf. Section A.2),

$$k_{LD} = \frac{L_K}{D_K} = \frac{c_{LK}}{c_{DK}}, \quad (\text{A.25})$$

and typically has values of  $k_{LD} = 20 \dots 30$ . We will denote the relationship of the energy-generating force  $D_P$  to the aerodynamic drag  $D_K$  with

$$k_D = \frac{D_P}{D_K}. \quad (\text{A.26})$$

Based on the speed diagram (cf. Fig. A.4) we have

$$\frac{v_W}{v_{W,r}} = \sin \gamma = \frac{\tan \gamma}{\sqrt{1 + \tan^2 \gamma}} \quad (\text{A.27})$$

with

$$\tan \gamma = \frac{D_K + D_P}{L_K} = \frac{(1 + k_D)}{k_{LD}} \quad (\text{A.28})$$

and  $v_{W,r}$  results as

$$v_{W,r} = v_W \frac{\sqrt{k_{LD}^2 + (k_D + 1)^2}}{(k_D + 1)} \approx v_W \frac{k_{LD}}{(k_D + 1)} \quad (\text{A.29})$$

( $k_{LD} \gg 1$ ), i.e. the flying speed of the kite is several times higher than the actual wind speed  $v_W$ . The power extractable by the kite is

$$P_K = v_{W,r} D_P = v_{W,r} k_D \frac{L_K}{k_{LD}} = c_{LK} \frac{1}{2} \rho A_K \frac{k_D}{k_{LD}} v_{W,r}^3 \approx c_{LK} \frac{1}{2} \rho A_K v_W^3 k_{LD}^2 \frac{k_D}{(k_D + 1)^3}. \quad (\text{A.30})$$

Accordingly, the power generation for given aerodynamic properties  $k_{LD}$  and  $c_{LK}$  can be maximized by proper choice of  $k_D$ , i.e.

$$\frac{dP_K}{dk_D} = 0 \longrightarrow k_{D,i} = \frac{1}{2}, \quad D_{P,i} = \frac{1}{2} D_K. \quad (\text{A.31})$$

Eq. (A.31) has to be interpreted such, that for small values  $k_D$  or  $D_P$ , despite a high speed  $v_K$ , a small product value (A.30) results. In contrast, a considerable reduction of  $v_K$  results from a high  $D_P$  and with this once again a low power generation. By the use of (A.31) in (A.30) we have

$$P_{K,i} \approx \frac{4}{27} c_{LK} k_{LD}^2 \frac{1}{2} \rho A_K v_W^3 = c_{PK,i} \frac{1}{2} \rho A_K v_W^3. \quad (\text{A.32})$$

Thereby, it becomes clear that the kite's coefficient of performance  $c_{PK,i}$  is considerably higher than that of a CWT [cf.  $c_{P,i}$ , (A.8)], i.e. in order to generate a predefined power value, the kite surface  $A_K$  (cf. Fig. A.6) can be considerably smaller than the swept area  $A_T$  of a ground-based turbine; e.g. for  $c_{LK} = 1.2$  and  $k_{LD} = 20$  we have  $c_{PK,i}/c_{P,i} = 120$  clearly showing the kite's relationship with the rotor blades of the CWT mentioned above. It is important to point out that based on (A.31) one should not assume that in order to generate more power a greater kite wind resistance (drag)  $D_K$  is desirable. On the contrary, as shown by (A.32), the maximum power  $P_{K,i}$  increases with increasing  $k_{LD}$ , i.e. reducing  $D_K$ . However, in any case twice the generated power is lost to the aerodynamic drag  $D_K$  also in the optimal case.

At optimal  $k_D$ , i.e.  $k_{D,i} = 1/2$ , the wind speed seen from the kite (according to Fig. A.5 wind speed  $v_{W,r,i}$  for large  $k_{LD}$  is approximately the same as the flying speed of the kite  $v_K$  measured in a fixed coordinate system) is

$$v_{W,r,i} \approx v_W \frac{k_{LD}}{(k_D + 1)} = \frac{2}{3} k_{LD} v_W. \quad (\text{A.33})$$

This is 2/3 of the speed of a kite which is not retarded by a turbine counteracting force  $D_P$ , but nevertheless still several times higher than

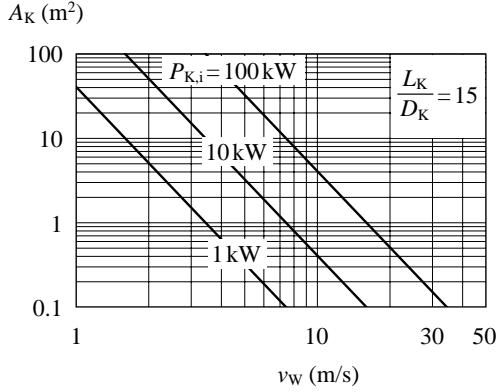


**Fig. A.6:** Dependency of the power kite output power on the effective air velocity  $v_{W,r}$  and the kite area  $A_K$  under the assumption of optimal selection of  $D_P$ , i.e.  $D_P = D_{P,i} = 1/2 D_K$ ; cf. (A.31).

the wind speed  $v_W$ , advantageously resulting in a very small swept area  $A_{TK}$  (cf. Section A.4) requirement for the kite's turbines.

## A.4 Power Kite Area and Turbines

Finally the swept area  $A_{TK}$  of the wind turbines mounted on the kite and their rotational speed  $\omega_{TK}$ , and the rotor blade area  $A_{BK}$  must be calculated, whereby it will again be assumed that a twin blade turbine is used.

Dimensioning of the kite for optimal operation results in a very high speed  $v_{W,r,i}$  (in the case of a kite turbine  $v_{W,r}$  replaces the wind speed  $v_W$  applicable to a ground-based turbine) and thus, according (A.13), a very small turbine area  $A_{TK}$

$$A_{TK} = \frac{P_G}{z_T \frac{2}{9} \rho v_{W,r}^3} = r_{TK}^2 \pi \quad (\text{A.34})$$

or short rotor blades  $r_{TK}$  ( $P_G$  is the total power to be generated,  $z_T$  the number of kite mounted turbines, cf. Fig. 1.3). Furthermore, as a result of the tip speed ratio resulting from the number of rotor blades

according to (A.16)

$$\lambda_{\text{TK}} = \frac{r_{\text{TK}}\omega_{\text{TK}}}{v_{\text{W,r}}}, \quad (\text{A.35})$$

a very high angular frequency  $\omega_{\text{TK}}$  of the turbine will result.

It is therefore advantageous to take an opposite approach and to choose sufficiently long rotor blades  $r_{\text{TK}}$  respectively a sufficiently large swept area  $A_{\text{TK}}$  (sufficiently larger than the outer radius of the generator positioned behind the turbine). The necessary wind speed  $v_{\text{W,r}}$  can then be calculated by use of (A.12)

$$v_{\text{W,r}}^3 = \frac{P_{\text{G}}}{\frac{2}{9}\rho z_{\text{T}}A_{\text{TK}}}. \quad (\text{A.36})$$

The rotational speed  $\omega_{\text{TK}}$  of the turbine then results from the choice of  $\lambda_{\text{TK}}$  (A.35). The area  $A_{\text{BK}}$  and width  $w_{\text{BK}}$  of the kite turbine rotor blades can be calculated according to Section A.2.

It should be pointed out that in general the optimum application of the kite to generate power according (A.32) cannot be achieved, hence a larger kite surface area  $A_{\text{K}}$  than defined by (A.35), is required. In order to calculate  $A_{\text{K}}$  it can be assumed that the force acting on the kite due to the mounted turbines  $z_{\text{T}}$  is

$$F_{\text{TK,a}} \approx z_{\text{T}} \frac{3}{2} \frac{P_{\text{TK}}}{v_{\text{W,r}}} = \frac{3}{2} \frac{P_{\text{G}}}{v_{\text{W,r}}} \quad (\text{A.37})$$

[compare comment to (A.10)]. This force is directly the same as  $D_{\text{P}}$ ,

$$D_{\text{P}} = F_{\text{TK,a}} \approx \frac{3}{2} \frac{P_{\text{G}}}{v_{\text{W,r}}}, \quad (\text{A.38})$$

whereby  $D_{\text{P}}$  is specified; furthermore  $v_{\text{W,r}}$  is known from (A.36). Thus the kite's output power is

$$P_{\text{K}} = v_{\text{W,r}}D_{\text{P}} = \frac{3}{2}P_{\text{G}}, \quad (\text{A.39})$$

i.e. a power of 3/2 of the total turbine output power has to be supplied by the kite. By rearranging (A.29) we obtain

$$k_{\text{D}} = \left( \frac{v_{\text{W}}}{v_{\text{W,r}}} k_{\text{LD}} - 1 \right) \quad (\text{A.40})$$

and thus by use of (A.30)

$$P_G \approx c_{LK} \frac{1}{3} \rho A_K \left( \frac{v_W}{v_{W,r}} - \frac{1}{k_{LD}} \right) v_{W,r}^3 \quad (\text{A.41})$$

from which the necessary kite area

$$A_K \approx \frac{P_G}{c_{LK} \frac{1}{3} \rho \left( \frac{v_W}{v_{W,r}} - \frac{1}{k_{LD}} \right) v_{W,r}^3} \quad (\text{A.42})$$

immediately results.

## A.5 Numerical Results

In this section a calculation example of a conventional ground-based wind turbine and an airborne crosswind power kite with  $z_T = 8$  turbines is presented based on the equations derived in the course of the previous description. Both wind turbine systems are designed for a total mechanical shaft power  $P_G = 100 \text{ kW}$ , a wind speed  $v_W = 10 \text{ m/s}$ , and a rotor blade number  $z_B = 2$  (two-blade rotor). The aim is to briefly investigate and compare the physical dimensions and properties of both systems.

Firstly, the conventional wind turbine is considered. According to (A.13), the necessary swept area of the rotor equals to

$$A_T = \frac{P_G}{\frac{2}{9} \rho v_W^3} = 367.3 \text{ m}^2, \quad (\text{A.43})$$

leading to a rotor radius

$$r_T = \sqrt{\frac{A_T}{\pi}} = 10.8 \text{ m}. \quad (\text{A.44})$$

The resultant angular speed  $\omega_T$ , assuming an optimal tip speed ratio can be determined by combination of (A.15) and (A.16) and is given by

$$\omega_T = \frac{v_W}{r_T} \sqrt{\frac{80}{z_B}} = 5.8 \text{ rad/s}^{-1}. \quad (\text{A.45})$$

This corresponds to a rotational speed of 56 rpm. The required blade area can then be determined by solving (A.22) for  $A_B$ , which leads to

$$A_B = \frac{4P_G}{z_B \rho v_W^3 \lambda_{T,\text{opt}} \sqrt{1 + \frac{9}{16} \lambda_{T,\text{opt}}^2}} = 4.4 \text{ m}^2 \quad (\text{A.46})$$

for a lift coefficient  $c_L = 1.2$  and an optimal tip speed ratio  $\lambda_{T,\text{opt}}$  according to (A.16). Ultimately, (A.23) allows for the calculation of the required rotor blade width

$$w_B = \frac{2A_B}{r_T} = 0.8 \text{ m}. \quad (\text{A.47})$$

Next, the characteristic quantities of the power kite are determined for a lift coefficient  $c_{LK} = 1.2$ , a lift-to-drag ratio  $k_{LD} = 25$ , and a rotor radius  $r_{TK} = 0.625 \text{ m}$  (equals to a diameter of 1.25 m). The rotational speed of the generator/motor is assumed with 2000 rpm at generator operation and 3000 rpm at motor operation.

The required relative wind speed  $v_{W,r}$ , seen by the kite wind turbines, can be calculated by (A.36)

$$v_{W,r} = \sqrt[3]{\frac{P_G}{\frac{2}{9}\rho z_T A_{TK}}} = 33.4 \text{ m/s}, \quad (\text{A.48})$$

which corresponds to a speed of  $120 \text{ km/h} \approx 65 \text{ kts}$ . The necessary kite (wing) area can then immediately be obtained from (A.42)

$$A_K \approx \frac{P_G}{c_{LK} \frac{1}{3} \rho \left( \frac{v_W}{v_{W,r}} - \frac{1}{k_{LD}} \right) v_{W,r}^3} = 21.1 \text{ m}^2. \quad (\text{A.49})$$

Finally, the resulting tip speed ratio has to be determined for generator operation ( $\lambda_{TK,g}$ ) and for motor operation ( $\lambda_{TK,m}$ ) using (A.35) to verify the turbine rotor design

$$\lambda_{TK,g} = \frac{r_{TK} \omega_{TK,g}}{v_{W,r}} = 3.9, \quad (\text{A.50})$$

$$\lambda_{TK,m} = \frac{r_{TK} \omega_{TK,m}}{v_{W,r}} = 5.9. \quad (\text{A.51})$$

For motor operation, the tip speed ratio is close to the optimal value ( $\approx 6.32$ ) for a two-blade rotor as desired.

By considering the rotor radius  $r_T$  and  $r_{TK}$ , it can be shown that the total swept area of the turbines on the power kite, operating at 2000 rpm, is approximately 37 times smaller than the swept area of the ground-based wind turbine, operating at 56 rpm.

# List of Publications

Different parts of the research findings presented in this thesis have already been published or will be published in international scientific journals and conference proceedings. The publications developed in the course of this thesis are listed below.

## Journal Papers

- ▶ C. Gammeter, F. Krismer, and J. W. Kolar, "Weight Optimization of a Cooling System Composed of Fan and Extruded-Fin Heat Sink," *IEEE Transactions on Industry Applications*, vol. 51, no. 1, pp. 509–520, Jan. 2015. DOI: [10.1109/TIA.2014.2336977](https://doi.org/10.1109/TIA.2014.2336977)
- ▶ C. Gammeter, F. Krismer, and J. W. Kolar, "Comprehensive Conceptualization, Design, and Experimental Verification of a Weight-Optimized All-SiC 2 kV/700 V DAB for an Airborne Wind Turbine," *IEEE Journal of Emerging and Selected Topics in Power Electronics*, vol. 4, no. 2, pp. 638–656, Jun. 2016. DOI: [10.1109/jestpe.2015.2459378](https://doi.org/10.1109/jestpe.2015.2459378)
- ▶ J. Azurza Anderson, C. Gammeter, L. Schrittwieser, and J. W. Kolar, "Accurate Calorimetric Switching Loss Measurement for 900 V 10 mΩ SiC MOSFETs," *IEEE Transactions on Power Electronics*, vol. 32, no. 12, pp. 8963–8968, Dez. 2017. DOI: [10.1109/TPEL.2017.2701558](https://doi.org/10.1109/TPEL.2017.2701558)
- ▶ I. Subotic, C. Gammeter, A. Tüysüz, and J. W. Kolar, "Weight Optimization of Coreless Axial-Flux PM Machines," under review at IET Electric Power Applications.

## Conference Papers

- ▶ C. Gammeter, F. Krismer, and J. W. Kolar, "Weight Optimization of a Cooling System Composed of Fan and Extruded Fin Heat Sink," in *Proceedings of the IEEE Energy Conversion Congress and Exposition (ECCE USA 2013)*, Denver, Colorado, USA, Sept. 15–19, 2013. DOI: [10.1109/ECCE.2013.6646978](https://doi.org/10.1109/ECCE.2013.6646978)

- ▶ C. Gammeter, Y. Drapela, A. Tüysüz, and J. W. Kolar, "Weight Optimization of a Machine for Airborne Wind Turbines," in *Proceedings of the 40th Annual Conference of the IEEE Industrial Electronics Society (IECON 2014)*, Dallas, Texas, USA, Oct. 29–Nov. 1, 2014. DOI: [10.1109/IECON.2014.7048616](https://doi.org/10.1109/IECON.2014.7048616)
- ▶ C. Gammeter, F. Krismer, and J. W. Kolar, "Weight and Efficiency Analysis of Switched Circuit Topologies for Modular Power Electronics in MEA," in *Proceedings of the 42nd Annual Conference of the IEEE Industrial Electronics Society (IECON 2016)*, Florence, Italy, Oct. 23–27, 2016. DOI: [10.1109/IECON.2016.7793239](https://doi.org/10.1109/IECON.2016.7793239)
- ▶ I. Subotic, C. Gammeter, A. Tüysüz, and J. W. Kolar, "Weight Optimization of an Axial-Flux PM Machine for Airborne Wind Turbines," in *Proceedings of the IEEE International Conference on Power Electronics, Drives and Energy Systems (PEDES 2016)*, Trivandrum, India, Dec. 14–17, 2016. DOI: [10.1109/PEDES.2016.7914327](https://doi.org/10.1109/PEDES.2016.7914327)

## Further Scientific Contributions

- ▶ G. Ortiz, C. Gammeter, J. W. Kolar, and O. Apeldoorn, "Mixed MOSFET-IGBT Bridge for High-Efficient Medium-Frequency Dual-Active-Bridge Converter in Solid State Transformers," in *Proceedings of the 14th IEEE Workshop on Control and Modeling for Power Electronics (COMPEL 2013)*, Salt Lake City, USA, Jun. 23–26, 2013. DOI: [10.1109/COMPEL.2013.6626461](https://doi.org/10.1109/COMPEL.2013.6626461)

## Awards

- ▶ C. Gammeter, F. Krismer, and J. W. Kolar, "Weight Optimization of a Cooling System Composed of Fan and Extruded Fin Heat Sink," William M. Portnoy Award. DOI: [10.1109/ECCE.2013.6646978](https://doi.org/10.1109/ECCE.2013.6646978)
- ▶ G. Ortiz, C. Gammeter, J. W. Kolar, and O. Apeldoorn, "Mixed MOSFET-IGBT Bridge for High-Efficient Medium-Frequency Dual-Active-Bridge Converter in Solid State Transformers," Best Paper Award. DOI: [10.1109/COMPEL.2013.6626461](https://doi.org/10.1109/COMPEL.2013.6626461)

# Bibliography

- [1] J. W. Kolar, T. Friedli, F. Krismer, A. Looser, M. Schweizer, P. Steimer, and J. Bevirt, “Conceptualization and multi-objective optimization of the electric system of an airborne wind turbine,” in *Proc. 20th Int. IEEE Symposium on Industrial Electronics (ISIE 2011), Gdansk, Poland*, June 2011, pp. 32–55. DOI: [10.1109/isie.2011.5984131](https://doi.org/10.1109/isie.2011.5984131)
- [2] A. Betz, *Windenergie und ihre Ausnutzung durch Windmühlen (in German)*. Bandenhoeck & Ruprecht: Göttingen, 1926.
- [3] M. L. Loyd, “Crosswind kite power (for large-scale wind power production),” *Journal of energy*, vol. 4, no. 3, pp. 106–111, 1980. DOI: [10.2514/3.48021](https://doi.org/10.2514/3.48021)
- [4] *SwissKitePower*, [Online]. Available: [www.swisskitepower.ch](http://www.swisskitepower.ch). [Accessed: April, 2013].
- [5] *Kite Gen*, [Online]. Available: <http://kitegen.com>. [Accessed: April, 2013].
- [6] L. Fagiano, M. Milanese, and D. Piga, “High-altitude wind power generation,” *IEEE Transactions on Energy Conversion*, vol. 25, no. 1, pp. 168–180, March 2010. DOI: [10.1109/TEC.2009.2032582](https://doi.org/10.1109/TEC.2009.2032582)
- [7] W. J. Ockels, B. Lansdorp, J. Breukels, and G. Spierenburg, “The laddermill: work in progress,” in *Proc. European Wind Energy Conference*, London, UK, November 22–25, 2004, pp. 1–7.
- [8] M. Diehl and B. Houska, “Windenergienutzung mit schnell fliegenden Flugdrachen: Eine Herausforderung für die Optimierung und Regelung (in German) – Wind power via fast flying kites: A challenge for optimization and control,” *at-Automatisierungstechnik Methoden und Anwendungen der Steuerungs-, Regelungs- und Informationstechnik*, vol. 57, no. 10, pp. 525–533, July 2009. DOI: [10.1524/auto.2009.0798](https://doi.org/10.1524/auto.2009.0798)
- [9] B. Houska and M. Diehl, “Optimal control for power generating kites,” in *Proc. 9th European Control Conference (ECC 2007)*, Kos, Greece, July 2–5, 2007, pp. 3560–3567.

- [10] M. Diehl, *Airborne Wind Energy: Basic Concepts and Physical Foundations*. Berlin, Heidelberg: Springer Berlin Heidelberg, 2013, pp. 3–22. DOI: [10.1007/978-3-642-39965-7](https://doi.org/10.1007/978-3-642-39965-7)
- [11] *Joby Energy*, [Online]. Available: <http://www.jobyenergy.com>. [Accessed: April, 2013].
- [12] *Sky Wind Power*, [Online]. Available: [www.skywindpower.com](http://www.skywindpower.com). [Accessed: April, 2013].
- [13] *Windlift*, [Online]. Available: [www.windlift.com](http://www.windlift.com). [Accessed: April, 2017].
- [14] *Makani Power*, [Online]. Available: <http://www.makanipower.com>. [Accessed: April, 2013].
- [15] J. Sun, “Small-signal methods for ac distributed power systems – A review,” *IEEE Transactions on Power Electronics*, vol. 24, no. 11, pp. 2545–2554, November 2009. DOI: [10.1109/TPEL.2009.2029859](https://doi.org/10.1109/TPEL.2009.2029859)
- [16] D. Boroyevich, I. Cvetković, D. Dong, R. Burgos, F. Wang, and F. Lee, “Future electronic power distribution systems – A contemplative view,” in *Proc. 12th Int. Conf. on Optimization of Electrical and Electronic Equipment (OPTIM 2010)*, Brasov, Romania, May 20–22, 2010, pp. 1369–1380. DOI: [10.1109/optim.2010.5510477](https://doi.org/10.1109/optim.2010.5510477)
- [17] J. W. Kolar, J. Biela, and J. Miniböck, “Exploring the pareto front of multi-objective single-phase pfc rectifier design optimization - 99.2% efficiency vs. 7kW/dm<sup>3</sup> power density,” in *Proc. 6th IEEE International Power Electronics and Motion Conference (IPEMC 2009)*, Wuhan, China, May 17–20, 2009, pp. 1–21. DOI: [10.1109/IPEMC.2009.5289336](https://doi.org/10.1109/IPEMC.2009.5289336)
- [18] J. W. Kolar, J. Biela, S. Waffler, T. Friedli, and U. Badstübner, “Performance trends and limitations of power electronic systems,” in *Proc. 6th Int. Conf. on Integrated Power Electronics Systems*, March 2010, pp. 1–20.
- [19] P. Ragot, M. Markovic, and Y. Perriard, “Optimization of electric motor for a solar airplane application,” *IEEE Transactions on*

- Industry Applications*, vol. 42, no. 4, pp. 1053–1061, July 2006. DOI: [10.1109/TIA.2006.876073](https://doi.org/10.1109/TIA.2006.876073)
- [20] P. Ragot, P. Germano, M. Markovic, and Y. Perriard, “Brushless DC motor for a solar airplane application: Comparison between simulations and measurements,” in *Proc. IEEE Industry Applications Society Annual Meeting*, October 2008, pp. 1–6. DOI: [10.1109/08IAS.2008.75](https://doi.org/10.1109/08IAS.2008.75)
- [21] M. van der Geest, H. Polinder, J. A. Ferreira, and D. Zeilstra, “Optimization and comparison of electrical machines using particle swarm optimization,” in *Proc. 20th Int. IEEE Conf. Electrical Machines*, September 2012, pp. 1380–1386. DOI: [10.1109/ICEIMach.2012.6350058](https://doi.org/10.1109/ICEIMach.2012.6350058)
- [22] M. van der Geest, H. Polinder, J. A. Ferreira, and D. Zeilstra, “Machine selection and initial design of an aerospace starter/generator,” in *Proc. Int. IEEE Electric Machines and Drives Conf*, May 2013, pp. 196–203. DOI: [10.1109/IEMDC.2013.6556253](https://doi.org/10.1109/IEMDC.2013.6556253)
- [23] J. Cros and P. Viarouge, “Synthesis of high performance pm motors with concentrated windings,” *IEEE Transactions on Energy Conversion*, vol. 17, no. 2, pp. 248–253, June 2002. DOI: [10.1109/TEC.2002.1009476](https://doi.org/10.1109/TEC.2002.1009476)
- [24] Y. Huang, B. Ge, J. Dong, H. Lin, J. Zhu, and Y. Guo, “3-D analytical modeling of no-load magnetic field of ironless axial flux permanent magnet machine,” *IEEE Transactions on Magnetics*, vol. 48, no. 11, pp. 2929–2932, November 2012. DOI: [10.1109/TMAG.2012.2194699](https://doi.org/10.1109/TMAG.2012.2194699)
- [25] O. Winter, C. Kral, and E. Schmidt, “Design and loss assessment of air cored axial flux permanent magnet machines,” in *Proc. Int. IEEE Electric Machines and Drives Conf*, May 2013, pp. 602–606. DOI: [10.1109/IEMDC.2013.6556156](https://doi.org/10.1109/IEMDC.2013.6556156)
- [26] *Launchpoint*, [Online]. Available: [www.launchpnt.com](http://www.launchpnt.com). [Accessed: Feb, 2014].
- [27] Z. Q. Zhu, D. Howe, E. Bolte, and B. Ackermann, “Instantaneous magnetic field distribution in brushless permanent magnet

- DC motors. i. open-circuit field,” *IEEE Transactions on Magnetism*, vol. 29, no. 1, pp. 124–135, January 1993. DOI: [10.1109/20.195557](https://doi.org/10.1109/20.195557)
- [28] Z. Q. Zhu, D. Howe, and C. C. Chan, “Improved analytical model for predicting the magnetic field distribution in brushless permanent-magnet machines,” *IEEE Transactions on Magnetism*, vol. 38, no. 1, pp. 229–238, January 2002. DOI: [10.1109/20.990112](https://doi.org/10.1109/20.990112)
- [29] Y. Shen, G. Y. Liu, Z. P. Xia, and Z. Q. Zhu, “Determination of maximum electromagnetic torque in pm brushless machines having two-segment halbach array,” *IEEE Transactions on Industrial Electronics*, vol. 61, no. 2, pp. 718–729, February 2014. DOI: [10.1109/TIE.2013.2254101](https://doi.org/10.1109/TIE.2013.2254101)
- [30] Z. Q. Zhu and D. Howe, “Instantaneous magnetic field distribution in permanent magnet brushless DC motors. iv. magnetic field on load,” *IEEE Transactions on Magnetism*, vol. 29, no. 1, pp. 152–158, January 1993. DOI: [10.1109/20.195560](https://doi.org/10.1109/20.195560)
- [31] Z. Q. Zhu and D. Howe, “Instantaneous magnetic field distribution in brushless permanent magnet DC motors. ii. armature-reaction field,” *IEEE Transactions on Magnetism*, vol. 29, no. 1, pp. 136–142, January 1993. DOI: [10.1109/20.195558](https://doi.org/10.1109/20.195558)
- [32] J. Mühlethaler, “Modeling and multi-objective optimization of inductive power components,” Ph.D. dissertation, Swiss Federal Institute of Technology Zurich (ETH Zurich), 2012.
- [33] J. Pyrhonen, T. Jokinen, and V. Hrabovcova, *Design of Rotating Electrical Machines*. Wiley, 2009. DOI: [10.1002/9781118701591](https://doi.org/10.1002/9781118701591)
- [34] G. Bertotti, “General properties of power losses in soft ferromagnetic materials,” *IEEE Transactions on Magnetism*, vol. 24, no. 1, pp. 621–630, 1988. DOI: [10.1109/20.43994](https://doi.org/10.1109/20.43994)
- [35] A. Boglietti, A. Cavagnino, D. Staton, M. Shanel, M. Mueller, and C. Mejuto, “Evolution and modern approaches for thermal analysis of electrical machines,” *IEEE Transactions on Industrial Electronics*, vol. 56, no. 3, pp. 871–882, March 2009. DOI: [10.1109/TIE.2008.2011622](https://doi.org/10.1109/TIE.2008.2011622)

- [36] A. Boglietti, A. Cavagnino, M. Lazzari, and M. Pastorelli, “A simplified thermal model for variable-speed self-cooled industrial induction motor,” *IEEE Transactions on Industry Applications*, vol. 39, no. 4, pp. 945–952, July 2003. DOI: [10.1109/TIA.2003.814555](https://doi.org/10.1109/TIA.2003.814555)
- [37] D. A. Howey, P. R. N. Childs, and A. S. Holmes, “Air-gap convection in rotating electrical machines,” *IEEE Transactions on Industrial Electronics*, vol. 59, no. 3, pp. 1367–1375, March 2012. DOI: [10.1109/TIE.2010.2100337](https://doi.org/10.1109/TIE.2010.2100337)
- [38] *Emetor*, [Online]. Available: [www.emetor.com](http://www.emetor.com). [Accessed: April, 2017].
- [39] *Wellascent*, [Online]. Available: [www.wellascent.com](http://www.wellascent.com). [Accessed: April, 2017].
- [40] A. Mahmoudi, N. A. Rahim, and H. W. Ping, “Axial-flux permanent-magnet motor design for electric vehicle direct drive using sizing equation and finite element analysis,” *Progress in Electromagnetics Research*, vol. 122, pp. 467–496, 2012. DOI: [10.2528/pier11090402](https://doi.org/10.2528/pier11090402)
- [41] W. K. Thompson, “Three-dimensional field solutions for multipole cylindrical halbach arrays in an axial orientation,” *Report, NASA Glenn Research Center, Cleveland, Ohio*, 2006.
- [42] J. F. Gieras, R.-J. Wang, and M. J. Kamper, *Axial Flux Permanent Magnet Brushless Machines*. Springer, 2008.
- [43] Loctite, “Hysol 9497,” datasheet, 2008.
- [44] P. O. Lauritzen and C. L. Ma, “A simple diode model with reverse recovery,” *IEEE Transactions on Power Electronics*, vol. 6, no. 4, pp. 188–191, 1991. DOI: [10.1109/63.76804](https://doi.org/10.1109/63.76804)
- [45] M. Leibl, “Three-phase rectifier and high-voltage generator for x-ray systems,” Ph.D. dissertation, Swiss Federal Institute of Technology Zurich (ETH Zurich), 2017.
- [46] V. C. V. A. van den Bossche, *Inductors and Transformers for Power Electronics*. CRC Taylor & Francis Group, London, New York, 2005. DOI: [10.1201/9781420027280](https://doi.org/10.1201/9781420027280)

- [47] M. B. Dogruoz and M. Arik, "On the conduction and convection heat transfer from lightweight advanced heat sinks," *IEEE Transactions on Components and Packaging Technologies*, vol. 33, no. 2, pp. 424–431, June 2010. DOI: [10.1109/TCAPT.2009.2039794](https://doi.org/10.1109/TCAPT.2009.2039794)
- [48] S. Lee, "Optimum design and selection of heat sinks," *IEEE Transactions on Components, Packaging, and Manufacturing Technology: Part A*, vol. 18, no. 4, pp. 812–817, December 1995. DOI: [10.1109/95.477468](https://doi.org/10.1109/95.477468)
- [49] M. F. Holahan, "Fins, fans, and form: Volumetric limits to air-side heatsink performance," *IEEE Transactions on Components and Packaging Technologies*, vol. 28, no. 2, pp. 255–262, June 2005. DOI: [10.1109/TCAPT.2005.848490](https://doi.org/10.1109/TCAPT.2005.848490)
- [50] U. Drogenik, A. Stupar, and J. W. Kolar, "Analysis of theoretical limits of forced-air cooling using advanced composite materials with high thermal conductivities," *IEEE Transactions on Components, Packaging, and Manufacturing Technology*, vol. 1, no. 4, pp. 528–535, April 2011. DOI: [10.1109/TCPMT.2010.2100730](https://doi.org/10.1109/TCPMT.2010.2100730)
- [51] P. Ning, F. Wang, and K. D. T. Ngo, "Forced-air cooling system design under weight constraint for high-temperature SiC converter," *IEEE Transactions on Power Electronics*, vol. 29, no. 4, pp. 1998–2007, April 2014. DOI: [10.1109/TPEL.2013.2271259](https://doi.org/10.1109/TPEL.2013.2271259)
- [52] S. Song, V. Au, and K. P. Moran, "Constriction/spreading resistance model for electronics packaging," in *Proc. ASME/JSME Thermal Engineering Conference*, vol. 4, 1995, pp. 199–206.
- [53] R. J. Moffat, "Modeling air-cooled heat sinks as heat exchangers," in *Proc. 23rd Annual IEEE Semiconductor Thermal Measurement and Management Symp*, March 2007, pp. 200–207. DOI: [10.1109/STHERM.2007.352424](https://doi.org/10.1109/STHERM.2007.352424)
- [54] Y. S. Muzychka, "Generalized models for laminar developing flows in heat sinks and heat exchangers," *Heat Transfer Engineering*, vol. 34, no. 2-3, pp. 178–191, January 2013. DOI: [10.1080/01457632.2013.703517](https://doi.org/10.1080/01457632.2013.703517)

- 
- [55] P. Teertstra, M. M. Yovanovich, and J. R. Culham, “Analytical forced convection modeling of plate fin heat sinks,” *Journal of Electronics Manufacturing*, vol. 10, no. 04, pp. 253–261, 2000. DOI: [10.1142/s0960313100000320](https://doi.org/10.1142/s0960313100000320)
- [56] Y. S. Muzychka and M. M. Yovanovich, “Laminar forced convection heat transfer in the combined entry region of non-circular ducts,” *Journal of Heat Transfer*, vol. 126, no. 1, pp. 55–61, February 2004. DOI: [10.1115/1.1643752](https://doi.org/10.1115/1.1643752)
- [57] Y. S. Muzychka and M. M. Yovanovich, “Pressure drop in laminar developing flow in noncircular ducts: A scaling and modeling approach,” *Journal of Fluids Engineering*, vol. 131, no. 11, p. 111105, 2009. DOI: [10.1115/1.4000377](https://doi.org/10.1115/1.4000377)
- [58] F. M. White, *Fluid Mechanics (McGraw-Hill Series in Mechanical Engineering)*. McGraw-Hill Education, 1998.
- [59] Y. Shabany, *Heat Transfer: Thermal Management of Electronics*. CRC Press, 2009.
- [60] J. R. Culham, W. A. Khan, M. M. Yovanovich, and Y. S. Muzychka, “The influence of material properties and spreading resistance in the thermal design of plate fin heat sinks,” *Journal of Electronic Packaging*, vol. 129, no. 1, pp. 76–81, 2007. DOI: [10.1115/1.2429713](https://doi.org/10.1115/1.2429713)
- [61] W. M. Kays and M. E. Crawford, *Convective Heat and Mass Transfer*. McGraw-Hill Science/Engineering/Math, 1993.
- [62] R. Parsons, *2005 ASHRAE HANDBOOK: Fundamentals: Inch-Pound Edition (2005 ASHRAE HANDBOOK: Fundamentals: I-P Edition)*. American Society of Heating, 2005.
- [63] Verein Deutscher Ingenieure, *VDI-Wärmeatlas (VDI-Buch) (German Edition)*. Springer, 2005.
- [64] S. L. Dixon and C. Hall, *Fluid Mechanics and Thermodynamics of Turbomachinery*. Butterworth-Heinemann, 2010.
- [65] H. Ertl, T. Wiesinger, and J. W. Kolar, “Active voltage balancing of DC-link electrolytic capacitors,” *IET Power Electronics*, vol. 1, no. 4, pp. 488–496, December 2008. DOI: [10.1049/iet-pel:20070390](https://doi.org/10.1049/iet-pel:20070390)

- [66] *Cortland Cable*, [Online]. Available: <http://www.cortlandcable.com>. [Accessed: April, 2013].
- [67] E. Murtola, S. M. Neuhold, and P. Anliker, "Hyperelastic high voltage conductor for electric drilling," in *Proc. 4th Int. Conf. on Composite Materials & Structures for Offshore Operations (CMOO 2005)*, Houston (TX), USA, October 4-6, 2005, pp. 1-11.
- [68] S. M. Neuhold, "A hyper elastic conductor for bulk energy transfer in the wall of spoolable tubes for electric deep drilling," Ph.D. dissertation, Swiss Federal Institute of Technology Zurich (ETH Zurich), 2007.
- [69] Huber+Suhner, "Radox GWK Cables," datasheet, 2011.
- [70] Klotz a+i+s, "AWG Tabelle," data table, 2005.
- [71] S. Mounce, B. McPherson, R. Schupbach, and A. B. Lostetter, "Ultra-lightweight, high efficiency SiC based power electronic converters for extreme environments," in *Proc. IEEE Aerospace Conf.*, 2006, pp. 1-19. DOI: [10.1109/AERO.2006.1655979](https://doi.org/10.1109/AERO.2006.1655979)
- [72] J. Millán, P. Godignon, X. Perpiñà, A. Pérez-Tomás, and J. Rebollo, "A survey of wide bandgap power semiconductor devices," *IEEE Transactions on Power Electronics*, vol. 29, no. 5, pp. 2155-2163, May 2014. DOI: [10.1109/TPEL.2013.2268900](https://doi.org/10.1109/TPEL.2013.2268900)
- [73] B. Wrzecionko, D. Bortis, and J. W. Kolar, "A 120 °C ambient temperature forced air-cooled normally-off SiC JFET automotive inverter system," *IEEE Transactions on Power Electronics*, vol. 29, no. 5, pp. 2345-2358, May 2014. DOI: [10.1109/TPEL.2013.2294906](https://doi.org/10.1109/TPEL.2013.2294906)
- [74] M. Schweizer and J. W. Kolar, "Design and implementation of a highly efficient three-level t-type converter for low-voltage applications," *IEEE Transactions on Power Electronics*, vol. 28, no. 2, pp. 899-907, February 2013. DOI: [10.1109/TPEL.2012.2203151](https://doi.org/10.1109/TPEL.2012.2203151)
- [75] R. A. Friedemann, F. Krismer, and J. W. Kolar, "Design of a minimum weight dual active bridge converter for an airborne wind turbine system," in *Proc. 27th Annual IEEE Applied Power*

- Electronics Conf. and Exposition (APEC 2012)*, February 2012, pp. 509–516. DOI: [10.1109/APEC.2012.6165868](https://doi.org/10.1109/APEC.2012.6165868)
- [76] M. R. Islam, G. Lei, Y. Guo, and J. Zhu, “Optimal design of high-frequency magnetic links for power converters used in grid-connected renewable energy systems,” *IEEE Transactions on Magnetics*, vol. 50, no. 11, pp. 1–4, November 2014. DOI: [10.1109/TMAG.2014.2329939](https://doi.org/10.1109/TMAG.2014.2329939)
- [77] W. Water and J. Lu, “Shielding analysis of high-frequency coaxial transformers used for electric vehicle on-board charging systems,” *IEEE Transactions on Magnetics*, vol. 49, no. 7, pp. 4005–4008, July 2013. DOI: [10.1109/TMAG.2013.2239267](https://doi.org/10.1109/TMAG.2013.2239267)
- [78] W. Wang, K. W. E. Cheng, K. Ding, and T. F. Chan, “A polymer-bonded magnetic core for high-frequency converters,” *IEEE Transactions on Magnetics*, vol. 48, no. 11, pp. 4328–4331, November 2012. DOI: [10.1109/TMAG.2012.2197597](https://doi.org/10.1109/TMAG.2012.2197597)
- [79] R. A. Jabr, “Application of geometric programming to transformer design,” *IEEE Transactions on Magnetics*, vol. 41, no. 11, pp. 4261–4269, November 2005. DOI: [10.1109/TMAG.2005.856921](https://doi.org/10.1109/TMAG.2005.856921)
- [80] G. Ortiz, J. Biela, and J. W. Kolar, “Optimized design of medium frequency transformers with high isolation requirements,” in *Proc. 36th Annual Conf. IEEE Industrial Electronics Society (IECON 2010)*, November 2010, pp. 631–638. DOI: [10.1109/IECON.2010.5675240](https://doi.org/10.1109/IECON.2010.5675240)
- [81] M. Leibl, G. Ortiz, and J. W. Kolar, “Design and experimental analysis of a medium-frequency transformer for solid-state transformer applications,” *IEEE Journal of Emerging and Selected Topics in Power Electronics*, vol. 5, no. 1, pp. 110–123, March 2017. DOI: [10.1109/JESTPE.2016.2623679](https://doi.org/10.1109/JESTPE.2016.2623679)
- [82] T. Guillod, J. E. Huber, G. Ortiz, A. De, C. M. Franck, and J. W. Kolar, “Characterization of the voltage and electric field stresses in multi-cell solid-state transformers,” in *Proc. IEEE Energy Conversion Congress and Exposition (ECCE USA 2014)*, September 2014, pp. 4726–4734. DOI: [10.1109/ECCE.2014.6954048](https://doi.org/10.1109/ECCE.2014.6954048)

- [83] F. Krismer and J. W. Kolar, “Closed form solution for minimum conduction loss modulation of DAB converters,” *IEEE Transactions on Power Electronics*, vol. 27, no. 1, pp. 174–188, January 2012. DOI: [10.1109/TPEL.2011.2157976](https://doi.org/10.1109/TPEL.2011.2157976)
- [84] J. Everts, “Closed-form solution for efficient ZVS modulation of DAB converters,” *IEEE Transactions on Power Electronics*, vol. 32, no. 10, pp. 7561–7576, October 2017. DOI: [10.1109/TPEL.2016.2633507](https://doi.org/10.1109/TPEL.2016.2633507)
- [85] R. Kotte, E. Gockenbach, and H. Borsi, “About the breakdown and partial discharge behavior of different heat-resistant cast resins,” in *Proc. 6th Int. IEEE Conf. on Properties and Applications of Dielectric Materials*, vol. 2, 2000, pp. 583–586. DOI: [10.1109/ICPADM.2000.876076](https://doi.org/10.1109/ICPADM.2000.876076)
- [86] A. Kaindl, L. Schon, R. Rockelein, and H. Borsi, “Influence of processing parameters on electrical insulation properties for epoxy-resin materials - An investigation by experiment and finite element analysis simulation,” in *Proc. IEEE Int. Symp. Electrical Insulation*, 2000, pp. 48–51. DOI: [10.1109/ELINSL.2000.845434](https://doi.org/10.1109/ELINSL.2000.845434)
- [87] M. Beyer, W. Boeck, K. Möller, and W. Zaengl, “Hochspannungsmeßtechnik,” in *Hochspannungstechnik*. Springer, January 1986.
- [88] R. Schifani and V. Gagliardo, “Partial discharge patterns and aging phenomena at different temperatures in filled and unfilled epoxy, by a modified cigre setup, method i,” in *Proc. 5th Int. IEEE Conf. on Conduction and Breakdown in Solid Dielectrics*, July 1995, pp. 329–333. DOI: [10.1109/ICSD.1995.523003](https://doi.org/10.1109/ICSD.1995.523003)
- [89] F. Krismer and J. W. Kolar, “Accurate small-signal model for the digital control of an automotive bidirectional dual active bridge,” *IEEE Transactions on Power Electronics*, vol. 24, no. 12, pp. 2756–2768, December 2009. DOI: [10.1109/TPEL.2009.2027904](https://doi.org/10.1109/TPEL.2009.2027904)
- [90] R. W. Erickson, “Optimal single resistors damping of input filters,” in *Proc. 14th Annual IEEE Applied Power Electronics Conf. and Exposition (APEC 1999)*, vol. 2, March 1999, pp. 1073–1079. DOI: [10.1109/APEC.1999.750502](https://doi.org/10.1109/APEC.1999.750502)

- 
- [91] R. W. S. A. V. Oppenheim, *Discrete-Time Signal Processing*. Pearson Education Limited, 2013.
- [92] K. Edelmoser, H. Ertl, and F. Zach, “A multi-cell switch-mode power-supply concept featuring inherent input voltage balancing,” in *Proc. 10th Int. World Scientific and Engineering Academy and Society (WSEAS) Conf. on Circuits (ICC 2006)*, Stevens Point, Wisconsin, USA, 2006, pp. 201–206.
- [93] M. Kasper, D. Bortis, and J. W. Kolar, “Novel high voltage conversion ratio ”rainstick” DC/DC converters,” in *Proc. IEEE Energy Conversion Congress and Exposition (ECCE USA 2013)*, September 2013, pp. 789–796. DOI: [10.1109/ECCE.2013.6646783](https://doi.org/10.1109/ECCE.2013.6646783)
- [94] R. L. Steigerwald, “A review of soft-switching techniques in high performance DC power supplies,” in *Proc. 21st Annual Conf. IEEE Industrial Electronics Society (IECON 1995)*, vol. 1, November 1995, pp. 1–7. DOI: [10.1109/IECON.1995.483324](https://doi.org/10.1109/IECON.1995.483324)
- [95] STMicroelectronics, “Datasheet, STB20NM60-1 STP20NM60FP STB20NM60 STP20NM60 STW20NM60, Revision 12,” datasheet, 2007.
- [96] L. Dalessandro, F. da Silveira Cavalcante, and J. W. Kolar, “Self-capacitance of high-voltage transformers,” *IEEE Transactions on Power Electronics*, vol. 22, no. 5, pp. 2081–2092, September 2007. DOI: [10.1109/TPEL.2007.904252](https://doi.org/10.1109/TPEL.2007.904252)
- [97] R. Burkart and J. W. Kolar, “Component cost models for multi-objective optimizations of switched-mode power converters,” in *Proc. IEEE Energy Conversion Congress and Exposition (ECCE USA 2013)*, September 2013, pp. 2139–2146. DOI: [10.1109/ECCE.2013.6646971](https://doi.org/10.1109/ECCE.2013.6646971)
- [98] C. Soutis, “Fibre reinforced composites in aircraft construction,” *Progress in Aerospace Sciences*, vol. 41, no. 2, pp. 143–151, February 2005. DOI: [10.1016/j.paerosci.2005.02.004](https://doi.org/10.1016/j.paerosci.2005.02.004)
- [99] H. P. Feustel and J. Koszescha, “ECPE-roadmap 2025 automotive & aerospace power electronics,” in *Proc. ECPE Roadmap Workshop*, Munich, Germany, March 2015.

- [100] F. W. Lanchester, “A contribution to the theory of propulsion and the screw propeller,” *Journal of the American Society for Naval Engineers*, vol. 27, no. 2, pp. 509–510, 1915. DOI: [10.1111/j.1559-3584.1915.tb00408.x](https://doi.org/10.1111/j.1559-3584.1915.tb00408.x)
- [101] A. J. Healey, S. M. Rock, S. Cody, D. Miles, and J. P. Brown, “Toward an improved understanding of thruster dynamics for underwater vehicles,” *IEEE Journal of Oceanic Engineering*, vol. 20, no. 4, pp. 354–361, October 1995. DOI: [10.1109/48.468252](https://doi.org/10.1109/48.468252)
- [102] G. G. Carlos, M. G. Bulmaro, A. C. Honorato, and P. M. Amparo, “Design of a 3.5 meters rotor two bladed horizontal axis wind turbine,” in *Proc. 20th Int. Conf. on Electronics, Communications and Computer (CONIELECOMP 2010)*, February 2010, pp. 247–251. DOI: [10.1109/CONIELECOMP.2010.5440758](https://doi.org/10.1109/CONIELECOMP.2010.5440758)

# Curriculum Vitae

## Personal Information



Name	Christoph GAMMETER
Date of birth	January 30, 1985
Nationality	Swiss / USA
Citizen of	Zürich, Switzerland
Contact	<a href="mailto:cgammete@gmail.com">cgammete@gmail.com</a> +41 (0)76 397 84 08

## Education

2012 – 2017	Doctorate at the Power Electronic Systems Laboratory (PES), ETH Zurich
2012	Master Thesis at Power Electronic Systems Laboratory (PES), ETH Zurich
2006 – 2012	BSc and MSc studies in information technology and electrical engineering, ETH Zurich
2004 – 2005	Officers Training, Swiss Military Services
1997 – 2004	State College of Higher Educations Rämibühl, Zürich

## Work Experience

2012 – 2017	Research assistant at the Power Electronic Systems Laboratory (PES), ETH Zurich
2009 – 2010	Internship at Bombardier Transportation Switzerland, Zürich
2007 – 2009	Teaching Assistant at ETH Zurich